



HAL
open science

Identification of strainrate dependent hardening sensitivity of metallic sheets under in-plane biaxial loading

Wei Liu

► **To cite this version:**

Wei Liu. Identification of strainrate dependent hardening sensitivity of metallic sheets under in-plane biaxial loading. Mechanical engineering [physics.class-ph]. INSA de Rennes, 2015. English. NNT : 2015ISAR0005 . tel-01149144

HAL Id: tel-01149144

<https://theses.hal.science/tel-01149144>

Submitted on 6 May 2015

HAL is a multi-disciplinary open access archive for the deposit and dissemination of scientific research documents, whether they are published or not. The documents may come from teaching and research institutions in France or abroad, or from public or private research centers.

L'archive ouverte pluridisciplinaire **HAL**, est destinée au dépôt et à la diffusion de documents scientifiques de niveau recherche, publiés ou non, émanant des établissements d'enseignement et de recherche français ou étrangers, des laboratoires publics ou privés.

Résumé

Les procédés de mise en forme des tôles métalliques sont largement utilisés dans l'industrie mécanique. La simulation numérique des opérations de mise en forme nécessite une caractérisation précise des modèles de comportement rhéologique des matériaux. Dans de nombreuses opérations de mise en forme des tôles métalliques telle que l'emboutissage, l'hydroformage, ..., de grandes déformations et des vitesses de déformations dites intermédiaires peuvent être atteintes sous des états biaxiaux de déformation ou de contrainte.

L'objectif de ce travail est de montrer le potentiel de l'essai de traction bi-axiale pour caractériser l'érouissage des tôles métalliques pour de grandes déformations et dans une gamme de vitesse de déformation dite intermédiaire. A partir de simulations numériques, une forme optimale d'éprouvette en croix, permettant d'atteindre 30% de déformation plastique équivalente dans la zone centrale de l'éprouvette sous un chargement équi-biaxial, a été proposée.

Par la suite, des essais quasi-statiques et dynamiques de traction bi-axiale ont été réalisés sur la forme d'éprouvette proposée à partir d'une machine dédiée d'essais servo-hydraulique à quatre vérins. Dans un premier temps, le matériau choisi est un alliage d'aluminium AA5086 ne présentant pas de dépendance à la vitesse de déformation. Les déformations expérimentales sont déterminées à partir de la technique de corrélation d'images. L'érouissage isotrope de différents modèles est identifié à partir d'une procédure inverse basée sur une modélisation éléments finis de l'essai de traction bi-axiale. Trois critères de plasticité (Mises, Hill 48 et Bron et Besson) ont été successivement utilisés pour l'identification des paramètres des lois d'érouissage. Les résultats obtenus montrent d'une part que la modélisation est très sensible au critère de plasticité choisi, et d'autre part que le critère de Bron et Besson permet d'obtenir une très bonne corrélation entre les courbes d'érouissage identifiées à partir de l'essai bi-axial et de l'essai uni-axial. Pour les tests dynamiques bi-axiaux, les phénomènes de résonance du dispositif mécanique, générés à l'impact initial de début d'essai et matérialisés par de fortes oscillations du signal d'effort, sont atténués par l'interposition d'un élément en élastomère dans le système d'ancrage de chaque bras de l'éprouvette.

Pour finir, la méthodologie d'identification proposée est appliquée à la caractérisation du comportement viscoplastique d'un acier dual phase DP600. Les courbes d'érouissage identifiées à partir des essais bi-axiaux ont été comparées à celles obtenues par des essais uni-axiaux pour une gamme de vitesse de déformation allant de $10^{-3}s^{-1}$ à 10^1s^{-1} . Le DP600 présente une même sensibilité à la vitesse de déformation quelque soit la sollicitation, uni-axiale ou bi-axiale. Les lois d'érouissage de Ludwick et de Voce, identifiées jusqu'à 30% de déformation plastique équivalente sur la base de données expérimentales constituées des essais bi-axiaux, sont relativement proches. Les différences observées entre ces courbes d'érouissage et celles identifiées à partir des essais de traction uni-axiaux montrent tout l'intérêt de l'essai de traction bi-axiale sur éprouvette en croix.

Abstract

Sheet metal forming processes are widely adopted to produce panels, tubes, profiled parts in manufacturing industry. The numerical simulation of the forming processes requires accurate constitutive models of material. In many sheet metal working operations such as stamping, hydroforming, ..., large strains and intermediate strain rates can be reached under biaxial strain or stress states.

The objective of this work is to show the potential of the biaxial in-plane tensile test to characterize the hardening behaviour of metal sheets up to large strain levels. By numerical investigation, an optimal cruciform shape is designed to obtain large equivalent plastic strain, up to 30%, at the central zone under equi-biaxial strain path. As expected, the initial cracks of tested specimens are always observed at the central zone.

Then, quasi-static and dynamic biaxial tensile tests on in-plane cross specimens have been performed on a dedicated servo-hydraulic machine. These biaxial tensile tests have been carried out on aluminium alloy AA5086 to validate the identification methodology of hardening behaviour under biaxial loading. This alloy has been chosen since its hardening behaviour is not dependent on the strain rate. Digital Image Correlation (DIC) technique is used for strain measurement. The parameters of isotropic hardening models are identified by inverse analysis based on the finite element model of the biaxial tensile test. Three yield criteria of Mises, Hill48 and Bron and Besson are compared for the parameter identification of different hardening laws. It is shown that the hardening law identified by biaxial test is precise only if an appropriate yield function is preliminarily determined. The biaxial flow stress curve identified with Bron and Besson yield function have been found in good agreement with the experimental flow stress curve obtained from uniaxial tensile tests. For biaxial tests at intermediate strain rates, damping layers are adopted to reduce oscillations on force versus time curves. The comparison of flow stress curves, identified from quasi-static and dynamic biaxial in-plane tensile tests on the non strain rate-dependent material AA5086, validates the identification methodology of strain-rate dependent hardening models.

Finally, the proposed methodology is applied to the hardening characterization of a strain-rate dependent Dual Phase steel DP600 at room temperature. Identified biaxial flow stress curves have been compared with uniaxial ones for different strain rates ($\dot{\epsilon} = 10^{-3}s^{-1}$, $10^{-1}s^{-1}$ and 10^1s^{-1}). DP600 steel exhibits the same positive strain rate sensitivity for uniaxial and biaxial strain states. The biaxial flow stress curves identified on the basis of Ludwick and Voce hardening models are close, up to equivalent plastic strains of 30%. The benefits of the proposed methodology, based on a biaxial in-plane tensile test carried out on cross specimen, are clearly shown since the hardening behaviour identified in this case for large strains (up to 30%) is very different from the one identified from uniaxial tensile test on a smaller strain range.

Thèse

2015

Wei LIU



THESE INSA Rennes présentée par
sous le sceau de l'Université européenne de Bretagne Wei LIU
pour obtenir le titre de
DOCTEUR DE L'INSA DE RENNES ECOLE DOCTORALE : SDLM
Spécialité : Génie Mécanique LABORATOIRE : LGCGM

Identification of strain-rate dependent hardening sensitivity of metallic sheets under in-plane biaxial loading

Thèse soutenue le 10.03.2015
devant le jury composé de :

Franck Morel
Professeur, ENSAM d' Angers / Président du jury
Salima Bouvier
Professeur, Université Technologique de Compiègne / Rapporteur
Vincent Grolleau
Professeur, ENSI de Bretagne-Sud / Rapporteur
Dominique Guines
Maître de Conférences, INSA Rennes / Co-encadrant
Lionel Léotoing
Maître de Conférences, INSA Rennes / Co-encadrant
Eric Ragneau
Professeur, INSA Rennes / Directeur de thèse

Identification of strain-rate dependent hardening sensitivity of metallic sheets under in-plane biaxial loading

Wei LIU



En partenariat avec



Acknowledgements

First and foremost, I would like to express my sincere appreciation to my supervisors, Professor Eric RAGNEAU, Dr. Dominique GUINES and Dr. Lionel LETOING, for giving me the opportunity to work in Laboratory of Civil and Mechanical Engineering (LGCGM). Thank you so much for your patience, encouragement and inspiration. I have greatly benefited from your instructions and attitudes for the thesis.

I would like to express my great gratitude to Professor Salima Bouvier (Université Technologique de Compiègne), Professor Vincent Grolleau (ENSI de Bretagne-Sud) and Professor Franck Morel (ENSAM Angers) for your work as members of jury.

I would also like to say many thanks to all the colleagues at LGCGM. Thank you so much for your discussion and friendship. I 'd like to express my special appreciation to engineers for specimen preparation and technical support. I could not complete the work without your help. I will cherish my experiences of working and living in INSA de Rennes.

I would like to express great acknowledgement to China Scholarship Council (CSC) for the financial support during my work. I would like to acknowledge Northwestern Polytechnical University (NPU) for helping me to apply for studying in France.

I am willing to express my heartfelt appreciation to my parents, my sister, my family and my friends. Your endless support and confidence are great treasure in my life.

Abstract

Sheet metal forming processes are widely adopted to produce panels, tubes, profiled parts in manufacturing industry. The numerical simulation of the forming processes requires accurate constitutive models of material. In many sheet metal working operations such as stamping, hydroforming, ..., large strains and intermediate strain rates can be reached under biaxial strain or stress states.

The objective of this work is to show the potential of the biaxial in-plane tensile test to characterize the hardening behaviour of metal sheets up to large strain levels. By numerical investigation, an optimal cruciform shape is designed to obtain large equivalent plastic strain, up to 30%, at the central zone under equi-biaxial strain path. As expected, the initial cracks of tested specimens are always observed at the central zone.

Then, quasi-static and dynamic biaxial tensile tests on in-plane cross specimens have been performed on a dedicated servo-hydraulic machine. These biaxial tensile tests have been carried out on aluminium alloy AA5086 to validate the identification methodology of hardening behaviour under biaxial loading. This alloy has been chosen since its hardening behaviour is not dependent on the strain rate. Digital Image Correlation (DIC) technique is used for strain measurement. The parameters of isotropic hardening models are identified by inverse analysis based on the finite element model of the biaxial tensile test. Three yield criteria of Mises, Hill48 and Bron and Besson are compared for the parameter identification of different hardening laws. It is shown that the hardening law identified by biaxial test is precise only if an appropriate yield function is preliminarily determined. The biaxial flow stress curve identified with Bron and Besson yield function have been found in good agreement with the experimental flow stress curve obtained from uniaxial tensile tests. For biaxial tests at intermediate strain rates, damping layers are adopted to reduce oscillations on force versus time curves. The comparison of flow stress curves, identified from quasi-static and dynamic biaxial in-plane tensile tests on the non strain rate-dependent material AA5086, validates the identification methodology of strain-rate dependent hardening models.

Finally, the proposed methodology is applied to the hardening characterization of a strain-rate dependent Dual Phase steel DP600 at room temperature. Identified biaxial flow stress curves have been compared with uniaxial ones for different strain rates ($\dot{\epsilon} = 10^{-3} s^{-1}, 10^{-1} s^{-1}$ and $10^1 s^{-1}$). DP600 steel exhibits the same positive strain rate sensitivity for uniaxial and biaxial strain states. The biaxial flow stress curves identified on the basis of Ludwick and Voce hardening models are close, up to equivalent plastic strains of 30%. The benefits of the proposed methodology, based on

a biaxial in-plane tensile test carried out on cross specimen, are clearly shown since the hardening behaviour identified in this case for large strains (up to 30%) is very different from the one identified from uniaxial tensile test on a smaller strain range.

Contents

General introduction	1
1. Phenomenological modelling of sheet metal	3
1.1 Introduction	5
1.2 Influence of deformation mode	6
1.2.1 Strain state and path	6
1.2.2 Strain rate	7
1.3 Mathematical modelling of elastoplastic behavior	9
1.3.1 Constitutive relations	9
1.3.2 Yield criterion	10
1.3.2.1 Mises yield criterion	11
1.3.2.2 Hill 48 yield criterion	12
1.3.2.3 Yld2000-2d yield criterion	12
1.3.2.4 Yld2004-18p and Yld2004-13p yield criteria.....	14
1.3.2.5 BBC 2005 yield criterion	14
1.3.2.6 Bron and Besson 2004 yield criterion	15
1.3.3 Hardening law	16
1.3.3.1 Strain hardening.....	16
1.3.3.2 Influence of temperature and strain rate	17
1.3.3.3 Simple models	19
1.3.3.4 Integrated models	21
1.4 Mechanical tests of sheet metal	23
1.4.1 Uniaxial test	24
1.4.1.1 Quasi-static uniaxial test	24
1.4.1.2 Dynamic uniaxial test.....	25
1.4.1.3 Split Hopkinson pressure bar	30
1.4.2 Bulge test	31
1.4.2.1 Quasi-static bulge test.....	31
1.4.2.2 Dynamic bulge test.....	33
1.4.3 Plane strain test	34
1.4.4 Simple shear test	35
1.4.4.1 Quasi-static simple shear test	35
1.4.4.2 Dynamic simple shear test.....	36
1.4.5 Multi-axial tests	37
1.4.5.1 Biaxial tensile test	37
1.4.5.2 Combined test.....	38
1.5 Conclusion.....	40

2. Shape design of cruciform specimen	41
2.1 Introduction	43
2.2 Biaxial testing devices	43
2.3 Application of cruciform specimen	46
2.3.1 Characterization of yield locus	46
2.3.2 Identification of hardening model	49
2.3.3 Determination of forming limit curve	51
2.4 Numerical investigation of cruciform shapes	55
2.4.1 Basic shape	56
2.4.2 Notches at intersections	58
2.4.3 Slits along arms	60
2.4.4 Thickness reduction	62
2.4.5 Optimal shape design	64
2.5 Conclusion	67
3. Identification methodology of hardening behaviour under in-plane biaxial loading	69
3.1 Introduction	71
3.2 Uniaxial test of AA5086	71
3.2.1 Digital image correlation	71
3.2.1 Experimental result	73
3.2.2 Uniaxial flow stress curve	75
3.3 Quasi-static biaxial test of AA5086	77
3.3.1 Experimental result	77
3.3.2 Procedure of inverse analysis	82
3.3.3 Finite element model	84
3.3.3.1 Solid element	84
3.3.3.2 Shell element	86
3.3.4 Parameter identification	88
3.3.4.1 Material models	88
3.3.4.2 Identified results	90
3.4 Dynamic biaxial test of AA5086	94
3.4.1 Load ringing phenomenon	94
3.4.2 Damping and experimental results	99
3.4.3 Parameter identification	105
3.5 Conclusion	106
4. Identification of strain-rate dependent hardening laws of DP600 by biaxial tests	109
4.1 Introduction	111
4.2 Uniaxial test of DP600	111
4.2.1 Experimental result	111
4.2.2 Strain rate sensitivity	114
4.3 Experimental results of biaxial tests	120
4.3.1 Loading speed of 0.02mm/s	121

4.3.2 Loading speed of 1mm/s.....	124
4.3.2 Loading speed of 250mm/s.....	127
4.4 Parameter identification of DP600.....	130
4.4.1 Material models	131
4.4.2 Identified results.....	132
4.5 Conclusion.....	137
Conclusions and perspectives	139
A. Appendix	141
(I) Drafting of cruciform specimen	141
(II) modeFRONTIER flowchart with subroutine UHARD.....	142
(III) modeFRONTIER flowchart with subroutine UMAT	143
(IV) modeFRONTIER flowchart with SRS by uniaxial tensile tests.....	144
(V) modeFRONTIER flowchart with SRS by biaxial tensile tests	145
References.....	147

Figures

Fig. 1-1 Physical based and phenomenological modelling of metals	5
Fig. 1-2 Drawing of cylinder part	6
Fig. 1-3 Stress and strain state of cylinder part.....	6
Fig. 1-4 Strain paths for cylinder part.....	6
Fig. 1-5 Strain rate jump-down test ^[22]	8
Fig. 1-6 Hardening models	10
Fig. 1-7 Uniaxial tensile tests along different directions	11
Fig. 1-8 Schematic representation of four types stress-strain curves ^[37]	19
Fig. 1-9 Representative strain and stress states on yield locus	24
Fig. 1-10 Schematic of strain rate ranges and experimental techniques ^[52]	24
Fig. 1-11 Uniaxial tensile specimen.....	25
Fig. 1-12 Shortened upper grip and measured force curve ^[56]	26
Fig. 1-13 Dynamic testing device with long bar ^[58]	27
Fig. 1-14 A simplified schematic of the modified servo-hydraulic machine ^[59]	27
Fig. 1-15 Position of strain gauges on specimen for local force measurement ^[60]	28
Fig. 1-16 Comparisons of force measured by local force transducer and DLC ^[60]	28
Fig. 1-17 Dynamic tensile testing device with damping ^[61]	29
Fig. 1-18 Experimental set-up for dynamic uniaxial compression ^[64]	30
Fig. 1-19 Schematic of Split Hopkinson Pressure Bar and travelling wave diagram..	31
Fig. 1-20 Bulge test ^[70]	32
Fig. 1-21 Dynamic bulge testing device ^[75]	33
Fig. 1-22 Plane strain specimens ^{[79] [82]}	34
Fig. 1-23 Cruciform shape for plane-strain tension ^[83]	34
Fig. 1-24 Shear testing specimen (ASTM B831-11) ^[87]	35
Fig. 1-25 Specimen of double shear test ^[89]	36
Fig. 1-26 Experimental setup of direct impact ^[89]	37
Fig. 1-27 Biaxial tensile tests.....	37
Fig. 1-28 Uniaxial tension-internal pressure testing machine	38
Fig. 1-29 Combined plane strain-simple shear test ^[12]	39
Fig. 1-30 Experimental tools and sample under heterogeneous deformation ^[107]	39
Fig. 2-1 Applications of biaxial tests for material modelling	43
Fig. 2-2 Link mechanism attachments for biaxial test (FER 1988).....	44
Fig. 2-3 Stand-alone biaxial testing machines (MAK 1992, KUW 1998).....	44
Fig. 2-4 Dynamic biaxial testing machine	45
Fig. 2-5 Biaxial testing machine and measurement systems	45
Fig. 2-6 Cruciform shape (MUL, 1996).....	46
Fig. 2-7 Cruciform shape (NAK, 2003).....	46
Fig. 2-8 Cruciform Shape (KUW, 1998)	47
Fig. 2-9 Cruciform shape (MER, 2008).....	47
Fig. 2-10 Cruciform shape of UT/PST (a) and UT/EBT (b) specimen (TEA, 2010) ..	48

Fig. 2-11 Cruciform shape (PRA, 2014).....	48
Fig. 2-12 Cruciform shape (ZHA, 2014)	49
Fig. 2-13 Cruciform shapes (MAK, 1992; GRE, 2004)	50
Fig. 2-14 Cruciform shapes (GOZ, 2004; KUL, 2011)	51
Fig. 2-15 Cruciform shape (MER, 2013).....	51
Fig. 2-16 Cruciform shape (YU, 2002).....	52
Fig. 2-17 Cruciform shape (TAS, 2008).....	52
Fig. 2-18 Cruciform shapes (ABU, 2009)	53
Fig. 2-19 Cruciform Shapes (LEE, 2015)	53
Fig. 2-20 Cruciform specimen with further curved thickness reduction	54
Fig. 2-21 FLC by cruciform biaxial tests.....	55
Fig. 2-22 True stress-plastic strain curve for FE analysis.....	56
Fig. 2-23 Basic cruciform shape	57
Fig. 2-24 Mesh of basic shape	57
Fig. 2-25 Major principal, equivalent plastic strain and strain state of basic shape	57
Fig. 2-26 Shape with notches.....	58
Fig. 2-27 Effect of distance D (R=5mm).....	58
Fig. 2-28 Effect of radius (D-R=10mm)	59
Fig. 2-29 Mesh of shape with notches (D=13mm, R=3mm).....	59
Fig. 2-30 Major principal, equivalent plastic strain and strain state of shape with notches	60
Fig. 2-31 Shape with slits.....	60
Fig. 2-32 Comparison of shapes with slits.....	61
Fig. 2-33 Mesh of shape with slits	61
Fig. 2-34 Major principal, equivalent plastic strain and strain state of shape with slits	62
Fig. 2-35 Shape with thickness reduction	62
Fig. 2-36 Effect of radius of thickness reduced zone.....	63
Fig. 2-37 Effect of thickness of thickness-reduced zone	63
Fig. 2-38 FE model of shape with thickness reduction and notch (r=5mm, t=0.5mm)	64
Fig. 2-39 Major principal, equivalent plastic strain and strain state of shape with thickness reduction and notch	64
Fig. 2-40 Optimal shape for large strains.....	65
Fig. 2-41 Mesh of optimal shape	65
Fig. 2-42 Major principal, equivalent plastic strain and strain state of optimal shape	66
Fig. 2-43 Strain paths of optimal shape	66
Fig. 3-1 Procedure of strain measurement by DIC	72
Fig. 3-2 Subsets for DIC	73
Fig. 3-3 Mode for strain calculation	73
Fig. 3-4 Shape of uniaxial testing specimen	73
Fig. 3-5 Gauge zone of uniaxial testing specimen.....	74
Fig. 3-6 Strain curves of static (1mm/s) and dynamic (500mm/s) uniaxial test.....	74

Fig. 3-7 Force curves of static (1mm/s) and dynamic (500mm/s) uniaxial test	75
Fig. 3-8 Static and dynamic uniaxial true stress-true strain curves of AA5086	75
Fig. 3-9 Extrapolation of static and dynamic uniaxial flowing curve.....	77
Fig. 3-10 Cruciform specimen of AA5086	77
Fig. 3-11 Linkage between specimen and sliding bar.....	78
Fig. 3-12 Central zone of quasi-static specimen (speckle pattern and initial crack) ..	78
Fig. 3-13 Gauge zone of static specimen	79
Fig. 3-14 Displacement vectors of static specimen	79
Fig. 3-15 Equivalent strain, principal strain field and strain state of quasi-static biaxial specimen	79
Fig. 3-16 Experimental strain curves of quasi-static biaxial testing specimen.....	80
Fig. 3-17 Strain path and strain rate evolution at central point of quasi-static specimen	81
Fig. 3-18 Measured force curves of quasi-static biaxial test	81
Fig. 3-19 Pre-processed experimental force and strain curves of quasi-static biaxial test.....	82
Fig. 3-20 Flowchart of parameter identification	83
Fig. 3-21 Zone to be refined (C3D4_1, Size:0.5, Elements:66322, CPU Time: 786.4s)	85
Fig. 3-22 Equivalent strain fields for different mesh size.....	85
Fig. 3-23 Comparison of major and minor principal strains.....	86
Fig. 3-24 Three zones of specimen	86
Fig. 3-25 Comparison of equivalent strain fields between solid (a) and shell (b) elements	87
Fig. 3-26 Comparison of principal strain evolutions between solid (C3D4_5) and shell elements	88
Fig. 3-27 Comparison of yield criteria.....	89
Fig. 3-28 Results of DOE with Mises yield criterion	91
Fig. 3-29 Results of DOE with Hill 48 yield criterion.....	91
Fig. 3-30 Comparison of quasi-static flow stress curves of AA5086	92
Fig. 3-31 Comparison of principal strains between experiments and simulation with Mises	93
Fig. 3-32 Comparison of principal strains between experiments and simulation with Hill48	93
Fig. 3-33 Comparison of principal strains between experiments and simulation with B & B.....	94
Fig. 3-34 Process of dynamic biaxial tensile test.....	94
Fig. 3-35 Velocity of each actuator during dynamic biaxial test.....	95
Fig. 3-36 Crack of dynamic specimen	96
Fig. 3-37 Displacement vectors of dynamic specimen	96
Fig. 3-38 Experimental equivalent and principal strain fields of dynamic biaxial testing specimen.....	96
Fig. 3-39 Experimental strain curves of dynamic biaxial test	97

Fig. 3-40 Strain path and equivalent strain rate at the central point during dynamic test	97
Fig. 3-41 Oscillation of measured force during dynamic biaxial test.....	98
Fig. 3-42 Finite element model for modal analysis	98
Fig. 3-43 First and second modes by numerical simulation	99
Fig. 3-44 Position of damping layer	100
Fig. 3-45 Experimental force-displacement curves of damping layer	100
Fig. 3-46 Loaded velocity of dynamic biaxial test with damping	101
Fig. 3-47 Crack of damped specimen	101
Fig. 3-48 Displacement vectors of damped specimen	101
Fig. 3-49 Experimental equivalent and principal strain field of dynamic specimen with damping.....	102
Fig. 3-50 Experimental strain curves of dynamic biaxial test with damping	102
Fig. 3-51 Strain path and strain rate of dynamic biaxial test with damping	103
Fig. 3-52 Measured force curves of dynamic biaxial test with damping.....	103
Fig. 3-53 Smoothed force curves of dynamic biaxial test with damping	104
Fig. 3-54 Pre-processed curves of force and principal strain of dynamic test with damping.....	104
Fig. 3-55 Comparison of static and dynamic biaxial flow stress curves	105
Fig. 3-56 Comparison of experimental and simulated principal strains for dynamic test	106
Fig. 4-1 Gauge zones of specimen at speeds of 1, 100, 500, 1000 mm/s	112
Fig. 4-2 Uniaxial test of DP600 (1mm/s).....	113
Fig. 4-3 Uniaxial test of DP600 (100mm/s).....	113
Fig. 4-4 Uniaxial test of DP600 (500mm/s).....	113
Fig. 4-5 Uniaxial test of DP600 (1m/s).....	113
Fig. 4-6 True stress-true strain curves of DP600 at different strain rates	114
Fig. 4-7 True stress-plastic strain curves of DP600 by uniaxial tensile tests	114
Fig. 4-8 Parameter identification for rate-dependent hardening model of uniaxial tests	116
Fig. 4-9 Comparison of experimental and identified curves on basis of Ludwick	118
Fig. 4-10 Comparison of experimental and identified curves on basis of Voce.....	120
Fig. 4-11 Cruciform specimen of DP600.....	120
Fig. 4-12 Initial crack at 0.02mm/s.....	121
Fig. 4-13 Displacement vectors at 0.02mm/s.....	121
Fig. 4-14 Equivalent and principal strain fields and strain state at 0.02mm/s	122
Fig. 4-15 Equivalent and principal strain evolutions at the central zone (0.02mm/s).....	122
Fig. 4-16 Strain path and strain rate evolution at the central point (0.02mm/s)	123
Fig. 4-17 Measured forces along two arms (0.02mm/s)	123
Fig. 4-18 Experimental forces and principal strains for identification (0.02mm/s)...	124
Fig. 4-19 Initial crack at 1mm/s	124
Fig. 4-20 Displacement vectors at 1mm/s.....	124
Fig. 4-21 Equivalent and principal strain fields and strain state at 1mm/s	125

Fig. 4-22 Equivalent and principal strain evolutions at the central point (1mm/s)....	125
Fig. 4-23 Strain path and strain rate evolution at the central point (1mm/s)	126
Fig. 4-24 Measured forces along two arms (1mm/s)	126
Fig. 4-25 Experimental forces and principal strains for identification (1mm/s).....	127
Fig. 4-26 Loading velocities of dynamic biaxial test on DP600.....	127
Fig. 4-27 Initial crack at 250mm/s	128
Fig. 4-28 Displacement vectors at 250mm/s.....	128
Fig. 4-29 Equivalent and principal strain fields and strain state at 250mm/s	128
Fig. 4-30 Equivalent, principal strain evolution at the central zone (250mm/s).....	129
Fig. 4-31 Strain path and strain rate evolution at the central zone (250mm/s).....	129
Fig. 4-32 Measured forces along two arms (250mm/s)	130
Fig. 4-33 Experimental forces and principal strains for identification (250mm/s)....	130
Fig. 4-34 Comparison of yield criteria for DP600	131
Fig. 4-35 Comparison of experimental and simulated principal strains (Mises + Ludwick)	133
Fig. 4-36 Comparison of experimental and simulated principal strains (Hill 48 + Ludwick)	134
Fig. 4-37 Comparison of experimental and simulated principal strains (Hill 48 + Voce)	135
Fig. 4-38 Strain-rate dependent hardening laws identified by uniaxial tests.....	136
Fig. 4-39 Strain-rate dependent hardening laws identified by biaxial tests.....	136

Tables

Table 1-1 Forming velocity and strain rate ranges of different forming processes	8
Table 2-1 Optimal dimensions in mm	65
Table 3-1 Main parameters of DIC in CORRELA 2006	72
Table 3-2 Main parameters of measurement system for uniaxial tests of AA5086....	73
Table 3-3 Ludwick parameters identified from uniaxial test on AA5086	76
Table 3-4 Voce parameters identified from uniaxial test on AA5086.....	76
Table 3-5 Main parameters of measurement system for quasi-static biaxial test	78
Table 3-6 Comparison between solid and shell elements	87
Table 3-7 Parameters of Hill 48 yield function for AA5086	89
Table 3-8 Parameters of Bron and Besson 2004 yield function for AA5086	89
Table 3-9 Lower and upper bounds of parameters	90
Table 3-10 Identified parameters of hardening laws with different yield criteria	92
Table 3-11 Main parameters of measurement system for dynamic biaxial test on AA5086	95
Table 3-12 Comparison of identified hardening laws by quasi-static and dynamic tests.....	105
Table 4-1 Main parameters of measurement system for uniaxial tests on DP600....	111
Table 4-2 Identified results on basis of Ludwick law by uniaxial tests on DP600...	116
Table 4-3 Identified results on basis of Voce law by uniaxial tests on DP600	118
Table 4-4 Main parameters of measurement system for biaxial tests on DP600.....	121
Table 4-5 Parameters of Hill 48 yield criterion for DP600	131
Table 4-6 Identified results of DP600 on basis of Mises and Ludwick	132
Table 4-7 Identified results of DP600 on basis of Hill 48 and Ludwick	132
Table 4-8 Identified results of DP600 on basis of Hill 48 and Voce	132

Notations

ε_{ij}	Components of strain tensor
ε_i	Components of principal strains
$\bar{\varepsilon}_p$	Equivalent plastic strain
$\dot{\bar{\varepsilon}}$	Equivalent strain rate
σ_{ij}	Components of stress tensor
σ_i	Components of principal stresses
$\bar{\sigma}$	Equivalent stress
σ_0	Initial yield stress
ε	True strain in one dimension
ε_p	Plastic strain in one dimension
$\dot{\varepsilon}$	True strain rate in one dimension
σ	True stress in one dimension
r_θ	Anisotropic coefficient or Lankford parameter
E	Young's modulus
ν	Poisson's ratio
t	Time
T	Temperature
AA	Aluminium Alloy
DP	Dual Phase
BCC	Body Centred Cubic
FCC	Face Centred Cubic
HCP	Hexagonal Close Packed
DIC	Digital Image Correlation
FE	Finite Element
FLC	Forming Limit Curve
PLC	Portevin-Le Châtelier
SHPB	Split Hopkinson Pressure Bar

SRS	Strain Rate Sensitivity
RD	Rolling Direction
TD	Transverse Direction
ND	Normal Direction
S3	Shell, 3-node, linear triangular element in ABAQUS
C3D4	Continuum, 3-D, 4-node, linear tetrahedral element in ABAQUS

General introduction

Sheet metal forming processes are widely adopted to produce panels, tubes, profiled parts in industry. Numerical simulation can be used to predict the defects of parts and optimize the forming process. An accurate constitutive model of material is critically demanded for numerical simulation. For phenomenological modelling of sheet metals, many aspects should be considered: anisotropy of rolled sheet metals, strain path, large strain level, strain rate, temperature, ... Many constitutive models have been proposed to characterize the plastic behaviour of sheet metals.

Various conventional quasi-static and dynamic tests have been suggested to identify the parameters of material models with some specific limitations for each of them. For example, the deformation level of standardised uniaxial tensile test until necking is not enough large for forming application or the range of strain paths deserved in a bulge test is rather limited. Because the loading ratio along two axes can be online controlled, the in-plane biaxial tests on cruciform specimen can be carried out to realize various proportional or nonproportional strain paths. The biaxial tests on cruciform specimen have been applied for characterization of yield loci, identification of hardening models and determination of Forming Limit Curves (FLC). The shape design of cruciform specimen is a key issue for tests. Many cruciform shapes have been proposed.

A dynamic biaxial tensile testing machine with four independent servo-hydraulic actuators have been developed in LGCGM (Laboratoire de Génie Civil et Génie Mécanique) of INSA de Rennes. Various linear or nonlinear strain paths can be realised by this biaxial machine. The deformation fields of specimen can be calculated by Digital Image Correlation (DIC).

In this work, a cruciform shape is designed to obtain large strains at the central zone of specimen under quasi-equibiaxial tensile path. Quasi-static and dynamic biaxial tensile tests are performed to identify strain-rate dependent hardening behaviour from quasi-static to intermediate ($10^1 s^{-1}$) strain rates. Due to a little strain rate sensitivity at room temperature, Aluminium Alloy AA5086 sheet is firstly tested to validate the identification methodology of hardening laws under dynamic biaxial tensile loadings. Then, this methodology is applied to Dual Phase DP600 steel to identify different strain-rate dependent hardening laws.

The main contents of this work are presented in four chapters as follows:

In chapter 1, the literature about constitutive models and mechanical tests is reviewed. Various hardening laws have been suggested with thermal softening effects and strain rate sensitivity. Several conventional tests under different strain paths have been proposed to identify the parameters of material models. Meanwhile, dynamic testing methods have been especially focused on.

In chapter 2, an optimal cruciform shape is designed by numerical investigations. The dynamic biaxial testing machine with four independent servo-hydraulic actuators is briefly introduced. From literature, various cruciform shapes have been designed for biaxial tensile tests. The effects of notches at the intersections, slits in each arm and thickness reduction at the central zone on the equivalent plastic strain level and distribution are investigated by Finite Element (FE) simulations. An optimal shape of cruciform specimen is designed to obtain large strain level at the central zone under biaxial tensile strain path.

In chapter 3, the identification methodology of hardening behaviour under dynamic biaxial loadings is validated by tests on aluminium alloy AA5086. The proposed shape of cruciform specimen is experimentally validated to obtain large strains. The parameters of isotropic hardening laws are identified by inverse analysis based on a FE model of the test. The biaxial flow stress curves identified by biaxial tensile tests are compared with flow stress curves from uniaxial tensile tests. By comparison of major and minor principal strains, the advanced anisotropic yield function of Bron and Besson 2004 has been further validated for parameter identification of hardening laws.

In chapter 4, the proposed biaxial tensile test and parameter identification strategy are applied to identify the strain-rate dependent hardening model of Dual Phase DP600 steel. Different strain-rate dependent hardening models are compared to describe the hardening behaviour. Quasi-static and dynamic biaxial tensile tests on DP600 steel are performed at different loading velocities. Flow stress curves from uniaxial and biaxial tests are compared in order to show the benefits of the proposed methodology.

Finally, a summary of contributions of this work is given and some perspectives for further research on this subject are considered.

1. Phenomenological modelling of sheet metal

1.1 Introduction

For many industrial fields such as automobile and aeronautical industry, sheet metal forming processes are of great importance to produce panels, tubes, profile parts and so on ^[1]. Sheet metal forming process consists in making use of the plasticity of metal to obtain the desired shapes by applying loads. The main defects of deformed parts during sheet metal forming processes include: crack, wrinkle, springback and surface deflections ^{[2] [3]}. For prediction of failures and optimization of sheet metal forming processes, numerical simulation is widely adopted instead of experimental trial-and-error method to reduce the time and cost of development ^[4]. An accurate material model is critically demanded for finite element (FE) simulation in the ranges of strain level and strain rate that cover the whole process.

Metal plasticity is fundamentally associated with the nucleation and migration of dislocations in the crystals and polycrystals as the underlying basis for microstructure rearrangement or evolution during plastic flow ^[5]. Up to date, the dislocation slip theory is the most well-known mechanism for plastic deformation during metal forming processes ^[6]. As shown in Fig. 1-1, although quantifying plastic deformation at microstructure scale is playing an increasing role, the simulation at micro-scale needs very large storage and is very time-consuming. Especially, it is not practical for simulation of sheet metal forming processes on the basis of physically based model ^[7].

Therefore, phenomenological modelling of material behaviour remains predominant for numerical simulation of sheet metal forming processes ^[8]. For characterization of elastoplastic behaviour, experimental techniques and specimens should be carefully designed to carry out the tests at the conditions met in sheet metal forming processes.

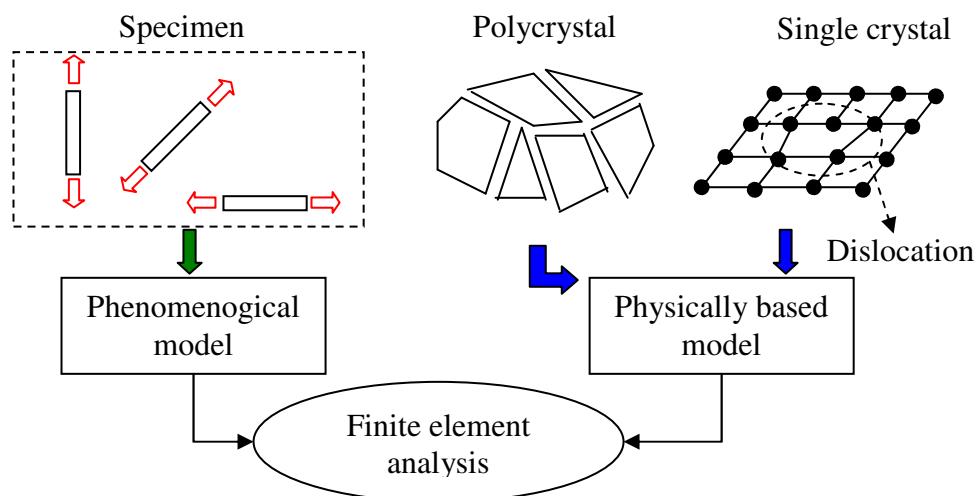


Fig. 1-1 Physical based and phenomenological modelling of metals

1.2 Influence of deformation mode

1.2.1 Strain state and path

In the principal strain space $(\epsilon_1, \epsilon_2, \epsilon_3)$ with the assumption of $\epsilon_1 \geq \epsilon_2 \geq \epsilon_3$, ϵ_1 and ϵ_2 are named as the major and minor principal strains in the plane of sheet metal. In the principal stress space $(\sigma_1, \sigma_2, \sigma_3)$, the stress along thickness direction is neglected ($\sigma_3 = 0$), because thickness is much smaller than length and width. Then, sheet metal is supposed to deform under plane stress state.

During deformation, the strain state (defined by the ratio of minor and major principal strains ϵ_2/ϵ_1) may keep unchanged or changed. Strain path is usually defined to describe the evolution of the strain state. Due to the geometrical constraints and boundary conditions during sheet metal forming processes, regions of the blank are usually deformed under various strain states and paths [9] [10]. A drawing process of a cylinder part is taken as an example in Fig. 1-2. Stress and strain states, strain path for different regions (A, B, C) are described in Fig. 1-3 and Fig. 1-4.

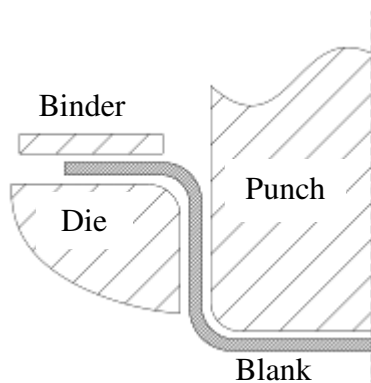


Fig. 1-2 Drawing of cylinder part

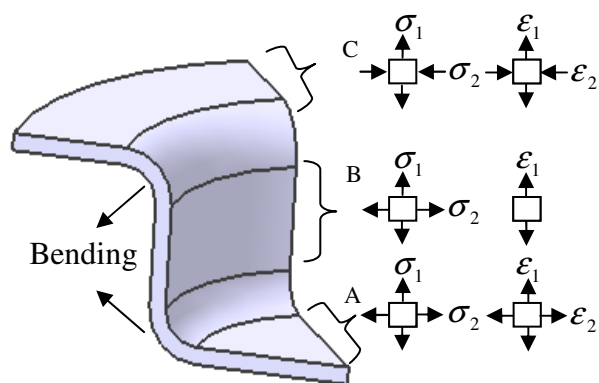


Fig. 1-3 Stress and strain state of cylinder part

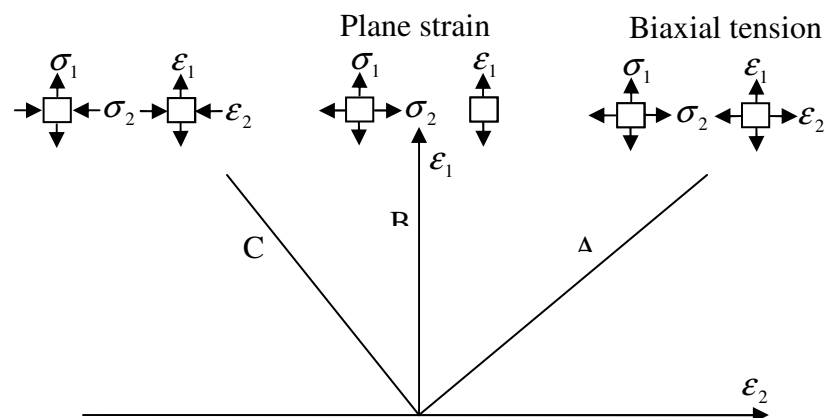


Fig. 1-4 Strain paths for cylinder part

Strain paths may be proportional or non-proportional during deformation ^[11]. As it is known, plastic deformation is strain path dependent. To study the effect of strain path changes, the two-stage strain path change tests have been adopted. As an example, a large specimen of uniaxial tension test is firstly deformed, then a smaller specimen is cut from the deformed specimen at an angle, and finally the smaller specimen is uniaxially tested ^{[12] [13]}. To study the forming limits under nonlinear strain paths, a two-stage continuous forming process (Benchmark 1 of Numisheet 2014) is studied for a draw/reverse draw panel with a significant strain path change. For these two experimental processes, the strain path can not be changed online.

1.2.2 Strain rate

During sheet metal forming processes, the deformation of material occurs in the time interval dt , and strain rate $\dot{\epsilon}$ is defined by the strain increment per unit time:

$$\dot{\epsilon} = \frac{d\epsilon}{dt} \quad \text{Eq. 1-1}$$

The strain rates of typical sheet metal forming processes in the automotive industry are approximately $10^1/s$. For most autobody parts, stamping is a basic process for forming shallow parts in a press by stretching the sheet over a punch and die set.

With an increasing demand of forming lightweight and more complicated components in automotive and aerospace industry, hydroforming is developed as a set of internal high pressure forming processes by using liquid as the forming media ^{[14] [15] [16]}. For manufacturing small series and single products, incremental sheet forming (ISF) is developed as a family of sheet forming processes where the deformation is highly localized and the final shape is determined by three dimensional movement of some tool part without the need of a die ^[17].

Nowadays, high speed metal forming (HSMF) technologies have been developed with higher strain rates ($10^2/s - 10^4/s$). For example, the electromagnetic metal forming (EMF) ^{[18] [19]} uses pulse magnetic fields to apply forces to the tubular or sheet metal workpieces, of which the material is high electrical conductive. Due to the extremely high velocities in comparison with the conventional quasi-static forming processes, the forming limits can be extended depending on materials ^[20]. The approximate forming velocity and strain rate ranges are compared between the high speed forming and conventional processes, as shown in Table 1-1.

For metallic alloys, the elastoplastic behaviour at high strain rates can be very different from the one under quasi-static state. In this case, they are called as rate-dependent materials. Otherwise, they are called as rate-independent ones. Therefore, it

is necessary to investigate the elastoplastic properties of materials at various strain rates.

Table 1-1 Forming velocity and strain rate ranges of different forming processes ^[21]

Process	Forming velocity (<i>m/s</i>)	Strain rate (<i>s</i> ⁻¹)
Hydraulic press	0.03	10 ⁰
Brake press	0.03	10 ⁰
Mechanical press	0.03-0.73	10 ⁰ -10 ¹
Drop hammer	0.24-4.2	10 ¹ -10 ²
Gas-actuated ram	2.4-82	10 ²
Explosive forming	9-228	10 ² -10 ⁴
Magnetic forming	27-228	10 ³ -10 ⁴
Electrohydraulic forming	27-228	10 ³ -10 ⁴

To study the strain rate sensitivity, the strain rate jump test with abrupt changes of the strain rate can be performed to remove specimen-to-specimen variations. Sung et al. ^[22] have adopted a strain rate jump-down test from a higher strain rate to lower strain rate (in Fig. 1-5). The transient response of stress after the jump is minimized by extrapolating the flow curve. A logarithmic strain rate sensitivity index *m* can be determined by the flow stresses σ_A and σ_B at the corresponding strain rates $\dot{\epsilon}_A$ and $\dot{\epsilon}_B$ as following:

$$\frac{\sigma_B}{\sigma_A} = \left(\frac{\dot{\epsilon}_B}{\dot{\epsilon}_A} \right)^m, \quad m = \frac{\ln(\sigma_B/\sigma_A)}{\ln(\dot{\epsilon}_B/\dot{\epsilon}_A)} \quad \text{Eq. 1-2}$$

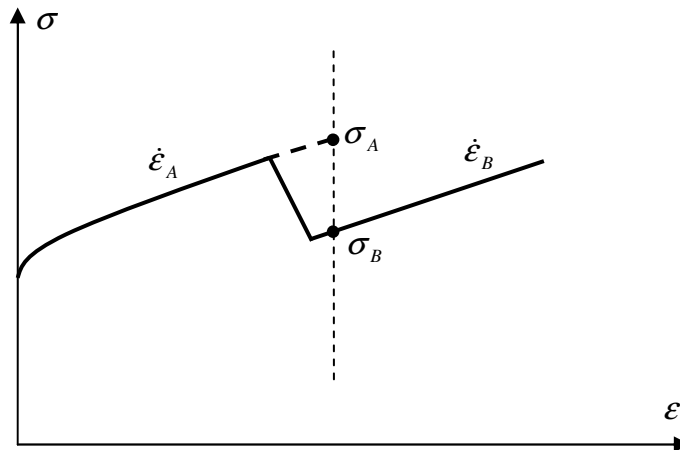


Fig. 1-5 Strain rate jump-down test ^[22]

1.3 Mathematical modelling of elastoplastic behavior

1.3.1 Constitutive relations

The phenomenological modelling of elastoplastic behaviour are developed on the basis of thermodynamics. The plastic deformation of material is dissipative and irreversible, and the internal variables should be reasonably chosen to represent the evolution of plastic behaviour. In general, the constitutive relations of elastoplasticity include the following aspects ^[23] ^[24] :

- (1) A decomposition of strain increment $d\boldsymbol{\varepsilon}_{ij}$ into an elastic, reversible part $d\boldsymbol{\varepsilon}_{ij}^e$ and an irreversible, plastic part $d\boldsymbol{\varepsilon}_{ij}^p$:

$$d\boldsymbol{\varepsilon}_{ij} = d\boldsymbol{\varepsilon}_{ij}^e + d\boldsymbol{\varepsilon}_{ij}^p \quad \text{Eq. 1-3}$$

- (2) A elastic law which governs the relation between the stress increment $d\boldsymbol{\sigma}_{ij}$ and elastic strain increment $d\boldsymbol{\varepsilon}_{ij}^e$, for which the elasticity law is often adopted as follows:

$$d\boldsymbol{\sigma}_{ij} = C_{ijkl} d\boldsymbol{\varepsilon}_{kl}^e \quad \text{Eq. 1-4}$$

where C_{ijkl} is the elastic tensor.

- (3) A yield function f which governs the onset of plastic deformation, for which the yield function should be verified as the following relation:

$$f(\boldsymbol{\sigma}_{ij}, q) = 0 \quad \text{Eq. 1-5}$$

where q is a set of internal variables.

- (4) A flow rule which governs the plastic flow and the determination of plastic strain increment $d\boldsymbol{\varepsilon}_{ij}^p$, for which the associated flow rule is often used for many cases of metal plasticity:

$$d\boldsymbol{\varepsilon}_{ij}^p = d\lambda \frac{\partial f}{\partial \boldsymbol{\sigma}_{ij}} \quad \text{Eq. 1-6}$$

where the plastic flow is assumed to occur along the normal direction of the yield function and the scale is defined by the increment of plastic multiplier $d\lambda$.

(5) A hardening model which governs the evolution of yield function.

During the plastic deformation of material, the size, position and shape of subsequent yield locus may change. For simplicity, the shape of yield locus ψ is often supposed to be unchangeable during plastic flowing and the subsequent yield criterion can be expressed as follows:

$$\psi(\sigma_{ij} - \alpha_{ij}) - \bar{\sigma} = 0 \quad \text{Eq. 1-7}$$

Here, the size of yield locus is controlled by the equivalent stress $\bar{\sigma}$ and the position of yield in stress space is determined by the back stress α_{ij} . When $\alpha_{ij} = 0$ and $\bar{\sigma}$ is changed, it becomes the isotropic hardening model. When $\alpha_{ij} \neq 0$ and $\bar{\sigma}$ is constant, it becomes the kinematical hardening model. When $\alpha_{ij} \neq 0$ and $\bar{\sigma}$ is changed, the material model is supposed to be isotropic-kinematical combined hardening, as shown in Fig. 1-6. ^[25]

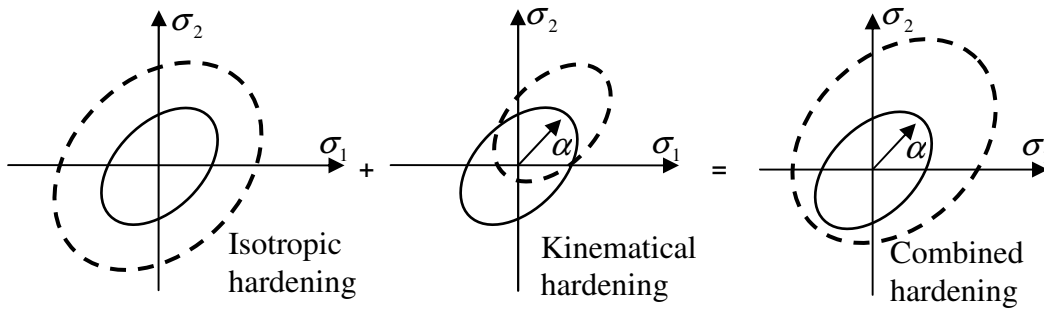


Fig. 1-6 Hardening models

For the monotonic deformation without any abrupt change of strain path, the isotropic hardening model is usually adopted. It is assumed that the shape of yield locus is not distorted and the position does not move. The isotropic hardening behaviour is characterized only by the evolution of $\bar{\sigma}$. To characterize strain path dependency under nonlinear strain path, the position of subsequent yield locus is assumed to move in the stress space, especially for the Bauschinger phenomenon of reverse loading.

1.3.2 Yield criterion

In the plane stress space, the yield criterion is defined to separate the elastic and plastic states of material. The convexity of yield surface should be assured ^[26]. Due to the crystallographic structure and the characteristics of rolling process, sheet metals usually exhibit a significant anisotropy of mechanical behaviour ^[27]. It is necessary to consider the anisotropic yield criteria. For the rolled sheet metals, the orientation is usually defined: rolling direction (RD), transverse direction (TD) and normal direction

(ND). The variation of plastic behaviour along the direction with an angle θ from RD is assessed by a quantity called Lankford parameter or anisotropic coefficient, which is defined as the ratios of true strains along the width and thickness directions of the tensile testing specimens, as shown in Fig. 1-7.

$$r_{\theta} = \frac{\epsilon_{22}}{\epsilon_{33}} = -\frac{\epsilon_{22}}{\epsilon_{11} + \epsilon_{22}} \quad \text{Eq. 1-8}$$

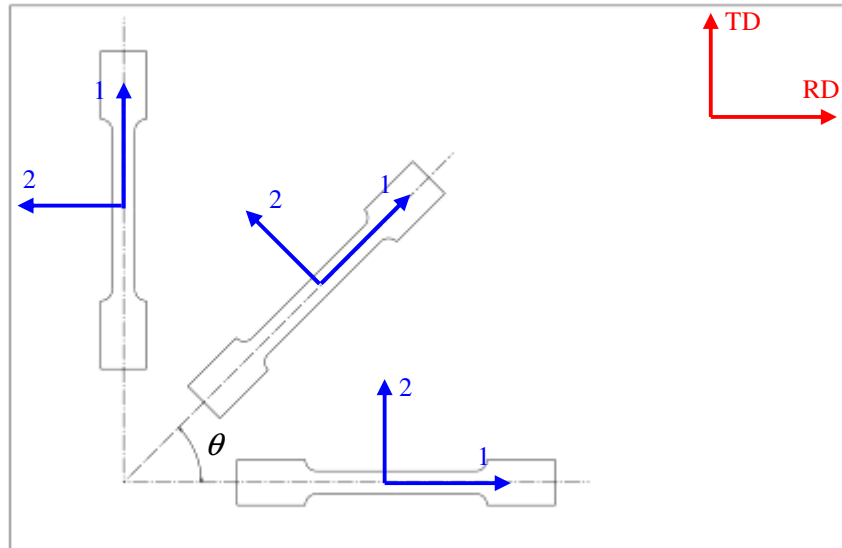


Fig. 1-7 Uniaxial tensile tests along different directions

Here, the classic isotropic yield criterion of Mises, classic anisotropic yield criterion of Hill 48 and advanced anisotropic yield criteria of Yld2000-2d, Yld2004-18p, Yld2004-13p, BBC2005, and Bron and Besson 2004 are briefly introduced.

1.3.2.1 Mises yield criterion

Based on the observation that a hydrostatic pressure cannot cause plastic yielding, the conclusion that only the elastic energy of distortion influences the transition from elastic to plastic was proposed by von Mises (1913) :

$$\psi(\sigma_{ij}) = \sqrt{\frac{1}{2} [(\sigma_{11} - \sigma_{22})^2 + (\sigma_{22} - \sigma_{33})^2 + (\sigma_{33} - \sigma_{11})^2 + 6\sigma_{12}^2 + 6\sigma_{23}^2 + 6\sigma_{31}^2]} \quad \text{Eq. 1-9}$$

For the plane stress case of sheet metal:

$$\psi(\sigma_{ij}) = \sqrt{\sigma_{11}^2 + \sigma_{22}^2 - 2\sigma_{11}\sigma_{22} + 3\sigma_{12}^2} \quad \text{Eq. 1-10}$$

1.3.2.2 Hill 48 yield criterion

For the Hill 48 yield criterion, the axis 1 is parallel to RD, the axis 2 is parallel to TD and the axis 3 is parallel to ND. The yield criterion is presented as follows:

$$\psi(\sigma_{ij}) = \sqrt{F(\sigma_{22} - \sigma_{33})^2 + G(\sigma_{33} - \sigma_{11})^2 + H(\sigma_{11} - \sigma_{22})^2 + 2(L\sigma_{23}^2 + M\sigma_{31}^2 + N\sigma_{12}^2)}$$

Eq. 1-11

For the plane stress case of sheet metal:

$$\psi(\sigma_{ij}) = \sqrt{(G + H)\sigma_{11}^2 + (H + F)\sigma_{22}^2 - 2H\sigma_{11}\sigma_{22} + 2N\sigma_{12}^2}$$

Eq. 1-12

The parameters F , G , H , N of Hill 48 yield criterion for sheet metals can be determined by three anisotropic coefficients r_0 , r_{45} and r_{90} as follows:

$$F = \frac{r_0}{r_{90}(1+r_0)}; G = \frac{1}{1+r_0}; H = \frac{r_0}{1+r_0}; N = \frac{(1+2r_{45})(r_0+r_{90})}{2r_{90}(1+r_0)}$$

Eq. 1-13

When $F = G = H = 0.5$ and $N = 1.5$, Hill 48 yield criterion becomes Mises criterion.

Due to the simplicity of mathematical formulation and parameter identification, Hill 48 yield criterion is widely used in practice. Unfortunately, because the mathematical expression is limited and the number of experimental information for parameter identification is only a few, there are also some important drawbacks of Hill 48 yield criterion. For some materials, especially aluminium alloys, Hill 48 yield surface is located inside the Mises yield surface, while the experimental yield surface is located outside Mises yield surface. This phenomenon is called as the anomalous behaviour and was observed by Woodthrope and Pearce. Only four ears can be predicted by Hill 48 yield criterion for the axisymmetric deep drawing process^[28].

1.3.2.3 Yld2000-2d yield criterion

Barlat et al.^[29] have introduced a plane stress yield function (Yld2000-2d) using two linear transformations as follows:

$$\psi(\sigma_{ij}) = \frac{1}{2}(\phi' + \phi'')^{1/a}$$

Eq. 1-14

where a is an exponent based on the crystallographic structure of material and a should be 6 and 8 for BCC and FCC materials respectively.

$$\phi' = |X'_1 - X'_2|^a \quad \text{Eq. 1-15}$$

$$\phi'' = |2X''_2 + X''_1|^a + |2X''_1 + X''_2|^a \quad \text{Eq. 1-16}$$

where X'_i and X''_i are principal values of the linearly transformed stress tensors X'_{ij} and X''_{ij} . X'_{ij} and X''_{ij} are obtained by linear transformations C' and C'' of the deviatoric stress tensor s_{ij} . s_{ij} is derived from stress tensor σ_{ij} by the transformation matrix T :

$$X'_{ij} = C' s_{ij} = C' T \sigma_{ij} = L' \sigma_{ij} \quad \text{Eq. 1-17}$$

$$X''_{ij} = C'' s_{ij} = C'' T \sigma_{ij} = L'' \sigma_{ij} \quad \text{Eq. 1-18}$$

Finally, the coefficients of L' and L'' can be expressed as follows:

$$\begin{bmatrix} L'_{11} \\ L'_{12} \\ L'_{21} \\ L'_{22} \\ L'_{66} \end{bmatrix} = \begin{bmatrix} 2/3 & 0 & 0 \\ -1/3 & 0 & 0 \\ 0 & -1/3 & 0 \\ 0 & 2/3 & 0 \\ 0 & 0 & 1 \end{bmatrix} \begin{bmatrix} \alpha_1 \\ \alpha_2 \\ \alpha_7 \end{bmatrix} \quad \text{Eq. 1-19}$$

$$\begin{bmatrix} L''_{11} \\ L''_{12} \\ L''_{21} \\ L''_{22} \\ L''_{66} \end{bmatrix} = \frac{1}{9} \begin{bmatrix} -2 & 2 & 8 & 12 & 0 \\ 1 & -4 & -4 & 4 & 0 \\ 4 & -4 & -4 & 1 & 0 \\ -2 & 8 & 2 & -2 & 0 \\ 0 & 0 & 0 & 0 & 9 \end{bmatrix} \begin{bmatrix} \alpha_3 \\ \alpha_4 \\ \alpha_5 \\ \alpha_6 \\ \alpha_8 \end{bmatrix} \quad \text{Eq. 1-20}$$

where all the independent coefficients α_k can be determined with eight material characteristics.

It is validated on binary Al-Mg alloy sheet metal sample that the predicted yield surface using Yld2000-2d is in excellent agreement with both the experimental and polycrystal yield surfaces. The yield function Yld2000-2d was also applied to the aluminium alloy sheet sample, AA2090-T3 and AA6022-T4. The coefficients are determined by three uniaxial tensile tests along the rolling, diagonal and transversal directions, the bulge test and the through-thickness disk compression^[29].

1.3.2.4 Yld2004-18p and Yld2004-13p yield criteria

Barlat et al. ^[30] have presented the general terms of anisotropic yield functions based on linear transformations of the stress deviator and discussed the methods to determine yield surface experimentally, including uniaxial tensile tests, hydraulic bulge test, disk compression test, crystal plasticity with microstructure modelling and so on. Two yield functions, Yld2004-18p and Yld2004-13p, have been proposed to describe the anisotropic behaviour of metallic alloys for a full stress state (3D).

The Yld2004-18p yield criterion is proposed with 18 material parameters as follows:

$$\begin{aligned} \psi(\sigma_{ij}) = & \left(\frac{1}{4} \left(|\tilde{S}'_1 - \tilde{S}_1|^a + |\tilde{S}'_1 - \tilde{S}_2|^a + |\tilde{S}'_1 - \tilde{S}_3|^a + |\tilde{S}'_2 - \tilde{S}_1|^a + |\tilde{S}'_2 - \tilde{S}_2|^a \right. \right. \\ & \left. \left. + |\tilde{S}'_2 - \tilde{S}_3|^a + |\tilde{S}'_3 - \tilde{S}_1|^a + |\tilde{S}'_3 - \tilde{S}_2|^a + |\tilde{S}'_3 - \tilde{S}_3|^a \right) \right)^{1/a} \end{aligned} \quad \text{Eq. 1-21}$$

The Yld2004-13p yield criterion is proposed with 13 material parameters as follows:

$$\begin{aligned} \psi(\sigma_{ij}) = & \left(\frac{1}{2} \left(|\tilde{S}'_1 - \tilde{S}'_2|^a + |\tilde{S}'_1 - \tilde{S}'_3|^a + |\tilde{S}'_2 - \tilde{S}'_3|^a - \left(|\tilde{S}_1|^a + |\tilde{S}_2|^a + |\tilde{S}_3|^a \right) \right. \right. \\ & \left. \left. + |\tilde{S}_1|^a + |\tilde{S}_2|^a + |\tilde{S}_3|^a \right) \right)^{1/a} \end{aligned} \quad \text{Eq. 1-22}$$

In these two yield criteria, the diagonal tensor representation \tilde{S} are defined by the principal values of \tilde{s}_{ij} , and the tensor \tilde{s}_{ij} is defined as a linear transformation of the stress deviator s_{ij} .

$$\tilde{s}_{ij} = C s_{ij} \quad \text{Eq. 1-23}$$

where the symmetric tensor C contains 18 and 13 material parameters, respectively.

The Yld2004-18p and Yld2004-13p yield criteria were applied to a mildly anisotropic 6111-T4 and a strongly anisotropic 2090-T3 aluminium alloy sheet samples. The first one with 18 parameters describe accurately the anisotropic behaviour. The second one with 13 parameters can reasonably describe the main trends ^[30].

1.3.2.5 BBC 2005 yield criterion

Banabic et al. ^[31] have proposed a BBC 2005 yield criterion for the orthotropic sheet materials in the plane stress space (2D) as follows:

$$\psi(\sigma_{ij}) = \left[a \cdot (\Gamma + \Psi)^{2k} + a \cdot (\Gamma - \Psi)^{2k} + (1-a) \cdot (2\Lambda)^{2k} \right]^{\frac{1}{2k}} \quad \text{Eq. 1-24}$$

The terms Γ , Ψ and Λ are defined as follows:

$$\Gamma = \frac{L\sigma_{11} + M\sigma_{22}}{2} \quad \text{Eq. 1-25}$$

$$\Psi = \sqrt{\frac{(N\sigma_{11} - P\sigma_{22})^2}{4} + Q^2\sigma_{12}\sigma_{21}} \quad \text{Eq. 1-26}$$

$$\Lambda = \sqrt{\frac{(R\sigma_{11} - S\sigma_{22})^2}{4} + T^2\sigma_{12}\sigma_{21}} \quad \text{Eq. 1-27}$$

The parameters L , M , N , P , Q , R , S , T can be determined by the error minimization calibration method, and eight experimental data should be provided. Those data includes: three directional yield stresses obtained from uniaxial tests along the rolling, diagonal and transversal directions; three anisotropic coefficients r_0 , r_{45} , r_{90} ; the equibiaxial yield stress obtained by cross tensile test or bulge test and the equibiaxial anisotropy coefficient. BBC2005 can also be deduced from Yld2000-2d, and they are not fundamentally different. BBC2005 yield criterion has been validated for characterization of the yield locus of aluminium alloy AA6181-T4 sheet ^[31].

1.3.2.6 Bron and Besson 2004 yield criterion

In order to represent complex yield surfaces, Bron and Besson (2004) ^[32] have proposed a phenomenological yield function with 16 parameters as follows:

$$\psi(\sigma_{ij}) = \left(\sum_{k=1}^K \alpha^k (\bar{\sigma}^k)^a \right)^{1/a} \quad \text{Eq. 1-28}$$

Where the K functions $\bar{\sigma}^k$ are convex with respect to the definition of a yield surface. Here, only two functions ($K = 2$) and they are defined by:

$$\bar{\sigma}^k = (\phi^k)^{1/b^k} \quad \text{Eq. 1-29}$$

$$\phi^1 = \frac{1}{2} \left(|S_2^1 - S_3^1|^{b^1} + |S_3^1 - S_1^1|^{b^1} + |S_1^1 - S_2^1|^{b^1} \right) \quad \text{Eq. 1-30}$$

$$\phi^2 = \frac{3^{b^2}}{2^{b^2} + 2} \left(|S_1^2|^{b^2} + |S_2^2|^{b^2} + |S_3^2|^{b^2} \right) \quad \text{Eq. 1-31}$$

Where $S_{i=1-3}^k$ are the principal values of a modified stress deviator s_{ij}^k :

$$s_{ij}^k = L_{ij}^k \sigma_{ij} \quad \text{Eq. 1-32}$$

$$L_{ij}^k = \begin{pmatrix} (c_2^k + c_3^k)/3 & -c_3^k/3 & -c_2^k/3 & 0 & 0 & 0 \\ -c_3^k/3 & (c_1^k + c_2^k)/3 & -c_1^k/3 & 0 & 0 & 0 \\ -c_2^k/3 & -c_1^k/3 & (c_1^k + c_2^k)/3 & 0 & 0 & 0 \\ 0 & 0 & 0 & c_4^k & 0 & 0 \\ 0 & 0 & 0 & 0 & c_5^k & 0 \\ 0 & 0 & 0 & 0 & 0 & c_6^k \end{pmatrix} \quad \text{Eq. 1-33}$$

The shape of yield surface is influenced by 4 parameters: a , b^1 , b^2 and α^1 ($\alpha^2 = 1 - \alpha^1$). The anisotropy is only controlled by 12 parameters $c_{i=1-6}^{k=1-2}$. When $\alpha_1 = 1$ and $c_i^1 = 1$, it becomes Mises yield function.

Bron and Besson 2004 yield function was applied to an aluminium alloys 2024-T4. The uniaxial tests of smooth tensile samples and U-notched samples with two different notches along the rolling, transverse and diagonal directions are performed for parameter identification by inverse analysis. This yield function was also applied to other sheets of binary Al-Mg, 6022-T4, 2090-T3 and 7075-T351. It was found to be very accurate to describe the plastic anisotropy of these various aluminium sheets^[32].

1.3.3 Hardening law

On the micro-scale, when the material is deformed, dislocations will be generated and annihilated, and the texture evolution will occur. It is usually assumed that the concept of dislocation density links the flow stress to the underlying microstructure evolution. The flow stress σ can be calculated as follows^[33]:

$$\sigma = \sigma_0 + \alpha G b (\delta - \delta_0) \quad \text{Eq. 1-34}$$

Where σ_0 is initial yield stress corresponding to the initial density δ_0 of dislocation, α is a material coefficient, G is the transversal elastic modulus, b is the Burgers vector and δ is the current dislocation density.

1.3.3.1 Strain hardening

On the macro-scale, if the material is deformed under monotonic strain path without the thermal and strain-rate effect, the equivalent plastic strain $\bar{\epsilon}_p$ is usually chosen to

represent the dislocation density δ . In the similar way of Eq. 1-34, the hardening law can be expressed by a one-internal-variable model as following:

$$\bar{\sigma} = \sigma_0 + H(\bar{\epsilon}_p) \quad \text{Eq. 1-35}$$

Where σ_0 is initial yield stress and $H(\bar{\epsilon}_p)$ represents the strain hardening effect.

Several mathematical formulas of hardening laws have been widely used as follows: Ludwick law is an unsaturated one:

$$\bar{\sigma} = \sigma_0 + K\bar{\epsilon}_p^n \quad \text{Eq. 1-36}$$

Voce law is a saturated one:

$$\bar{\sigma} = \sigma_0 + K(1 - \exp(-n\bar{\epsilon}_p)) \quad \text{Eq. 1-37}$$

Because it is found to become saturated too fast sometimes, the Voce law has been modified to decrease the saturating speed, such as Hockett-Sherby law:

$$\bar{\sigma} = \sigma_0 + K(1 - \exp(-n\bar{\epsilon}_p^m)) \quad \text{Eq. 1-38}$$

A generalized Voce law^[34] has also been suggested as follows:

$$\bar{\sigma} = \sigma_0 + K(1 - \exp(-n\bar{\epsilon}_p))^{1/\alpha} \quad \text{Eq. 1-39}$$

The value of α varies with the type of crystallographic system: $\alpha = 1/2$ for a HCP structure, $\alpha = 1$ for a BCC structure and $\alpha = 2$ for a FCC one.

1.3.3.2 Influence of temperature and strain rate

When the material is deformed at various temperature and strain rate, the hardening law should take three items into account: strain hardening $H(\bar{\epsilon}_p)$, thermal softening $T(T)$ and strain-rate sensitivity $V(\dot{\bar{\epsilon}})$ ^{[35] [36]}. The thermal softening effect $T(T)$ and strain-rate sensitivity term $V(\dot{\bar{\epsilon}})$ can be manipulated additively or multiplicatively with the basic formulations of strain hardening law. Generally speaking, according to the coupling effect, four types of flow stress curve^[37] can be presented in Fig. 1-8. The examples are given as follows:

- 1) Type-1: initial yield stress σ_0 is not influenced by the temperature and strain rate, but the strain hardening behaviour $H(\bar{\epsilon}_p)$ is influenced by temperature $T(T)$ and strain rate $V(\dot{\bar{\epsilon}})$. A simple multiplicative form is given as follows:

$$\bar{\sigma} = \sigma_0 + H(\bar{\epsilon}_p) T(T) V(\dot{\bar{\epsilon}}) \quad \text{Eq. 1-40}$$

The flow stress curves have the same initial point and different hardening rate. The Zerilli-Armstrong model (1987) for FCC ^[38] is an example of Type-1.

- 2) Type-2: initial yield stress σ_0 is influenced by the temperature $T(T)$ and strain rate $V(\dot{\bar{\epsilon}})$, but the strain hardening behaviour $\bar{H}(\bar{\epsilon}_p)$ is not influenced by the temperature and strain rate. A simple multiplicative form is given as follows:

$$\bar{\sigma} = \sigma_0 T(T) V(\dot{\bar{\epsilon}}) + H(\bar{\epsilon}_p) \quad \text{Eq. 1-41}$$

It appears that the flow stress curves move upwards or downwards with the same hardening rate. The examples includes: Zerilli-Armstrong model (1987) for BCC, Modified Khan-Huang model (2009) proposed by H. Yu et al ^[39].

- 3) Type-3: both initial yield stress σ_0 and strain hardening behaviour $\bar{H}(\bar{\epsilon}_p)$ are influenced by the temperature $\bar{T}(t)$ and strain rate $\bar{V}(\dot{\bar{\epsilon}})$, and the influences are the same. A simple multiplicative form is given as follows:

$$\bar{\sigma} = (\sigma_0 + H(\bar{\epsilon}_p)) \bar{T}(t) \bar{V}(\dot{\bar{\epsilon}}) \quad \text{Eq. 1-42}$$

The examples can be given by Johnson-Cook model (1983), Khan-Huang model (1992) ^[40].

- 4) Type-4: both initial yield stress σ_0 and strain hardening behaviour $H(\bar{\epsilon}_p)$ are influenced by the temperature $T_i(T)$ and strain rate $V_i(\dot{\bar{\epsilon}})$, but the influences are different. A simple multiplicative form is given as follows:

$$\bar{\sigma} = \sigma_0 T_1(T) V_1(\dot{\bar{\epsilon}}) + H(\bar{\epsilon}_p) T_2(T) V_2(\dot{\bar{\epsilon}}) \quad \text{Eq. 1-43}$$

This type is a generalised form of other three types. There are many examples, such as Lin-Wagoner model (1987) ^[41], Zhao model (1997) ^[42], Khan-Liang model (1999) ^[43], Rusinek-Klepaczko (2007) ^[44], H/V model (2010) ^[45], Paul model (2012) ^[46].

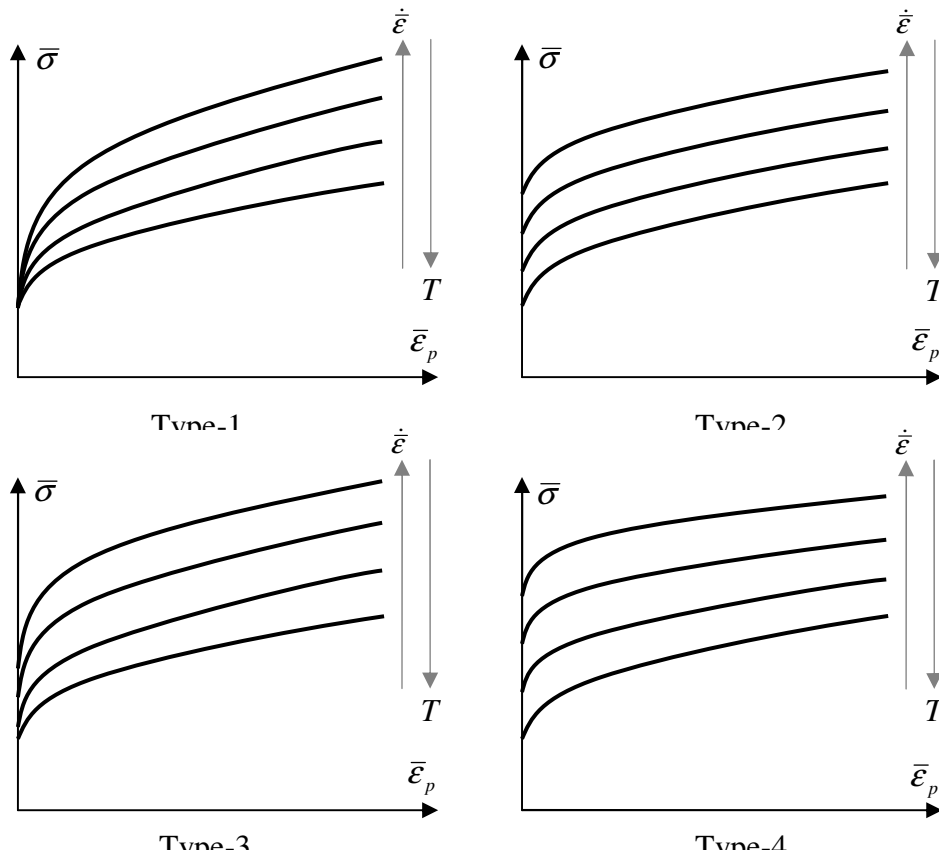


Fig. 1-8 Schematic representation of four types stress-strain curves^[37]

1.3.3.3 Simple models

The temperature sensitivity $T(T)$ is traditionally described as follows:

Power model:

$$T(T) = \left(\frac{T}{T_0} \right)^\beta \quad \text{Eq. 1-44}$$

where T , T_0 are the current and reference temperatures, β is a material constant.

Exponential model:

$$T(T) = \exp\left(\frac{\beta}{T}\right) \quad \text{Eq. 1-45}$$

Johnson-Cook model:

$$\bar{T}(T) = 1 - \left(\frac{T - T_0}{T_m - T_0} \right)^m \quad \text{Eq. 1-46}$$

where T_m are the melting temperature of material and m is a material constant.

The strain-rate sensitivity $V(\dot{\epsilon})$ is traditionally described as follows:

Power model:

$$V(\dot{\epsilon}) = \left(\frac{\dot{\epsilon}}{\dot{\epsilon}_0} \right)^m \quad \text{Eq. 1-47}$$

where $\dot{\epsilon}$, $\dot{\epsilon}_0$ are the current and reference strain rates, m is a material parameter.

Cowper-Symonds model:

$$V(\dot{\epsilon}) = \left(1 + \frac{\dot{\epsilon}}{C} \right)^{1/m} \quad \text{Eq. 1-48}$$

where C , m are the material parameters

Johnson-Cook model:

$$V(\dot{\epsilon}) = 1 + C \ln \frac{\dot{\epsilon}}{\dot{\epsilon}_0} \quad \text{Eq. 1-49}$$

The hyperbolic arcsine model ^[47] :

$$V(\dot{\epsilon}) = \operatorname{arcsinh} \left(\frac{e}{2} \left(\frac{\dot{\epsilon}}{\dot{\epsilon}_0} \right)^m \right) \approx \begin{cases} \frac{e}{2} \left(\frac{\dot{\epsilon}}{\dot{\epsilon}_0} \right)^m & \text{when } \dot{\epsilon} \text{ is small} \\ 1 + m \ln \left(\frac{\dot{\epsilon}}{\dot{\epsilon}_0} \right) & \text{when } \dot{\epsilon} \text{ is large} \end{cases} \quad \text{Eq. 1-50}$$

The power model is suitable for low strain rates, while the Cowper-Symonds and Johnson-cook models are used for high strain rate. Although the Johnson-Cook model is widely adopted for high strain rate model due to the simplicity, it cannot reasonably describe the experimental flow stresses when the strain rate changes from quasi-static strain rate ($10^{-3} / s$) to high strain rate ($10^3 / s$). The hyperbolic arcsine model is proposed to transit very well between quasi-static and high strain rates.

1.3.3.4 Integrated models

- Zerilli-Armstrong model (1987) ^[38]:

$$\bar{\sigma} = \sigma_0 + (C_1 + C_2 \sqrt{\bar{\epsilon}_p}) \exp(-C_3 T + C_4 T \ln \dot{\bar{\epsilon}}) + C_5 \bar{\epsilon}_p^n \quad \text{Eq. 1-51}$$

for FCC ($C_1 = C_5 = 0$): $\bar{\sigma} = \sigma_0 + C_2 \sqrt{\bar{\epsilon}_p} \exp[-C_3 T + C_4 T \ln \dot{\bar{\epsilon}}]$ Eq. 1-52

for BCC ($C_2 = 0$): $\bar{\sigma} = \sigma_0 + C_1 \exp(-C_3 T + C_4 T \ln \dot{\bar{\epsilon}}) + C_5 \bar{\epsilon}_p^n$ Eq. 1-53

Where σ_0 , C_1 , C_2 , C_3 , C_4 and C_5 are the material constants. Based on the results of high speed impact tests, this model has been applied for characterization of OHFC copper (FCC) and Armco iron (BCC).

- Lin-Wagoner model (1987) ^[41]:

$$\bar{\sigma} = A \left[1 - B \exp((C_1 + C_2(T - T_0)) \bar{\epsilon}_p) \right] \left(\frac{\dot{\bar{\epsilon}}}{\dot{\bar{\epsilon}}_0} \right)^m \left(\frac{T}{T_0} \right)^\beta \quad \text{Eq. 1-54}$$

Where A , B , C_1 , C_2 , m and β are the material parameters, $\dot{\bar{\epsilon}}_0$ and T_0 are the reference strain rate and temperature. This model was applied to characterize Armco interstitial-free (IF) steel and stainless steel type 310SS.

- Khan-Huang model (1992) ^[40]:

$$\bar{\sigma} = \left[\sigma_0 + E_\infty \bar{\epsilon}_p - a \exp(-\alpha \bar{\epsilon}_p) \right] \left[1 - \frac{\ln(\dot{\bar{\epsilon}})}{\ln(\dot{\bar{\epsilon}}_0)} \right]^{-1} \quad \text{Eq. 1-55}$$

Where σ_0 , a , D , E_∞ , m and α are the material parameters and the reference strain rate $\dot{\bar{\epsilon}}_0 = 10^6/s$. This model is applied to a quite strain rate sensitive material of 1100-0 aluminium over the strain rates $\dot{\bar{\epsilon}}$ from $10^{-5}/s$ to $10^4/s$.

- Zhao model (1997) ^[42]:

$$\bar{\sigma} = \left[\sigma_0 + B \bar{\epsilon}_p^n + (C - D \bar{\epsilon}_p^m) \ln \left(\frac{\dot{\bar{\epsilon}}}{\dot{\bar{\epsilon}}_0} \right) + E \dot{\bar{\epsilon}}^k \right] (1 - \mu \Delta T) \quad \text{Eq. 1-56}$$

Where σ_0 , B , C , D , E , k , m , n and $\dot{\bar{\epsilon}}_0$ are the material parameters, and ΔT is the temperature difference with respect to the room temperature. In this model, the influence of temperature on the initial yield stress and strain hardening are the same,

while the influence of the strain rate on the initial yield stress and strain hardening is different. This model is applied to characterize the plastic behaviour of mild steel and commercial aluminium sheets.

- Khan-Liang model (1999) ^[43]:

$$\bar{\sigma} = \left[\sigma_0 + B \left(1 - \frac{\ln \dot{\bar{\epsilon}}}{\ln \dot{\bar{\epsilon}}_0} \right)^{n_1} \bar{\epsilon}^{n_0} \right] \dot{\bar{\epsilon}}^C \left[1 - \left(\frac{T - T_0}{T_m - T_0} \right)^m \right] \quad \text{Eq. 1-57}$$

Where σ_0 , B , C , n_0 , n_1 , m are the material parameters, the reference strain rate $\dot{\bar{\epsilon}}_0 = 10^6 / s$. In this model, the influence of temperature on the initial yield stress and strain hardening are the same. The model has been adopted to describe three BBC metals, tantalum, tantalum alloy and AerMet 100 steel over a wide range of strains (15%), strain rates ($10^{-6} - 10^4 / s$) and temperatures (25-315°C).

- Modified Khan-Huang model (2009) proposed by H. Yu ^[39]:

$$\bar{\sigma} = \sigma_0 \left[1 + D \left(\ln \frac{\dot{\bar{\epsilon}}_p}{\dot{\bar{\epsilon}}_0} \right)^m \right] + E_\infty \bar{\epsilon}_p - a \exp(-\alpha \bar{\epsilon}_p) \quad \text{Eq. 1-58}$$

Where σ_0 , a , D , E_∞ , m and α are the material parameters and the reference strain rate $\dot{\bar{\epsilon}}_0 = 10^{-4} / s$. This model describes well the hardening behaviour for DP600 steel at the strain rates $\dot{\bar{\epsilon}}$ from $10^{-3} / s$ to $10^3 / s$, and shows that the strain hardening of DP600 have little dependence on the strain rate.

- H/V model (2010) ^[45]:

$$\bar{\sigma} = f(\bar{\epsilon}_p, \dot{\bar{\epsilon}}, T) = f(\bar{\epsilon}_p, T) \cdot g(\dot{\bar{\epsilon}}) \cdot h(T) \quad \text{Eq. 1-59}$$

The strain hardening $f(\bar{\epsilon}_p, T)$ is given by a linear combination of Voce and power law as follows:

$$f(\bar{\epsilon}_p, T) = \alpha(T) f_H + (1 - \alpha(T)) \cdot f_V \quad \text{Eq. 1-60}$$

$$\begin{cases} \alpha(T) = \alpha_1 - \alpha_2 (T - T_0) \\ f_H = H_{HV} \bar{\epsilon}_p^{n_{HV}} \\ f_V = V_{HV} (1 - A_{HV} \exp(-B_{HV} \bar{\epsilon}_p)) \end{cases} \quad \text{Eq. 1-61}$$

Where α_1 , α_2 , H_{HV} , n_{HV} , V_{HV} , A_{HV} and B_{HV} are the material constants, and the reference temperature $T_0 = 25^\circ C$.

The strain rate sensitivity $g(\dot{\epsilon})$ and thermal effect $h(T)$ are respectively given by:

$$g(\dot{\epsilon}) = \left(\frac{\dot{\epsilon}}{\dot{\epsilon}_0} \right)^{\gamma_2 + (\gamma_1/2) \log(\dot{\epsilon}/\dot{\epsilon}_0)} \quad \text{Eq. 1-62}$$

$$h(T) = 1 - \beta(T - T_0) \quad \text{Eq. 1-63}$$

Where γ_1 , γ_2 and β are material constants, and $\dot{\epsilon}_0$ is the reference strain rate.

The H/V model has been adopted for modelling of DP590, DP780 and DP980 steels in the uniform strain range at 25, 50 and 100°C by the strain rate jump tests and the isothermal tensile tests.

- Paul model (2012) [46]:

$$\sigma = \sigma_0 \exp \left(A \ln \left(\frac{\dot{\epsilon}}{\dot{\epsilon}_0} \right) - k(T - T_0) \right) + [B\bar{\epsilon}_p + C(1 - \exp(-\beta\bar{\epsilon}_p))] \left(1 - H \ln \left(\frac{\dot{\epsilon}}{\dot{\epsilon}_0} \right) \right) (1 - G(T - T_0)) \quad \text{Eq. 1-64}$$

Where σ_0 , A , B , C , β , k , H , G are the material parameters and T_0 is room temperature. This model is validated on mild steel ES, DP600 steel and TRIP700 steel over a wide strain, strain rate and temperature range.

1.4 Mechanical tests of sheet metal

To investigate phenomenological modelling of materials for numerical simulation of sheet metal forming processes, many key issues should be considered, such as: plastic anisotropy of rolled sheet metals, multiaxial loading conditions, large plastic strain, temperature and strain rate effects, strain path changes, and so on. The experimental techniques and specimen design should be proposed to consider specific conditions met in the practical sheet metal forming processes. In this section, the tests under different proportional deformation paths and dynamic conditions will be focused on.

First of all, four traditional tests of sheet metal (uniaxial tensile test, bulge test, plane strain test and simple shear test) are usually carried out to obtain different deformation modes and strain paths [48] [49] [50] [51]. These four tests are usually adopted for

characterization of plastic behaviour at four representative points in the principal stress space, as shown in Fig. 1-9.

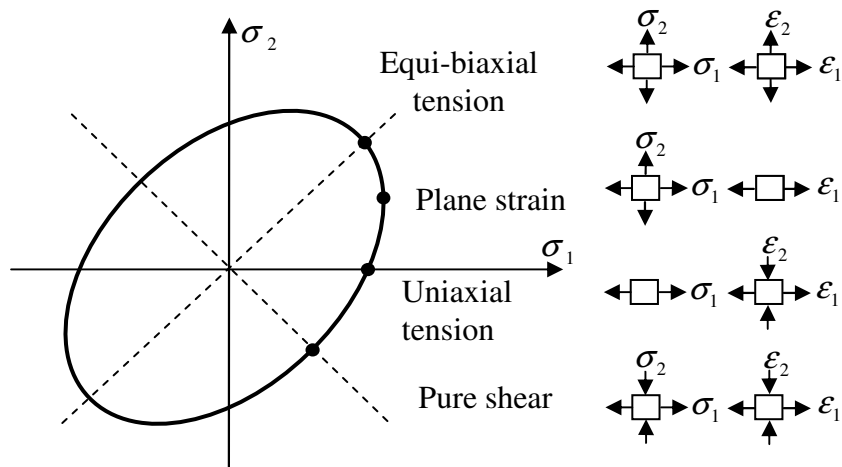


Fig. 1-9 Representative strain and stress states on yield locus

For material modelling at various strain rates, Field et al. [52] have suggested different experimental techniques: the conventional load frame for creep and stress relaxation, servo-hydraulic system for quasi-static and intermediate strain rates, dropweights, Split Hopkinson Pressure Bars (SHPB), Taylor impact and shock loading by plate impact for high strain rates, as shown in Fig. 1-10. Because dynamic tests are completed in a short time, the dynamic testing machines and measurement systems are usually different from those for quasi-static tests.

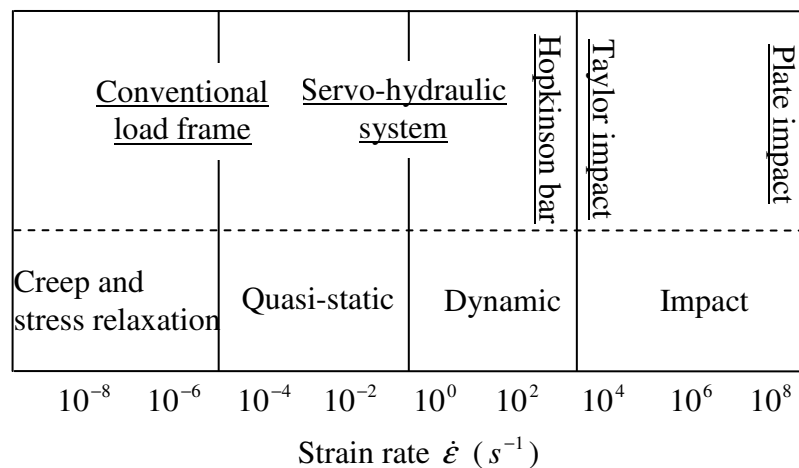


Fig. 1-10 Schematic of strain rate ranges and experimental techniques [52]

1.4.1 Uniaxial test

1.4.1.1 Quasi-static uniaxial test

The uniaxial tensile test at quasi-static condition is performed around the strain rate of $\dot{\epsilon} = 10^{-3}/s$. It is widely used to investigate the mechanical properties of metallic

materials, which has already been standardised ^[53] ^[54]. It can provide the Young's modulus, Poisson's ratio, yield strength, ultimate tensile strength (UTS), uniform elongation and anisotropic coefficients. The uniaxial tensile specimen is shown in Fig. 1-11. When the deformation is uniform before localisation, the true strain, stress and strain rate can be calculated.

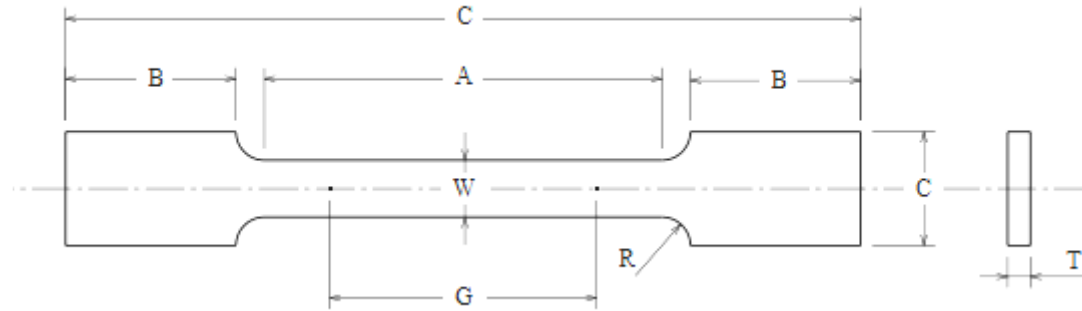


Fig. 1-11 Uniaxial tensile specimen

True strain is calculated by:

$$\varepsilon = \ln \frac{G}{G_0} \quad \text{Eq. 1-65}$$

where G is the gauge length and G_0 is the initial length.

True stress is calculated by:

$$\sigma = \frac{F}{S} = \frac{F \times \exp(\varepsilon)}{S_0} \quad \text{Eq. 1-66}$$

where F is the loading force, S_0 , S are the initial and current cross sections.

True strain rate is calculated by:

$$\dot{\varepsilon} = \frac{d\varepsilon}{dt} = \frac{V}{G} \quad \text{Eq. 1-67}$$

where V is the loading velocity.

1.4.1.2 Dynamic uniaxial test

For the dynamic tests at intermediate strain rate range ($0.1 \leq \dot{\varepsilon} \leq 500/s$), the servo-hydraulic system is usually adopted. International Iron and Steel Institute Committee (IISI) ^[55] has made recommendations for dynamic tensile testing for sheet steels. Several issues have been discussed such as machine type, specimen, clamping method

and measurement systems. For tests at strain rate above $10/s$, the measured force is greatly perturbed by multiple passages of the reflected elastic wave or by the vibratory response of mechanical parts of the experimental device. To solve this problem, various methods have been suggested.

- (1) The load cell is shorten to reduce the time for the wave to travel back several times, so that elastic deformation within load cell becomes homogeneous quickly;
- (2) The load cell is lengthen in order to finish the test before the return back of the reflected elastic wave, in other words, it is based on the SHPB method;
- (3) Strain gauge is attached on grip section of specimen, where deformation is elastic;
- (4) A damping method is adopted to improve the impact condition when a sudden loading is applied;
- (5) The forces applied on specimen are determined by inverse analysis. A numerical model of the test allowing to reproduce the oscillations of force signal is needed.

Kim et al. ^[56] ^[57] have developed a high speed tensile testing machine to investigate dynamic tensile behaviour of steel sheets at various strain rates from 0.003 to $200/s$. The oscillation phenomenon of the force signal measured by the load cell, called as load ringing, is caused by the vibratory response of the mechanical parts or by the propagation of elastic stress wave. The natural frequency increases as the length of grip decreases. The load cell is attached to the upper grip to measure the force, and the grip has been designed to effectively reduce the load ringing, as shown in Fig. 1-12. Meanwhile, because the strain of specimen is calculated from the displacement of the crosshead, it is different from the exact strain at the gauge section. The geometric effects are also studied to compensate the strain discrepancy.

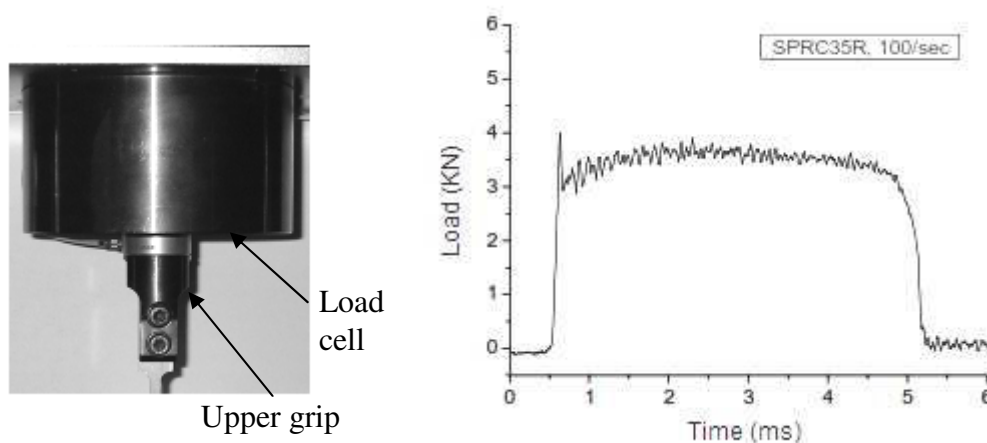


Fig. 1-12 Shortened upper grip and measured force curve ^[56]

For testing materials in compression at intermediate strain rate between about 10 and $200/s$, Gilat et al. ^[58] have introduced a new apparatus consisting in a large hydraulic actuator and a long transmitter bar of $40m$ length, as shown in Fig. 1-13. Once the specimen is loaded by the actuator that impact directly the free end of the specimen,

which is deformed between the actuator and the transmitter bar. A compressive wave propagates into the transmitter bar. The amplitude of wave is measured by the strain gages located on the transmitter bar to calculate the force of the specimen as in the SHPB. The transmitter bar is enough long that the experiment will be completed before the reflected wave in the transmitter bar return back to gages, and the measured force will not be disturbed. The strain in the specimen during the tests is measured by 3D Digital Image Correlation (DIC) with high speed cameras.

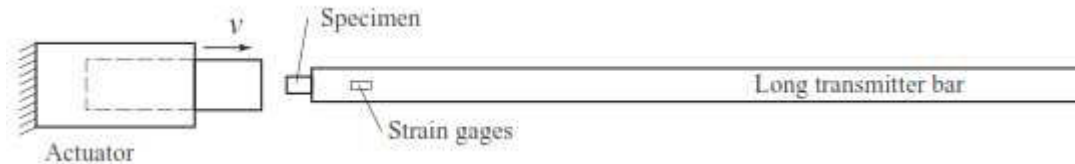


Fig. 1-13 Dynamic testing device with long bar ^[58]

Othman et al. ^[59] have developed a modified servo-hydraulic machine to assess the mechanical properties of aluminium alloy 2017-T4 at the strain rate of approximately 100/s, as shown in Fig. 1-14. A long duration Hopkinson bar technique and a wave separation method are adopted for less oscillating force measurement. The force at the bar-attaching device interface is firstly calculated the separation method. Then, the force applied to the specimen is secondly deduced by assuming a rigid mass model of the attaching device. The strain in the specimen is measured by using Digital Speckle Photographs (DSP) which is captured via high-speed video camera.

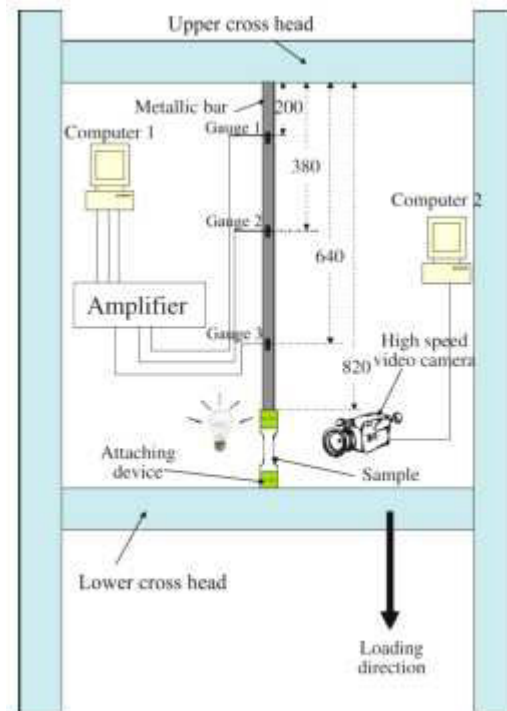


Fig. 1-14 A simplified schematic of the modified servo-hydraulic machine ^[59]

To develop tests at strain rates ranging from quasi-static to 500/s for application in automotive crash simulation, Wood et al. [60] have presented some recommendations and procedures about the test machine requirements, specimen design, force and strain measurements, data processing and strength hardening constitutive relations. Three types of specimen with different gauged lengths have been proposed for the tests at quasi-static strain rates, low to intermediate strain rates and intermediate to high strain rates. Two methods of force measurement are compared during the dynamic test. The dynamic load cell (DLC) is located between the static grip and the machine frame, which is called as "machine-based force sensor". Meanwhile, a load force transducer is proposed on the specimen using strain gauges, which is called as "local force transducer on specimen", as shown in Fig. 1-15. The measured force by two methods are shown in Fig. 1-16. It can be seen that the force measured by the local force transducer on the specimen is less oscillating than that measured by the DLC.

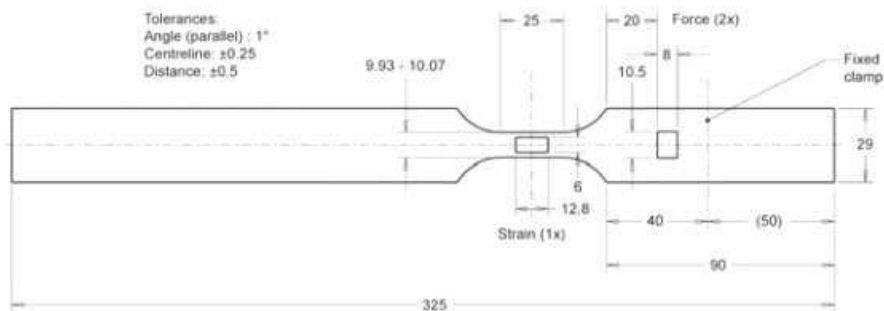


Fig. 1-15 Position of strain gauges on specimen for local force measurement [60]

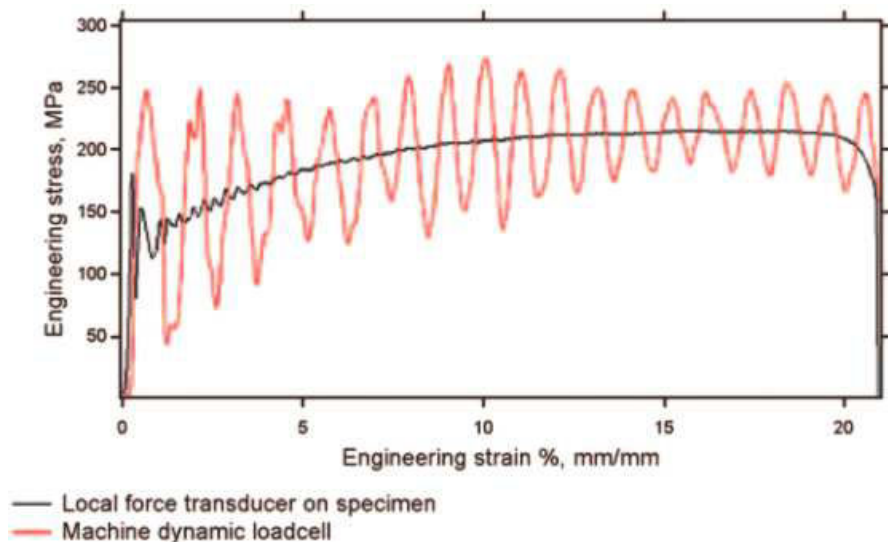


Fig. 1-16 Comparisons of force measured by local force transducer and DLC [60]

In order to conduct high speed tensile tests on fibre reinforced polymer composites, Fitoussi et al. [61] have adopted an experimental device on a servo-hydraulic machine,

in Fig. 1-17. The hydraulic jack is accelerated to reach the specific velocity over a straight displacement before the contact of sliding bar and hydraulic jack. A damping joint of a low impedance material is placed between the sliding bar and the hydraulic jack, which attenuated partially the wave effects caused by the dynamic shock. After testing with several geometries and materials, the rubber nitrile was chosen for the damping joint to obtain homogeneous deformation of specimen and minimise the amplitude of shock wave. Boyce et al. ^[62] have employed a servo-hydraulic device to perform tensile tests of tough, ultrahigh-strength steels at strain rates from 0.0002 up to 200/s. To reduce oscillations in the tensile bar and load cell, a custom-designed load cell has been used and it shows about 50% reduction of the oscillation amplitude. Studying the pulse-shaping materials used in split Hopkinson pressure bar test to smooth the elastic wave, a rubber damper have also been placed in the slack adapter and reduce the initial oscillations by more than 50%. Xiao ^[63] has carried out dynamic tensile tests of four plastic materials using a servo-hydraulic testing machine and a damping layer was also adopted. The single-degree freedom spring-mass model with and without damping was studied to obtain the analytical solutions, which describes the influence of loading rate and the natural frequency of testing system on the magnitude of system ringing and its decay rate.

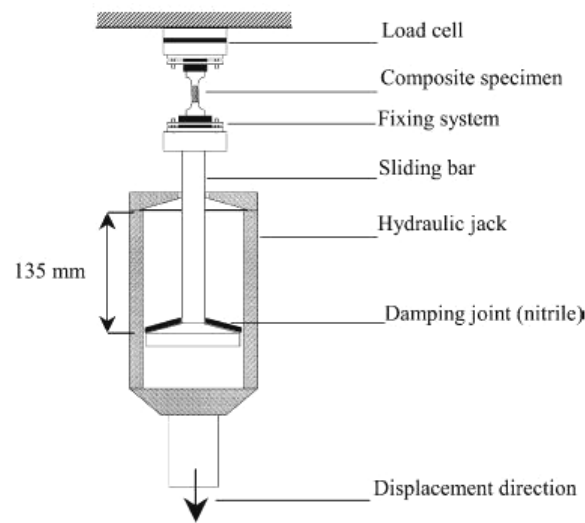


Fig. 1-17 Dynamic tensile testing device with damping ^[61]

In order to identify the constitutive model at large strains up to 150% and intermediate strain rates up to 500/s, Diot et al. ^[64] have carried out uniaxial compressive tests by a servo-hydraulic experimental set-up (in Fig. 1-18) . The dynamic response of the set-up is experimentally analyzed and a FE model of the whole experimental structure is validated to represent the elastic and inertia effects. To reduce the time consuming for parameter identification, a two-step sequential identification method based on inverse analysis has been suggested: the mathematical expression of the force on the bar/specimen interface is firstly identified on the basis of the previously defined FE model of tools. The material parameters is then identified, taking the identified force

as the boundary condition of specimen. Finally, the behaviour of a steel 27MnCr5 has been identified under different loading velocities and temperatures.

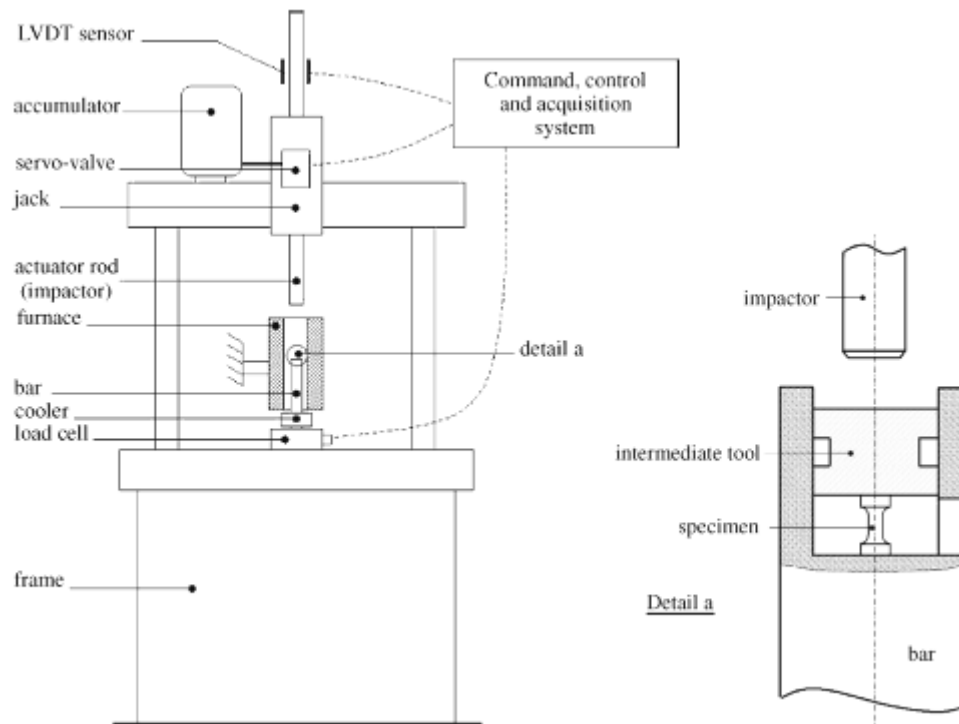


Fig. 1-18 Experimental set-up for dynamic uniaxial compression ^[64]

Zhu et al. ^[65] ^[66] have conducted dynamic tensile tests on aluminium alloy AA6061-T6 and engineering materials at intermediate strain rate up to approximately 200/s using a high-speed servo-hydraulic machine. The predominant frequencies of testing machine were identified by modal analysis, and the effect of loading rate and natural frequency of testing machine on the magnitude of machine ringing was also analyzed by a single degree-of-freedom spring-mass-damper model. Two methods for curve smoothing, which are a low-pass filter with a cut-off frequency and a power-law fitting function, are presented to extract the stress from the original data.

1.4.1.3 Split Hopkinson pressure bar

Because the Split Hopkinson Pressure Bar (SHPB) is not only very popular for dynamic uniaxial tests at high strain rate, $\dot{\epsilon} \geq 500/s$, but also widely used as the basis of other dynamic tests, the theory of SHPB is briefly presented here ^[67] ^[68]. It consists in the striker, incident bar and transmit bar. The test is completed in an impulse wave, as shown in Fig. 1-19 ^[69]. When the incident bar is impacted by the striker, a compressive impulse has emerged and propagates along the incident bar. The impulse will be recorded by the strain gauge 1 as the incident impulse ϵ_i . When ϵ_i has arrived at the interface of incident bar and specimen, it will reflect and transmit. The reflected

impulse will be recorded by the strain gauge 1 as the reflected tensile impulse ε_r . The transmit impulse will be measured by the strain gauge 2 as the transmit compressive impulse ε_t .

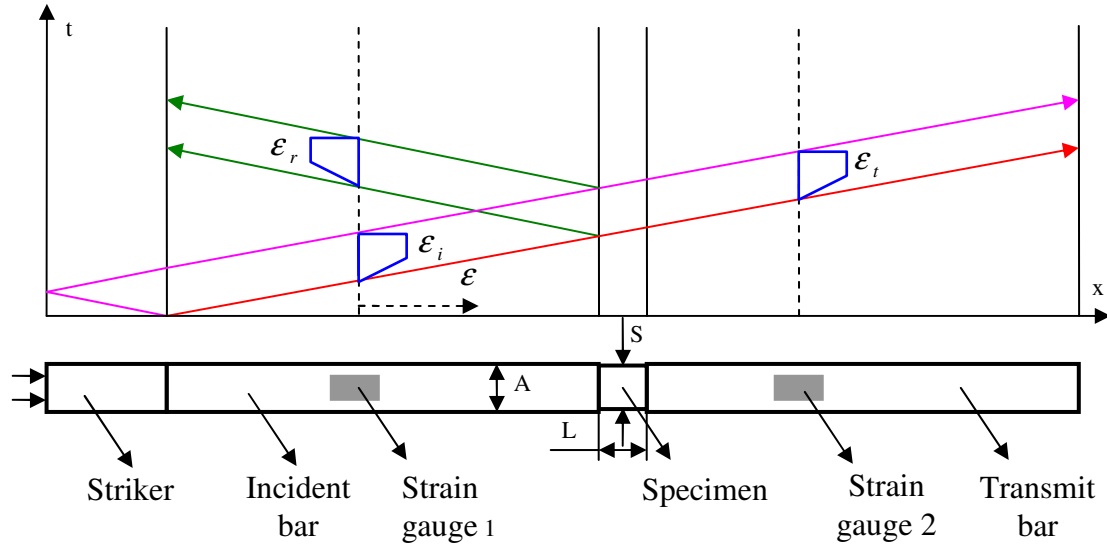


Fig. 1-19 Schematic of Split Hopkinson Pressure Bar and travelling wave diagram

The theory of one-dimensional elastic stress wave propagation is adopted. The specimen is considered to become in equilibrium because the stress wave can travel back several times in the specimen during the test. Therefore, the strain ε , strain rate $\dot{\varepsilon}$ and stress σ of specimen can be calculated as follows:

$$\varepsilon(t) = -\frac{C}{L} \int_0^t (\varepsilon_r(t) + \varepsilon_t(t) - \varepsilon_i(t)) dt = -\frac{2C}{L} \int_0^t \varepsilon_r(t) dt \quad \text{Eq. 1-68}$$

$$\dot{\varepsilon}(t) = -\frac{C}{L} (\dot{\varepsilon}_r(t) + \dot{\varepsilon}_t(t) - \dot{\varepsilon}_i(t)) = -\frac{2C}{L} \dot{\varepsilon}_r(t) \quad \text{Eq. 1-69}$$

$$\sigma(t) = \frac{A}{2S} E (\varepsilon_i(t) + \varepsilon_r(t) + \varepsilon_t(t)) = \frac{A}{S} E \varepsilon_t(t) \quad \text{Eq. 1-70}$$

Where A is the cross-section area of bars, L , S are the length and area of specimen, $C = \sqrt{E/\rho}$ is the velocity of wave in the bars, E is the Young's module of bars and ρ is the density of bars.

1.4.2 Bulge test

1.4.2.1 Quasi-static bulge test

For the bulge test, the central zone of circular plate is deformed under biaxial tensile state, as shown in Fig. 1-20^[70]. The hydraulic fluid, viscous materials or gas^[71] can

be chosen as the pressure medium. Compared with the uniaxial test, bulge test is usually adopted to obtain material behaviour under balanced tensile path, especially for the equivalent stress and equivalent strain curves, which can reach up to much larger deformation level, even two times of that obtained by uniaxial tensile test [72] [73]. The main drawbacks of bulge test are the bending effect and lack of changeable strain paths during tests [74]. The membrane theory is used to determine the stresses and strains.

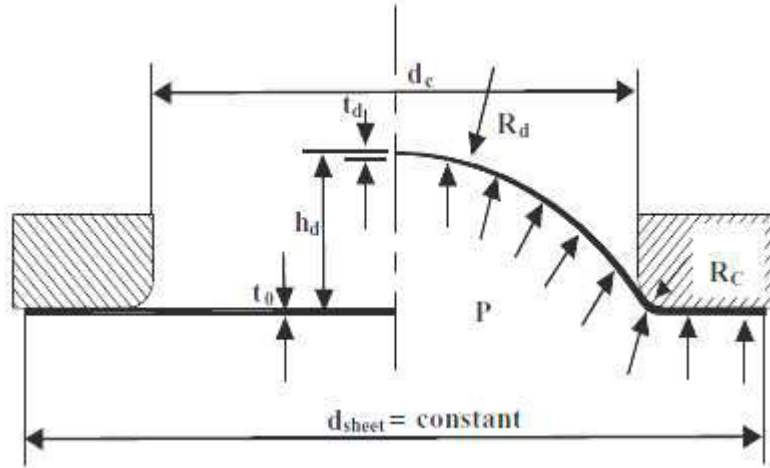


Fig. 1-20 Bulge test [70]

If the material is isotropic and Mises yield criterion is adopted, the equivalent stress $\bar{\sigma}$ can be calculated by:

$$\bar{\sigma} = \frac{1}{\sqrt{2}} \sqrt{(\sigma_1 - \sigma_2)^2 + \sigma_1^2 + \sigma_2^2} = \sigma_1 = \sigma_2 = \frac{pR_d}{2t_d} \quad \text{Eq. 1-71}$$

where p is the hydraulic pressure, R_d is the radius of dome, t_d is the current thickness at the top of dome.

The equivalent strain can be calculated with the assumption of constant volume:

$$\bar{\epsilon} = \frac{2}{\sqrt{3}} \sqrt{\epsilon_1^2 + \epsilon_2^2 + \epsilon_1 \cdot \epsilon_2} = 2\epsilon_1 = 2\epsilon_2 = -\epsilon_3 = -\ln\left(\frac{t_d}{t_0}\right) \quad \text{Eq. 1-72}$$

where t_0 is the initial thickness of sheet.

With a fillet R_c in the cavity, the radius R_d of dome can be calculated by:

$$R_d = \frac{((d_c/2) + R_c) + h_d^2 - 2R_c h_d}{2h_d} \quad \text{Eq. 1-73}$$

where d_c is the diameter of cavity and h_d is the dome height.

The thickness t_d at the top of dome can be estimated as follows:

$$t_d = t_0 \left(\frac{1}{1 + (2h_d/d_c)^2} \right) \quad \text{Eq. 1-74}$$

The unknown dome height h_d is measured during the test.

1.4.2.2 Dynamic bulge test

For the dynamic biaxial test at high strain rates of up to $500/s$, Grolleau et al. [75] [76] have proposed a dynamic bulge testing device, in Fig. 1-21. The idea is to design a movable bulge cell in a SHPB system. When the input bar is impacted at a speed, a pressure wave is generated and transmitted to the fluid. Then, the bulge cell and the output bar will move forward while the specimen will also be deformed by the pressure of fluid. During the test, the fluid pressure is calculated by the incoming and reflected waves measured by strain gages on the input bar. It is found that the bars should be made of low impedance materials to achieve a satisfactory pressure measurement accuracy. The effective piston displacement is calculated by the incoming and reflected waves, and the transmitted wave measured on the output bar. The Swift laws combined with Cowper-Symonds model are identified for A16111-T4 and DP450 sheets by inverse analysis. The objective function was defined by the pressure-time history and the effective displacement-time history. Ramezani et al. [77] have also developed a similar dynamic bulge test set-up on the basis of SHPB system. This high strain rate bulge test technique have been validated by comparison of the analytical and FE simulation with the experimental results.

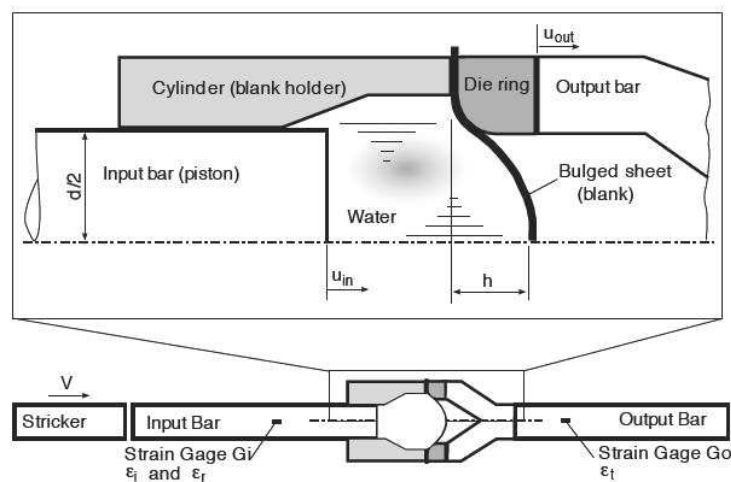


Fig. 1-21 Dynamic bulge testing device [75]

1.4.3 Plane strain test

The plane strain test is usually performed by the traditional uniaxial tensile testing machine. The testing specimen should be designed to keep the strain along the width direction zero ($\epsilon_{22} = 0$) during deformation. For specimen design of plane strain test, the width of deformed zone is usually much larger than the length, as shown in Fig. 1-22. The main drawback of plane strain test is the influence of the free edges on strain field homogeneity and stress calculation [78]. Wagoner et al. [79] [80] [81] has compared several types of plane strain specimen geometry to study the effects of dimension on the strain distribution and strain level. Flores et al. [82] have presented a methodology to experimentally identify the evolution of the homogeneous plane-strain field region during deformation. A general formula for calculating stress has been given by using experimental data and including the edge effect evolution.

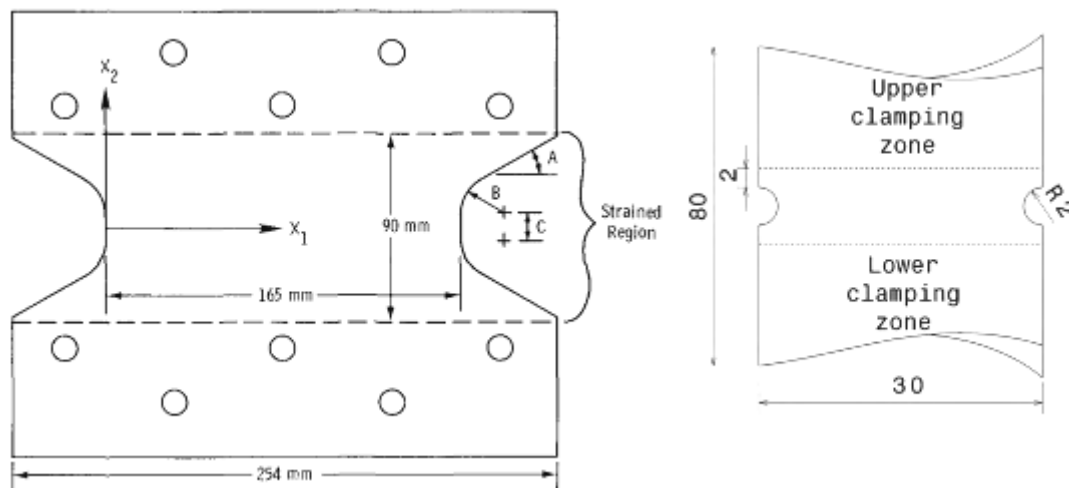


Fig. 1-22 Plane strain specimens [79] [82]

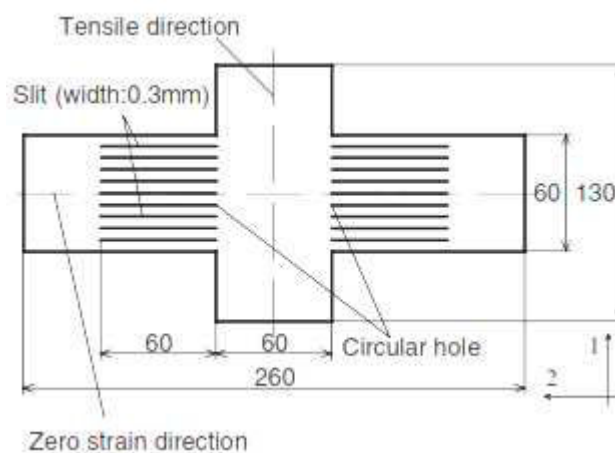


Fig. 1-23 Cruciform shape for plane-strain tension [83]

Kuwabara et al. [83] have developed a novel plane-strain tensile test of sheet metals to measure the stress-strain curves, using a hydraulically servo-controlled biaxial tensile testing machine and a newly-devised cruciform specimen, as shown in Fig. 1-23. The principal strains of the specimen are measured by strain gages, and strain rates can be calculated. By online controlling the strain rates, it has been succeeded in realizing plane strain tensile tests. Tensile direction is parallel to the shorter arms (axis-1). The total strain along the longer arms is kept almost to be zero. The slits are made along longer arms to exclude geometric constraint on the deformation of the gauge section.

1.4.4 Simple shear test

1.4.4.1 Quasi-static simple shear test

The simple shear test is usually adopted to carry out the cyclic loading tests [84] [85] [86]. American Society for Testing and Materials (ASTM) [87] has suggested a procedure to determine shear ultimate strengths, which can be carried out on the traditional uniaxial testing machine. The simple shear testing specimen is given in Fig. 1-24.

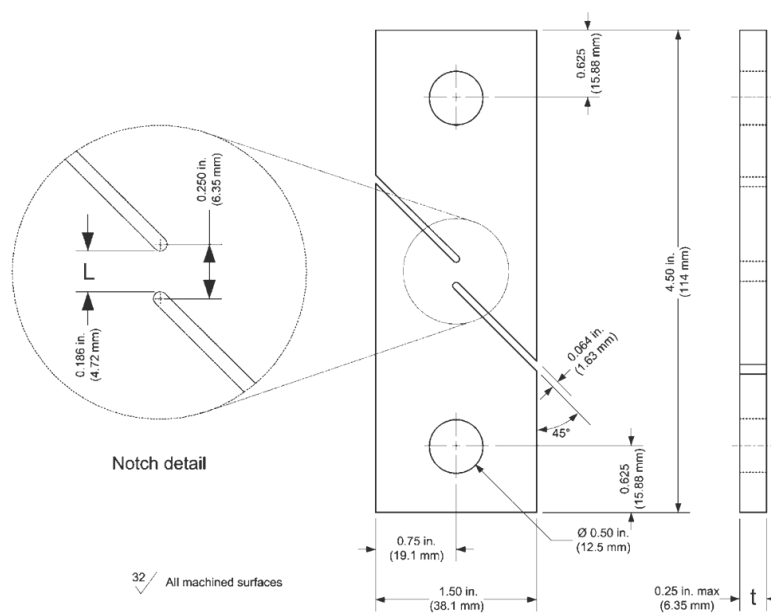


Fig. 1-24 Shear testing specimen (ASTM B831-11) [87]

For many simple shear tests, the experimental device can also be designed in order to impose a parallel displacement of two lateral grips along the opposite directions [88]. To carry out the simple shear test at the strain rate from 10^{-4} to $10^2 / s$, Rusinek et al. [89] have adopted a fast hydraulic machine and designed a double-shear specimen, in Fig. 1-25. The loading force F is measured by the machine load sensor and the mean displacement of the specimen U is calculated by using two linear variable differential

transducer (VDTL) displacement gauges. The shear strain, strain rate and stress of the quasi-static shear test can be calculated as follows.

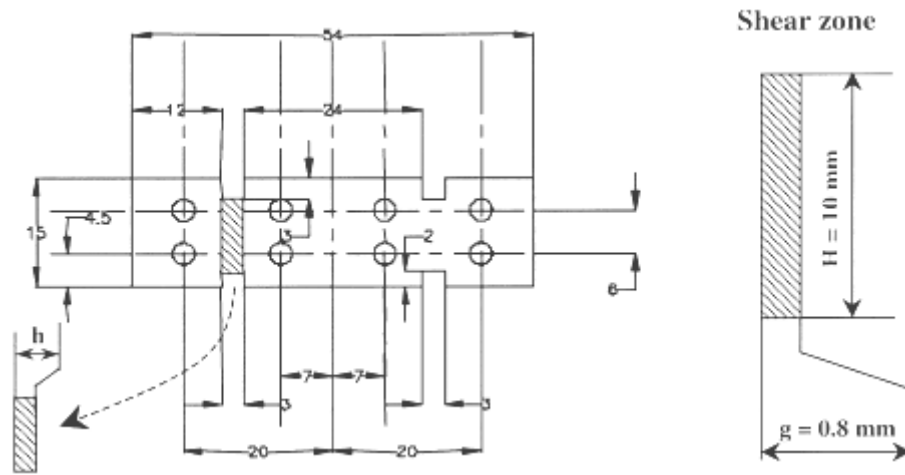


Fig. 1-25 Specimen of double shear test ^[89]

Shear strain is calculated by :

$$\gamma = \frac{U}{h} \quad \text{Eq. 1-75}$$

Here, h is the width of shear zone.

Shear stress is calculated by:

$$\tau = \frac{F}{2A_s} \quad \text{Eq. 1-76}$$

Here, A_s is the cross section of shear zone, $A_s = 2gH$, g is the thickness of shear zone and H the height of shear zone.

Shear strain rate is calculated by:

$$\dot{\gamma} = \frac{1}{h} \frac{dU}{dt} = \frac{V}{h} \quad \text{Eq. 1-77}$$

Where V is the loading velocity.

1.4.4.2 Dynamic simple shear test

For the strain rate higher than $10^2 / s$, Rusinek et al. ^[89] have directly attached the double-shear specimen to the Hopkinson tube and loaded by the direct impact of a

projectile, as shown in Fig. 1-26 . At the instant of impact, a transmitted elastic wave starts to propagate in the Hopkinson tube and recorded by the strain gages glued on the Hopkinson tube. With the measured transmitted wave, the displacement of tube can be determined by the analysis of propagation of the elastic wave in bars or tubes, and the force transmitted by the specimen can also be computed. The testing methods have been applied to determine the visco-plastic behaviour of cold rolled sheet steel under a wide range of strain rate. An original visco-plastic constitutive relation of Rusinek and Klepaczko (R-K) model has been identified.

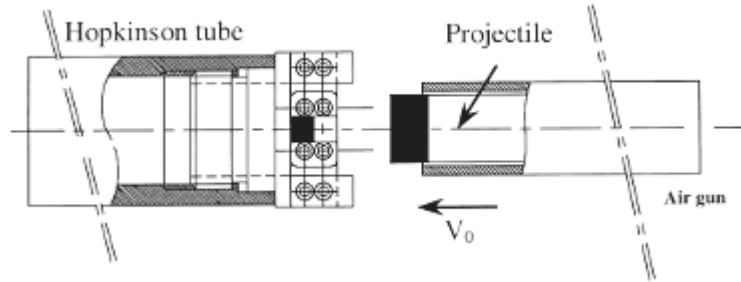


Fig. 1-26 Experimental setup of direct impact ^[89]

1.4.5 Multi-axial tests

1.4.5.1 Biaxial tensile test

Nowadays, there are several biaxial tensile tests, including bulge test of circular specimen, disk compression test, tension-internal pressure test of tubular specimen, biaxial test of cruciform specimen, as shown in Fig. 1-27 . The bulge test has already been presented in the section 1.4.2. The disk compression test is also used to acquire the material information under balanced tensile path, but the friction between the specimen and tools is the biggest problem. Biaxial tensile test of cruciform specimen will be studied in the next chapter.

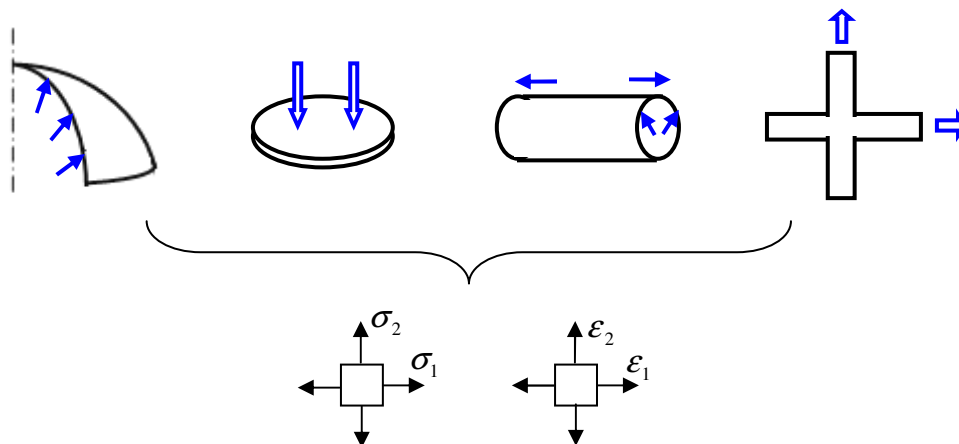


Fig. 1-27 Biaxial tensile tests

Kuwabara et al. ^[90] have developed a combined uniaxial tension-internal pressure testing machine. Various strain paths under large deformation can be realised by controlling the ratios of uniaxial tensile force T by hydraulic cylinders and the internal pressure P by an intensifier, as shown in Fig. 1-28. A spherometer is located on the top of specimen to measure the radius of curvature, R_ϕ , in the axial direction. The axial and circumferential true strain on the outer surface of specimen are measured by strain gauges. The true strains and true stresses along the axial and circumferential directions will be calculated on the midwall. For the tension-internal pressure test of tubular specimen, various biaxial strain paths can be realised, but it is limited for application because it is difficult to manufacture the tubular specimen for sheet metal ^{[91] [92] [93] [94]}.

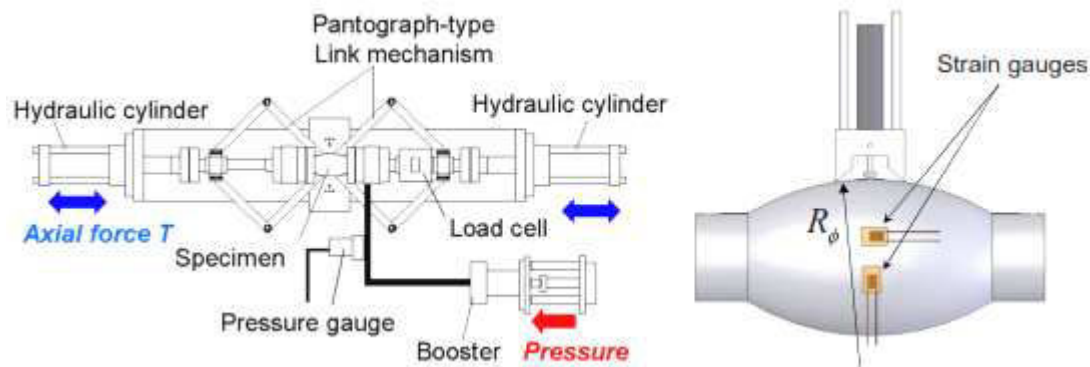


Fig. 1-28 Uniaxial tension-internal pressure testing machine ^[95]

The initial and subsequent yield locus of extruded aluminium alloy A5154-H112 tubes have been investigated under different strain paths, using this tension-internal pressure test of tubular specimen ^[96]. The forming limit stresses of steel tubes (JIS STKM11A) subjected to proportional and nonproportional loading paths have also been studied ^[97]. With the biaxial tests of cruciform and tubular specimens, the plastic behaviour of high strength steel sheet (JSC590R) have also been investigated for a equivalent strain range of $0.002 \leq \bar{\epsilon}_p \leq 0.16$ ^[95].

1.4.5.2 Combined test

To characterize sheet material behaviour under multi-axial and non proportional loads, Pijlman et al. ^[98] have designed a biaxial testing equipment, which can combine the plane strain test with the shear test on only one specimen, as shown in Fig. 1-29. The upper part can move along the horizontal direction to carry out shear test, and the lower part can move along the vertical direction to perform the plane strain test. Using this biaxial device, the shear and plane strain reference points of yield function can be determined. Meanwhile, the cyclic shear test and orthogonal tests can also be carried out on this device for material modelling under non-proportional loading paths. Forles et al. ^{[99] [100]} have developed a similar experimental device to study the plane

strain test and simple shear test. Mohr et al. ^[101] ^[102] have also developed a similar dual-actuator system and performed the tests of various combinations of the shear and tensile loadings to determine initial yield function and hardening laws of a stainless steel 301LN under isothermal quasi-static conditions at room temperature .

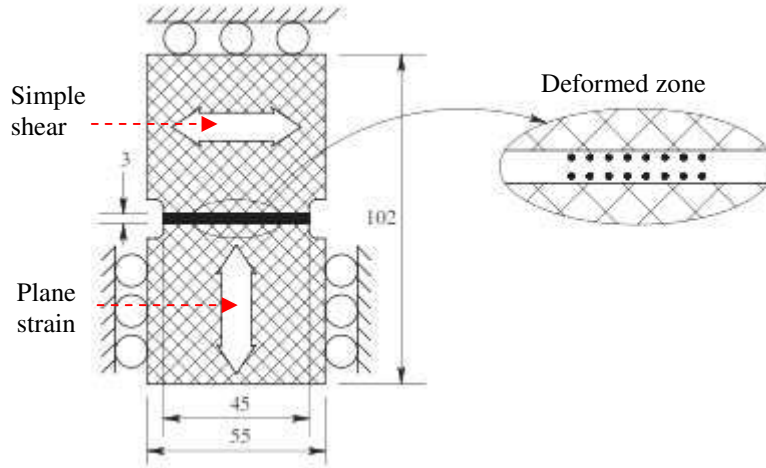


Fig. 1-29 Combined plane strain-simple shear test ^[12]

With the development of digital image correlation (DIC) and inverse analysis, many experiments with heterogeneous deformation have been proposed to identify the constitutive parameters of materials on a single sample ^[103] ^[104] ^[105] ^[106] ^[107] . Pottier et al. ^[108] have developed an out-of-plane testing procedure with a hemispherical punch to apply the prescribed displacement at the centre of sample, in Fig. 1-30. With the punch moving, the deformation of sample combines two uniaxial tensile paths, two shear paths and one biaxial tensile paths. The parameters of Hill 48 yield function and Ludwick hardening law have been identified for a commercial pure titanium sheet. The identified material parameters were validated by comparison the top profiles of a deep-drawing cup between experimental and simulated results.

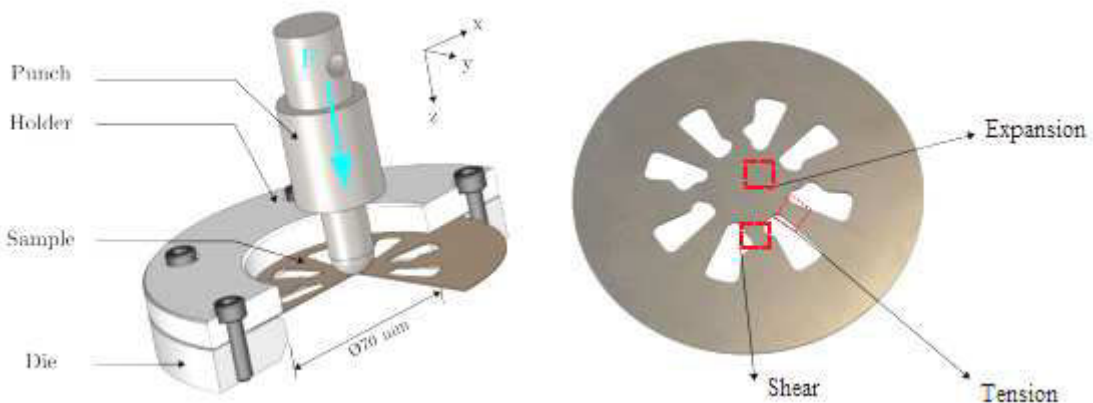


Fig. 1-30 Experimental tools and sample under heterogeneous deformation ^[107]

1.5 Conclusion

For FE simulation of sheet metal forming processes, accurate phenomenological models of material are demanded. In order to identify parameters of these models, appropriate experimental databases are needed. These databases must be obtained from experimental tests on sheet metal specimens at conditions encountered in the forming processes. In most sheet metal forming processes such as stamping, hydroforming, ... large strains can be reached in intermediate strain rate range (up to few hundred s^{-1}). Moreover, formed sheets are usually submitted both to in-plane biaxial loadings and to linear or nonlinear strain paths.

Many experimental techniques have been developed for material characterization, including: uniaxial tensile test, bulge test, plane strain test, simple shear test,... There are several specific limitations for each of these traditional experiment. In order to avoid these main drawbacks, an in-plane biaxial tensile tests of a cruciform specimen is proposed in this work. The potential of this test to identify hardening behaviour up to large strains in the range of intermediate strain rates is investigated at room temperature.

In the following work, an optimal shape of cruciform specimen is proposed to obtain large strains under equibiaxial tensile strain path. Then, the rate-dependent hardening sensitivity of sheet metals is identified by inverse analysis based on FE simulation of biaxial tensile tests.

2. Shape design of cruciform specimen

2.1 Introduction

Many biaxial tests using cruciform specimens under various strain paths, temperatures and strain rates ^[109] have been carried out with different goals of material modelling, including: (i) characterization of yield locus, (ii) identification of hardening model, (iii) determination of Forming Limit Curve (FLC), as shown in Fig. 2-1.

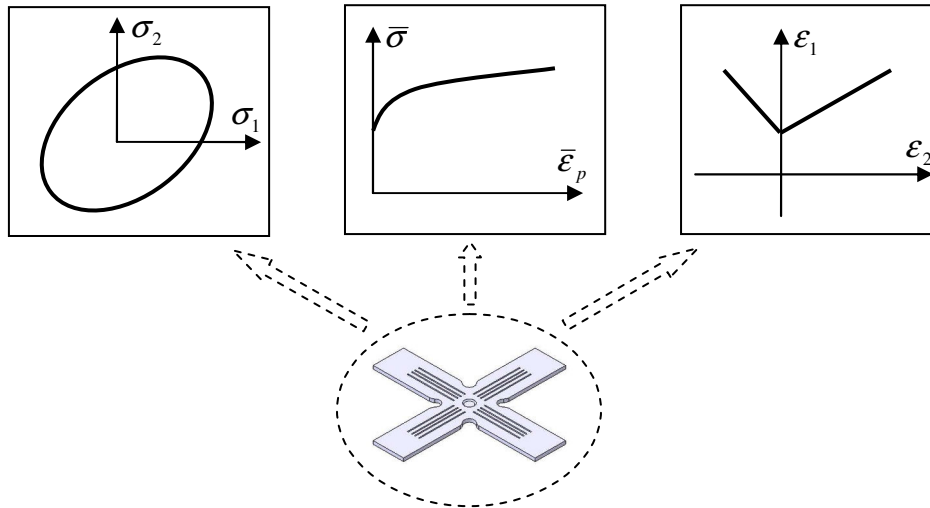


Fig. 2-1 Applications of biaxial tests for material modelling

Up to date, several types of biaxial devices have been developed for biaxial tests on cruciform specimen, including link mechanism attachments and stand-alone machines ^[110]. The experimental devices should be controlled to keep the centre of specimen unmoved ^[111] and apply the specific loading ratios along two perpendicular directions. In section 2.2, the two main types of biaxial device are presented. Although a newly standardised cruciform shape with seven slits in each arm has been proposed by International Organization for Standardization (ISO) ^[112], the maximum deformation at the central zone is very small. Therefore in following work, a review of the typical cruciform shapes is presented in section 2.3, in order to investigate the more efficient geometries allowing to obtain large strains. Then, an optimal cruciform shape is designed for large strains by means of the numerical simulation tool.

2.2 Biaxial testing devices

Many link mechanism attachments have been design and equipped in a conventional uniaxial testing machines to convert uniaxial tensile or compressive force into two forces along two perpendicular directions of cruciform specimen (in Fig. 2-2) ^[113] ^[114]. Although the attachments are economical, the disadvantage is that the load ratios can not be online changed during tests. Moreover, this kind of machine is not dedicated to dynamic tests. So, stand-alone machines seem more appropriate for such tests. Stand-

alone biaxial machines are developed with independent actuators along two directions, by which various linear and nonlinear load paths can be realised (in Fig. 2-3) ^{[115] [116]}.

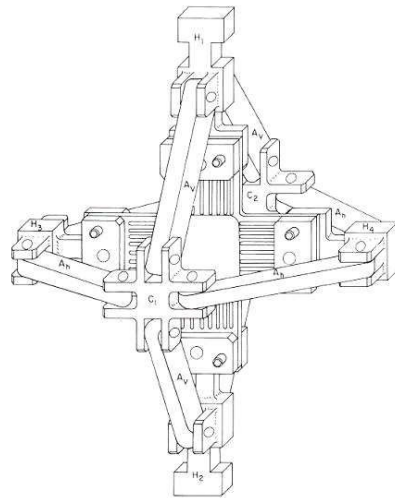


Fig. 2-2 Link mechanism attachments for biaxial test (FER 1988)

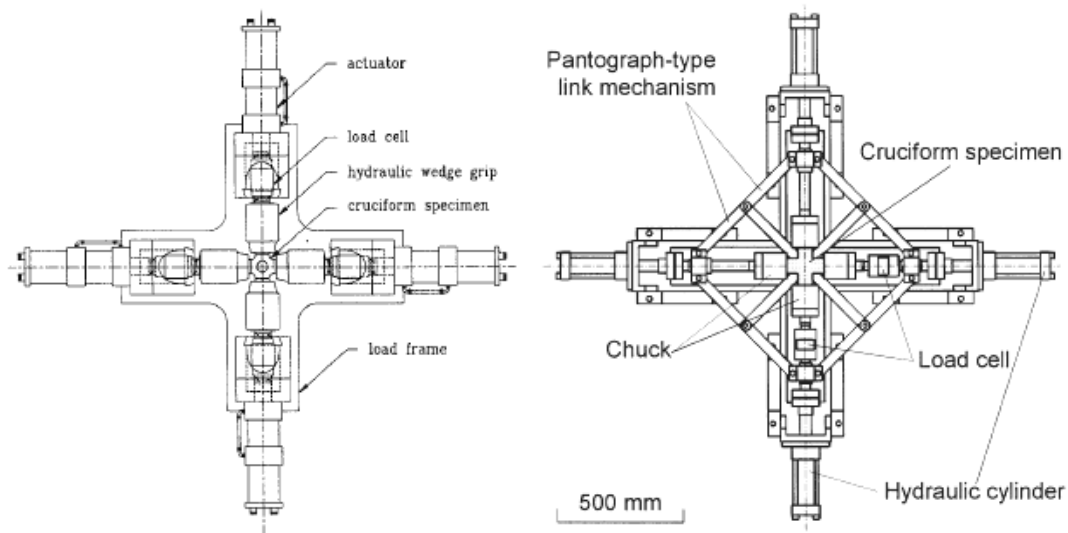


Fig. 2-3 Stand-alone biaxial testing machines (MAK 1992, KUW 1998)

A dynamic biaxial testing machine, which consists of four independent servohydraulic actuators, has been developed at the Laboratory GCGM of INSA de Rennes (in Fig. 2-4). The loading capacity for each actuator is 50KN . For quasi-static biaxial tensile tests, this machine is controlled by close-loop with displacement sensors and the loading speed range covers from 0.01m/s to about 2m/s . For dynamic biaxial tensile tests, the machine is controlled by open-loop and the loading speed range covers from 250m/s to 2000m/s . An additional mass of 100kg is adopted along each direction to maintain loading speed by inertia effect. As shown in Fig. 2-5, a high speed camera (Photron FASTCAM-APX RS) is placed over the specimen to record deformation during tests. Load sensor is adopted along each arm for force measurement. The loading speed of each actuator is measured by displacement sensors.

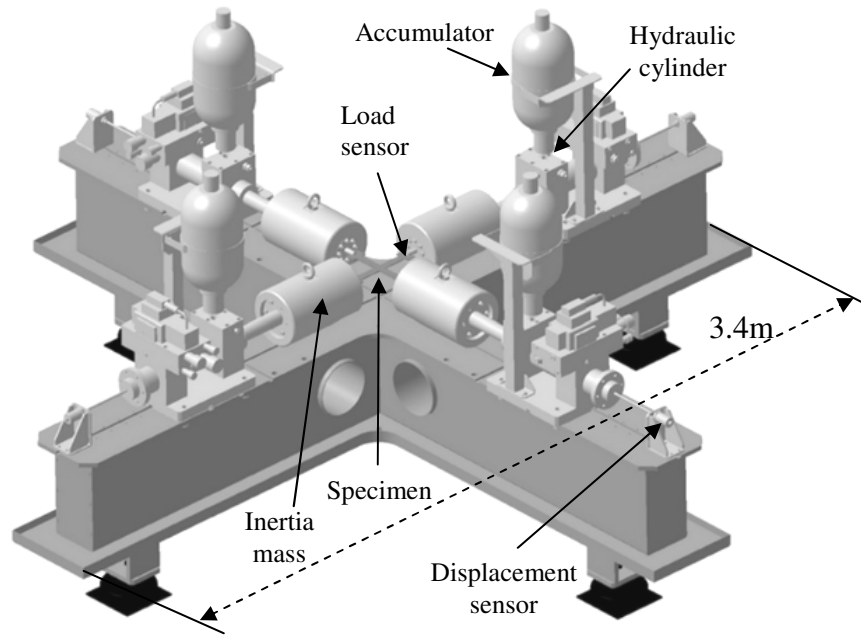


Fig. 2-4 Dynamic biaxial testing machine
(Loading capacity: 50KN , Quasi-static velocity: 0.01m/s ~ 2m/s ,
Dynamic velocity: 250m/s ~ 2000m/s)

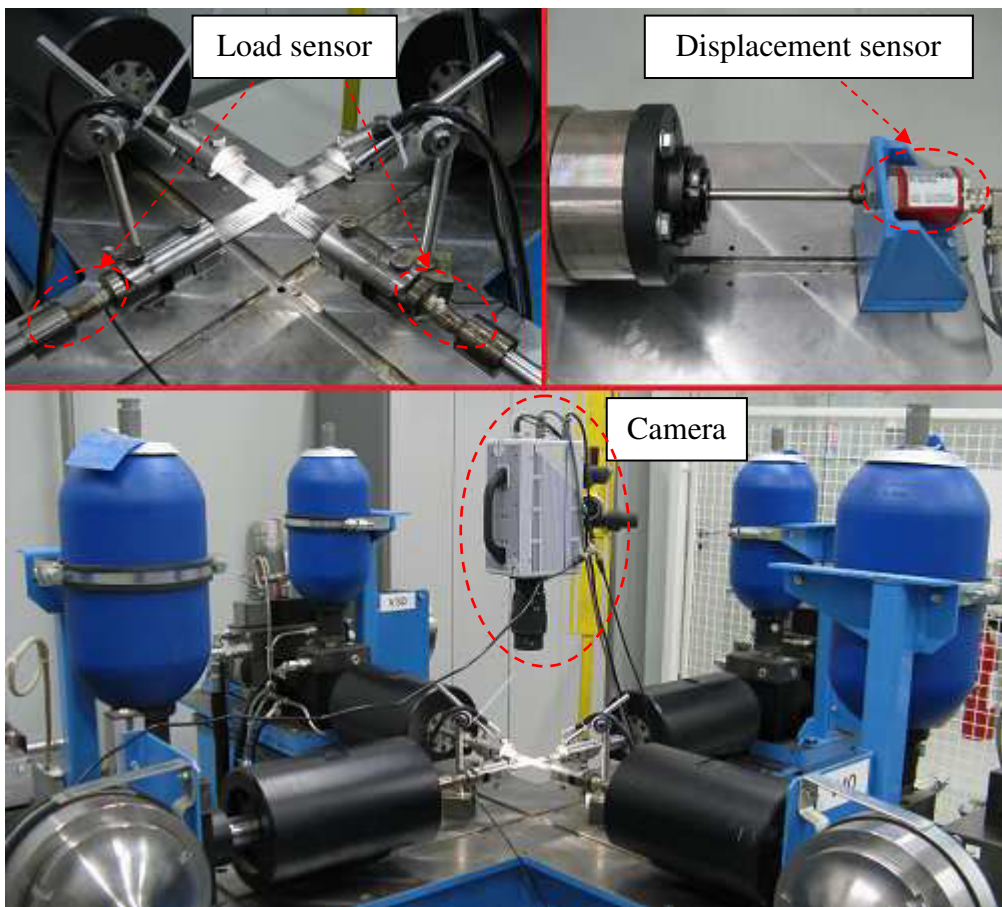


Fig. 2-5 Biaxial testing machine and measurement systems

2.3 Application of cruciform specimen

Since 1960s, biaxial tests on flat cross-shaped specimens, with various geometries of the central zone, have already been performed for characterization of yield locus, identification of hardening model and determination of FLC. Several typical shapes and applications of cruciform specimens are reviewed in this section.

2.3.1 Characterization of yield locus

Muller et al. ^[117] have adopted cruciform specimens with notches at intersections of arms. The shape was optimized by varying the parameters, R_1 and R_2 , to obtain a large zone of homogeneous deformation and high strain level before instability occurs, as shown in Fig. 2-6. The maximum strain at the central zone was affected by different materials. The stress components were calculated by dividing the forces through the cross section. The yield point was determined by a sharp increase of temperature due to dissipation of plastic work. Finally, the initial yield locus of a steel (St14 O5) and subsequent yield locus after prestraining of an aluminium alloy (AlMgSi1) have been investigated. Banabic ^[118] has used the same specimen to obtain yield points under different stress ratios for an aluminium alloy AA5182-0, and compared with BBC2005 yield criterion.

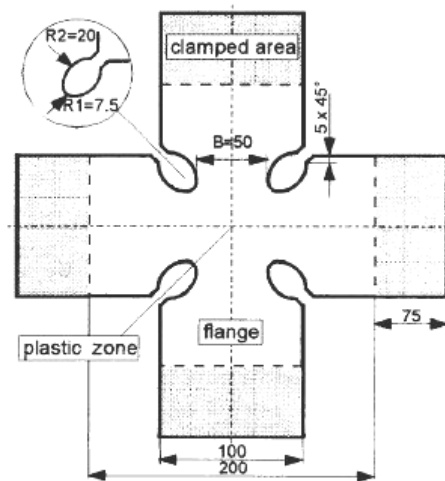


Fig. 2-6 Cruciform shape (MUL, 1996)

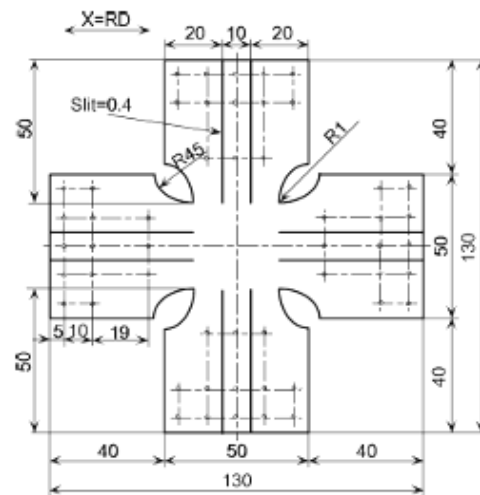


Fig. 2-7 Cruciform shape (NAK, 2003)

Naka et al. ^[119] ^[120] have performed biaxial tensile tests on an aluminum-magnesium alloy sheet at temperatures from 30°C to 300°C and strain rates from $10^{-5} / s$ to $10^{-2} / s$ to study the effects of temperature and strain rate on evolution of yield loci. A cruciform shape has been suggested with notches at the intersection of arms and two slits in each arm to avoid geometrical constrains on the gauge zone, as shown in Fig. 2-7. The maximum plastic strain was about 0.06 at room temperature. The strain and

strain rate were calculated by the recorded grid images. The yield stresses was defined by the points where the proportional relation between stress and strain disappeared.

Kuwabara et al. ^{[121] [122] [123]} have proposed a specimen shape with slits in arms to obtain homogeneous deformation field at the gauge zone, as shown in Fig. 2-8. The maximum equivalent strain of specimen was only 0.04. The strain components were measured by four biaxial strain gauges. The stress components were calculated from dividing the measured forces by current cross sectional areas. The successive contours of plastic work for particular plastic strains in the biaxial stress space have been determined for cold-rolled low-carbon or dual phase steel sheets and compared with various phenomenological or crystallographic yield criteria.

Merklein et al. ^{[124] [125]} have designed a new biaxial setup on a punch-load moving perpendicular to the sheet. Biaxial tensile tests have been carried out with a local heat on magnesium alloy AZ31 at the temperature from room temperature to 310°C. The shape with slits of different length has been adopted to assure that the maximum strains occur at the central zone and stress concentration is reduced to a minimum, as shown in Fig. 2-9. The strain fields of specimen were determined by DIC techniques. The stress components were calculated on the basis of experimental forces and cross sections. The stress points on the initial and subsequent yield loci were determined for the corresponding equivalent strains.

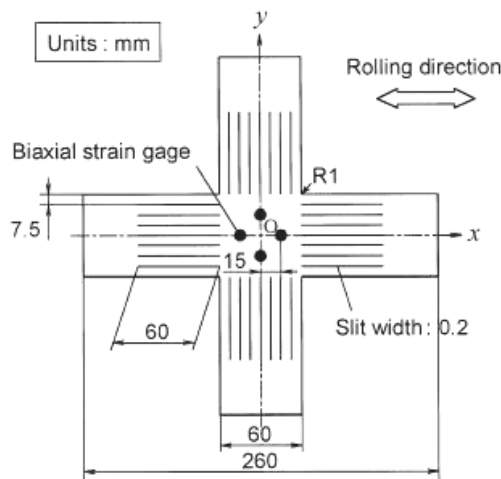


Fig. 2-8 Cruciform Shape (KUW, 1998)

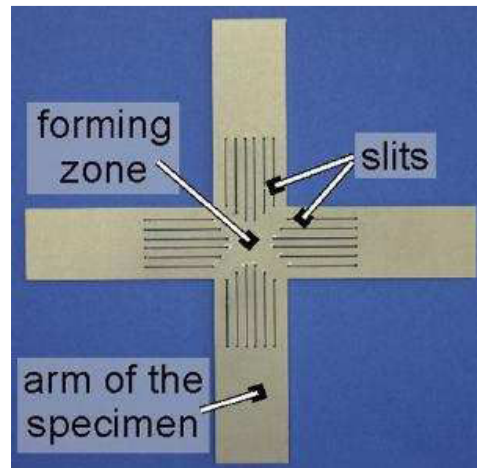


Fig. 2-9 Cruciform shape (MER, 2008)

Teaca et al. ^{[126] [127]} have proposed heterogeneous biaxial tensile tests to identify the plastic anisotropy of sheet metal. Two shapes of cruciform specimen were designed to cover the whole stress plane. The first one with hole at the central zone covered the stress states from uniaxial tension (UT) to plane-strain tension (PST). The second one covered the stress states from uniaxial tension (UT) to equibiaxial tension (EBT), as shown in Fig. 2-10. The equivalent strain at the central zone of second specimen is about 0.1. The strain fields were calculated by DIC method. A two-step strategy of

2. Shape design of cruciform specimen

parameter identification was performed to determine FMM yield function for ES steel and 1050A aluminium sheets. The parameters of hardening law were determined by uniaxial tensile tests. Then, the parameters of FMM yield function were identified by minimizing the difference between experimental and FE-simulated strain fields of specimen. With the identified parameters, the formation of ears in the cup drawing test is accurately predicted by the finite element simulation.

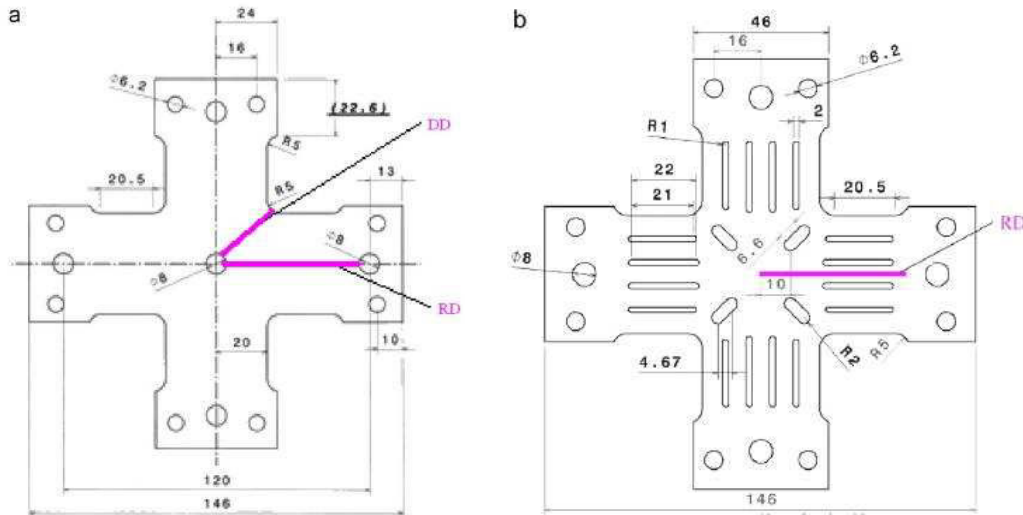


Fig. 2-10 Cruciform shape of UT/PST (a) and UT/EBT (b) specimen (TEA, 2010)

Prates et al. ^[128] have used a single equibiaxial tensile test of cruciform specimen to simultaneously identify the parameters of Hill 48 yield criterion and Swift isotropic hardening law by mixed numerical-experimental method. A cruciform shape (in Fig. 2-11) was proposed to reproduce heterogeneous deformation with strain paths ranging from uniaxial to equibiaxial tension. The strain fields were obtained by DIC method.

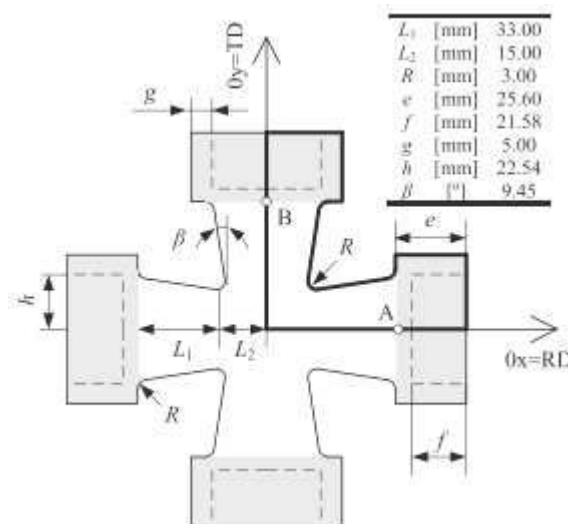


Fig. 2-11 Cruciform shape (PRA, 2014)

Zhang et al. ^[129] have adopted unique equibiaxial tensile test of cruciform specimen to identify the parameters of Bron and Besson 2004 yield criterion for AA5086 and DP980 sheets. As shown in Fig. 2-12, the specimen with notches was designed to realise a continuous strain states from $\varepsilon_2/\varepsilon_1 = -0.2$ to $\varepsilon_2/\varepsilon_1 = 1$. The strain fields were calculated by DIC techniques. The FE-simulated principal strains and strain paths along diagonal, longitudinal and transverse directions were compared with the experimental results. The identified parameters have been validated by comparison with those determined by uniaxial test, bulge test and simple shear test.

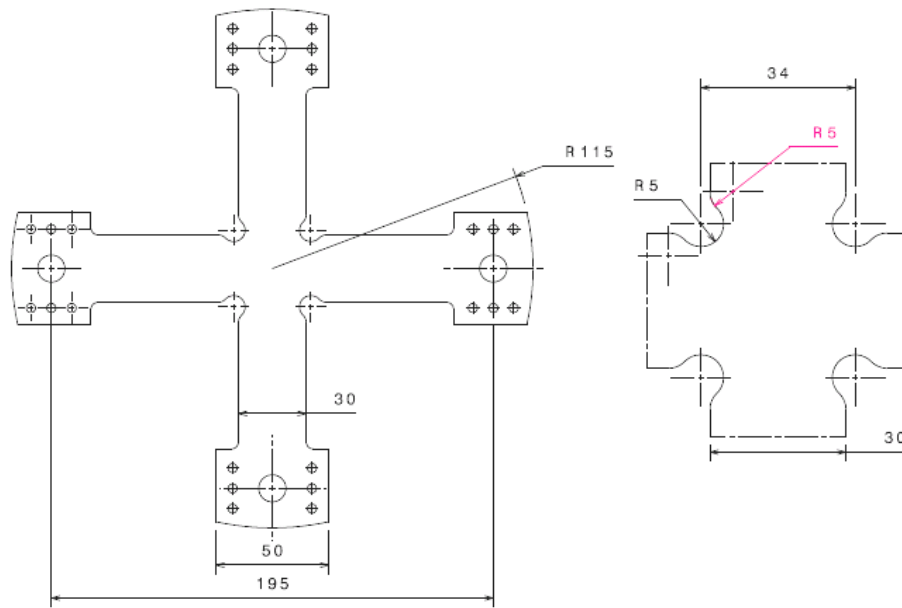


Fig. 2-12 Cruciform shape (ZHA, 2014)

2.3.2 Identification of hardening model

Makinde et al. ^[130] have presented two different geometries of cruciform specimen to investigate the mechanical behaviour of sheet metals and composite materials under monotonic and cyclic biaxial loading conditions, as shown in Fig. 2-13. One was shown with a circular thickness-reduced central zone. The other was given with a rectangular thickness-reduced central zone and slits in each arm. Green et al. ^[131] have adopted the second shape (as-received thickness, 6.3mm) with a thickness-reduced central zone (final thickness, 1.2954mm) to obtain maximum strain in the central zone and seven parallel slots in each arm to maintain the deformation as uniform as possible in the gauge section. The cruciform specimens were deformed up to equivalent strains of approximately 0.15 in the biaxial stretching zone. The strain at the central zone was measured by biaxial extensometers ^[132]. Several biaxial tensile tests were carried out for AA1145 sheet under different proportional strain paths. The biaxial flow curves were determined by an iterative procedure based on FE simulation.

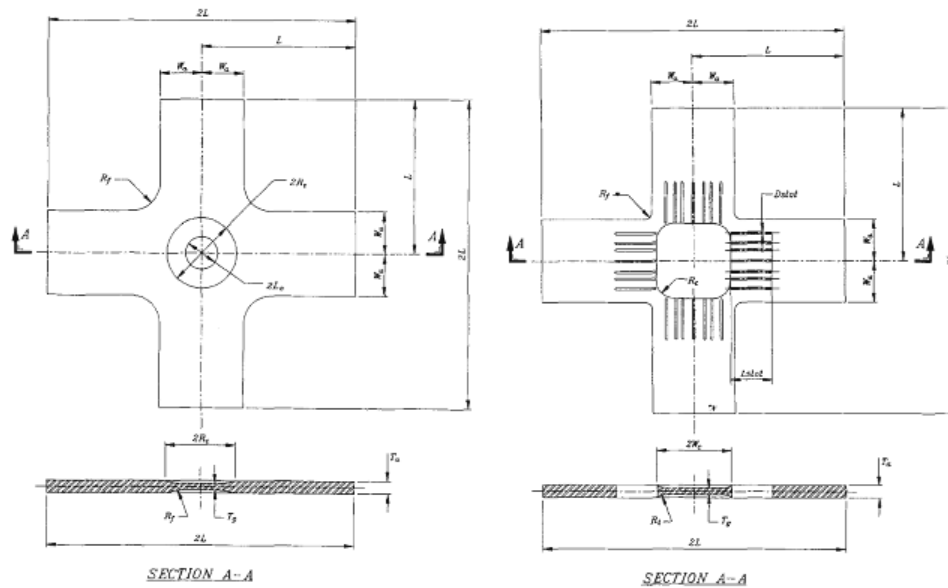


Fig. 2-13 Cruciform shapes (MAK, 1992; GRE, 2004)

Gozzi et al. ^[133] ^[134] ^[135] have used biaxial tests of cruciform specimen to investigate the plastic behaviour of extra high strength steel under nonlinear strain paths. Two shapes were designed with smooth transition to reduce stress concentration and three slits in each arm to make deformation uniform, as shown in Fig. 2-14. The stress distribution was improved by the different positions of slots in each arm. The maximum strain at the central zone is about 0.01. The strain at the central zone was measured by strain gauge. The stress was obtained from the forces dividing by the modified cross section. A series of tests have been carried out under two-stage loading paths, including a initial proportional loading path, an unloading and a subsequent proportional reloading path in a new direction. Compared with a simple isotropic hardening model, a kinematical hardening model was validated to predict the response of material subjected to non-monotonic loading. Kulawinski et al. ^[136] have adopted the second shape of cruciform specimen to carry out biaxial tests on a cast TRIP steel. The strain at the central zone of specimen was measured by biaxial extensometers. A new procedure, called as partial unloading method, was proposed to determine the stress of specimen. The influence of strain path changes on the equivalent stress and equivalent strain were investigated by biaxial sequential tests under two-stage loading paths.

Uemori et al. ^[137] have adopted the shape of cruciform specimen (in Fig. 2-7) to conducted several biaxial tests on high strength steel (HSS) sheet under proportional and non-proportional loading paths. The non-proportional loading paths were realised by the sequential proportional loading paths after initial equibiaxial loading and unloading path. Compared with the isotropic hardening (IH) model, the kinematical hardening model (Yoshida-Uemori model) was validated to capture the Bauschinger effect and describe the translation of loading surface.

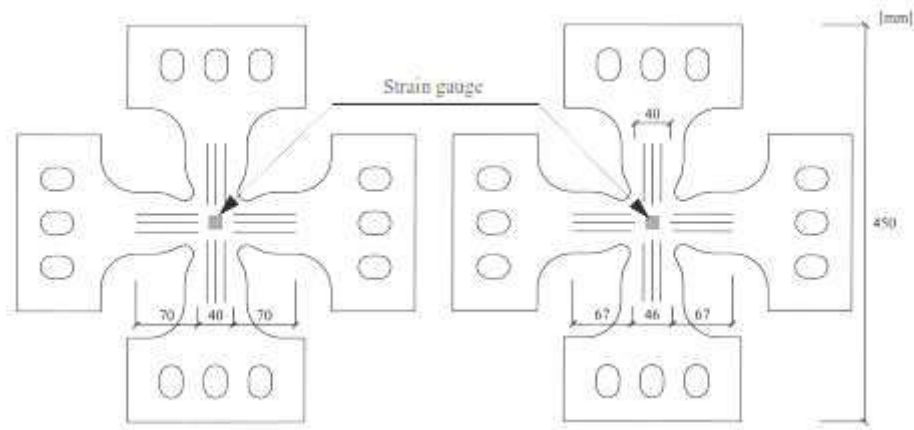


Fig. 2-14 Cruciform shapes (GOZ, 2004; KUL, 2011)

Merklein et al. ^[138] ^[139] have designed a stand-alone biaxial machine to realize an online continuous change of stress state from uniaxial tension to biaxial tension on cruciform specimen. A cruciform shape (as-received thickness, 1mm) with seven slits in each arm and the central section reduced by half on one side (final thickness, 0.5mm) is shown in Fig. 2-15. The maximum equivalent strain at the central zone is about 0.1. The strain fields were determined by DIC method. The stress components were calculated by the measured force and current cross sectional area. The isotropic and isotropic-kinematical hardening models have been compared with experimental results in the first quadrant of principal stress space for AA6016.

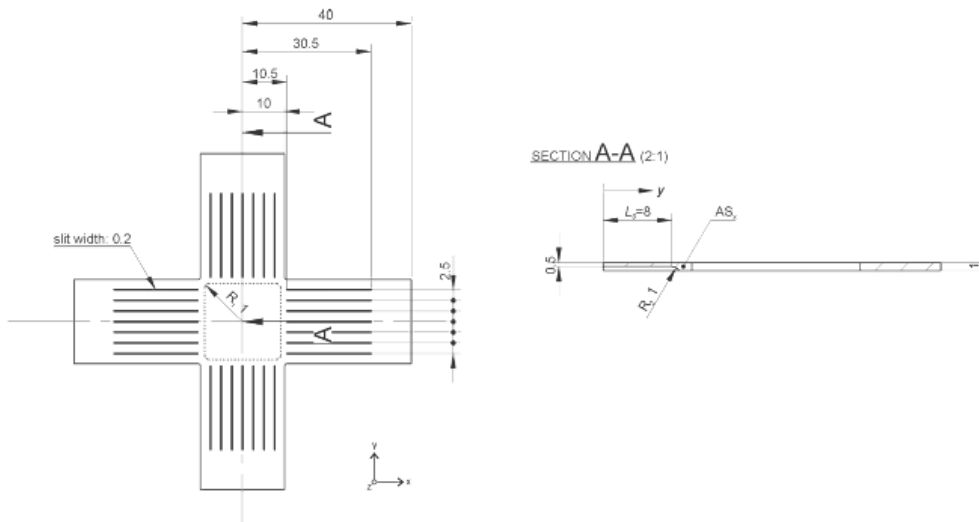


Fig. 2-15 Cruciform shape (MER, 2013)

2.3.3 Determination of forming limit curve

Yu et al. ^[140] have suggested biaxial tests of cruciform specimen to study forming limits under complex loading paths. An optimal shape (as-received thickness, 3mm)

with two-step thickness reduction was given by FE simulation for a low-carbon steel sheet, as shown in Fig. 2-16. A first cross-shaped thickness reduction (middle thickness, $1mm$) was made to transfer the main deformation to central zone. A further circular thickness reduction (final thickness, $0.7mm$) was used to concentrate limit strain at the central zone. The specimen shape has not been experimentally validated.

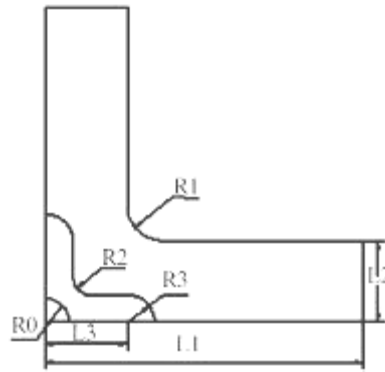


Fig. 2-16 Cruciform shape (YU, 2002)

Tasan et al. ^[141] ^[142] have suggested an optimal shape (as-received thickness, $0.7mm$) with circular thickness reduction for IF steel sheet. The thickness at the central zone is defined by a circular profile to make the smallest thickness at the central point (final thickness, $0.16mm$), as shown in Fig. 2-17. The specimens were produced by electro-discharge machining (EDM). It has been validated that there is little influence of manufacturing process on the material behaviour by several tests, such as surface profilometry, microscopy, grain size measurement, nano indentation and tensile tests.

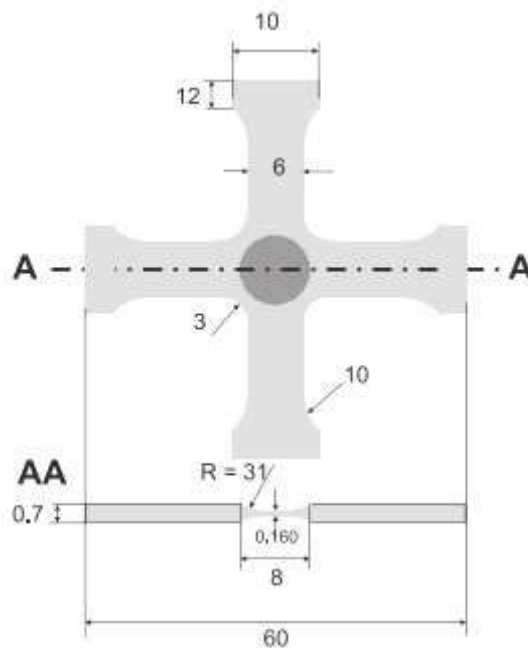


Fig. 2-17 Cruciform shape (TAS, 2008)

Abu-Farha et al. ^[143] ^[144] have carried out biaxial tensile tests on cruciform specimen to study microstructural mechanisms on biaxial deformation. Two cruciform shapes of various as-received thicknesses have been experimentally investigated for lightweight materials (AA5083, Mg AZ31B, TWIP steel) at elevated temperature (300°C) and quasi-static state. The shapes with thickness reduction (final thickness, around 1mm) have been designed for large strains up to crack at the central zone of specimen, as shown in Fig. 2-18. For the first one, each arm was tapered and a circular profile was used to define the thickness evolution. The other shape was suggested with notches at the corners and a circular flat-bottomed thickness reduction at the gauge area.

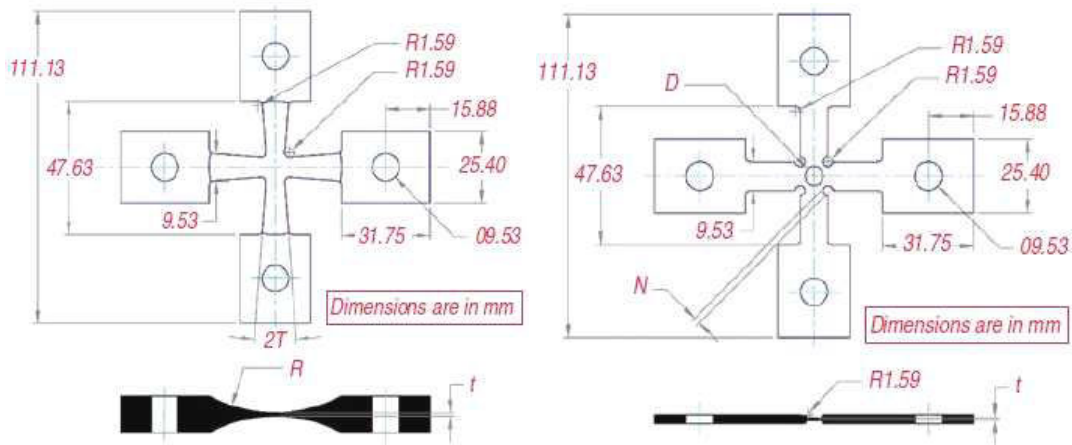


Fig. 2-18 Cruciform shapes (ABU, 2009)

Lee et al. ^[145] have adopted biaxial test of cruciform specimen to determine the first quadrant of FLC. A cruciform shape (as-received thickness, 1.6mm) with two-step thickness-reduction was proposed to make initial crack located at the central zone, as shown in Fig. 2-19. The square thickness-reduced zone (middle thickness, 1mm) with rounded corners is rotated by 45° relative to the arms. The second-step thickness-reduced zone (final thickness, 0.4mm) is circle.

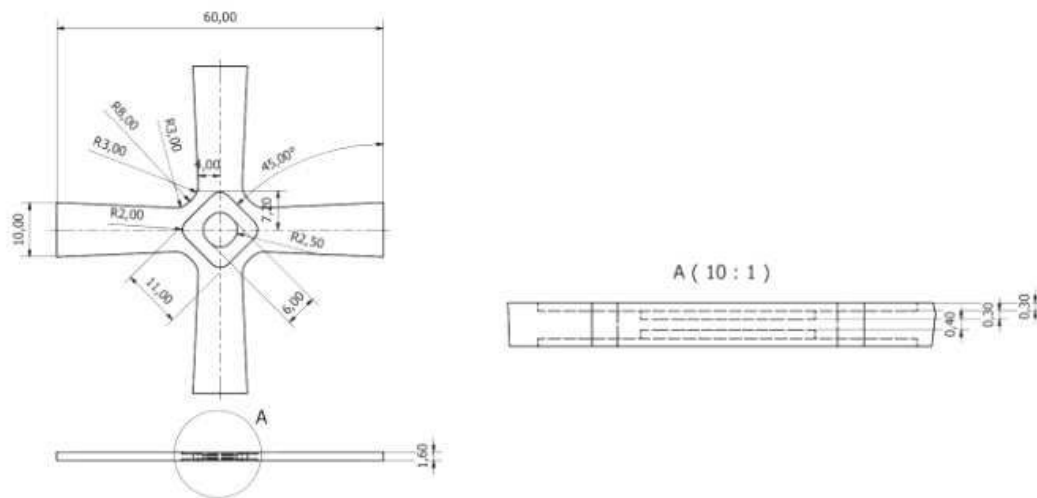


Fig. 2-19 Cruciform Shapes (LEE, 2015)

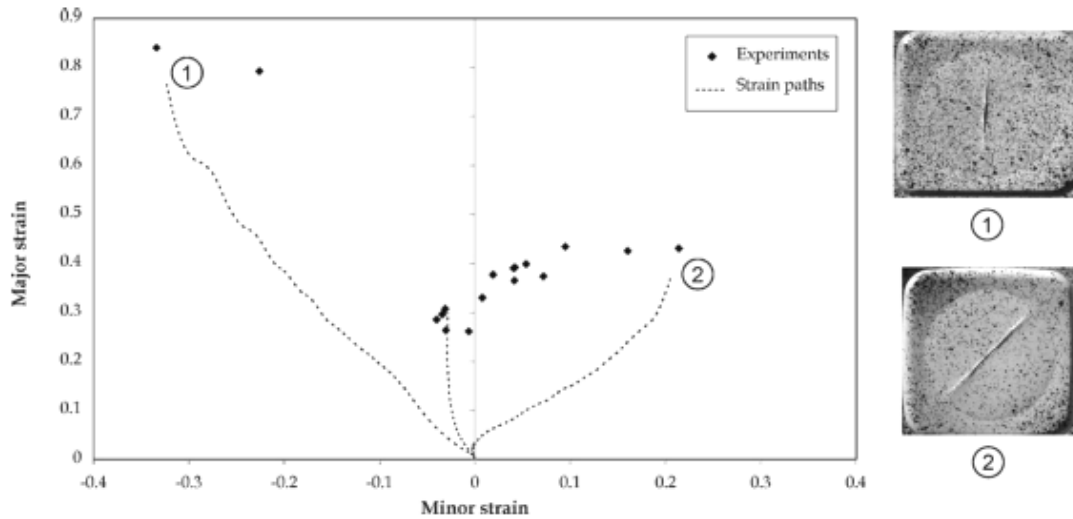


Fig. 2-21 FLC by cruciform biaxial tests

In conclusion, very few research about plastic behaviour modelling of sheet metals under large strains (up to the deformation level obtained by standardised uniaxial tensile tests) using biaxial tests on cruciform specimen have been reported. For large strains, shape design of cruciform specimen becomes usually very complex. Very few of them have been validated experimentally except the shape proposed by Zidane, which is based on two-step thickness reduction (from as received thickness 4mm to final thickness 0.75mm). Nevertheless, the use of this shape for any sheet thickness seems difficult, particularly for small initial thicknesses. Another drawback of the cruciform shape with a central thickness reduction defined by a curved profile is that large deformations are obtained only at the central point, which can lead some difficulties in the identification procedure. At the same time, most biaxial tensile tests on cruciform specimen have been carried out at quasi-static condition.

2.4 Numerical investigation of cruciform shapes

First of all, an optimal cruciform shape must be defined and the proposed geometry must verify the following specification:

- (1) Large strains must be reached at the central zone, which is deformed under biaxial tensile state;
- (2) Deformation field at the central zone must be as homogeneous as possible to facilitate the identification procedure;
- (3) Cruciform specimen should be as easy as possible to be manufactured;
- (4) Maximum load before necking for each actuator must be less than 50KN ;
- (5) For dynamic tests, the initial stiffness of the specimen is limited by capacities of the servo-hydraulic device. Consequently, dimensions of the square central zone of the cross specimen are chosen equal to 30mm .

In the following work, FE software ABAQUS (static-implicit algorithm) is adopted to simulate equibiaxial tensile tests. The initial thickness $2mm$ of sheet is chosen. A quarter FE model is adopted due to symmetries. Same displacements are applied along each arm of cruciform shape. Young's modulus $E = 69GPa$ and Poisson's ratio $\nu = 0.33$ are considered for elasticity. For plasticity, isotropic Mises yield criterion is used and the true stress-plastic strain curve, given in Fig. 2-22, is introduced point by point for the isotropic hardening behaviour.

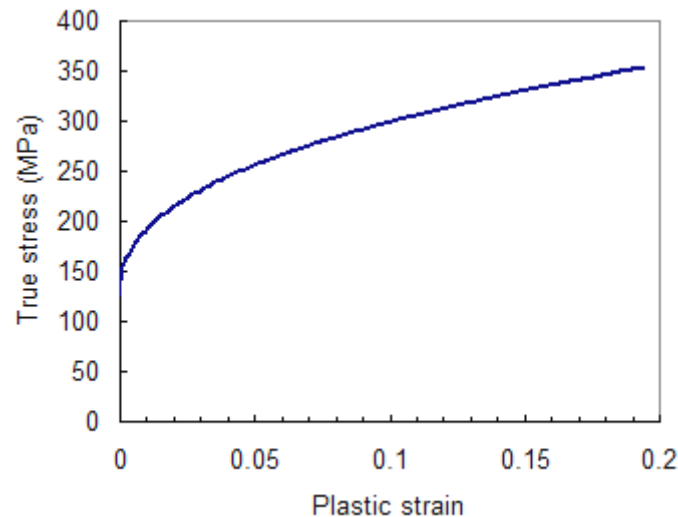


Fig. 2-22 True stress-plastic strain curve for FE analysis

FE simulations of equibiaxial tensile tests are performed up to a maximum value of major principal strain, $\varepsilon_1 = 0.20$. An equivalent plastic strain field $\bar{\varepsilon}_p$ and strain state (defined by the ratio of in-plane principal strains, $\varepsilon_2/\varepsilon_1$) field of specimen are investigated. Firstly, a basic cruciform shape, which is the simplest one, is studied to present the problems introduced by cruciform shape design. Then, various cruciform shapes with different geometries are investigated. Finally, an optimal cruciform shape is suggested to obtain large strains at the central zone.

2.4.1 Basic shape

A basic cruciform shape consists in three zones: the central zone, the arms and the intersections, as shown in Fig. 2-23. The model has been discretized by 5362 linear triangular shell elements of type S3. The element size at the central zone has been refined to $0.5mm$, as shown in Fig. 2-24.

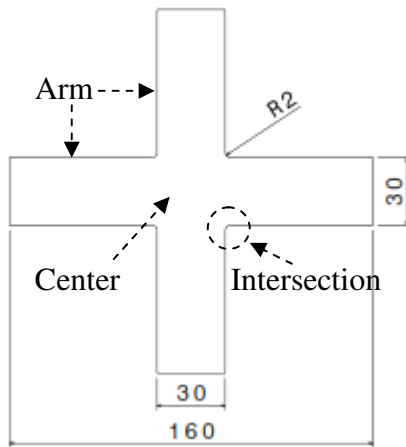


Fig. 2-23 Basic cruciform shape

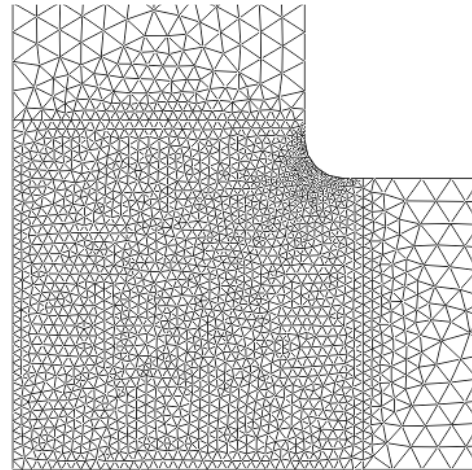


Fig. 2-24 Mesh of basic shape

A displacement of 3.6mm is applied along each arm of specimen. The maximum major principal strain reaches 20% at the intersection, as shown in Fig. 2-25. The maximum equivalent plastic strain is also located at the intersection while the equivalent plastic strain at the central zone is very small below 2%. The strain state at the central zone ranges from equibiaxial tension ($\epsilon_2/\epsilon_1 = 1$) to plane strain tension ($\epsilon_2/\epsilon_1 = 0$) and the arms are deformed under uniaxial tensile state ($\epsilon_2/\epsilon_1 = -0.5$).

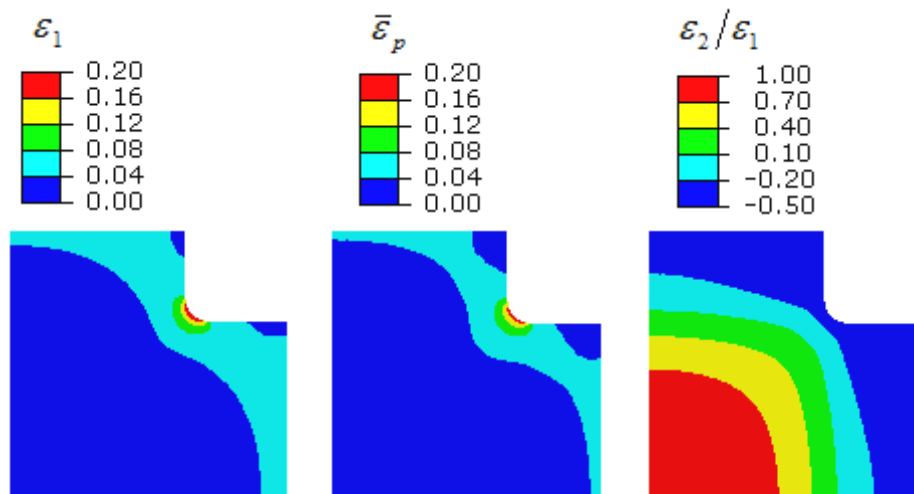


Fig. 2-25 Major principal, equivalent plastic strain and strain state of basic shape

Therefore, the central zone is the zone of interest under biaxial tensile state, but the deformation is very small. The arms are the force-transferring zones under uniaxial tensile state. The intersections are sharp geometries, where severe strain concentrations occur. For the basic shape, there are two main problems: strain localisation at the intersection and the necking of arms under uniaxial tensile state.

2.4.2 Notches at intersections

As explained above, notches have been suggested at the intersections to reduce the strain localisation. Here, the distance D from notch to symmetrical axis and the radius R of notches are changed for shape design, as shown in Fig. 2-26.

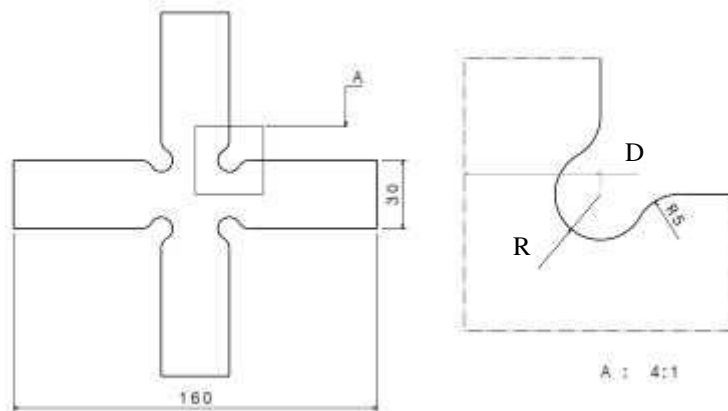


Fig. 2-26 Shape with notches

The effect of distance D on the equivalent plastic strains of specimens is studied with constant radius of notch, $R = 5\text{mm}$. The equivalent plastic strains at the notches are higher than those at the centre and arm, as shown in Fig. 2-27.

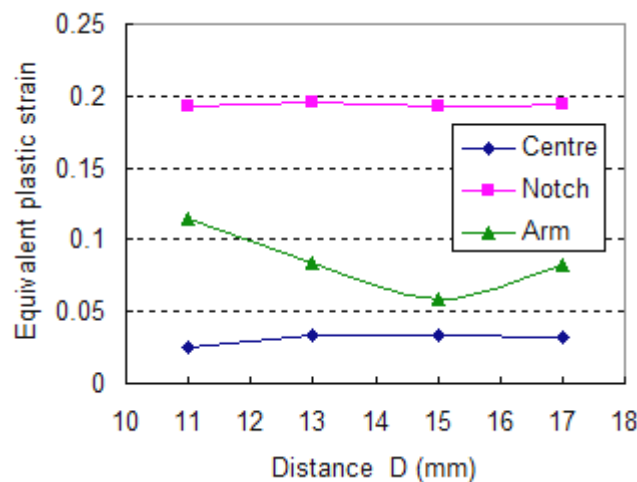


Fig. 2-27 Effect of distance D ($R=5\text{mm}$)

The effect of radius R on the equivalent plastic strains of specimens are studied with constant distance from notch edge to symmetrical axis, $D - R = 10\text{mm}$. It can be seen that the equivalent plastic strains at the notches are also higher than those at the centre and arm, as shown in Fig. 2-28.

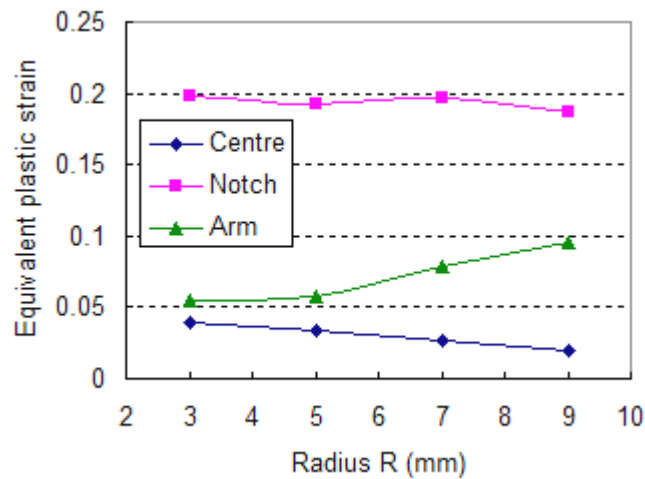


Fig. 2-28 Effect of radius ($D-R=10\text{mm}$)

An optimal shape with notches ($D = 13\text{mm}$ and $R = 3\text{mm}$) is chosen after comparison. One quarter of the model is discretized by 5528 linear triangular elements of type S3 (in Fig. 2-29).

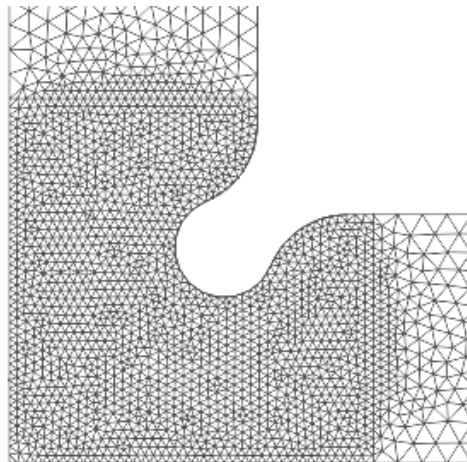


Fig. 2-29 Mesh of shape with notches ($D=13\text{mm}$, $R=3\text{mm}$)

A displacement of 1.8mm is applied along each arm of specimen. The localisations of major principal strain and equivalent plastic strain are located at the notch, as shown in Fig. 2-30. The deformation at the central zone is about 0.04. The central zone is deformed under equibiaxial tensile state.

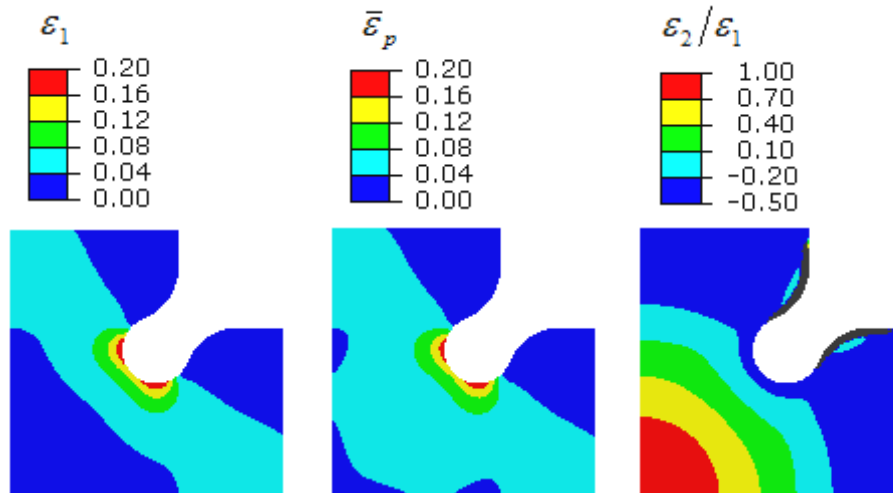


Fig. 2-30 Major principal, equivalent plastic strain and strain state of shape with notches

It is concluded that the effect of position and size of notch on the equivalent plastic strain at the central zone of cruciform shape is very small. Severe strain localisations always occur at the notches.

2.4.3 Slits along arms

Slits in each arm are proposed to reduce the transverse rigidity of arms and eliminate geometric constraint on the central zone. Here, the effect of position of slits on the deformation of specimen has been investigated. The number of slits in each arm is constant and equal to seven. The point P is fixed so that the end of outside slit is aligned with the arm edge. The ends of slits in each arm are aligned following a straight line. The inclination of this line is defined by θ , as shown in Fig. 2-31. The width of slits (0.5mm) and distance between slits are not changed.

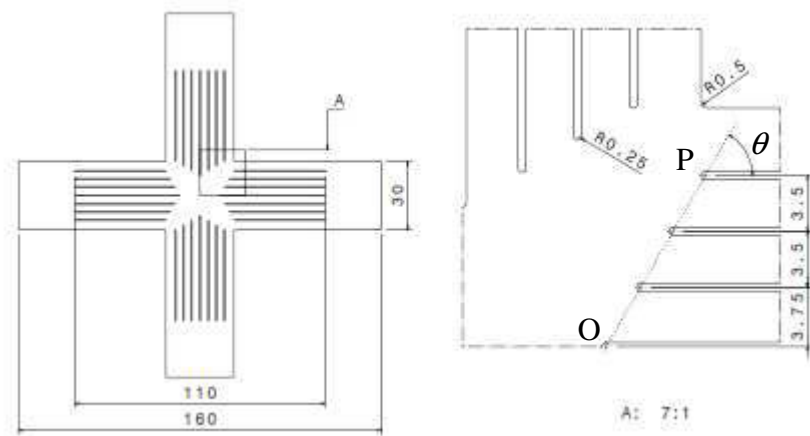


Fig. 2-31 Shape with slits

The equivalent plastic strain levels at the central zone, the end of central slit (point O) and intersection of arms are compared, as shown in Fig. 2-32. It can be seen that the equivalent plastic strain level at the end of slit (point O) is very high and the equivalent plastic strain level at the central zone is very low.

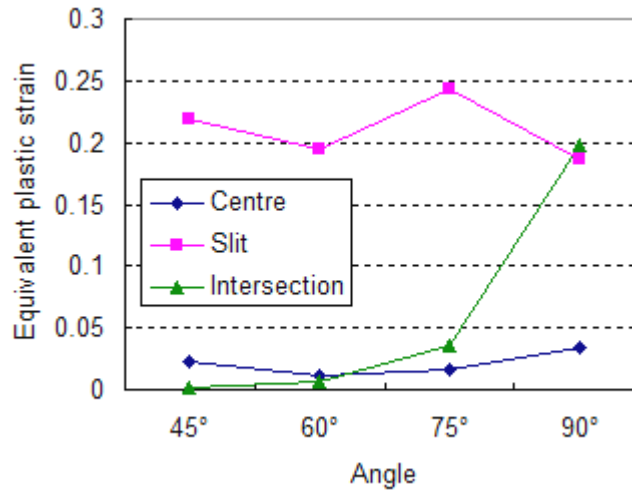


Fig. 2-32 Comparison of shapes with slits

A quarter of the model with slits ($\theta = 90^\circ$) is discretized by 7718 linear triangular element of type S3. The element size at the central zone of cruciform shape is refined to $0.4mm$, as shown in Fig. 2-33.

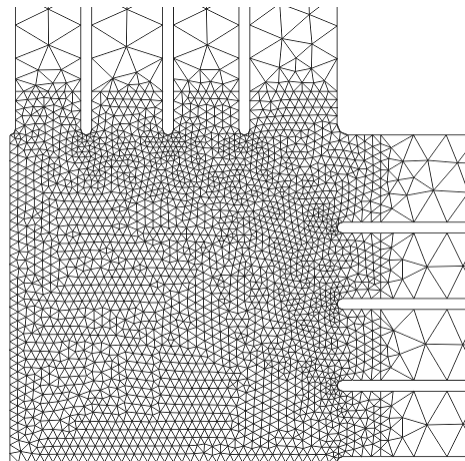


Fig. 2-33 Mesh of shape with slits

A displacement of $5.74mm$ is applied along each arm of specimen. The deformation field at the central zone of cruciform shape with slits ($\theta = 90^\circ$) is homogeneous, as shown in Fig. 2-34. The deformation localisation is located at the heads of slits. The strain level at the central zone is still very low, about 0.035.

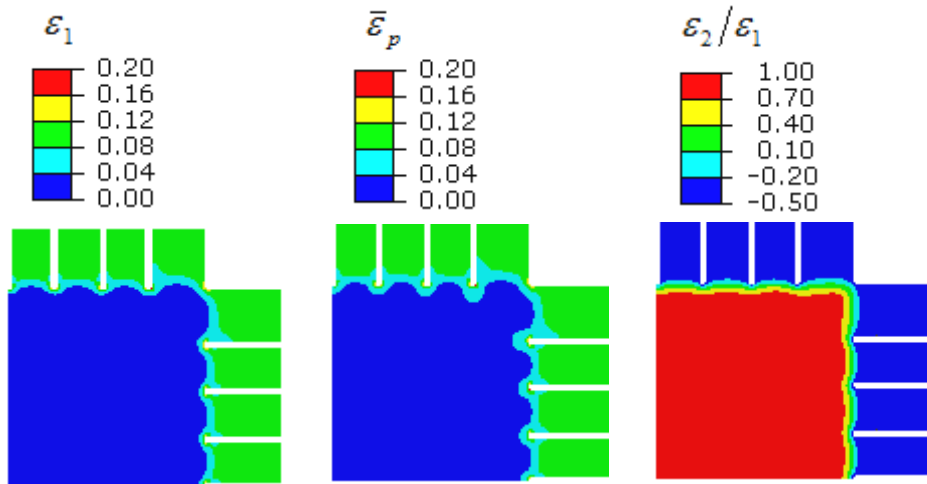


Fig. 2-34 Major principal, equivalent plastic strain and strain state of shape with slits

It is concluded that the effect of slits on the strain level at the central zone is also very small. But slits in each arm ($\theta = 90^\circ$) allow to obtain a homogeneous deformation field at the central zone.

2.4.4 Thickness reduction

Thickness reduction is suggested to decrease the stiffness of central zone and obtain large deformation. Here, a circular area of thickness reduction is adopted at the central zone. It has been chosen to reduce the thickness only on one side of sheet, which is easier for manufacturing. The radius r and thickness t of thickness-reduced zone are changed, as shown in Fig. 2-35. All the other geometries including width of arm, radius and position of notches are kept constant.

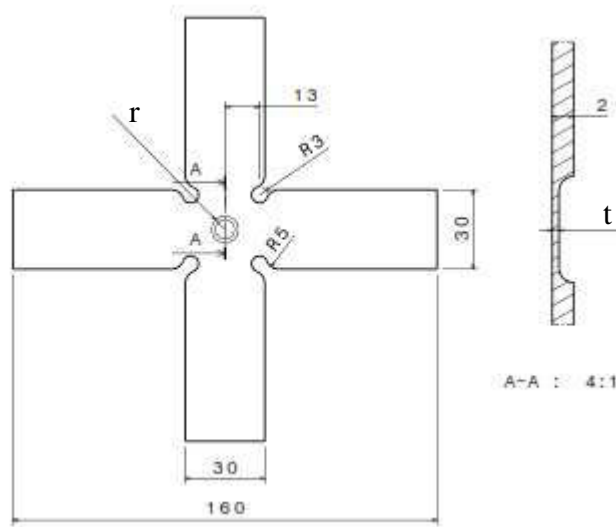


Fig. 2-35 Shape with thickness reduction

The effect of radius r of thickness-reduced zone on the equivalent plastic strains of specimen is studied with constant thickness of central zone, $t = 0.5$. When the radius r decreased, the equivalent plastic level at the central zone increased, as shown in Fig. 2-36. The strain level at the notch is still highest.

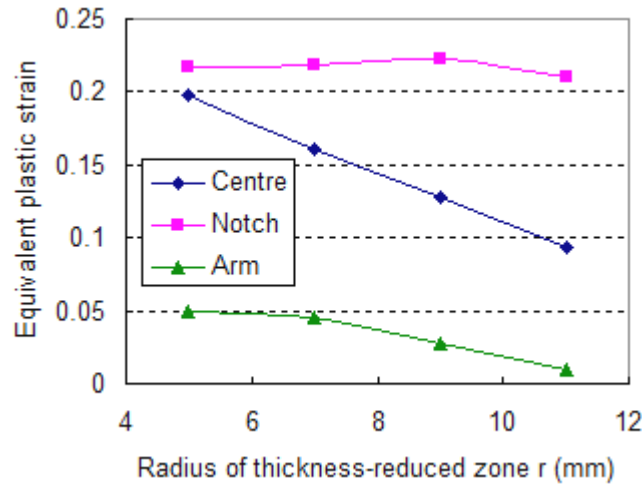


Fig. 2-36 Effect of radius of thickness reduced zone

The effect of thickness reduction on the equivalent plastic strain of specimen is studied with a constant radius of thickness-reduced zone, $r = 5$. When the thickness t decreased, the equivalent plastic level at the central zone increased greatly, as shown in Fig. 2-37. The strain level at the notch is always highest.

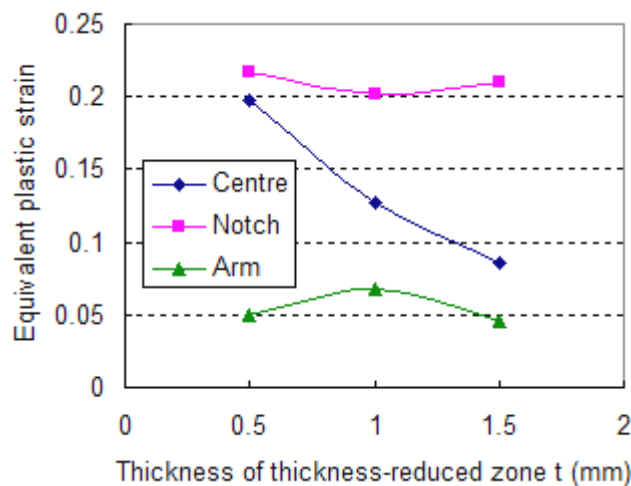


Fig. 2-37 Effect of thickness of thickness-reduced zone

A quarter of the model with thickness reduction ($r = 5$ and $t = 0.5$) and notch is discretized by 57951 linear tetrahedral elements of type C3D4. The element size at the thickness-reduced zone and notch is refined to 0.5mm , as shown in Fig. 2-38.

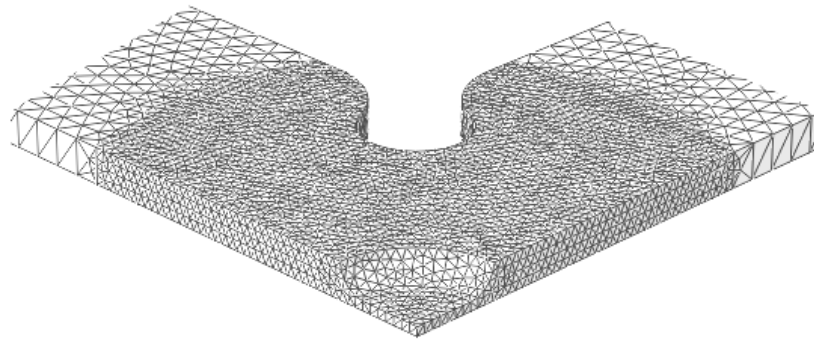


Fig. 2-38 FE model of shape with thickness reduction and notch ($r=5\text{mm}$, $t=0.5\text{mm}$)

A displacement of 1.36mm is applied along each arm of cruciform specimen. The major principal strain localisation is located at the notch, are shown in Fig. 2-39. The equivalent plastic strain at the central zone is about 0.20. The central zone of shape is deformed under equibiaxial tensile state.

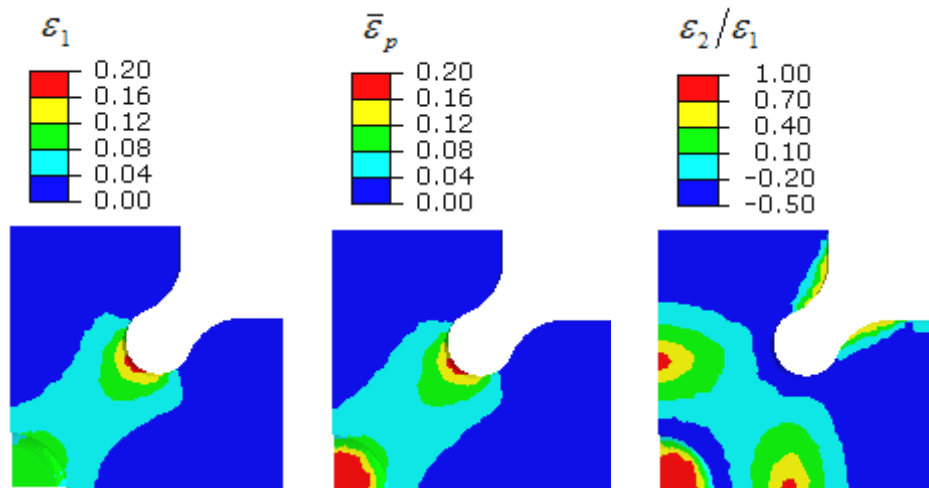


Fig. 2-39 Major principal, equivalent plastic strain and strain state of shape with thickness reduction and notch

It is concluded that the deformation level at the central zone can be elevated by using thickness reduction. When the size and thickness of thickness-reduced zone become smaller, the strain level at the central zone is larger. A quasi-homogeneous strain field is observed at the central zone with thickness reduction.

2.4.5 Optimal shape design

A shape with circular thickness reduction at central zone, notches at intersections of arms and slits in each arm is suggested to obtain large strains under equibiaxial tensile path. Here, six free parameters are investigated in the shape of cruciform specimen:

the radius r and thickness t of flat central zone, the position D and radius R of notch and the positions $S1$ and $S2$ of slits, as shown in Fig. 2-40. After a parametric study, the optimal dimensions of shape are given in Table 2-1.

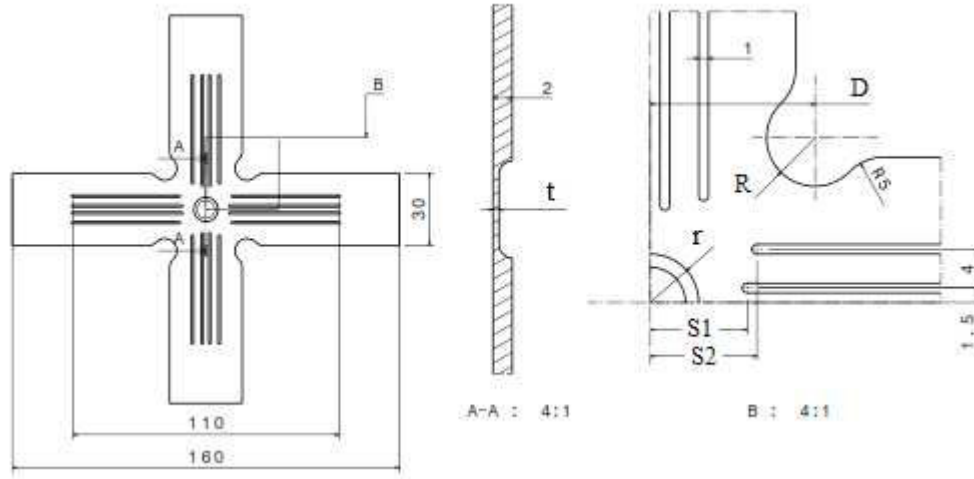


Fig. 2-40 Optimal shape for large strains

Table 2-1 Optimal dimensions in mm

r	t	D	R	$S1$	$S2$
5	0.625	17	5	10	11

A quarter of the model for optimal cruciform shape is discretized by 66322 linear tetrahedral elements of type C3D4. The element size at the central zone is refined to 0.5mm, as shown in Fig. 2-41.

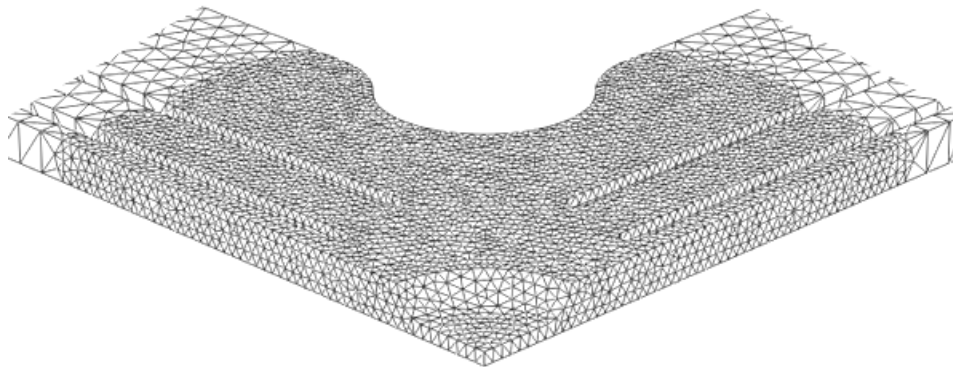


Fig. 2-41 Mesh of optimal shape

A displacement of 1.5mm is applied along each arm of optimal specimen. As shown in Fig. 2-42, the equivalent plastic strain at the central zone reaches 0.30 when the major principal strain is 0.20 near the ends of slits.

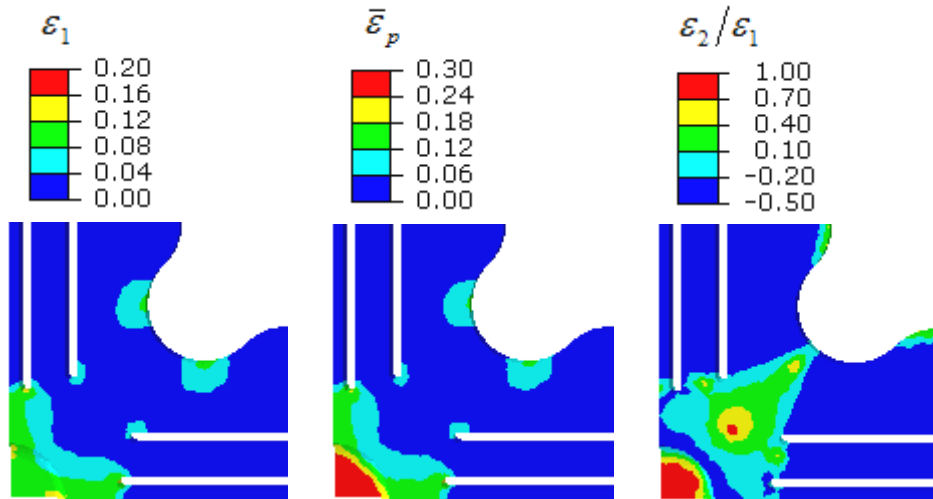


Fig. 2-42 Major principal, equivalent plastic strain and strain state of optimal shape

To examine the strain paths of specimen, the curves of major principal strain ϵ_1 and minor principal strain ϵ_2 are presented for the central zone, end of slits and notches during the simulation of equibiaxial tensile test. It is demonstrated the strain paths are linear, as shown in Fig. 2-43. The strain path at the central zone corresponds to an equibiaxial tensile strain path. The strain paths at the ends of slits and close to notch are between uniaxial tension and plane strain state. Sever localization of major principal strain reached about 0.20 at the head of slit S1.

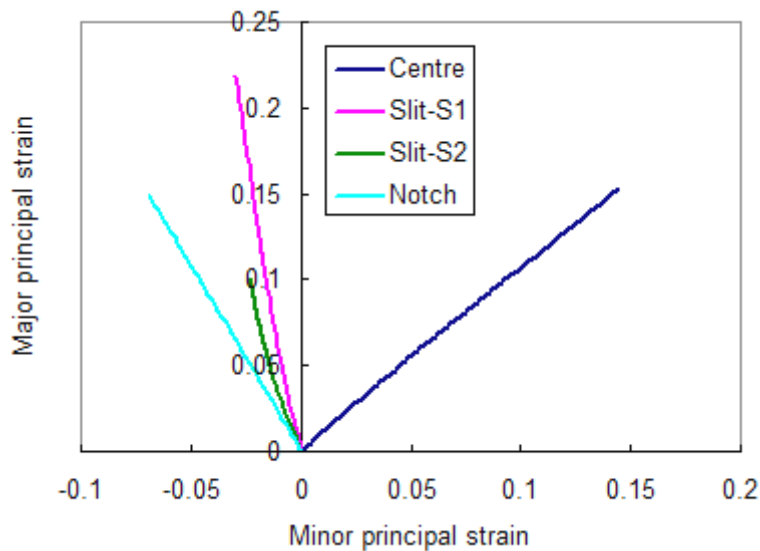


Fig. 2-43 Strain paths of optimal shape

It is concluded that an optimal cruciform shape with thickness reduction, slits and notches has been designed for large strains. The equivalent plastic strain at the central zone reaches about $\bar{\epsilon}_p = 0.30$.

2.5 Conclusion

To realize dynamic biaxial tests on cruciform specimens, servo-hydraulic stand-alone machine is more appropriate than mechanical device uses with conventional uniaxial testing machines which can have complex vibratory responses. So in this work, a stand-alone biaxial tensile testing machine with four independent servo-hydraulic actuators available in the Laboratory GCGM of INSA de Rennes will be used to perform both quasi-static and dynamic biaxial tensile tests. The deformation of specimen will be measured by DIC technique.

In the literature, biaxial tests on various well-defined cruciform specimens have been carried out under linear or nonlinear strain paths for characterization of yield criteria, identification of hardening models and determination of FLC. During previous works in the laboratory, anisotropic yield criterion has been calibrated by using a single biaxial tensile test on notched cruciform specimen, and FLC has also been determined by a set of biaxial tests under linear strain paths performed on a two-step thickness-reduced cruciform specimen.

From literature review and FE numerical investigations, the most sensitive geometric parameters have been studied (notches, slits, thickness reduction). A parametric study has been led to define a set of geometric parameters to obtain large equivalent plastic deformation ($\bar{\epsilon}_p = 0.30$) at the central zone of cruciform specimen under equibiaxial tensile test. The defined shape with one thickness reduction is proposed from an initial thickness sheet of $2mm$. The final thickness of the thickness-reduced central zone is $0.625mm$. This proposed shape could be used for other initial thickness sheet by considering the same thickness reduction ratio.

3. Identification methodology of hardening behaviour under in-plane biaxial loading

3.1 Introduction

The objective of this chapter is to present a procedure of identification applicable to in-plane biaxial tensile test. This procedure must be validated for static tests and dynamic tests as well. Quasi-static and dynamic biaxial tensile tests will be performed on cruciform specimen defined in chapter 2. Hardening behaviour of sheet metals from quasi-static to intermediate strain rates will be identified up to large strains. The experimental force measurement, which is a main problem for dynamic uniaxial tests, will also become a key issue in dynamic biaxial tensile tests. Therefore, the loading ringing problem will be investigated for dynamic biaxial tests. The experimental forces should be carefully pre-processed for parameter identification. Fortunately, the similar experiences of dynamic uniaxial tensile tests can be adopted for dynamic biaxial tensile tests.

Here, aluminium alloy AA5086 is tested at room temperature. This material has been chosen since it is known to present a very small dependency to strain rate. For biaxial tests, the parameters of hardening law will be identified by inverse analysis. The identified biaxial flow stress curve at quasi-static strain rate will be compared with the uniaxial flow stress curve to validate the procedures of experiment and identification. Then, the identified biaxial flow stress curve at intermediate strain rate will be compared with the curve identified from the quasi-static biaxial tensile test to validate the dynamic biaxial testing procedure.

3.2 Uniaxial test of AA5086

The 5XXX series aluminium alloys, with magnesium as the major alloying element, combine a wide range of strength, good forming and welding characteristics, and high resistance to general corrosion. The strength of this alloy can be generally increased with increasing magnesium content and further enhanced by cold work. The 5XXX alloys can be easily cold formed and the formability tends to increase as alloy strength decreases. They are widely used for the cryogenic application, pressure vessels, hulls and superstructures of ships, road transport and general engineering ^[149].

3.2.1 Digital image correlation

Measurement methods used for strain determination in sheet metal tests include: circle grid analysis (CGA), strain gauge, extensometers ^[150] and so on. Nowadays, with the technical development of high-resolution charge-couple device (CCD) cameras, the Digital Image Correlation (DIC) technique is a more popular strain measurement method ^[151]. It is a non-contact approach. The strain measurement by DIC contains three steps: (i) generation of speckle pattern on specimen, (ii) image record by camera, (iii) displacement and strain calculation, as shown in Fig. 3-1:

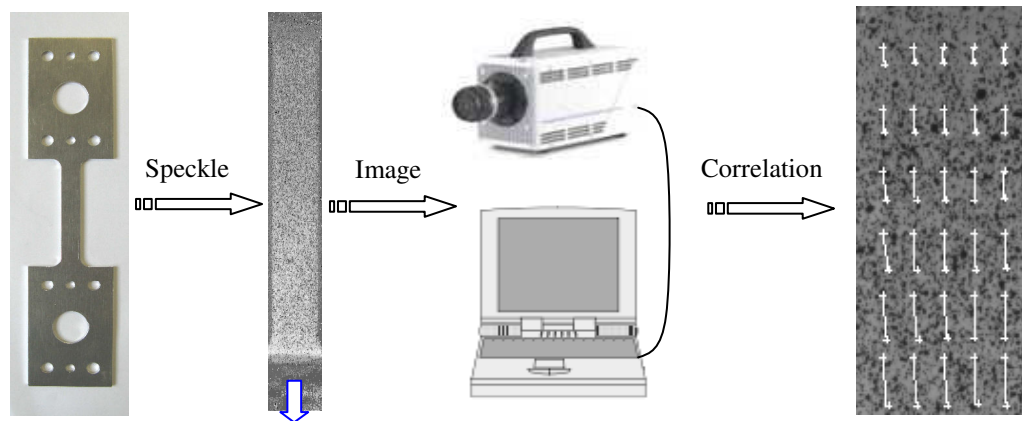


Fig. 3-1 Procedure of strain measurement by DIC

In this work, the DIC software CORRELA 2006 ^[152], which has been developed by the Laboratoire de Mécanique des Solides of Université de Poitiers, is adopted. Different sets of DIC parameters in CORRELA 2006 are compared to choose the best one for strain calculation. These parameters are given in Table 3-1 .

Table 3-1 Main parameters of DIC in CORRELA 2006

Subset	Size	32 pixels × 32 pixels
	Distance	16 pixels × 16 pixels
Correlation	Method	FFT and quadratic polynomial interpolation
	Initial value	By precedent displacement
	Displacement	Between precedent and current images
	Iterative accuracy	0.01 pixel
Strain	Mode	X2
	Lagrange	Large deformation, $n = 2$

The analysed zone of specimen should be assigned for calculation firstly. Then, the subsets should be defined for correlation. It needs to set four parameters: the length and width (L_1 , L_2) of subset, and the horizontal and vertical distances (D_1 , D_2) between the adjacent subsets, as shown in Fig. 3-2. After the displacements of all the subsets are determined by correlation, four subsets are chosen by setting a constant interval 2 to obtain a parallelogram. The strain will be calculated at the diagonal intersection of the parallelogram, as shown in Fig. 3-3. The accuracy of DIC method for strain measurement is dependent on the quality of speckle pattern and digital image, correlation algorithm ^[153] .

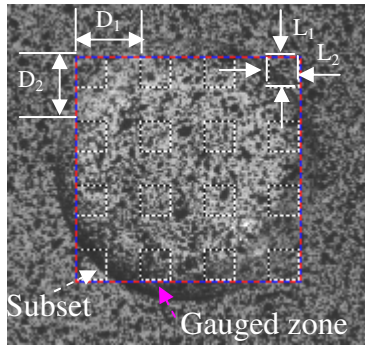


Fig. 3-2 Subsets for DIC

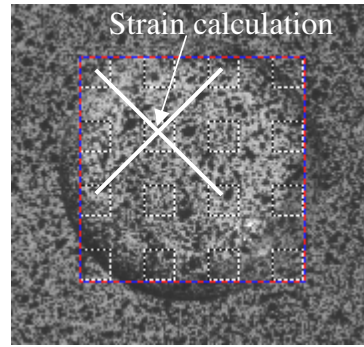


Fig. 3-3 Mode for strain calculation

3.2.1 Experimental result

A dynamic uniaxial tensile testing system has been developed in the Laboratory GCGM of INSA de Rennes, which includes a servo-hydraulic testing machine, controlling system, force sensor and deformation measurement by DIC. The shape of uniaxial tensile testing specimen is shown in Fig. 3-4. The quasi-static uniaxial test at the loading velocity of 1mm/s and dynamic uniaxial test at the loading velocity of 500mm/s are carried out to obtain the true stress-true strain curves at the quasi-static ($0.02/s$) and intermediate ($10/s$) strain rates, respectively. The main parameters for measurement systems are presented in Table 3-2.

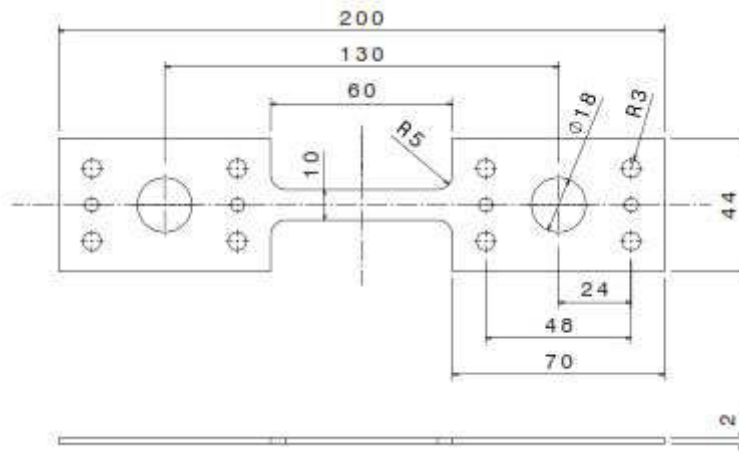


Fig. 3-4 Shape of uniaxial testing specimen

Table 3-2 Main parameters of measurement system for uniaxial tests of AA5086

Test	Camera (FASTCAM-APX RS 250K)			Load sensor
	Acquisition rate (fps)	Resolution (pixel)	Shutter speed (s)	Acquisition rate (Hz)
1mm/s	250	704×128	1/300	1000
500mm/s	15000	704×128	1/15000	45000

Before necking of specimen, 4623 images have been captured during the quasi-static test and 602 images have been recorded during the dynamic test. The DIC technique is adopted for strain calculation. The uniformly deformed region is chosen as the zone to be analyzed, as shown in Fig. 3-5. There are 29 and 5 subsets, 27 and 3 strain calculation points along the longitudinal and transverse directions of the specimen, respectively. The magnification factor from *pixel* to *mm* is $0.1\text{mm}/\text{pixel}$. Finally, components of strain ε are calculated by average value on gauge zone as follows:

$$\varepsilon(t) = \frac{1}{m \times n} \sum_{i=1}^m \sum_{j=1}^n \varepsilon(i, j, t) \quad \text{Eq. 3-1}$$

Where m and n are the total number of strain points along longitudinal and transverse directions. (i, j) is the position of strain point and t is the time.

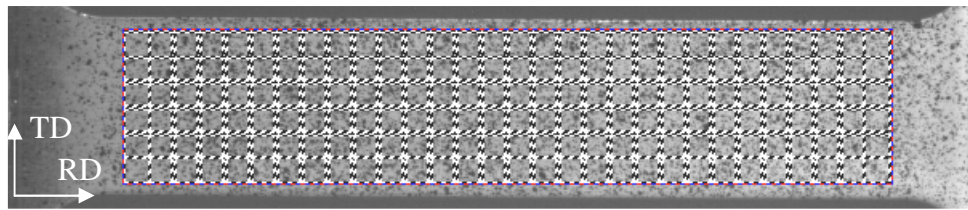


Fig. 3-5 Gauge zone of uniaxial testing specimen

The average true, principal strain curves of specimen are presented in Fig. 3-6. Because the shear strains ε_{xy} are very small, the true strains ε_{xx} along axis-x coincide with major principal strains ε_1 , and the true strains ε_{yy} along axis-y are nearly same with minor principal strains ε_2 . The order of true strain before tension is only 10^{-4} .

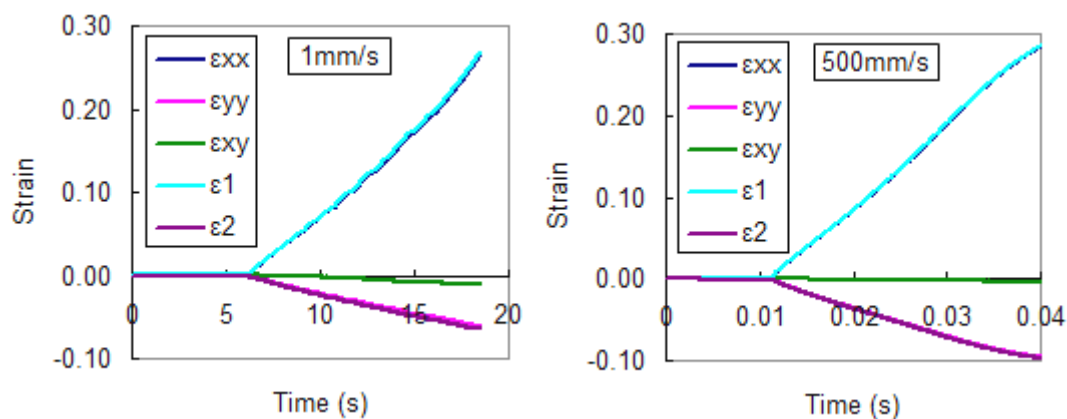


Fig. 3-6 Strain curves of static (1mm/s) and dynamic (500mm/s) uniaxial test

For the dynamic uniaxial test, the measured force is oscillating at the beginning due to load ringing phenomenon. Because the oscillation is not behaviour of testing material,

the measured force curve is mathematically pre-processed by the median value filtering method in MATLAB. The experimental force curves are shown in Fig. 3-7.

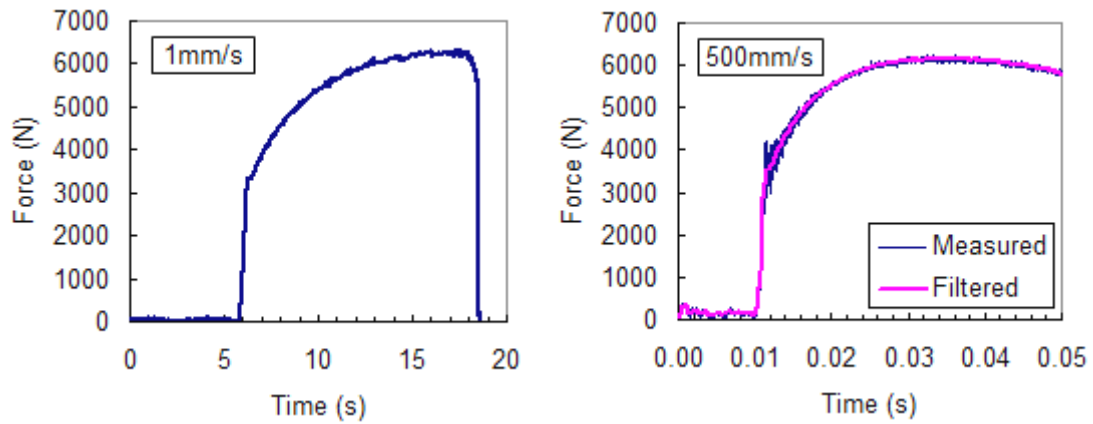


Fig. 3-7 Force curves of static (1mm/s) and dynamic (500mm/s) uniaxial test

3.2.2 Uniaxial flow stress curve

Before diffuse necking of specimens ($dF = 0$), the true stress σ_{xx} is calculated with the assumption of constant volume:

$$\sigma_{xx} = \frac{F}{S} = \frac{F \times \exp(\epsilon_{xx})}{S_0} \quad \text{Eq. 3-2}$$

where S_0 is the initial cross area. The true stress-true strain curves of AA5086 under quasi-static and dynamic uniaxial tension are compared in Fig. 3-8.

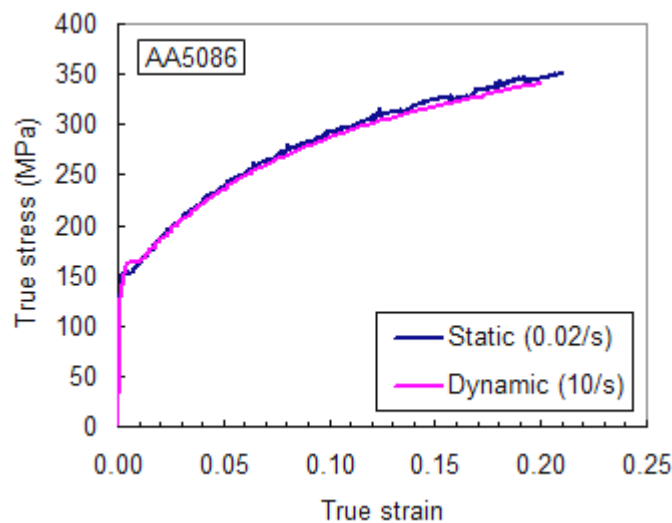


Fig. 3-8 Static and dynamic uniaxial true stress-true strain curves of AA5086

3. Identification methodology of hardening behaviour under in-plane biaxial loading

It can be seen that these curves are almost the same. This confirms that the choice of this alloy based on its strain rate independency property. For large strains, a very small effect of strain rate can be observed, which in this case would be negative strain rate sensitivity at room temperature. The negative strain rate sensitivity at room temperature have also been experimentally observed for AA5182-O [154] by uniaxial tension and compression tests at the strain rates between $10^{-4} s^{-1}$ and $10^0 s^{-1}$, and for AA6092 [155] at strain rate level of $10^{-4} s^{-1} \leq \dot{\epsilon} \leq 100 s^{-1}$.

Firstly, the parameters of well-known Ludwick and Voce models are determined based on the true stress-plastic strain curves. The plastic strain ϵ_p is calculated from the true stress-true strain curve as follows:

$$\epsilon_p = \epsilon - \epsilon_e = \epsilon - \frac{\sigma}{E} \quad \text{Eq. 3-2}$$

where E is Young's modulus. The fitting process is completed by MATLAB, and this nonlinear curve-fitting problem is solved in least-squares sense. The error δ of fitting is defined as follows:

$$\delta = \sqrt{\frac{1}{n} \sum_{i=1}^n (\sigma^{fit}(\epsilon_p^i) - \sigma^{exp}(\epsilon_p^i))^2} \quad \text{Eq. 3-3}$$

where σ^{fit} , σ^{exp} are the fit and experimental stress, n is number of experimental points. The identified results of static and dynamic uniaxial tests are compared in Table 3-3 and Table 3-4.

Table 3-3 Ludwick parameters identified from uniaxial test on AA5086

Parameters	Ludwick model: $\sigma = \sigma_0 + K \epsilon_p^n$			
	σ_0 (MPa)	K (MPa)	n	Error δ
Static	119.6	473.6	0.435	3.75
Dynamic	132	466.5	0.473	3.73

Table 3-4 Voce parameters identified from uniaxial test on AA5086

Parameters	Voce model: $\sigma = \sigma_0 + K(1 - \exp(-n\epsilon_p))$			
	σ_0 (MPa)	K (MPa)	n	Error δ
Static	158.9	212.5	10.68	2.27
Dynamic	161	202.8	10.59	1.5

The experimental and identified curves are compared in Fig. 3-9, where the identified hardening laws are extrapolated up to equivalent plastic strain of 34%. The two

identified hardening laws are very different when the plastic strain becomes larger than 19% beyond the uniform deformation of uniaxial tests. It is concluded that the strain level of uniaxial tensile test before necking is not enough to characterize the hardening behaviour of sheet metals for large strain level. Therefore, the experimental strain level should be elevated to determine more accurate hardening models.

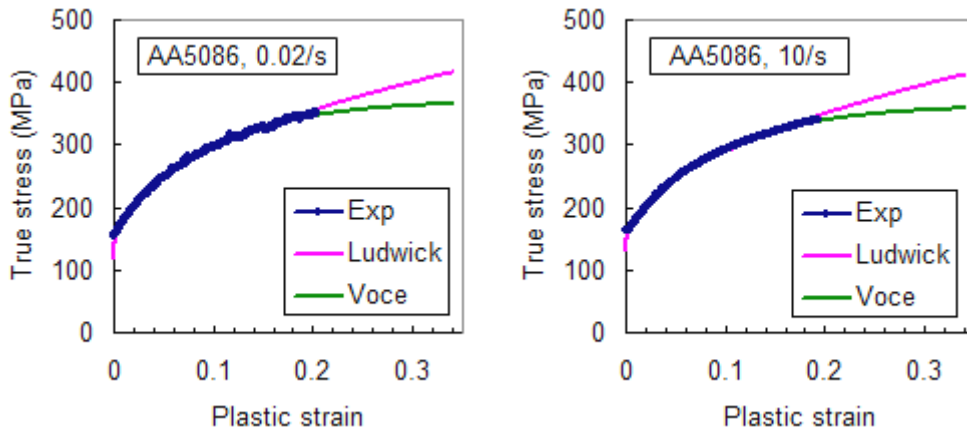


Fig. 3-9 Extrapolation of static and dynamic uniaxial flowing curve

3.3 Quasi-static biaxial test of AA5086

3.3.1 Experimental result

According to optimal shape in chapter 2, cruciform specimens of AA5086 have been prepared by milling. All the dimension of specimen is given in the Appendix (I). During quasi-static biaxial tensile test, a loading velocity of 1mm/s is applied. The high speed camera is adopted to record images at central zone, as shown in Fig. 3-10.

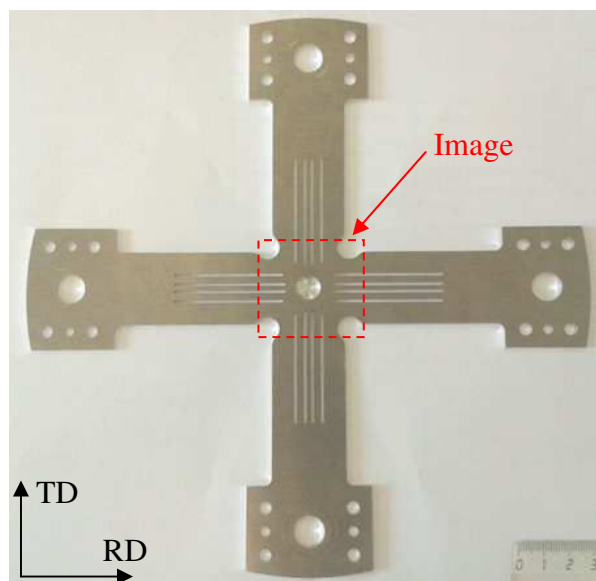


Fig. 3-10 Cruciform specimen of AA5086

The forces along the two perpendicular directions of the specimen are measured by deformation gauges, which are placed on the load sensors (in Fig. 3-11). The grips are used to align the loading directions and protect the load sensors from the asymmetric loading due to rupture of specimen. The main parameters of high speed camera and load sensors are defined for quasi-static biaxial tensile test, in Table 3-5 .

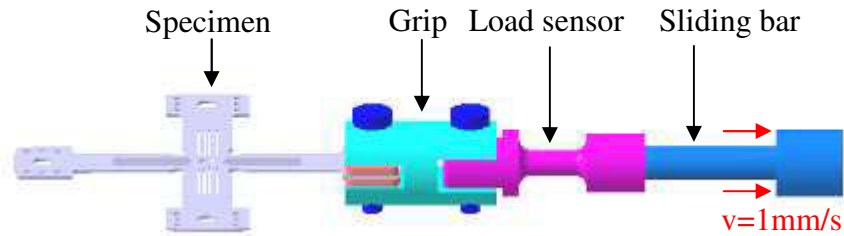


Fig. 3-11 Linkage between specimen and sliding bar

Table 3-5 Main parameters of measurement system for quasi-static biaxial test

Test	Camera (FASTCAM-APX RS 250K)			Load sensor
	Acquisition rate (fps)	Resolution (pixel)	Shutter speed (s)	Acquisition rate (Hz)
1mm/s	250	1024×1024	1/800	250

The random speckle pattern is generated at the central zone of specimen before test, and the initial crack are found to occur along the transverse direction in the circular thickness-reduced zone (in Fig. 3-12). There are 382 images before initial crack. For DIC, the circular thickness-reduced zone of specimen is defined as the gauge zone (in Fig. 3-13). There are 16 subsets and 14 strain points along each direction of specimen. The magnification factor from *pixel* to *mm* is 0.037 mm/pixel . The displacement vectors of gauge zone are shown in Fig. 3-14. It can be seen that the position of the central point is nearly kept fixed.

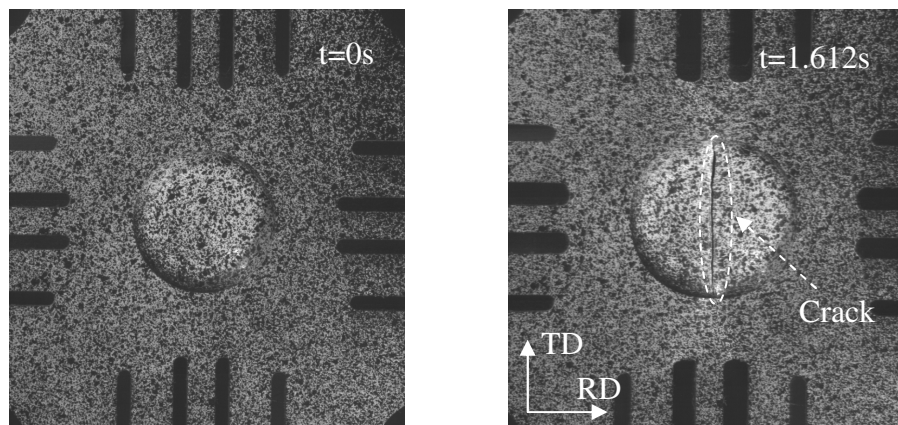


Fig. 3-12 Central zone of quasi-static specimen (speckle pattern and initial crack)

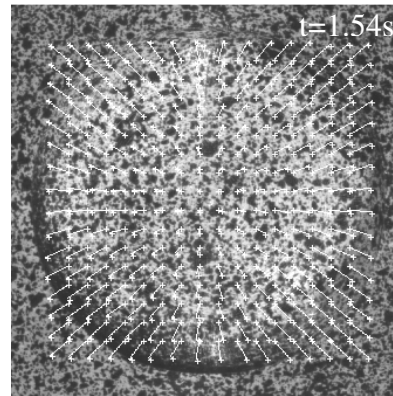
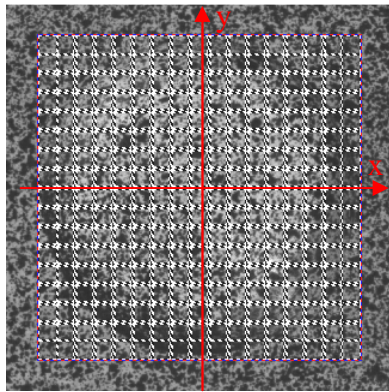


Fig. 3-13 Gauge zone of static specimen Fig. 3-14 Displacement vectors of static specimen

The equivalent and major, minor principal strain fields and strain state at the central zone before crack ($t = 1.5s$) are shown in Fig. 3-15. It is seen that the equivalent and principal strains are nearly homogeneous at the central zone ($-2mm \leq x, y \leq 2mm$). The equivalent strain at this central zone is above 30%. The major and minor principal strains at the central zone are about 20% and 14%, respectively. The major principal strain localised near the points ($x = 0, y = \pm 4mm$). The strain state is not uniform due to the localisation of major principal strain at the time $t = 1.5s$.

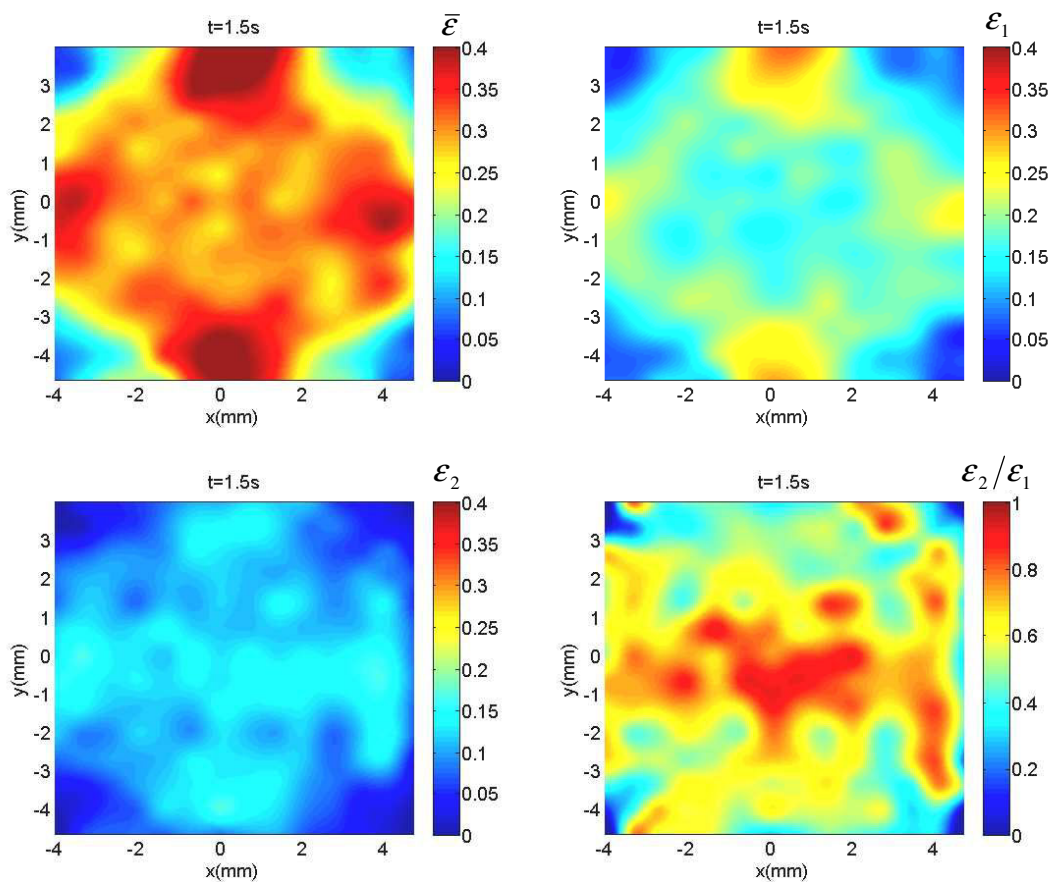


Fig. 3-15 Equivalent strain, principal strain field and strain state of quasi-static biaxial specimen

To obtain robust values of principal strains at the central point ($x = 0, y = 0$) of specimen, the principal strains are calculated by the average values as follows:

$$\varepsilon(t) = \frac{1}{m \times n} \sum_{j=1}^n \sum_{i=1}^m \varepsilon(i, j, t) \quad \text{Eq. 3-4}$$

where m, n are the number of points to be averaged. t is the time. Here, the average strains are calculated over the 3×3 points ($-0.6\text{mm} \leq x, y \leq 0.6\text{mm}$) to trace the principal strain history at the central point.

The equivalent and major, minor principal strain curves at the central point are presented in Fig. 3-16. It can be seen that the equivalent strain at the central point is above 35% when $t = 1.6\text{s}$. Due to little asynchronization between two axes and anisotropy of material, major principal strain curve does not exactly coincide with the minor principal strain. Portevin-Le Chatelier (PLC) effect^[156] can be observed on the evolution of strain curves which present steps especially between $t = 0.6\text{s}$ and $t = 1.2\text{s}$. The PLC effect has also been observed from uniaxial tension and simple shear tests from room temperature to 100°C for aluminium alloy AA5754-O^[157].

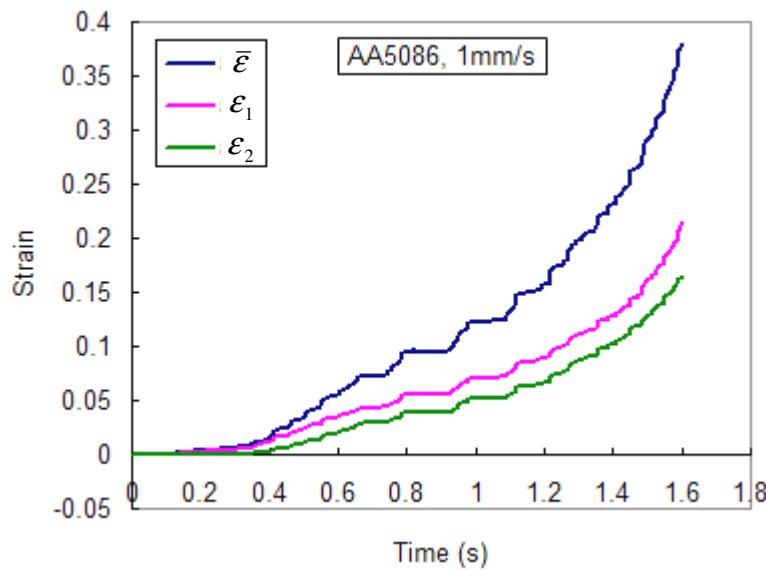


Fig. 3-16 Experimental strain curves of quasi-static biaxial testing specimen

The curves of strain path and strain rate at the central point are also shown in Fig. 3-17. The strain rate is calculated as follows:

$$\dot{\varepsilon} = \frac{\bar{\varepsilon}(t_{i+m}) - \bar{\varepsilon}(t_i)}{t_{i+m} - t_i}, \text{ when } t = \frac{t_i + t_{i+m}}{2} \quad \text{Eq. 3-5}$$

3. Identification methodology of hardening behaviour under in-plane biaxial loading

where m is time interval. The strain path at the central point is nearly proportional ($\varepsilon_2 / \varepsilon_1 \approx 0.75$) after $t = 0.6s$. The equivalent strain rate at the central point is fluctuating between 0 to $0.5/s$ from $t = 0.6s$ to $t = 1.5s$ due to the PLC effect.

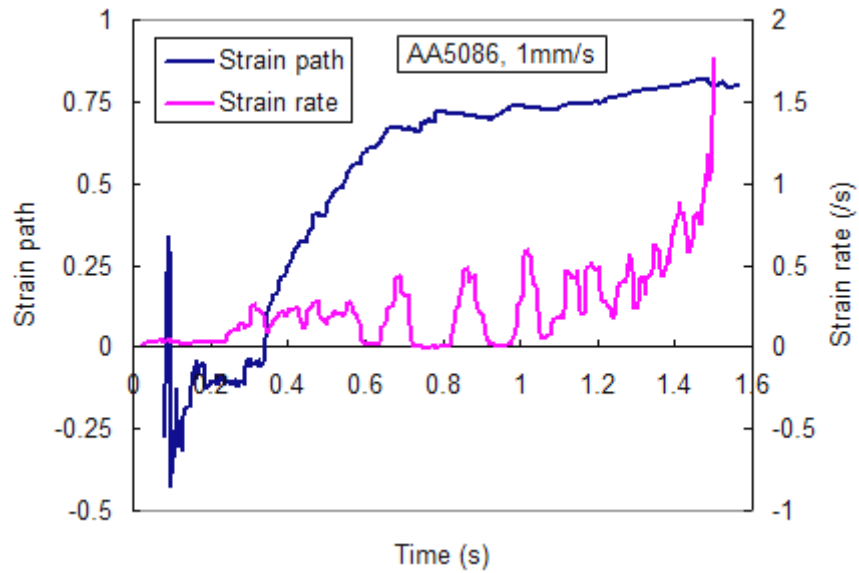


Fig. 3-17 Strain path and strain rate evolution at central point of quasi-static specimen

The experimental force curves are measured along the two directions of specimen, as shown in Fig. 3-18. The force F_x along axis-x began to increase about 0.1s later after F_y along axis-y.

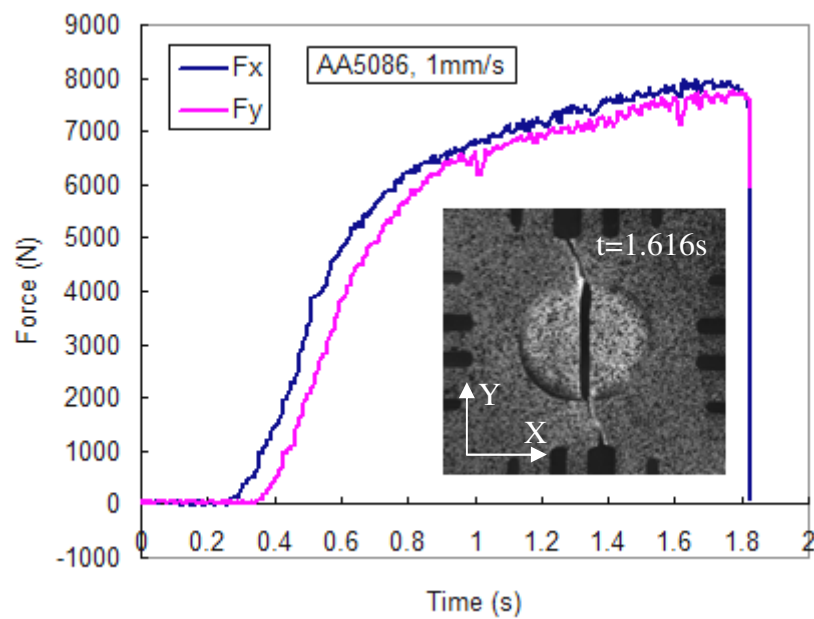


Fig. 3-18 Measured force curves of quasi-static biaxial test

For parameter identification by inverse analysis, the measured force curves along two directions have been synchronised with the strain curves. Then, the force curves are smoothed using a moving average filter in MATLAB. Finally, the experimental force and principal strain are prepared for parameter identification, as shown in Fig. 3-19.

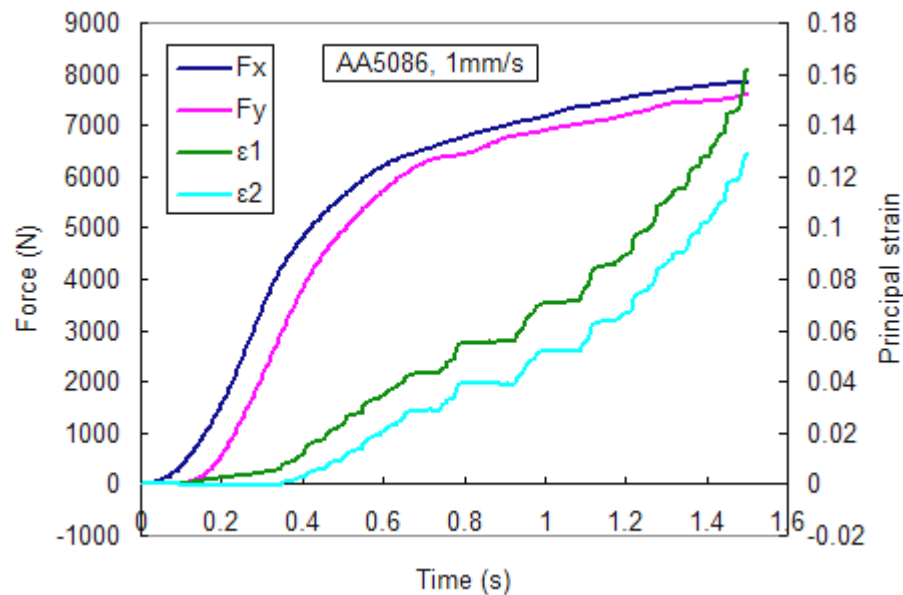


Fig. 3-19 Pre-processed experimental force and strain curves of quasi-static biaxial test

3.3.2 Procedure of inverse analysis

When the deformation of specimen is inhomogeneous, no analytical model can be adopted for stress determination. The inverse analysis is suggested for identification of material parameters ^[158]. In this work, the parameters of hardening models are determined by inverse analysis based on FE simulation of biaxial tensile tests on cruciform specimen. The procedure of parameter identification is shown in Fig. 3-20. The elastic parameters and the parameters of the yield criterion have been determined previously.

Because the experimental curves of displacement measured by displacement sensors along two axes are not exactly the displacements at the arms of specimen, they are not used for inverse analysis. The experimental curves of force along two axes are applied on the FE model. The experimental and simulated principal strains at the same time point t_i and the same position of central point on the specimen are compared to identify hardening behaviour of material. Therefore, the cost function to be minimized is defined by the error δ as follows:

$$\delta = \sqrt{\frac{1}{2} \sum_{i=1}^2 \left(\sum_j^n (\epsilon_i^{sim}(t_j) - \epsilon_i^{exp}(t_j))^2 / \sum_j^n (\epsilon_i^{exp}(t_j))^2 \right)} \quad \text{Eq. 3-6}$$

Where n is the total number of time points during simulation; ϵ_1^{sim} and ϵ_2^{sim} are the simulated major and minor principal strains at the central element of FE model; ϵ_1^{exp} and ϵ_2^{exp} are the experimental principal strain at each simulated time point.

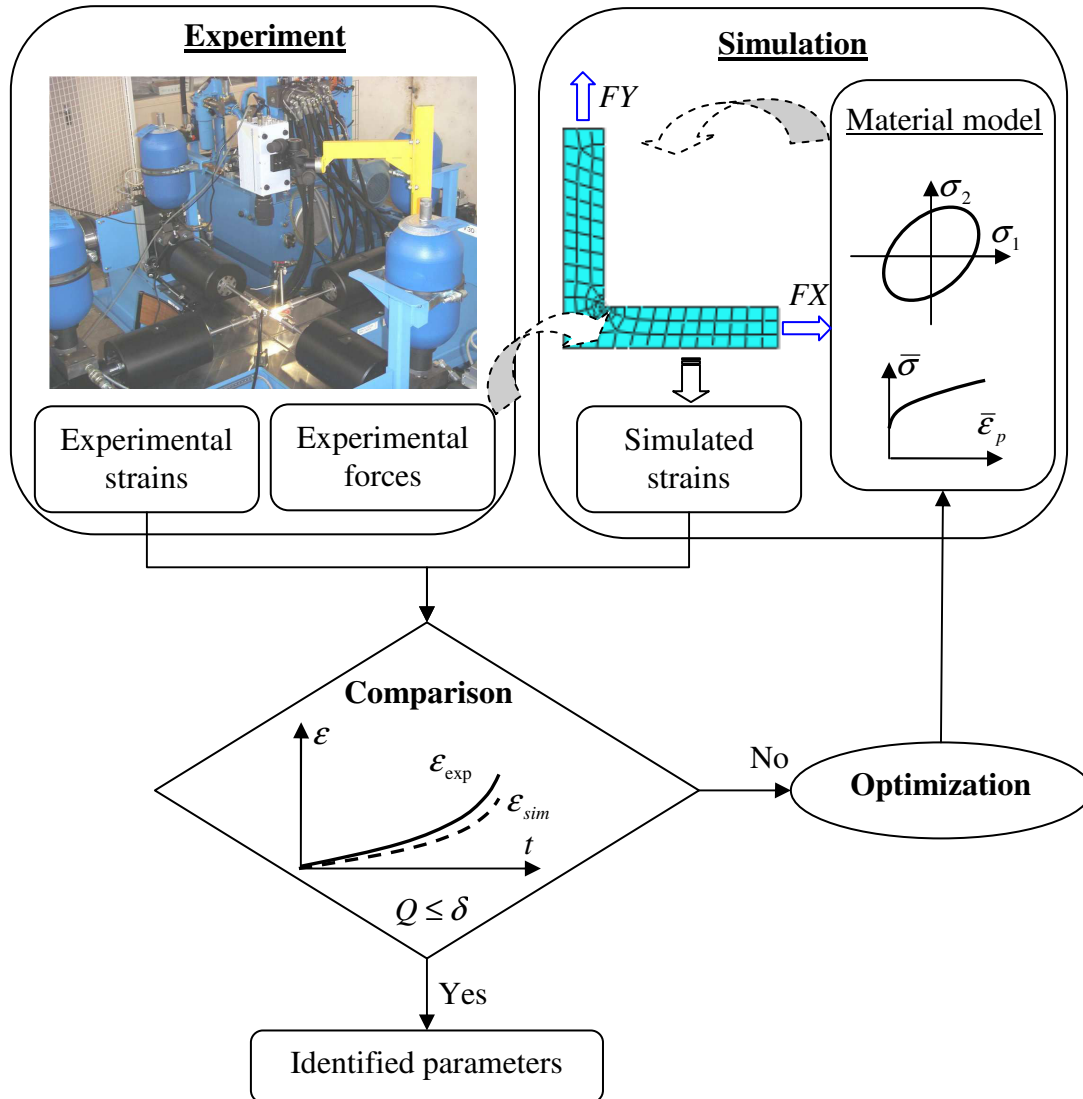


Fig. 3-20 Flowchart of parameter identification

The multi-disciplinary and multi-objective optimization platform of modeFRONTIER is used to perform the inverse analysis. A Workflow of modeFRONTIER should be well defined for each optimization problem.

Many optimization algorithms can be chosen to perform inverse analysis ^{[159] [160]}. Here, Simplex is chosen for parameter identification in modeFRONTIER. Simplex is a simple optimization algorithm seeking the vector of parameters corresponding to the extreme of a function, searching through the parameter space. The movement of Simplex is given by three operations: Reflection, Expansion and Contraction ^[161]. Like hill climbing algorithms, the Simplex method may stop at local optimization and not converge to the global minimum. To make sure that the global minimum is found, several optimizations are performed with different initial values. In order to cover a N-dimensional space, $N + 1$ initial sets are needed for Simplex while a first-order optimization algorithm requires more test. Nevertheless, the convergence for Simplex method is less efficient than that for many other algorithms when the parameter number is increased. A best approach could consist in applying a hybrid method to localize approximately the global minimum of the cost function and then converge efficiently with a first-order optimization algorithm.

3.3.3 Finite element model

Due to the symmetry, a quarter of the FE model of cruciform specimen is built in ABAQUS. Obviously, the accuracy of simulation is dependent on the finite element model. Here, the influence of mesh size at the central zone is studied for simulation. For the material model, Hooke's law is adopted with Young's modulus $E = 69GPa$ and Poisson's ratio $\nu = 0.33$, Hill 48 yield criterion ($F = 0.699$, $G = 0.638$, $H = 0.362$, $N = 1.494$) ^[162] and the hardening law $\bar{\sigma} = 150 + 320\sqrt{1 - \exp(-2.2\bar{\epsilon}_p)}$ are used. The experimental forces are applied to FE models.

3.3.3.1 Solid element

The model has been discretized by linear tetrahedral elements of type C3D4, and the element size at the central zone and notches is $0.5mm$. There are 66322 elements and the CPU time (Intel Core 3.2GHz, RAM 16Go) is $786.4s$ for simulation. The equivalent plastic strain field is shown in Fig. 3-21. It can be seen that the large deformation is primarily located near the central zone and the deformation outside this zone is very small. Therefore, the mesh at this central zone is further refined.

For FE models with linear tetrahedral element of type C3D4, the refined size at the central zone are varied with $0.3mm$, $0.2mm$, $0.15mm$ and $0.1mm$. There are 65881, 155035, 296035 and 814708 elements and the CPU times are $555.3s$, $2014.3s$, $589s$ and $31096s$, respectively. The equivalent plastic strain fields are compared in Fig. 3-22. It can be seen that the strain level and distribution at the refined zone are greatly influenced by the mesh size. The model C3D4_5 with the smallest mesh size ($0.1mm$) can capture the deformation localisation at the thickness reduced zone.

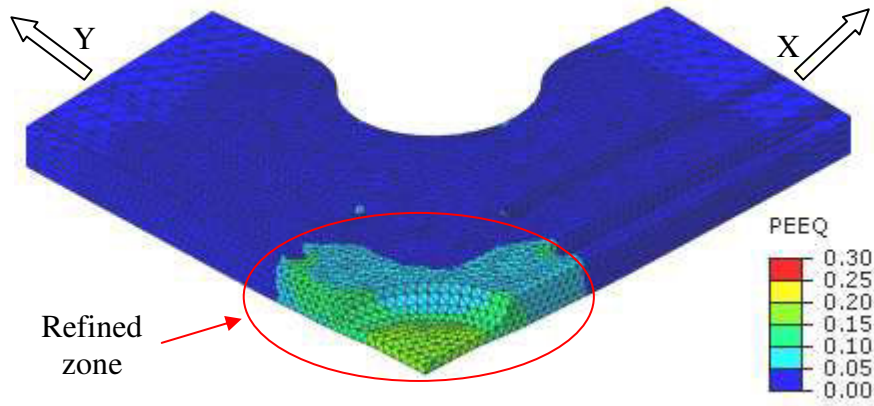


Fig. 3-21 Zone to be refined (C3D4_1, Size:0.5, Elements:66322, CPU Time: 786.4s)

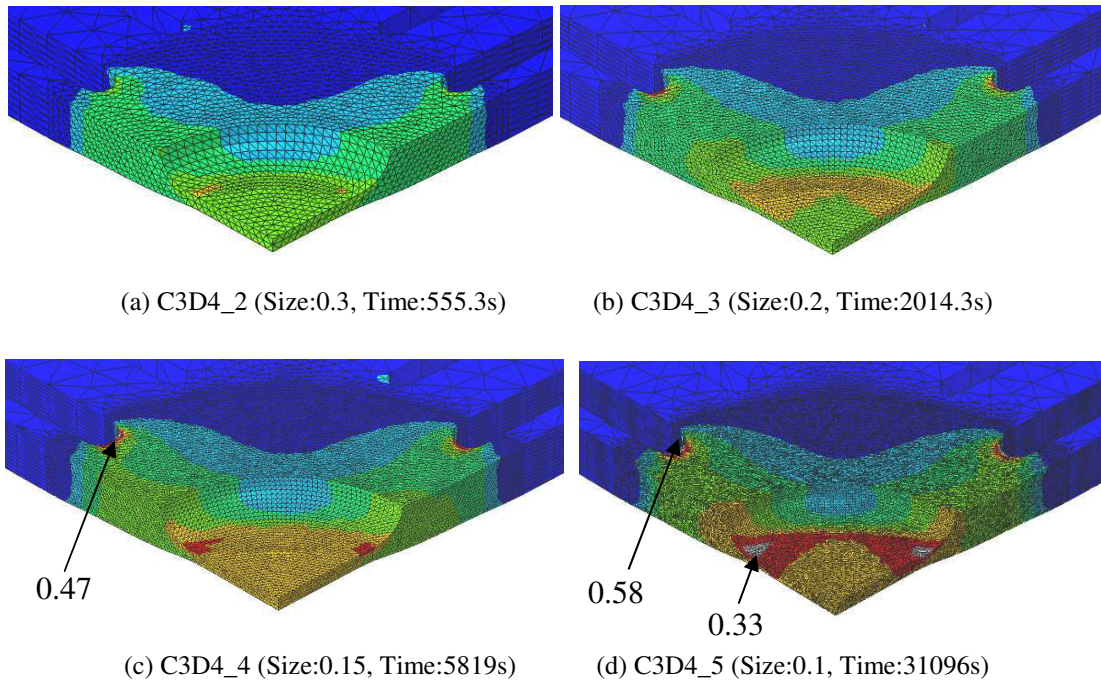


Fig. 3-22 Equivalent strain fields for different mesh size

The major and minor principal strain evolutions at the central point for different mesh sizes are also compared in Fig. 3-23. When the deformation is small, the strain is nearly the same. When the deformation becomes larger, the strain is critically affected by the element size. The deformation is larger with smaller element size, because the FE model becomes less rigid with smaller elements.

When the deformation field is inhomogeneous and the deformation level is higher, the mesh size of model C3D4_5 is small enough to capture the deformation localisation. Meanwhile, as the mesh size is refined for accurate simulation, the element number will increase and the FE simulation will become more time-consuming. For inverse

analysis, it becomes very hard to accept the time cost because it is necessary to perform a lot of simulation for optimization.

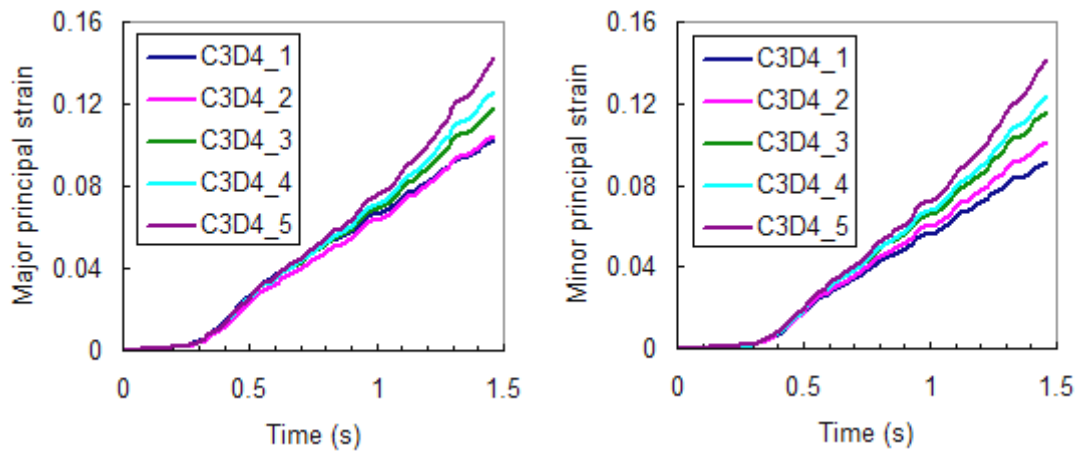


Fig. 3-23 Comparison of major and minor principal strains

3.3.3.2 Shell element

To reduce the time cost during FE simulation, the model is discretized by linear shell elements. For definition of shell elements, the model has been divided into three zones in Fig. 3-24: the flat thickness-reduced zone (Zone_1) with radius $R_1 = 3.63mm$ and thickness $t_1 = 0.625mm$, the zone (Zone_3) with initial thickness $t_3 = 2mm$, and the transition zone (Zone_2, hatching) with outer radius $R_2 = 5mm$ and inner radius $R_1 = 3.63mm$. The shell thickness of the transition zone (Zone_3) is the average value of t_1 and t_3 , $t_2 = 1.3125mm$.

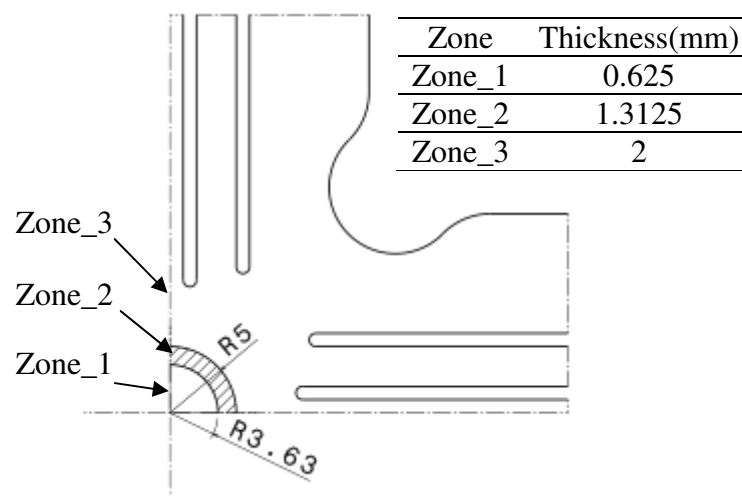


Fig. 3-24 Three zones of specimen

3. Identification methodology of hardening behaviour under in-plane biaxial loading

The mesh size, element number and CPU time for the models of solid (C3D4_5) and shell elements are compared in Table 3-6. The element sizes of Zone_1 and Zone_2 are the same for both the shell and solid element. It can be seen that the element number and time cost of shell element have been greatly reduced to 4460 and 221.9s, compared with 814708 and 31096s for the solid (C3D4_5) element.

Table 3-6 Comparison between solid and shell elements

		Solid (C3D4_5)	Shell
Mesh size (mm)	Zone_1	0.1 and 1.5	1.5
	Zone_2	0.1	0.1
	Zone_3	0.1	0.1
Simulation	Element number	814708	4660
	CPU Time (s)	31096	221.9

In order to examine the accuracy of shell element model, the equivalent plastic strain field is compared with that of solid element (C3D4_5), as shown in Fig. 3-25. The levels and distributions of equivalent plastic strain are almost the same for two models, although the localisation at the edge of central thickness-reduced zone in the solid model is a little more severe than that in the shell model.

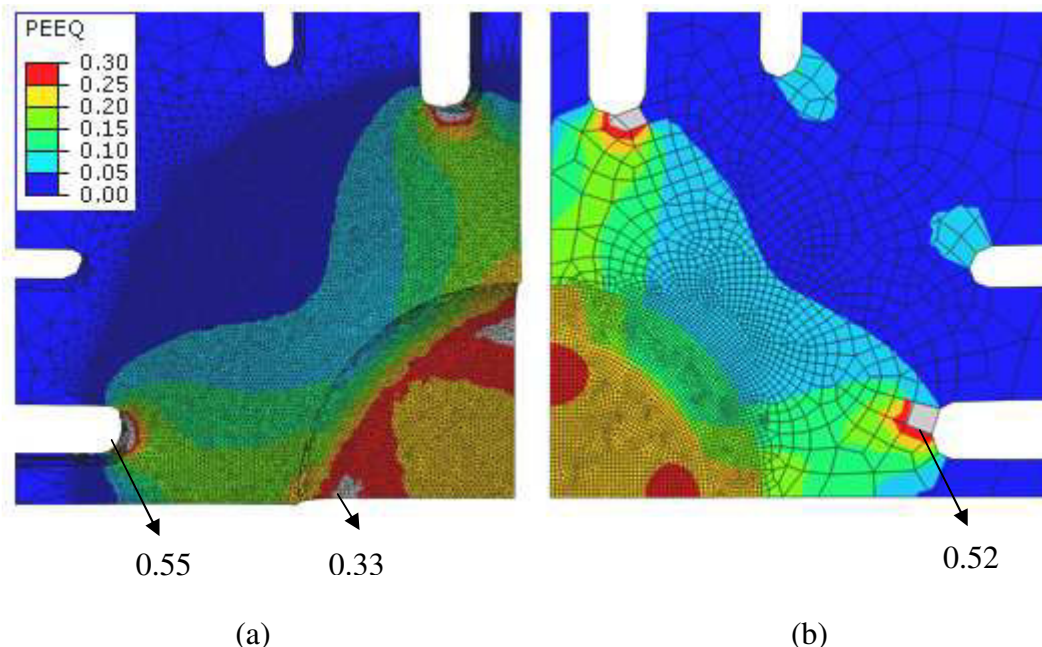


Fig. 3-25 Comparison of equivalent strain fields between solid (a) and shell (b) elements

The major and minor principal strain evolutions at the central point are compared between the two models, as shown in Fig. 3-26. It can be seen that the major and minor principal strains curves are nearly the same between the two models.

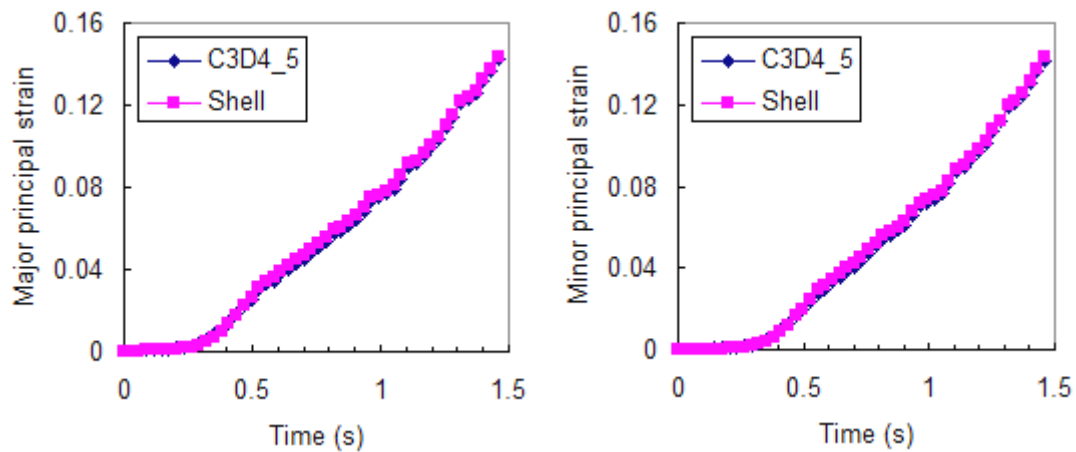


Fig. 3-26 Comparison of principal strain evolutions between solid (C3D4_5) and shell elements

In conclusion, it will be very beneficial to adopt the shell element for parameter identification by inverse analysis, because it not only fulfil the accuracy, but also greatly reduces the time cost of FE simulation.

3.3.4 Parameter identification

With the pre-processed experimental forces along two arms and principal strain curves at the central point of cruciform specimen, the parameters of hardening law are identified by inverse analysis based on the FE model of shell element. For material behaviour, the elasticity is described by isotropic Hooke's law, and the associated flow rule is used for the plastic behaviour. Because the strain path is nearly proportional during quasi-equibiaxial tensile tests on cruciform specimen, the isotropic hardening model is adopted. The preliminarily-known parameters of yield functions are given. The hardening law to be identified should be preliminarily defined.

3.3.4.1 Material models

For AA5086, the elasticity is described by Young's modulus $E = 73022\text{MPa}$ and Poisson's ratio $\nu = 0.33$. Here, three yield criteria of Mises, Hill 48, and Bron and Besson 2004 in 2D stress space are adopted to identify the isotropic hardening law.

In the FE software of ABAQUS, Mises and Hill 48 yield criteria can be chosen directly. The subroutine UHARD has been implemented by FORTRAN code for the user-defined hardening law. For the material model with Bron and Besson 2004 yield criterion, the subroutine UMAT has been implemented by FORTRAN code.

For parameter determination with Hill 48 yield function, the uniaxial tensile tests have been carried out along the rolling, diagonal and transverse directions of AA5086 sheet,

3. Identification methodology of hardening behaviour under in-plane biaxial loading

and three anisotropic coefficients r_0 , r_{45} and r_{90} are obtained ^[163]. The parameters F , G , H , N of Hill 48 yield criterion are calculated by the anisotropic coefficients, in Table 3-7.

Table 3-7 Parameters of Hill 48 yield function for AA5086

Anisotropic coefficients	$r_0 = 0.49, r_{45} = 0.62, r_{90} = 0.52$
Function parameters	$F = 0.632, G = 0.671, H = 0.329, N = 1.460$

For the aluminium alloy AA5086, the parameters of Bron and Besson 2004 yield criterion have been calibrated by a single biaxial test of notched cruciform specimen ^[163]. The identified parameters are given in Table 3-8. Compared with Mises and Hill48 yield criteria, the identified Bron and Besson 2004 yield criterion has been proved to be more accurate to characterize the anisotropy of AA5086.

Table 3-8 Parameters of Bron and Besson 2004 yield function for AA5086

$\alpha^1 = 0.72, \alpha^2 = 1 - \alpha^1 = 0.28, a = 0.16, b_1 = 13, b_2 = 8.41, c_1^1 = 1.06,$
$c_2^1 = 1.1, c_3^1 = 0.82, c_4^1 = 0.95, c_1^2 = 0.75, c_2^2 = 0.47, c_3^2 = 0.78, c_4^2 = 0.62$

The shapes of the three yield functions are compared in 2D principal stress space (in Fig. 3-27). The Mises yield criterion is completely outside the Bron and Besson 2004 yield criterion. The Hill 48 yield criterion is inside the B & B yield criterion under the equi-biaxial tensile state.

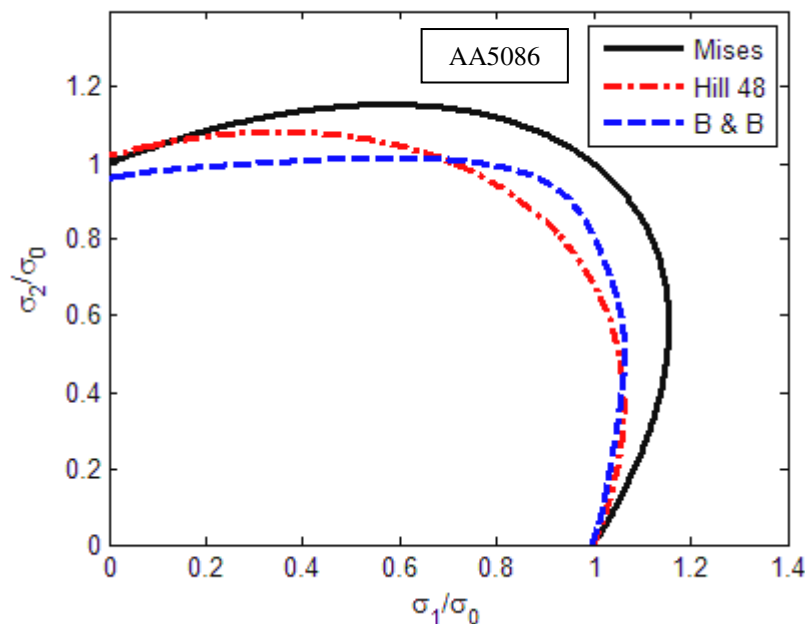


Fig. 3-27 Comparison of yield criteria

For parameter identification of isotropic hardening law, the generalized Voce hardening law for FCC alloys is chosen as follows:

$$\bar{\sigma} = \sigma_0 + K \sqrt{1 - \exp(-n\bar{\epsilon}_p)} \quad \text{Eq. 3-7}$$

3.3.4.2 Identified results

For parameters identification with Mises and Hill 48 yield criteria, the workflow of modeFRONTIER with UHARD is shown in Appendix (II). For Bron and Besson 2004 yield criterion, the workflow of modeFRONTIER with UMAT is shown in Appendix (III).

In order to study the effect of unknown parameters on the cost function, many parameter samples of hardening law have been adopted for simulation. The samples are uniformly distributed by design of experiment (DOE) based a pseudo random Sobol sequence in modeFRONTIER. The lower and upper bounds of parameters σ_0 , K and n are given in Table 3-9. In the design space, 150 samples have been chosen for forward analysis. The forward analysis based on DOE has performed with the Mises and Hill 48 criterion.

Table 3-9 Lower and upper bounds of parameters

σ_0 (MPa)	K (MPa)	n
[130,160]	[200,500]	[1,8]

Because too large strain may occur in the FE model applied by the experimental forces, the simulations are successful to converge until last only for 127 samples with the Mises yield criterion and for 118 samples with the Hill 48 yield criterion. The effects of parameters K and n on the optimization objectives are shown for the Mises and Hill 48 yield criteria (in Fig. 3-28 and Fig. 3-29). It can be seen that the objective is smaller when the parameters K and n decrease.

It seems that there exist a band, in which the parameters sets (K , n) are more feasible for optimization. For the Simplex optimization of parameter identification, the initial sets of parameters can be chosen from the more feasible band in DOE space. With the initial values given in this more feasible band, convergence by Simplex optimization will be faster and the problem of local optimization can be avoided as possible. Meanwhile, the effects of unknown parameters on the optimization function may be different for different mathematical form of hardening laws. Therefore, the hardening law should be well defined to represent the material behaviour as accurately as

possible. If an unsuitable mathematical form is used, the optimized parameters may not be obtained finally.

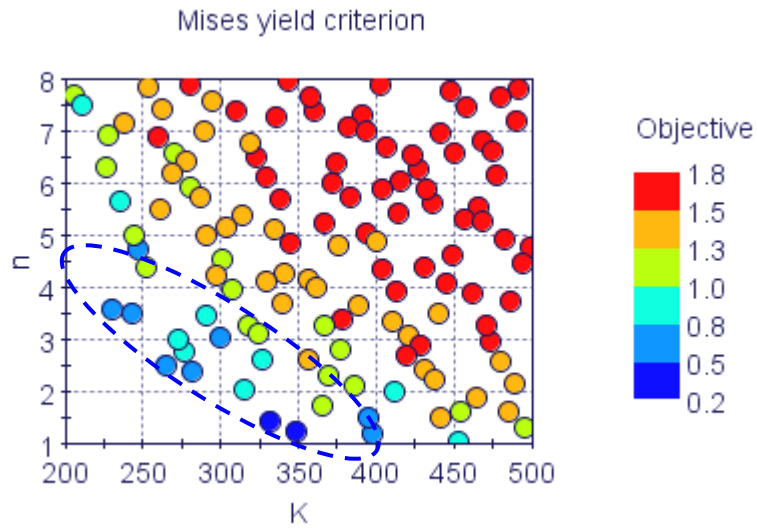


Fig. 3-28 Results of DOE with Mises yield criterion

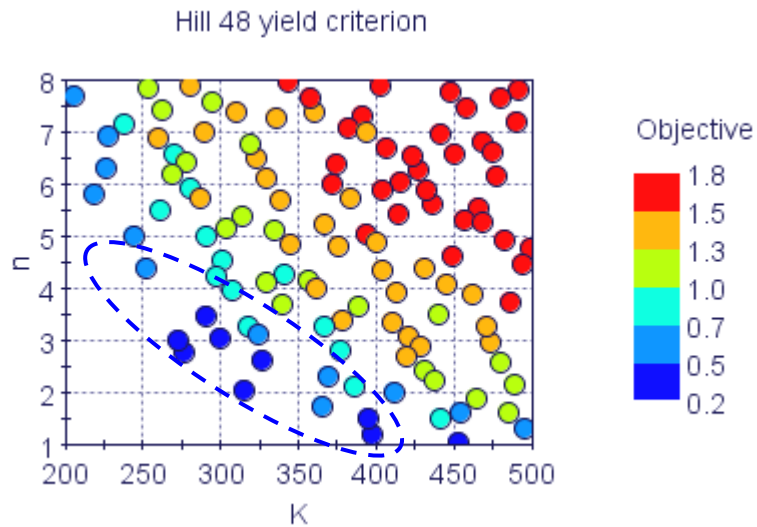


Fig. 3-29 Results of DOE with Hill 48 yield criterion

The parameters σ_0 , K and n of hardening laws have been identified for the Mises, Hill 48, and Bron and Besson 2004 yield criteria (in Table 3-10). The optimized objectives are given between experiment and simulation. The flow stress curves identified with different yield criteria by quasi-static biaxial tensile test on AA5086 are also compared with that calculated by quasi-static uniaxial tensile test in Fig. 3-30.

Table 3-10 Identified parameters of hardening laws with different yield criteria

Yield criteria	σ_0 (MPa)	K (MPa)	n	Objective δ	
				$\delta(\varepsilon_1)$	$\delta(\varepsilon_2)$
Mises	147.72	329.65	1.352	10.12%	10.88%
Hill 48	153.62	249.75	3.392	12.46%	12.10%
B & B	136.90	323.5	2.618	7.19%	16.09%

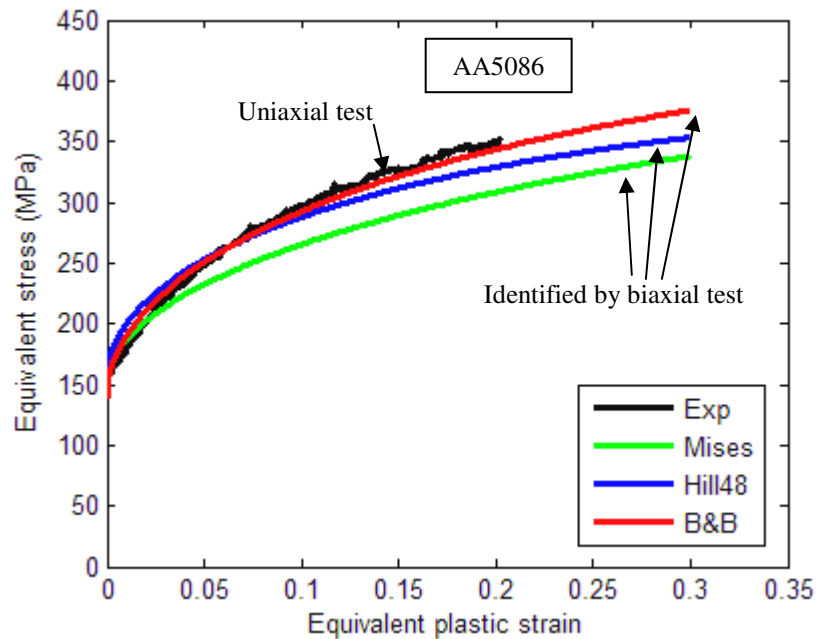


Fig. 3-30 Comparison of quasi-static flow stress curves of AA5086

The experimental equivalent plastic strain-equivalent stress curve (in Fig. 3-30) is directly calculated by the experimental deformation and force curves of uniaxial tensile test. It can be clearly seen that the equivalent stress-equivalent plastic strain curve identified with the Mises yield criterion is the lowest, and the equivalent stress-equivalent plastic strain curve identified with the Hill 48 yield criterion is lower than the uniaxial flow stress curve, especially for larger deformation, while the equivalent stress-equivalent plastic strain curve identified with the advanced yield criterion of Bron and Besson 2004 nearly coincide with the uniaxial flow stress curve.

In fact, all the equivalent stress-equivalent plastic strain curves for one material should be unique under different linear strain paths at the same temperature and strain rate, if the yield criterion is preliminarily well-defined. It can be concluded that the hardening behaviour of AA5086 sheet under the linear path of biaxial tension can be well characterised by the identified hardening law with Bron and Besson 2004 yield criterion.

The simulated principal strains with the different identified hardening laws and Mises, Hill 48, and Bron and Besson 2004 yield criteria are also compared with the experimental principal strains in Fig. 3-31, Fig. 3-32 and Fig. 3-33, respectively. It can be seen that the discrepancies of principal strains between the experiments and simulation by the identified hardening laws with Mises, Hill 48 yield criteria are more severe. For the simulation by the identified hardening law and the Bron and Besson 2004 yield criterion, the simulated major principal strain curve nearly coincide with the experimental one, while the simulated minor principal strain curves also coincide well with the experimental one until the strain becomes too large. Therefore, it can be concluded that the yield function of Bron and Besson 2004, which has been identified by a single biaxial tensile test of cruciform specimen, is further validated to describe the yielding anisotropy of AA5086 sheet.

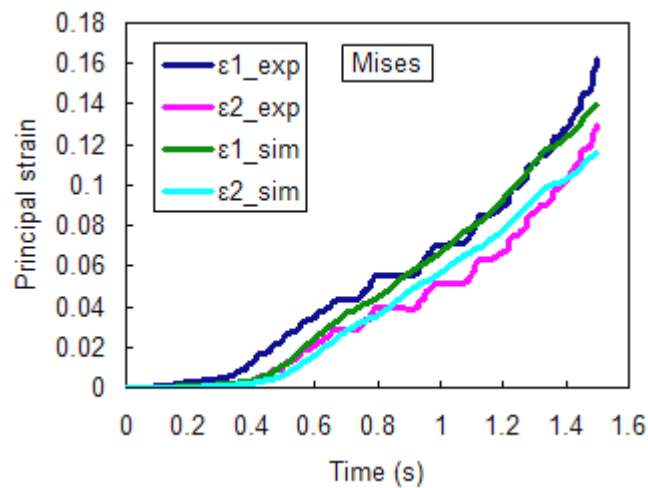


Fig. 3-31 Comparison of principal strains between experiments and simulation with Mises

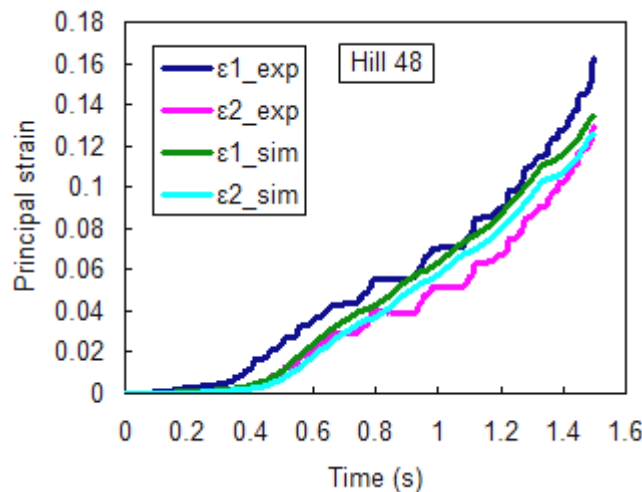


Fig. 3-32 Comparison of principal strains between experiments and simulation with Hill48

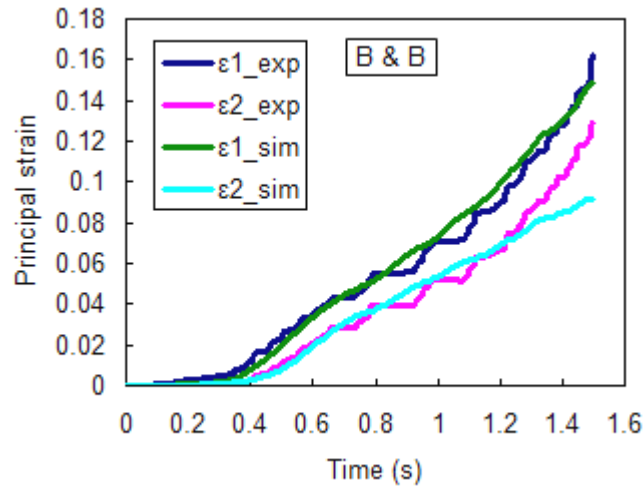


Fig. 3-33 Comparison of principal strains between experiments and simulation with B & B

3.4 Dynamic biaxial test of AA5086

For dynamic biaxial tensile test, the specimen is deformed at a specific velocity. The measured force curves must be treated before introduction into the parameter identification loop due to oscillations on the forces signals.

3.4.1 Load ringing phenomenon

For dynamic biaxial tests, the inertia masses are accelerated along the sliding bars to obtain the specific velocity before the specimen is loaded, then the specimen is impacted suddenly and the velocity is maintained due to the inertia effect of additional mass during the test, as shown in Fig. 3-34.

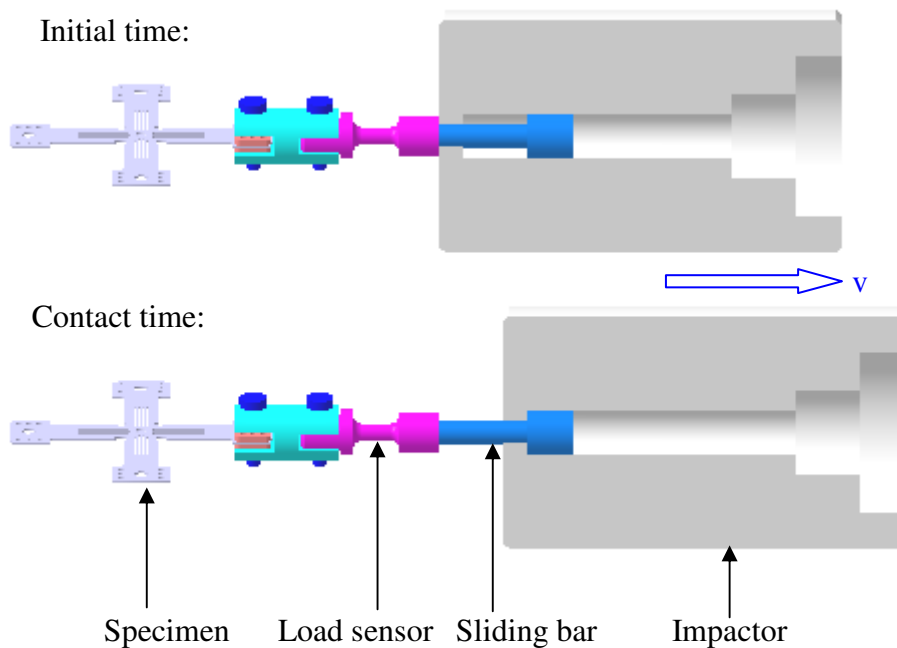


Fig. 3-34 Process of dynamic biaxial tensile test

3. Identification methodology of hardening behaviour under in-plane biaxial loading

To carry out dynamic biaxial tensile test of cruciform specimen at the speed of 250mm/s and room temperature, the main parameters of measurement system are given in Table 3-11 .

Table 3-11 Main parameters of measurement system for dynamic biaxial test on AA5086

Test	Camera (FASTCAM-APX RS 250K)			Load sensor
	Acquisition rate (fps)	Resolution (pixel)	Shutter speed (s)	Acquisition rate (Hz)
250mm/s	18000	384×320	1/18000	50000

The velocities of the four actuators (V10 and V20 along TD, V30 and V40 along RD) are measured by the displacement sensors, as shown in Fig. 3-35. The loading velocity for each actuator rises from 0 to about 250mm/s during the acceleration stage from about 4ms to 9ms . It can be seen that the loaded velocity are maintained at about 250mm/s during the test from 9ms to 16ms after acceleration.

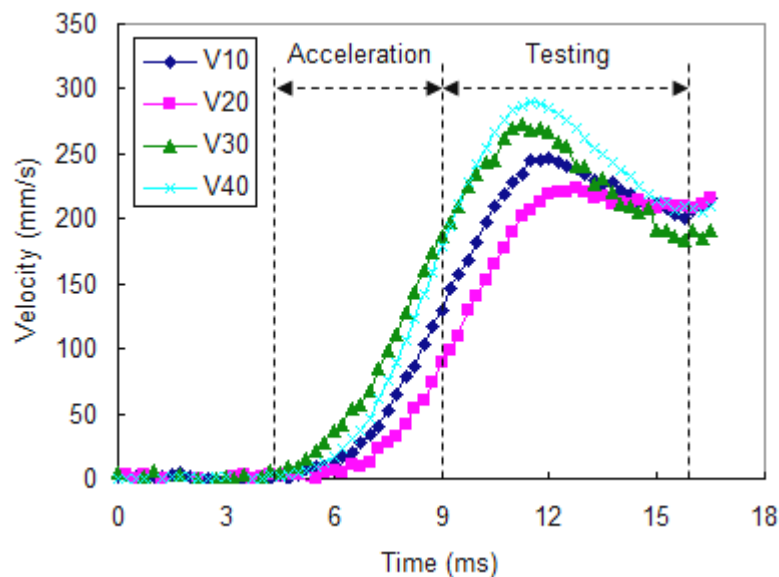


Fig. 3-35 Velocity of each actuator during dynamic biaxial test

During dynamic test, 290 images of specimen have been captured. The initial crack along the transverse direction at the central zone has been found in Fig. 3-36. The zone covering the thickness-reduced region of specimen has been analyzed by DIC technique with the same parameters of DIC presented in Table 3-1. There are 16 subsets and 14 strain points along each direction at the gauge zone. The displacement vectors at the gauge zone are shown in Fig. 3-37. It can be seen that the position of the central point is kept fixed.

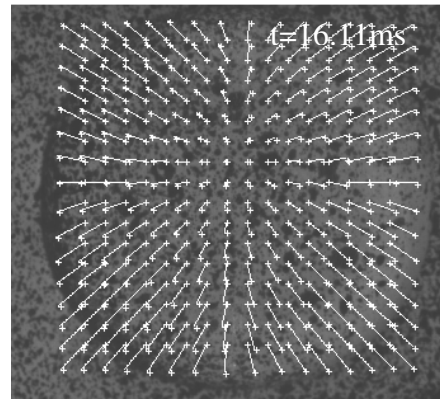
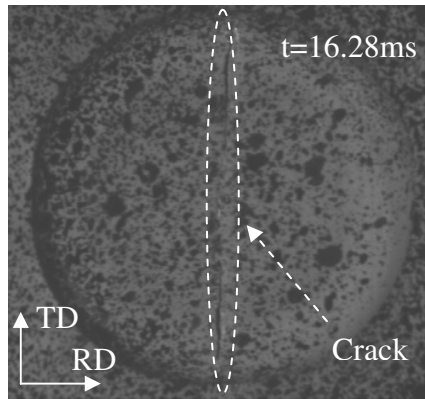


Fig. 3-36 Crack of dynamic specimen Fig. 3-37 Displacement vectors of dynamic specimen

The equivalent, principal strain fields and strain state are presented in Fig. 3-38. It is seen that the equivalent and principal strains are homogeneous at central zone ($-2mm \leq x, y \leq 2mm$). The equivalent strain at the central zone is about 30%. The equivalent and major principal strain localised near the points ($x = 0, y = \pm 4mm$). The strain state is not uniform because of the principal strain localisation at the time $t = 15.222ms$.

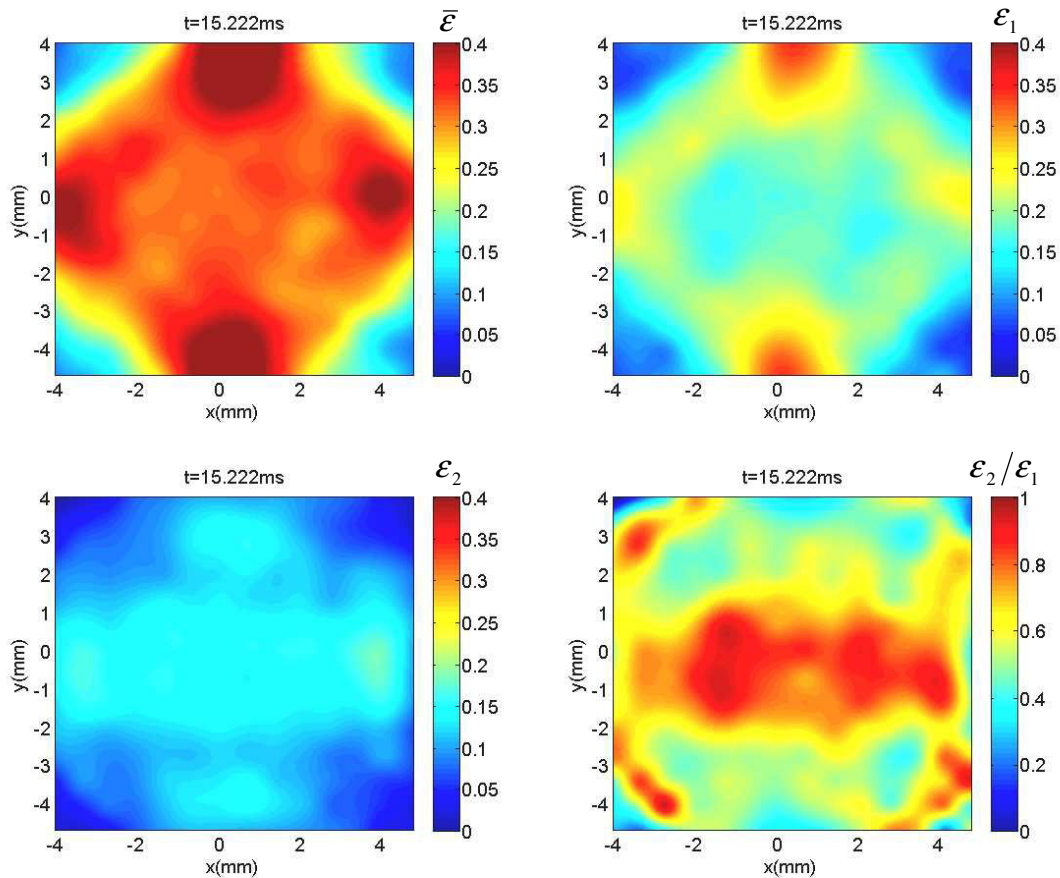


Fig. 3-38 Experimental equivalent and principal strain fields of dynamic biaxial testing specimen

The equivalent and principal strain curves averaged by the nine central points are presented in Fig. 3-39. Compared with those of quasi-static test, the PLC effect seems to disappear at higher strain rates. The order of equivalent strain before $t = 6ms$ is only 10^{-4} .

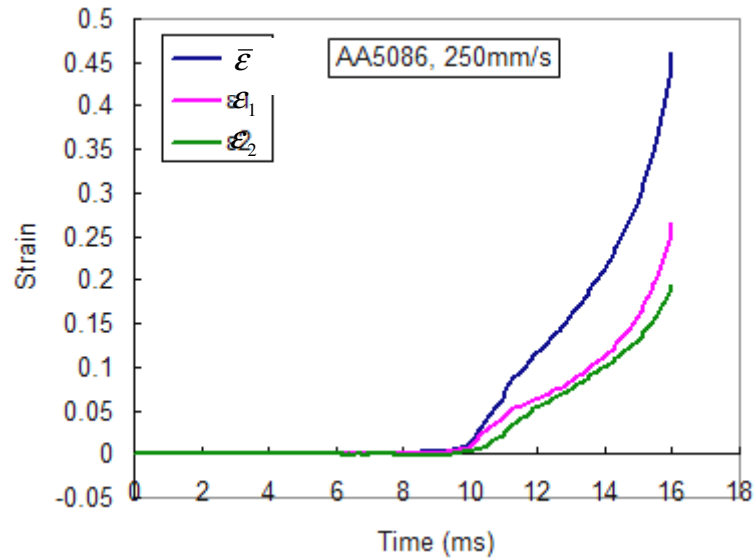


Fig. 3-39 Experimental strain curves of dynamic biaxial test

The evolutions of strain path and equivalent strain rate at the central point are shown in Fig. 3-40. The strain path varied between about 0.7 to 0.9 during test. The equivalent strain rate rise from $\dot{\bar{\epsilon}} = 20/s$ to $\dot{\bar{\epsilon}} = 60/s$ before server localisation.

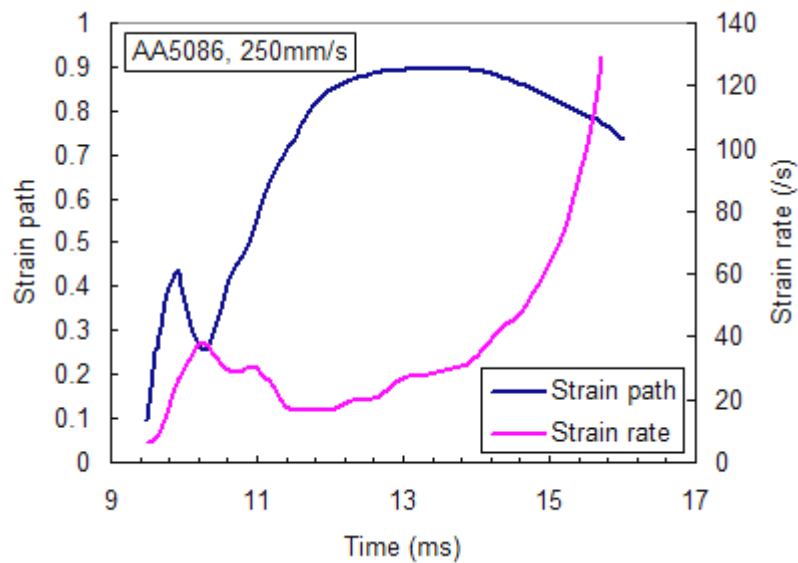


Fig. 3-40 Strain path and equivalent strain rate at the central point during dynamic test

The experimental forces along two directions have been measured during dynamic biaxial test, as shown in Fig. 3-41. The forces are very oscillating and amplitudes of oscillations decrease over time. The experimental frequency can be calculated by: $f_{exp} \approx 9 / (16.12ms - 10.1ms) = 1495Hz$.

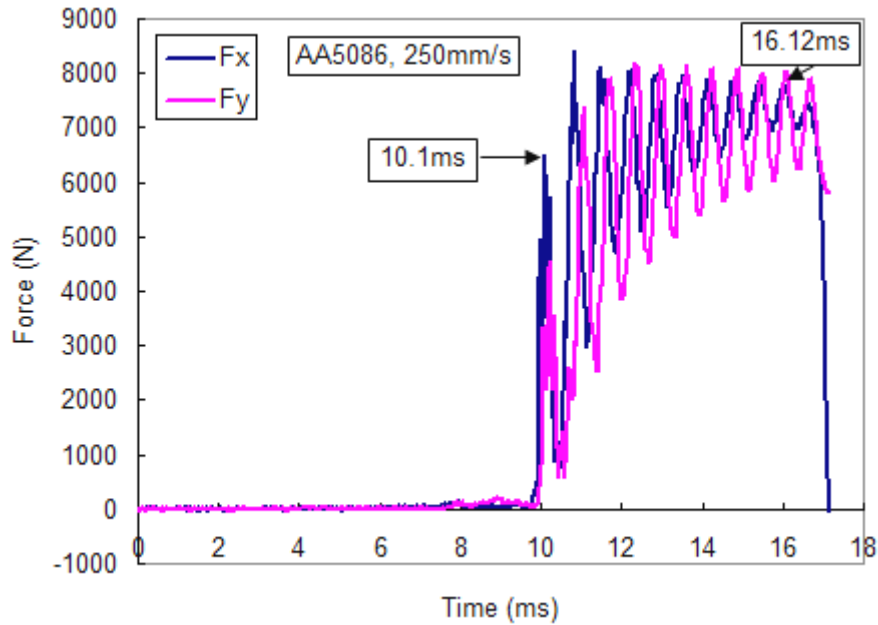


Fig. 3-41 Oscillation of measured force during dynamic biaxial test

Modal analysis by FE simulation is performed to study the load ringing phenomenon. The FE model of sliding bar, load sensor and link are built by linear tetrahedral elements of type C3D4 in ABAQUS, as shown in Fig. 3-42. To simplify the calculation, the mesh tie-up is adopted instead of contacts between the link and load sensor. The left side of model is fixed, and the displacement and rotational freedoms along Y and Z axis at the right side are also constrained. The material parameters are given with density of $\rho = 7.8 \times 10^3 kg \cdot m^{-3}$, Young's module of $E = 210GPa$ and Poisson's ratio of $\nu = 0.3$.

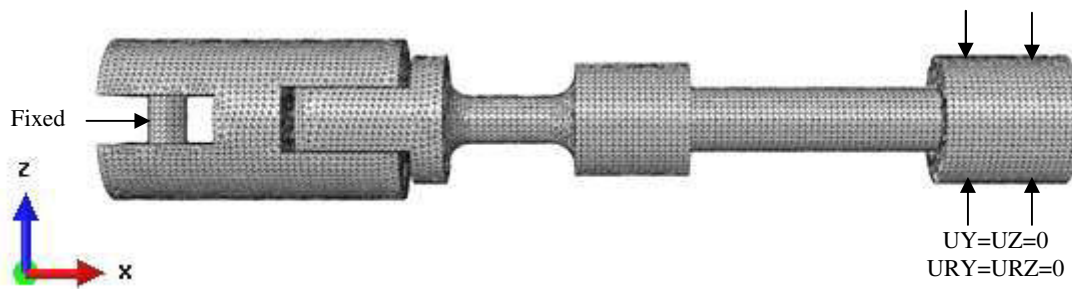


Fig. 3-42 Finite element model for modal analysis

The modes are calculated by Lanczos method in ABAQUS. It is found that the numerical first ($f_1 = 1216$) and second ($f_2 = 1439$) eigen frequencies are close to the experimental one ($f_{exp} \approx 1495Hz$). The simulated first and second modes are shown in Fig. 3-43. It can be seen that the maximal displacements occur at the load sensor along Y and Z axis respectively.

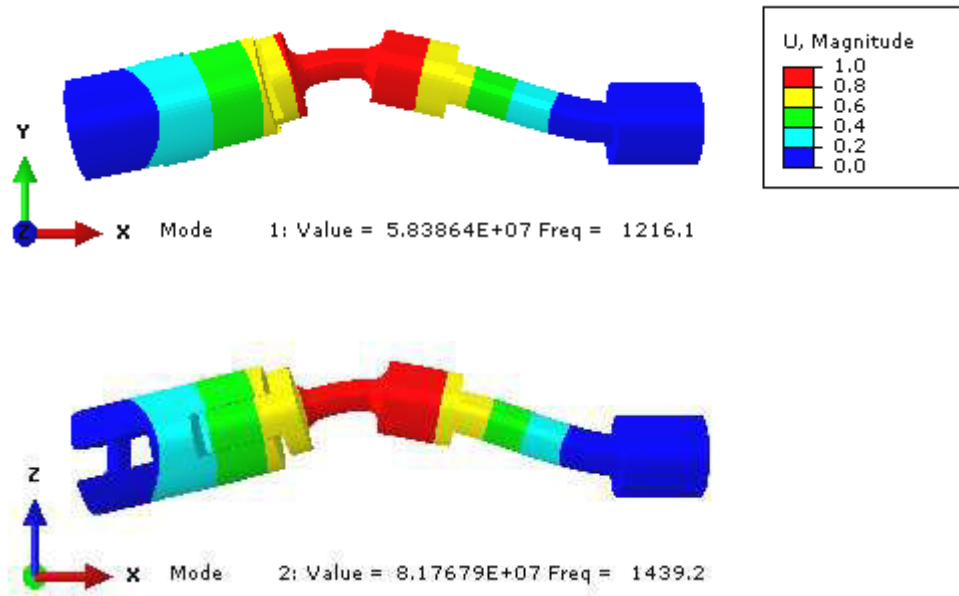


Fig. 3-43 First and second modes by numerical simulation

For dynamic biaxial tests, the load sensors will ring ^[164] at one of eigen frequencies when the sliding bars are suddenly impacted by the mass bloc. The measured forces can not be used to characterize the material behaviour of specimen without treatment, because they are the combination of dynamic elastic response of load sensor and the true material behaviour of specimen.

3.4.2 Damping and experimental results

In practice, a damping treatment can be adopted to reduce the level of vibration when the structure is subjected to impacts or other transient forces ^[165]. It consists in a material, which can increase the ability to store mechanical energy and dissipate a portion of energy through hysteresis. Viscoelastic dampers have long been used in the control of vibration in the engineering field ^[166].

In order to improve the quality of measured forces during dynamic biaxial tests, a damping layer of elastomer is placed at the interface between the sliding bar and inertia mass to improve the impact condition, as shown in Fig. 3-44.

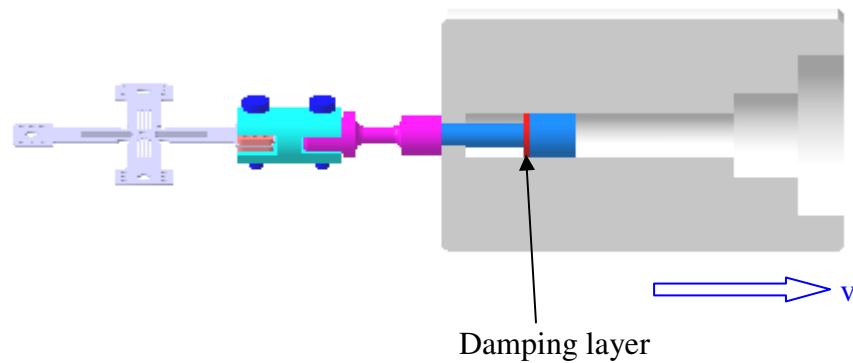


Fig. 3-44 Position of damping layer

The inner and outer diameters of circular damping layers are 22mm and 38.5mm , respectively. The initial thickness of 3mm is chosen. The uniaxial compression tests under quasi-static condition have been carried out on the damping. The experimental displacement-force curve is shown in Fig. 3-45. The average rigidity K of damping layer under quasi-static compression state is closed to $K \approx 20000\text{ N/mm}$.

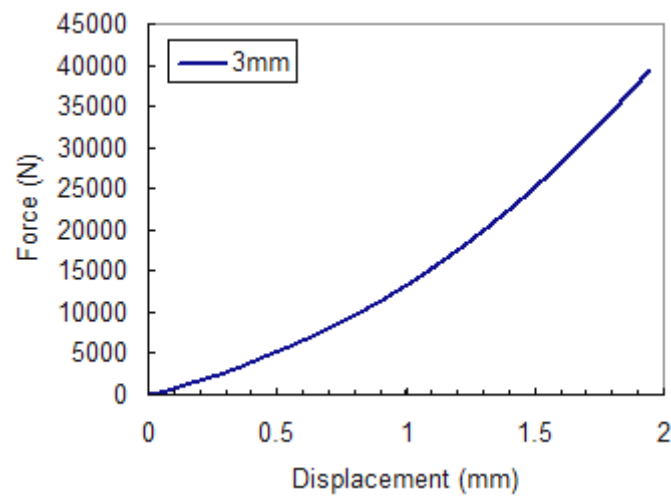


Fig. 3-45 Experimental force-displacement curves of damping layer

For dynamic biaxial tensile test with damping layers at the speed of 250mm/s , the same parameters of measurement system are used in Table 3-11. The velocity for each actuator are also measured, as shown in Fig. 3-46. It can be seen that the velocities are maintained at about 250mm/s during biaxial tension from 9ms to 19ms . Compared with the dynamic biaxial test without damping layers, the loading time is a little longer. The initial crack occurred along the rolling direction at central zone of specimen (in Fig. 3-47). There are 323 images at the central zone of specimen before initial crack. For strain calculation by DIC, there are 15 subsets and 13 strain points

on the analyzed zone. The displacement vectors in the gauge zone are shown in Fig. 3-48. It can be seen that the central point of specimen is a little moved.

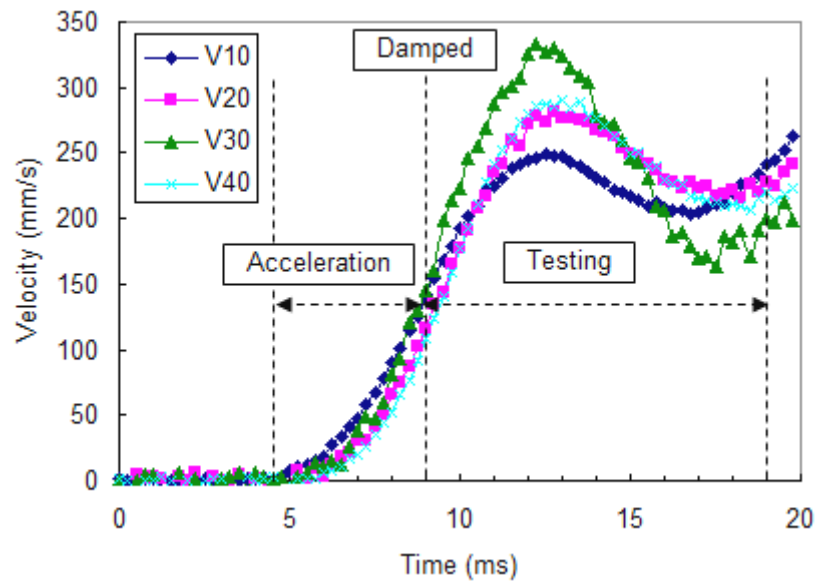


Fig. 3-46 Loaded velocity of dynamic biaxial test with damping

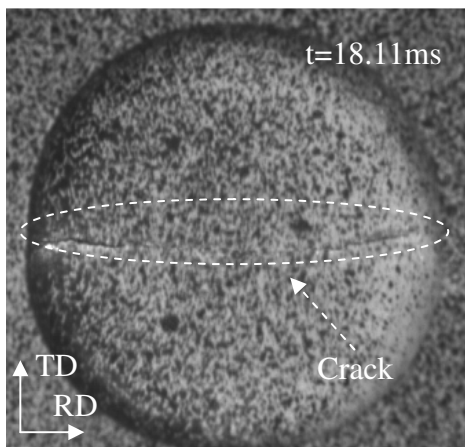


Fig. 3-47 Crack of damped specimen

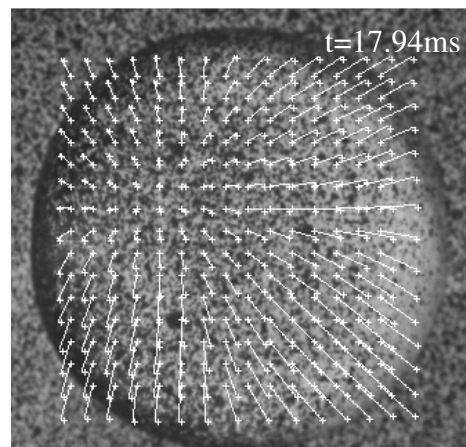


Fig. 3-48 Displacement vectors of damped specimen

The equivalent, principal strains field and strain state at the time $t = 17ms$ are presented in Fig. 3-49. It can be seen that the strains at the central zone ($-2mm \leq x, y \leq 2mm$) are nearly uniform. The equivalent strain at the central zone is about 30%. The equivalent and major principal strains localised near the points ($x = \pm 4mm, y = 0$). The strain state is not very uniform because of the principal strain localisation at $t = 17ms$.

3. Identification methodology of hardening behaviour under in-plane biaxial loading

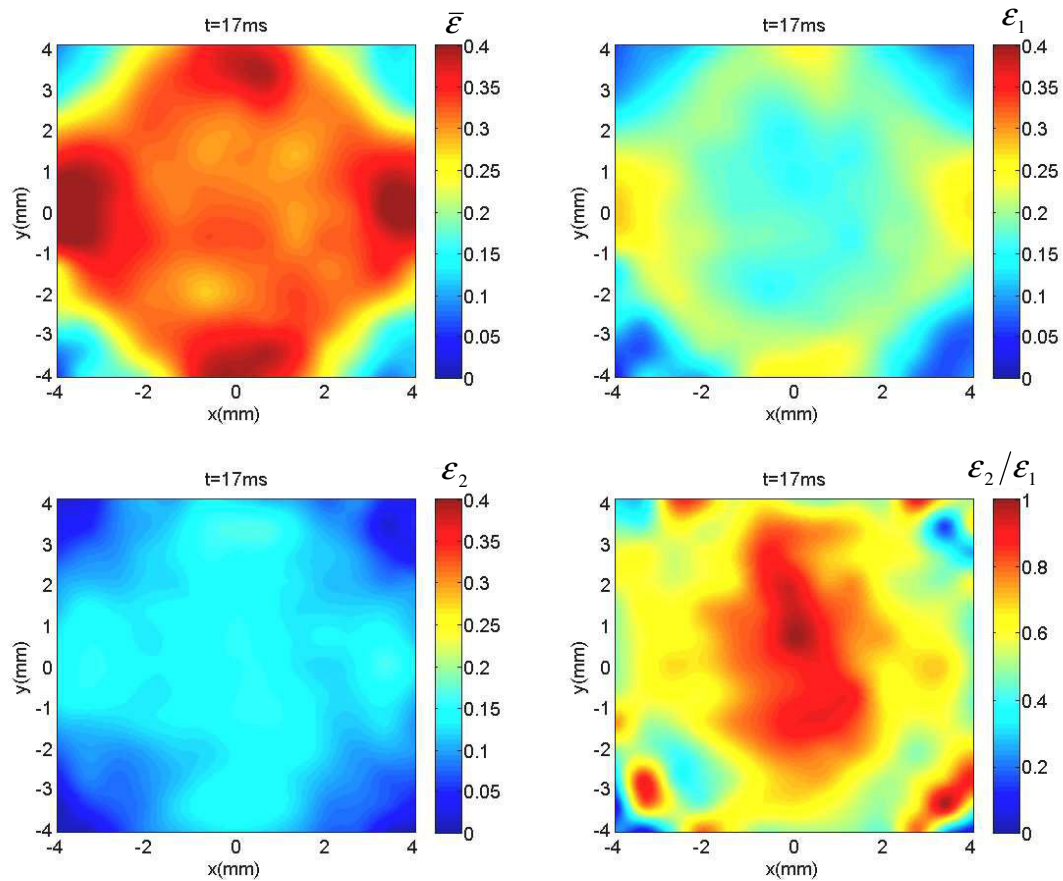


Fig. 3-49 Experimental equivalent and principal strain field of dynamic specimen with damping

The evolutions of equivalent, major and minor principal strains averaged by nine points are presented in Fig. 3-50. The order of equivalent strain before $t = 8ms$ is only 10^{-4} . The PLC effect of AA5086 seems to disappear at the higher strain rates.

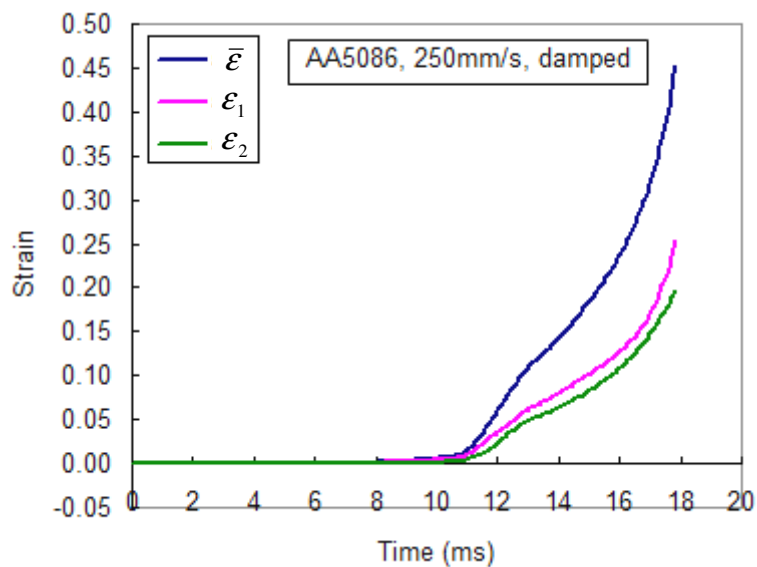


Fig. 3-50 Experimental strain curves of dynamic biaxial test with damping

The evolutions of strain path and equivalent strain rate at the central point of specimen are presented in Fig. 3-51. The strain path is about $\varepsilon_2 / \varepsilon_1 \approx 0.8$ after $t = 12ms$. The strain rate is about $\dot{\varepsilon} \approx 40/s$, and increased quickly after $t = 17ms$.

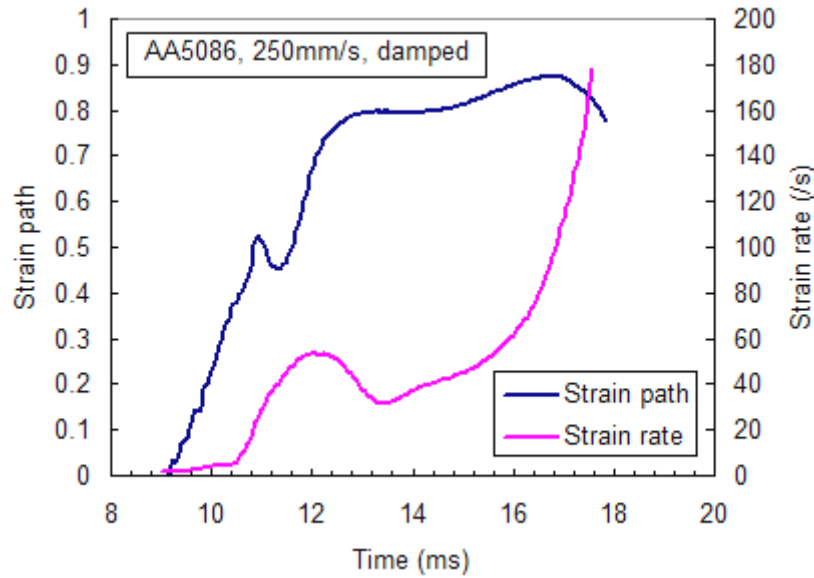


Fig. 3-51 Strain path and strain rate of dynamic biaxial test with damping

The experimental forces along two directions are measured in Fig. 3-52. There is a little oscillation of the force signal at the beginning of the tension stage. Compared with the measured force of dynamic test without damping, the amplitude and time of oscillation are greatly reduced.

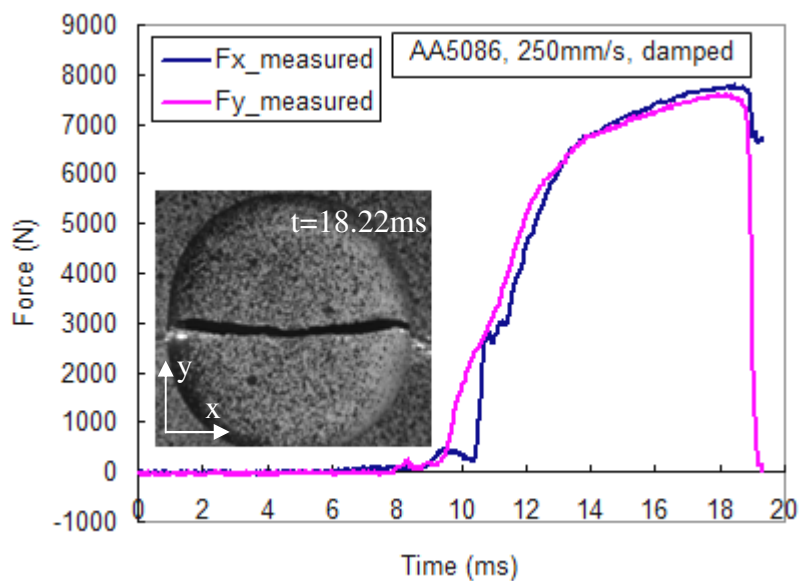


Fig. 3-52 Measured force curves of dynamic biaxial test with damping

The measured forces have been smoothed by a moving average method in Fig. 3-53. It is seen that the smoothed force coincide with the measured one along axis Y. The smoothed force along axis X is a little different from the measured one before 4000N . The smoothed forces and experimental principal strains have also been synchronized, as shown in Fig. 3-54. It can be seen that the strain level for the force of 4000N is very low and corresponds mainly to an elastic one. So, the influence of smooth process on the strain evolution can be neglected. Therefore, the experimental data presented in Fig. 3-54 will be used for parameter identification.

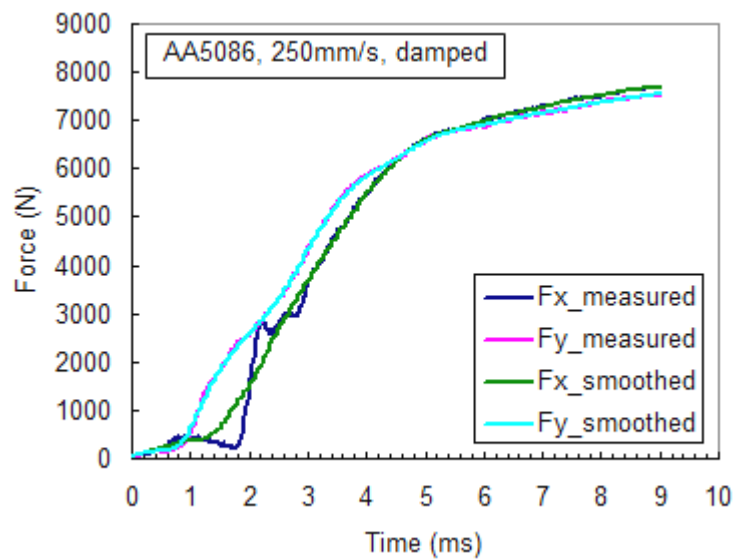


Fig. 3-53 Smoothed force curves of dynamic biaxial test with damping

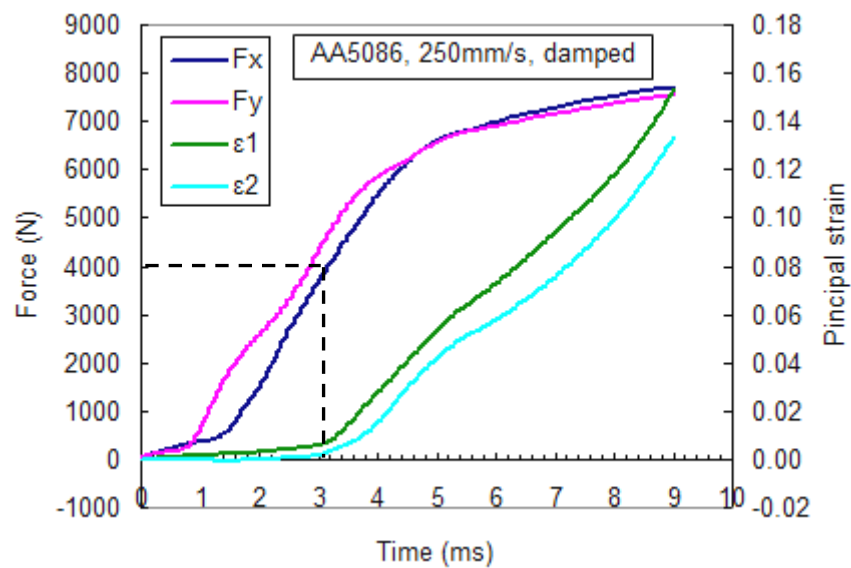


Fig. 3-54 Pre-processed curves of force and principal strain of dynamic test with damping

3.4.3 Parameter identification

With the pre-processed force curves along two directions and the principal strain curves at the central point from the dynamic biaxial tensile test with damping layers, a parameter identification has been performed to characterize the hardening behaviour of AA5086 sheet at intermediate strain rates. Here, the elastic behaviour and the shape of Bron and Besson 2004 yield function are assumed to be independent of strain rates. The elastic parameters and coefficients of Bon and Besson 2004 yield function have been determined respectively by uniaxial and biaxial tensile tests at the quasi-static conditions and room temperature.

The generalised Voce hardening law, which was used for parameter identification by the quasi-static biaxial tensile test, is also adopted. The identified parameters of this hardening law by dynamic biaxial tensile test are given in Table 3-12 and compared with those obtained by quasi-static one.

Table 3-12 Comparison of identified hardening laws by quasi-static and dynamic tests

Test	Hardening law $\bar{\sigma} = \sigma_0 + K\sqrt{1 - \exp(-n\varepsilon_p)}$			Objective	
	σ_0 (MPa)	K (MPa)	n	$\delta(\varepsilon_1)$	$\delta(\varepsilon_2)$
Quasi-static	136.9	323.5	2.618	7.19%	16.09%
Dynamic	148.4	422	1	2.84%	8.39%

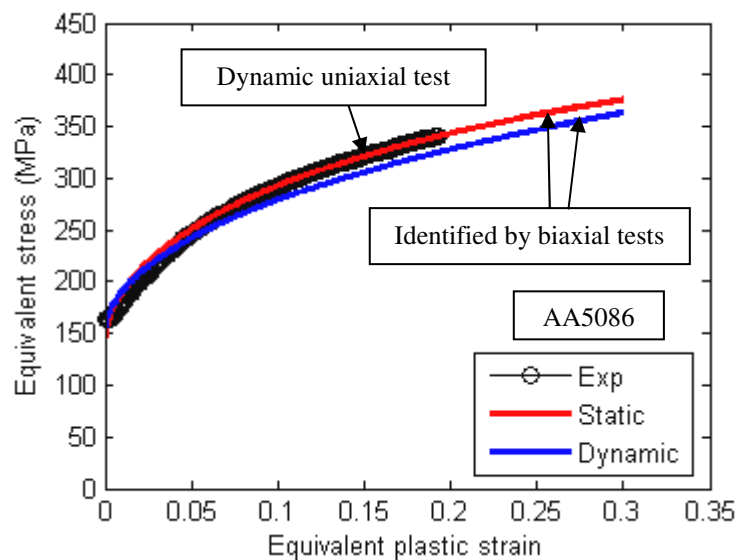


Fig. 3-55 Comparison of static and dynamic biaxial flow stress curves

The uniaxial and biaxial flow stress curves identified by quasi-static and dynamic biaxial tests are compared in Fig. 3-55. The uniaxial flow stress curve obtained from dynamic uniaxial test is also presented. It is seen that the identified flow stress curve by dynamic biaxial test is a little lower than the one by quasi-static biaxial test. The relative error between the two biaxial flow stress curves is about 5%. This difference can be explained by the small negative strain rate sensitivity of AA5086, also observed for uniaxial characterizations, and measurement errors.

The simulated principal strain curves are compared with the experimental ones of the dynamic biaxial test, as shown in Fig. 3-56. It can be seen that the simulated major principal strain curve is in a good agreement with the experimental one and the simulated minor principal strain curve is slightly higher than the experimental one after $t = 5ms$.

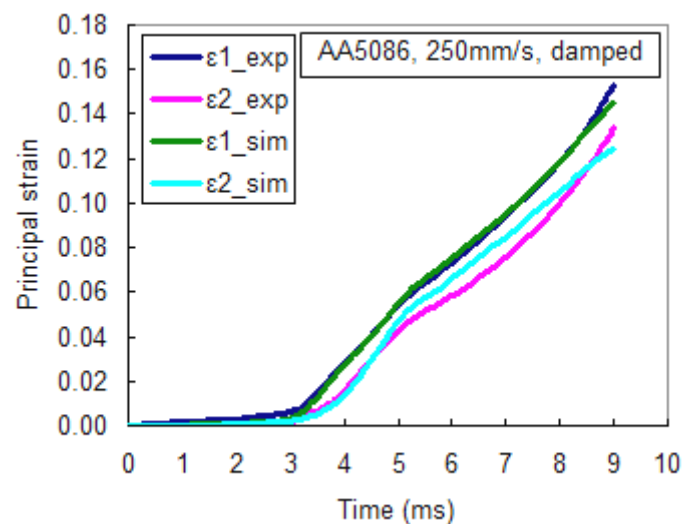


Fig. 3-56 Comparison of experimental and simulated principal strains for dynamic test

3.5 Conclusion

With the experimental and identified results from the quasi-static and dynamic biaxial tensile tests on aluminium alloy AA5086, it can be concluded that:

- (1) With the optimal shape of cruciform specimen, biaxial tensile tests on AA5086 sheet under quasi-static and dynamic conditions at room temperature have been carried out. The crack initially occurred at the central zone, so the optimal shape of cruciform specimen is experimentally validated to obtain larger strains.
- (2) For parameter identification by biaxial tensile test on cruciform specimen, the global forces along the two directions are applied to the FE model, and the local experimental and simulated principal strains at the central point are compared to

optimize the parameters of material model. The generalised Voce hardening law is chosen to characterize the hardening behaviour. This strategy of parameter identification is validated for a quasi-static biaxial tensile test.

- (3) In this work, three yield criteria of Mises, Hill 48 and Bron and Besson 2004 are preliminarily defined to identify the parameters of hardening laws for the quasi-static biaxial tensile test. The identified biaxial flow stress curves are also compared with uniaxial flow stress curve. The biaxial flow stress curve identified with the advanced anisotropic yield criterion of Bron and Besson 2004 coincide very well with the uniaxial experimental flow stress curve. It is further validated that Bron and Besson 2004 yield criterion can well describe the anisotropic behaviour of AA5086.
- (4) During the dynamic tests at intermediate strain rate, the dynamic response of the mechanical parts located between the specimen and actuator leads to oscillation on the force signal. To reduce these oscillations, an elastomer layer (thickness of 3mm) has been used. Comparison of experimental results with and without damping layer shows that the amplitude of oscillations is greatly reduced when using an elastomer. The hardening law under dynamic condition has also been identified with the yield criterion of Bron and Besson 2004, and compared with the one obtained under quasi-static condition, so the dynamic testing procedure has been validated for material characterization at intermediate strain rates.

4. Identification of strain-rate dependent hardening laws of DP600 by biaxial tests

4.1 Introduction

For sheet metal forming processes, elastoplastic behaviour of many materials exhibits strain rate sensitivity. The hardening laws should consider both strain hardening and strain rate effects for rate-dependent materials at room temperature.

In this chapter, uniaxial and biaxial tensile tests under quasi-static and dynamic conditions will be performed and compared on a rate-dependent sheet metal DP600. The same geometry of specimens, testing machines and strategy of parameter identification, which has been validated for characterization of AA5086, are applied for the characterization of viscoplastic behaviour of a DP600 sheet.

4.2 Uniaxial test of DP600

DP600 is a dual phase Advanced High Strength Steel (AHSS), which is designed to offer high strength, ductility and formability. DP steels consist in a ferritic matrix containing a hard martensitic second phase in the form of islands^[167]. The material is widely used for body-in-white structural end reinforcement components, such as pillar reinforcements, crash structures, as well as for light weight seat structures^[168].

4.2.1 Experimental result

Uniaxial tensile tests on DP600 have been performed by the dynamic uniaxial tensile testing machine at room temperature. The initial thickness of DP600 steel sheet is 2mm. The loading speeds, 1mm/s, 100mm/s, 500mm/s and 1m/s correspond to various strain rates, 0.02/s, 2/s, 10/s and 20/s, respectively. The high speed camera is also adopted to record the deformation of specimens. The main parameters of measurement system for each loading speed are presented in Table 4-1.

Table 4-1 Main parameters of measurement system for uniaxial tests on DP600

Test	Camera (FASTCAM-APX RS 250K)			Load sensor
	Acquisition rate (fps)	Resolution (pixel)	Shutter speed (s)	Acquisition rate (Hz)
1mm/s	250	704×128	1/600	250
100mm/s	3000	704×128	1/5000	9000
500mm/s	15000	704×128	1/15000	45000
1m/s	15000	704×128	1/15000	45000

DIC technique is adopted to calculate the true strain fields. The subsets in the gauge zone for each specimen have been shown in Fig. 4-1. The magnification factor from *pixel* to *mm* is $0.1\text{mm}/\text{pixel}$. Then, the true strains on the gauge zone are averaged for each specimen before the onset of necking.

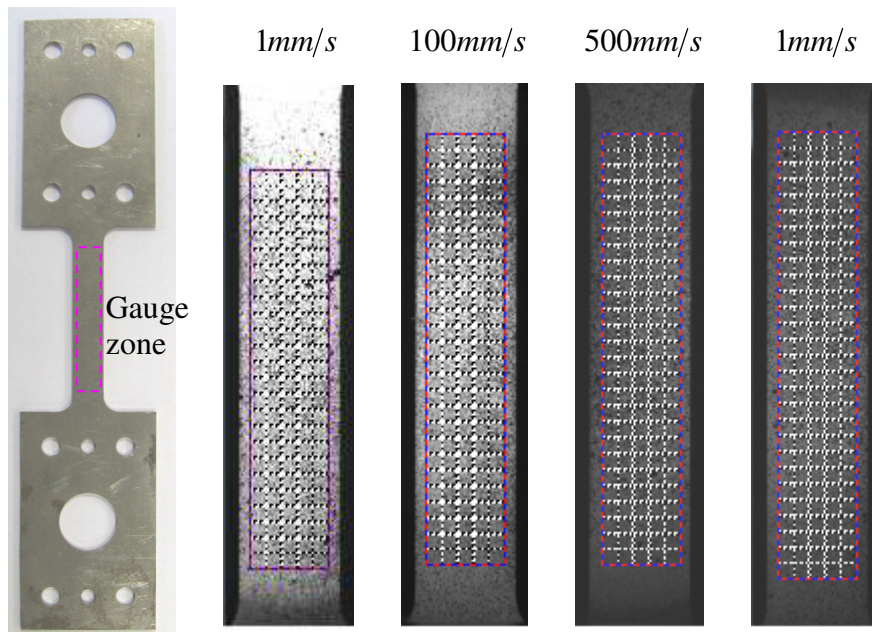


Fig. 4-1 Gauge zones of specimen at speeds of 1, 100, 500, 1000 mm/s

The experimental true strain and force curves are respectively presented in Fig. 4-2, Fig. 4-3, Fig. 4-4 and Fig. 4-5. The order of true strain before tension is 10^{-4} . When the loading speed is high ($500\text{mm}/\text{s}$ or $1\text{m}/\text{s}$), little oscillations appear on the measured force curves due to the dynamic response of mechanical parts of the experimental set-up. In order to characterize material behaviour, the measured forces of tests at high speeds are pre-processed by median filtering method in MATLAB, as shown in Fig. 4-4 and Fig. 4-5.

To calculate the true stress-true strain curves, the true stress σ is calculated from dividing the force by current cross section of specimen before diffuse necking. The current cross section is obtained by the initial cross section and true strain ε with the assumption of constant volume. If the measurement frequencies of experimental force and deformation are not the same, the experimental forces are interpolated by the method of piecewise cubic Hermit interpolation in MATLAB.

The true stress-true strain curves of DP600 at different strain rates of $0.02/\text{s}$, $2/\text{s}$, $10/\text{s}$ and $20/\text{s}$ are presented in Fig. 4-6. It is seen that the true stress-true strain curve of DP600 becomes higher when the strain rate is elevated. The hardening behaviour of DP600 sheet exhibits positive strain rate sensitivity at intermediate strain rate range and room temperature.

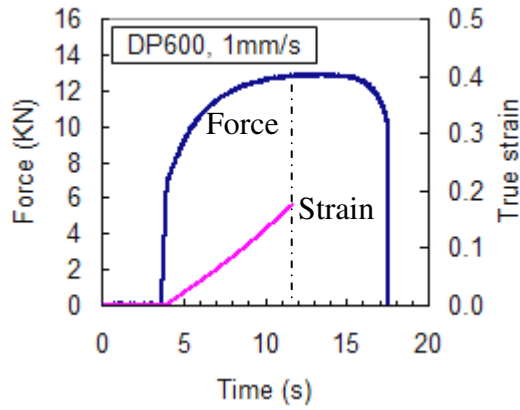


Fig. 4-2 Uniaxial test of DP600 (1mm/s)

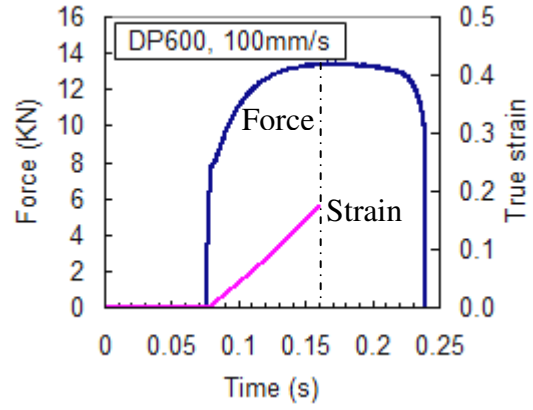


Fig. 4-3 Uniaxial test of DP600 (100mm/s)

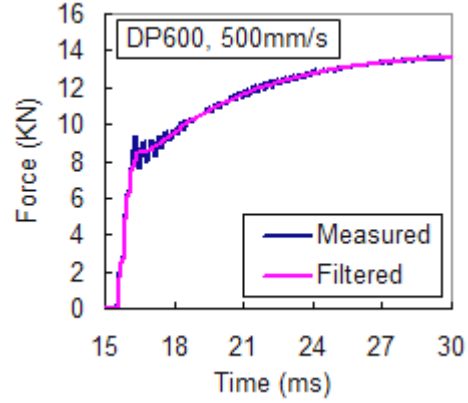
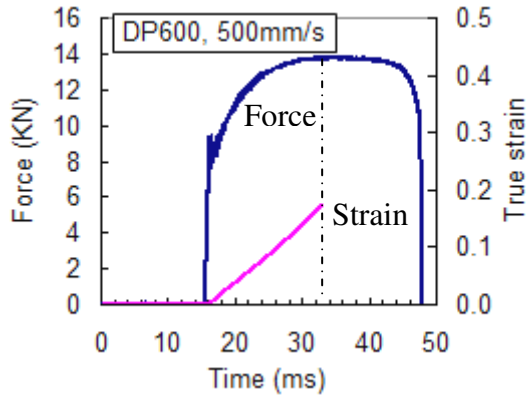


Fig. 4-4 Uniaxial test of DP600 (500mm/s)

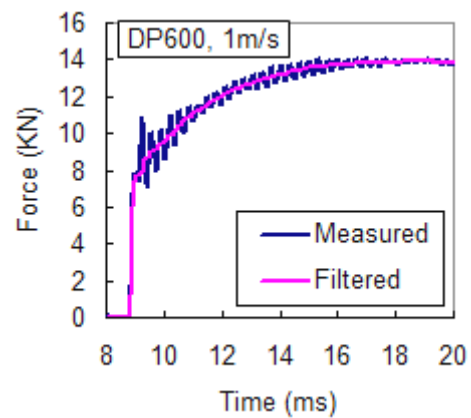
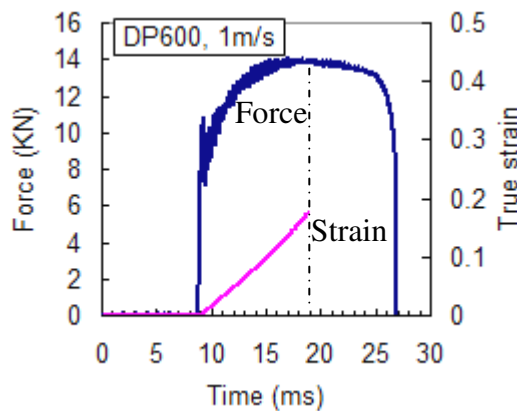


Fig. 4-5 Uniaxial test of DP600 (1m/s)

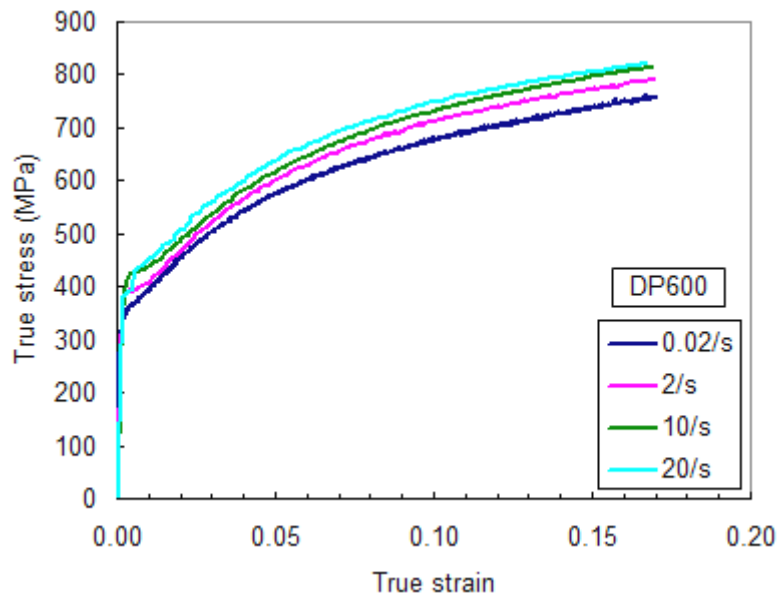


Fig. 4-6 True stress-true strain curves of DP600 at different strain rates

4.2.2 Strain rate sensitivity

For parameter identification of hardening laws, the true stress-plastic strain curves have been calculated from the true stress-true strain curves, as shown in Fig. 4-7. The yield points on the true stress-true strain curve are determined by the conventional limit at 0.2% plastic strain.

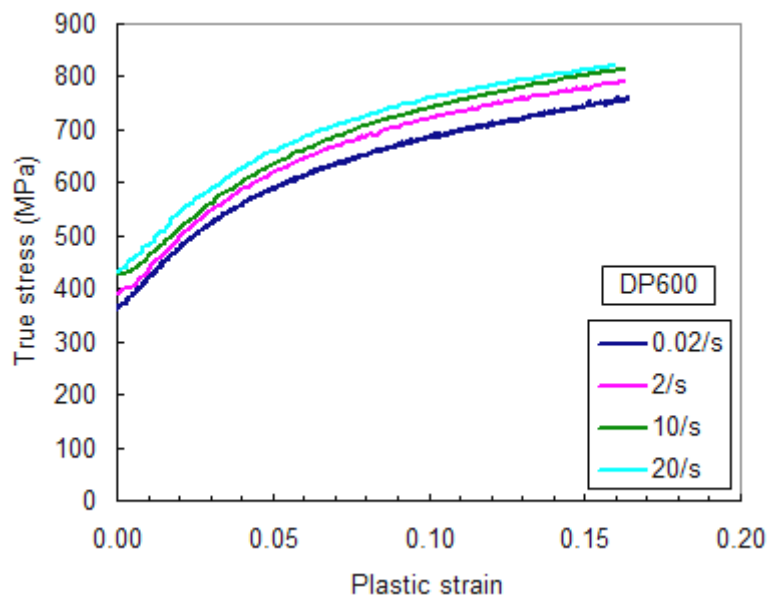


Fig. 4-7 True stress-plastic strain curves of DP600 by uniaxial tensile tests

For phenomenological modelling of hardening behaviour, Ludwick ($H(\epsilon_p) = K\epsilon_p^m$) and Voce ($H(\epsilon_p) = K(1 - \exp(-n\epsilon_p))$) models are compared for characterization of the strain hardening effect and simple power model is adopted to describe the strain rate sensitivity ($V(\dot{\epsilon}) = \dot{\epsilon}^m$). The adiabatic deformation-induced thermal effect is neglected^{[169] [170]}. As seen in chapter 1, four types of hardening law can be defined in a multiplicative way as follows:

- (1) multiplying the strain rate term $V(\dot{\epsilon})$ with the strain-hardening terms $H(\epsilon_p)$:

$$\sigma = \sigma_0 + H(\epsilon_p) \cdot V(\dot{\epsilon}) \quad \text{Eq. 4-1}$$

- (2) multiplying the strain rate term $V(\dot{\epsilon})$ with the initial yield stress σ_0 :

$$\sigma = \sigma_0 \cdot V(\dot{\epsilon}) + H(\epsilon_p)^n \quad \text{Eq. 4-2}$$

- (3) multiplying the same strain rate term $V(\dot{\epsilon})$ with the initial yield stress σ_0 and strain-hardening terms $H(\epsilon_p)$:

$$\sigma = (\sigma_0 + H(\epsilon_p)) \cdot V(\dot{\epsilon}) \quad \text{Eq. 4-3}$$

- (4) multiplying the different strain rate terms $V_1(\dot{\epsilon})$ and $V_2(\dot{\epsilon})$ with the initial yield stress σ_0 and strain-hardening terms $H(\epsilon_p)$, respectively:

$$\sigma = \sigma_0 \cdot V_1(\dot{\epsilon}) + H(\epsilon_p) \cdot V_2(\dot{\epsilon}) \quad \text{Eq. 4-4}$$

To determine the parameters of hardening laws, an iterative procedure is adopted to minimize the errors between the experimental and fitted flowing stress curves, as shown in Fig. 4-8. Here, the optimized objective δ is defined as follows:

$$\delta = \sum_j \delta_j = \sum_j \left(\frac{1}{n} \sum_i \sqrt{\left(\frac{\sigma^{fit}(\epsilon_p^{exp,i,j}) - \sigma^{exp}(\epsilon_p^{exp,i,j})}{\sigma^{exp}(\epsilon_p^{exp,i,j})} \right)^2} \right) \quad \text{Eq. 4-5}$$

Here, j is the curve number of true stress-plastic strain curve at specific strain rate, i is the point number on each curve, σ^{fit} and σ^{exp} are the fitted and experimental stress.

The optimization process is completed by modeFRONTIER, in Appendix (IV). The Bounded BFGS (B-BFGS) algorithm is chosen, which can handle the design variables on the actual bounds in a suitable way^[171]. It is an extension of the classical Broyden-

Fletcher-Goldfarb-Shanno (BFGS) algorithm. The BFGS optimization is a so-called quasi-Newton method. A descent direction is traced out by the Newton step using the gradient information. Therefore, it can achieve fast convergence.

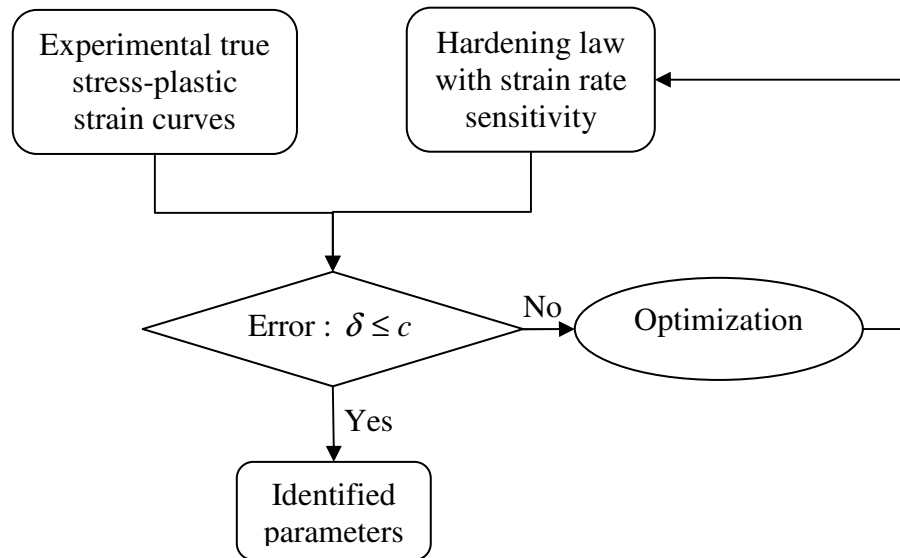


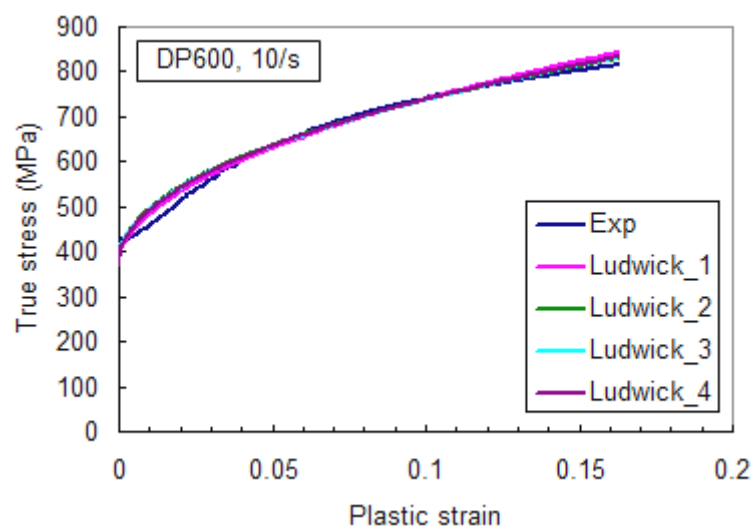
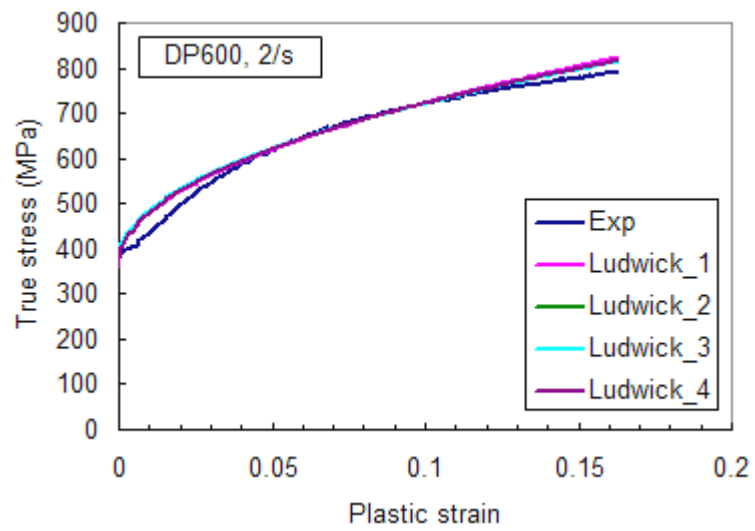
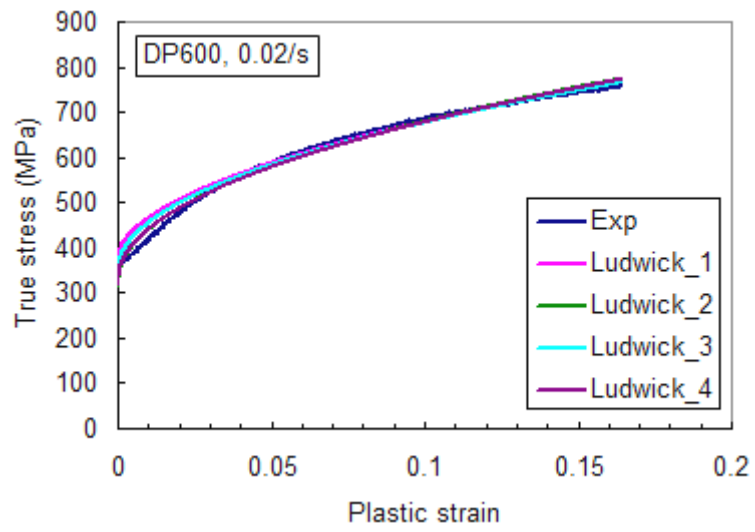
Fig. 4-8 Parameter identification for rate-dependent hardening model of uniaxial tests

The identified results of four rate-dependent hardening laws on the basis of Ludwick law are presented in Table 4-2. It can be seen that the error of identified hardening law Ludwick_4 is smallest. The strain hardening behaviour seems not to be affected by strain rate ($m_1 \gg m_2$). The strain rate sensitivity of DP600 can be multiplied only with initial yield stress. The similar conclusion has also been obtained by Yu et al.^[172] for DP600 at strain rates from 10^{-4} to $10^3 s^{-1}$. The identified hardening models have been compared with the experimental one at each strain rate, as shown in Fig. 4-9.

Table 4-2 Identified results on basis of Ludwick law by uniaxial tests on DP600

Type	Hardening law	Parameters	Error
Ludwick_1	$\sigma = \sigma_0 + K \varepsilon_p^n \dot{\varepsilon}^m$	$\sigma_0 = 372.0MPa$; $K = 1115.6MPa$ $n = 0.5116$; $m = 0.0286$	7.44%
Ludwick_2	$\sigma = \sigma_0 \dot{\varepsilon}^m + K \varepsilon_p^n$	$\sigma_0 = 351.3MPa$; $K = 1061.3MPa$ $n = 0.4658$; $m = 0.0267$	6.55%
Ludwick_3	$\sigma = (\sigma_0 + K \varepsilon_p^n) \dot{\varepsilon}^m$	$\sigma_0 = 365.5MPa$; $K = 1052.3MPa$ $n = 0.4799$; $m = 0.0135$	6.87%
Ludwick_4	$\sigma = \sigma_0 \dot{\varepsilon}^{m_1} + K \varepsilon_p^n \dot{\varepsilon}^{m_2}$	$\sigma_0 = 351.6MPa$; $K = 1079.4MPa$ $n = 0.4727$; $m_1 = 0.0223$; $m_2 = 0.0044$	6.53%

4. Identification of strain-rate dependent hardening laws of DP600 by biaxial tests



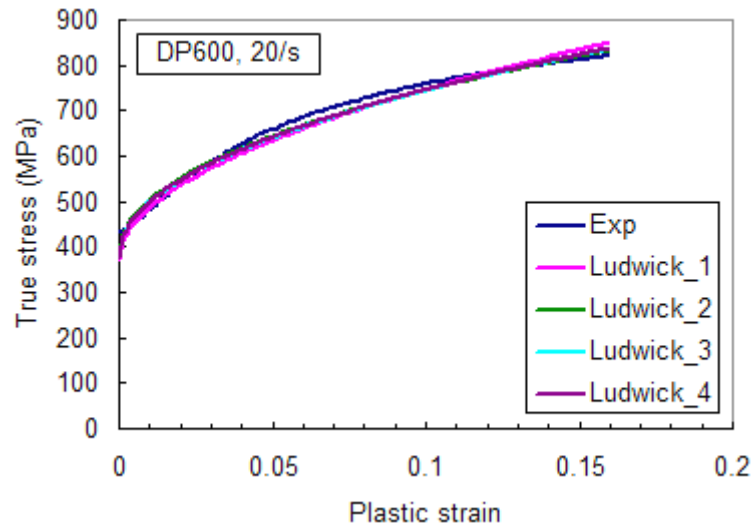


Fig. 4-9 Comparison of experimental and identified curves on basis of Ludwick

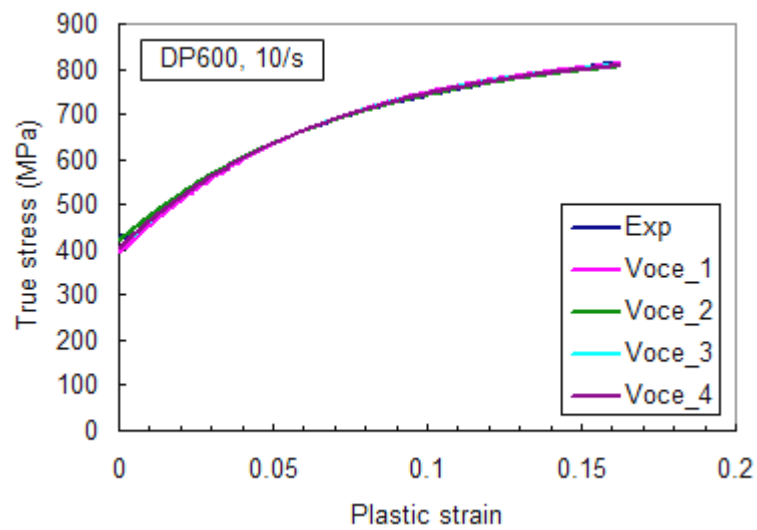
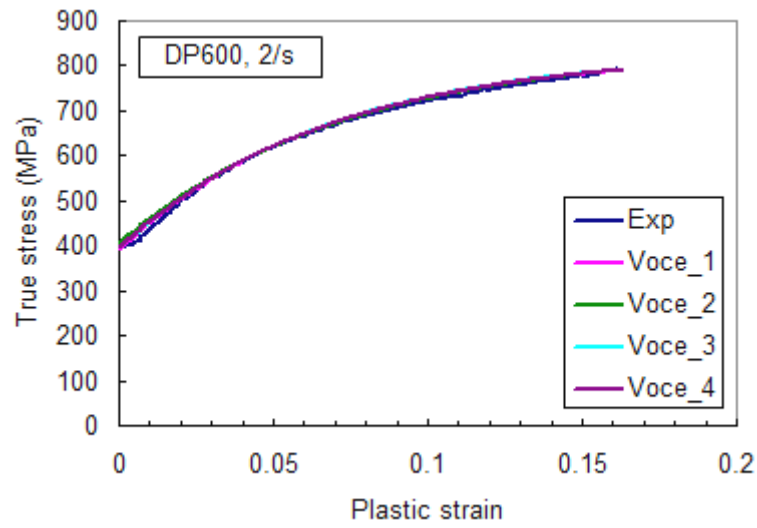
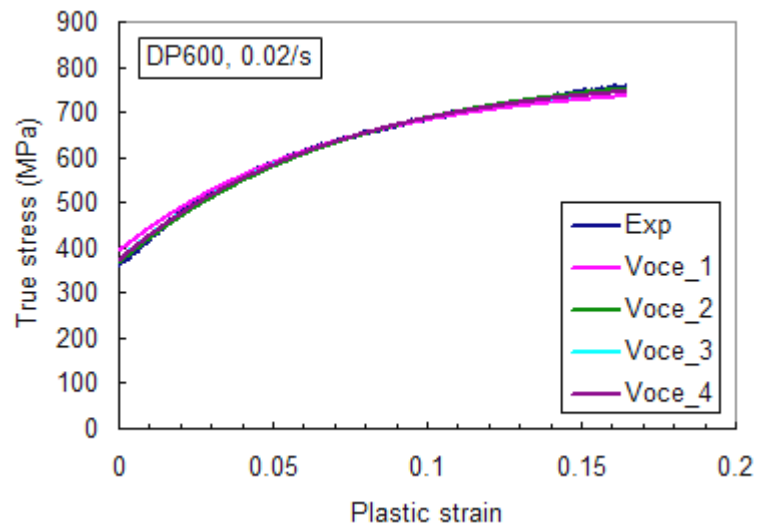
It is seen that the four identified hardening laws for each strain rate are nearly the same. The identified curves on the basis of Ludwick law are a little higher than the experimental ones for strain rates 0.02/s, 2/s and 10/s for low plastic strain (below 4%). The strain hardening effects identified on basis of Ludwick law are overestimated when the plastic strain reaches about 15%.

The identified results of four rate-dependent hardening laws on the basis of Voce law are presented in Table 4-3. The identified values of initial yield stress σ_0 are higher than those identified on the basis of Ludwick. Unlike strain rate sensitivity on the basis of Ludwick law, the influences of strain rate on the initial yield stress σ_0 and strain hardening term $H(\epsilon_p)$ are nearly equivalent. These identified curves nearly coincide with the experimental ones, as shown in Fig. 4-10.

Table 4-3 Identified results on basis of Voce law by uniaxial tests on DP600

Type	Hardening law	Parameters	Error
Voce_1	$\sigma = \sigma_0 + K(1 - \exp(-n\epsilon_p))\dot{\epsilon}^m$	$\sigma_0 = 392.4MPa; K = 427.1MPa$ $n = 14.75; m = 0.0321$	4.48%
Voce_2	$\sigma = \sigma_0\dot{\epsilon}^m + K(1 - \exp(-n\epsilon_p))$	$\sigma_0 = 399.9MPa; K = 431.3MPa$ $n = 13.65; m = 0.0225$	4.02%
Voce_3	$\sigma = (\sigma_0 + (1 - \exp(-n\epsilon_p)))\dot{\epsilon}^m$	$\sigma_0 = 392.3MPa; K = 433.1MPa$ $n = 14.43; m = 0.0132$	3.85%
Voce_4	$\sigma = \sigma_0\dot{\epsilon}^{m_1} + (1 - \exp(-n\epsilon_p))\dot{\epsilon}^{m_2}$	$\sigma_0 = 392.4MPa; K = 432.2MPa$ $n = 14.45; m_1 = 0.0137;$ $m_2 = 0.0123$	3.85%

4. Identification of strain-rate dependent hardening laws of DP600 by biaxial tests



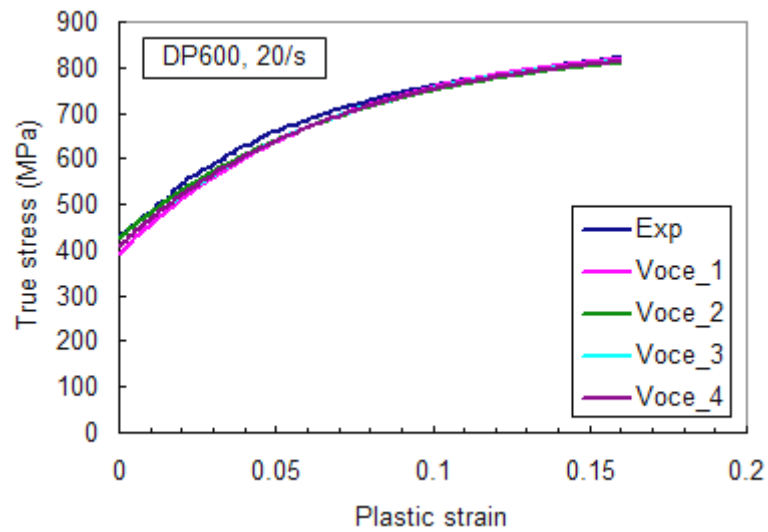


Fig. 4-10 Comparison of experimental and identified curves on basis of Voce

4.3 Experimental results of biaxial tests

The experimental procedures of quasi-static and dynamic biaxial tests on cruciform shape, which has been validated in previous chapter (on AA5086), have been applied to characterize viscoplastic behaviour of DP600. Three loading speeds for each actuator are adopted: 0.02mm/s , 1mm/s and 250mm/s . The cruciform specimens of DP600 have been prepared, as shown in Fig. 4-11.

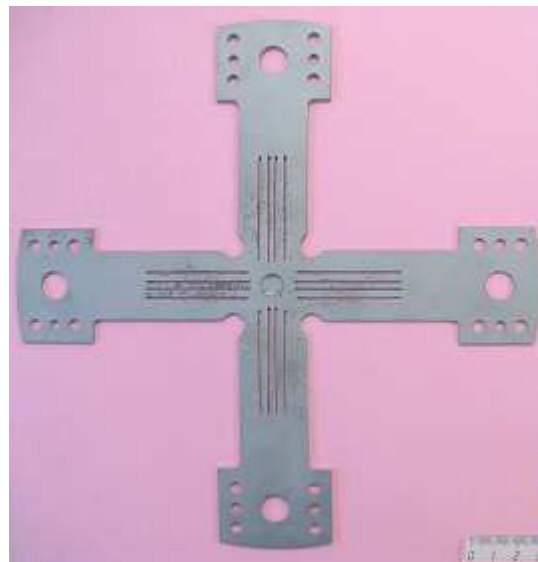


Fig. 4-11 Cruciform specimen of DP600

The main parameters of high speed camera and load sensors are respectively defined for biaxial tests at different loading speeds, as shown in Table 4-4.

Table 4-4 Main parameters of measurement system for biaxial tests on DP600

Test	Camera (FASTCAM-APX RS 250K)			Load sensor
	Acquisition rate (fps)	Resolution (pixel)	Shutter speed (s)	Acquisition rate (Hz)
0.02mm/s	50	384×384	1/500	50
1mm/s	250	1024×1024	1/1000	250
250mm/s	18000	384×352	1/18000	50000

4.3.1 Loading speed of 0.02mm/s

For quasi-static biaxial tensile test at the loading speed of 0.02mm/s , the initial crack of specimen can be seen at the central zone, as shown in Fig. 4-12. The deformation fields are calculated by DIC technique. There are 16 subsets and 14 strain points along each direction. The magnification factor is 0.37mm/pixel . The displacement vectors are shown in Fig. 4-13. It is seen that the central point is nearly unmoved.

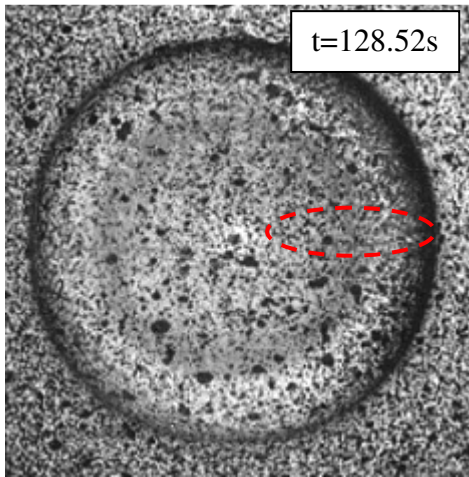


Fig. 4-12 Initial crack at 0.02mm/s

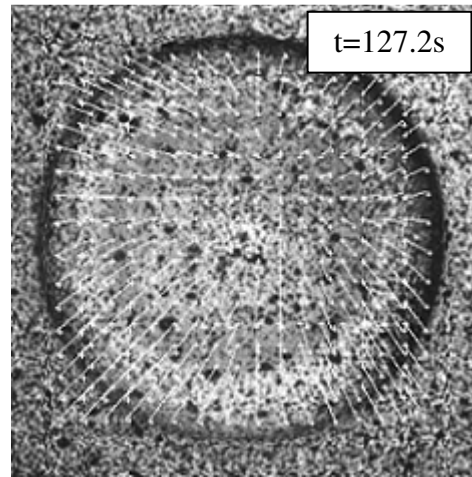


Fig. 4-13 Displacement vectors at 0.02mm/s

The equivalent, major and minor principal strain fields and strain state at the central zone of specimen have been presented in Fig. 4-14. The deformation fields at the zone ($-2\text{mm} \leq x, y \leq 2\text{mm}$) are rather homogeneous. The equivalent strain at this zone reaches up to 30%. The localization of major principal strain occurs near the points ($x = 0, y = \pm 4\text{mm}$) and points ($x = \pm 4\text{mm}, y = 0$). A quasi-equibiaxial tensile state is observed in the zone of interest ($-2\text{mm} \leq x, y \leq 2\text{mm}$).

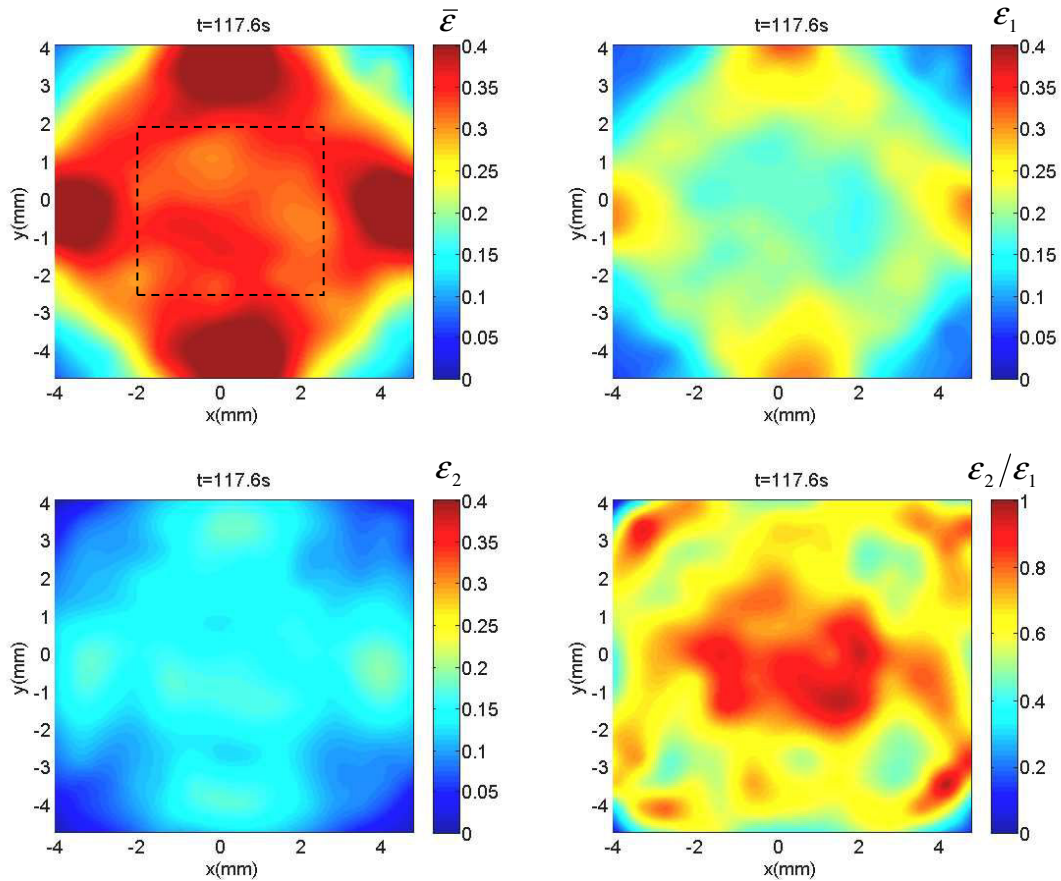


Fig. 4-14 Equivalent and principal strain fields and strain state at 0.02mm/s

The average equivalent and principal strain evolutions at the central zone of specimen have been given in Fig. 4-15.

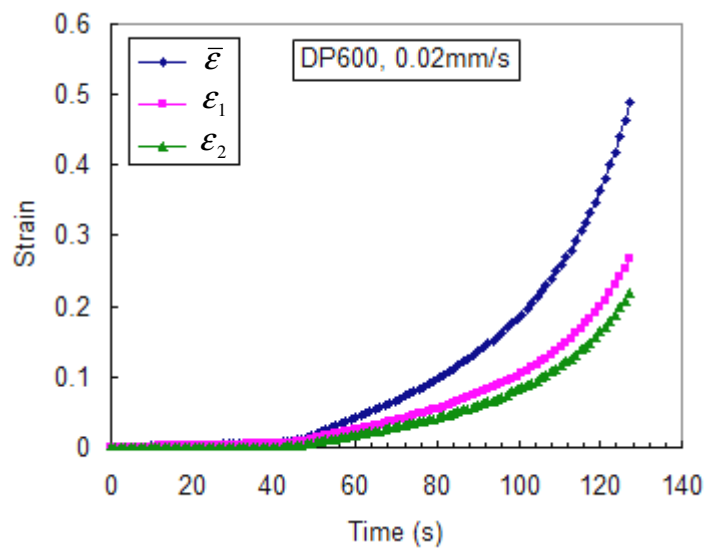


Fig. 4-15 Equivalent and principal strain evolutions at the central zone (0.02mm/s)

The strain path and strain rate evolution at the central zone of specimen is shown in Fig. 4-16. The strain path is almost constant ($\varepsilon_2/\varepsilon_1 = 0.8$) after $t = 60s$. The strain rate is about 0.002/s to 0.005/s from $t = 60s$ to $t = 100s$. The strain rate increased quickly after $t = 110s$ due to deformation localization at the central zone.

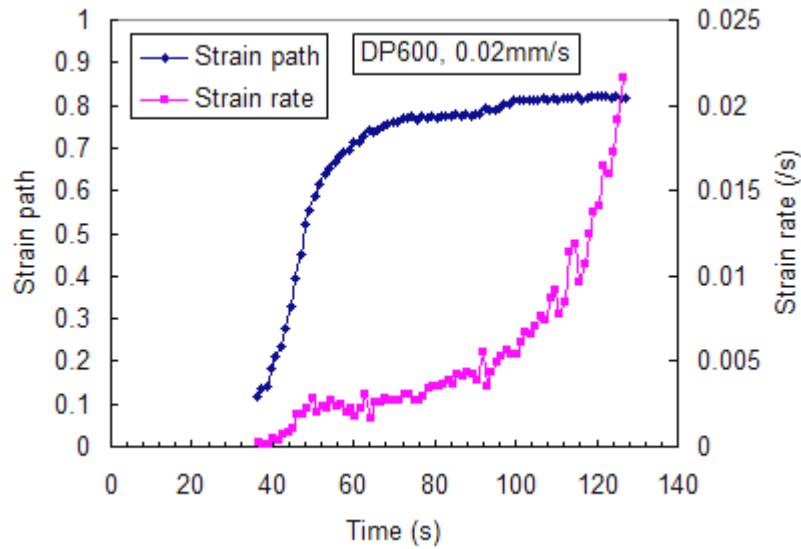


Fig. 4-16 Strain path and strain rate evolution at the central point (0.02mm/s)

The experimental forces along the two arms of specimen are measured, as shown in Fig. 4-17. It can be seen that the force curves nearly coincide with each other. The forces along two axes are well synchronized.

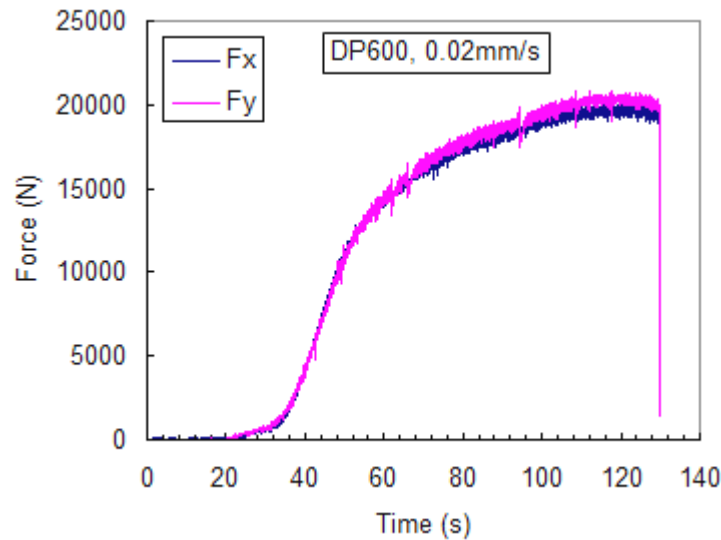


Fig. 4-17 Measured forces along two arms (0.02mm/s)

For parameter identification based on FE model, the experimental forces along two arms and principal strains at the central point of specimen have been pre-processed, as shown in Fig. 4-18. The forces have been smoothed by moving average method.

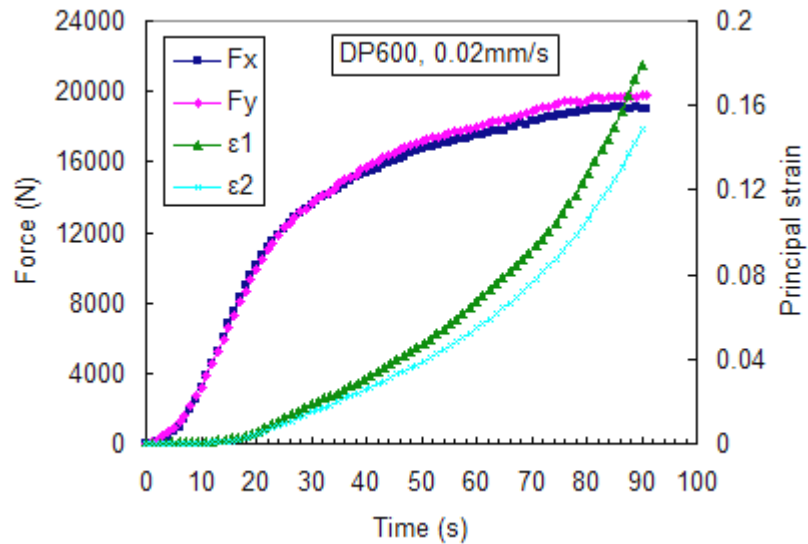


Fig. 4-18 Experimental forces and principal strains for identification (0.02mm/s)

4.3.2 Loading speed of 1mm/s

For quasi-static biaxial tensile test at the loading speed of 1mm/s , the initial crack of specimen can be seen at the central zone, as shown in Fig. 4-19. For strain calculation by DIC technique, there are 16 subsets and 14 strain points along each direction. The displacement vectors have been shown in Fig. 4-20. It can be seen that the central point is kept fixed.

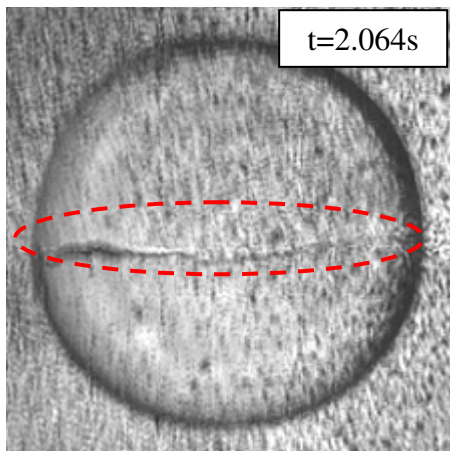


Fig. 4-19 Initial crack at 1mm/s

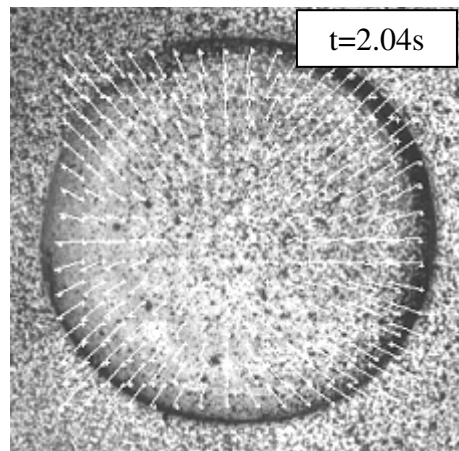


Fig. 4-20 Displacement vectors at 1mm/s

The equivalent, major and minor principal strain fields and strain state at the gauge zone of specimen are presented in Fig. 4-21. The average equivalent and principal strain evolutions at the central zone are shown in Fig. 4-22.

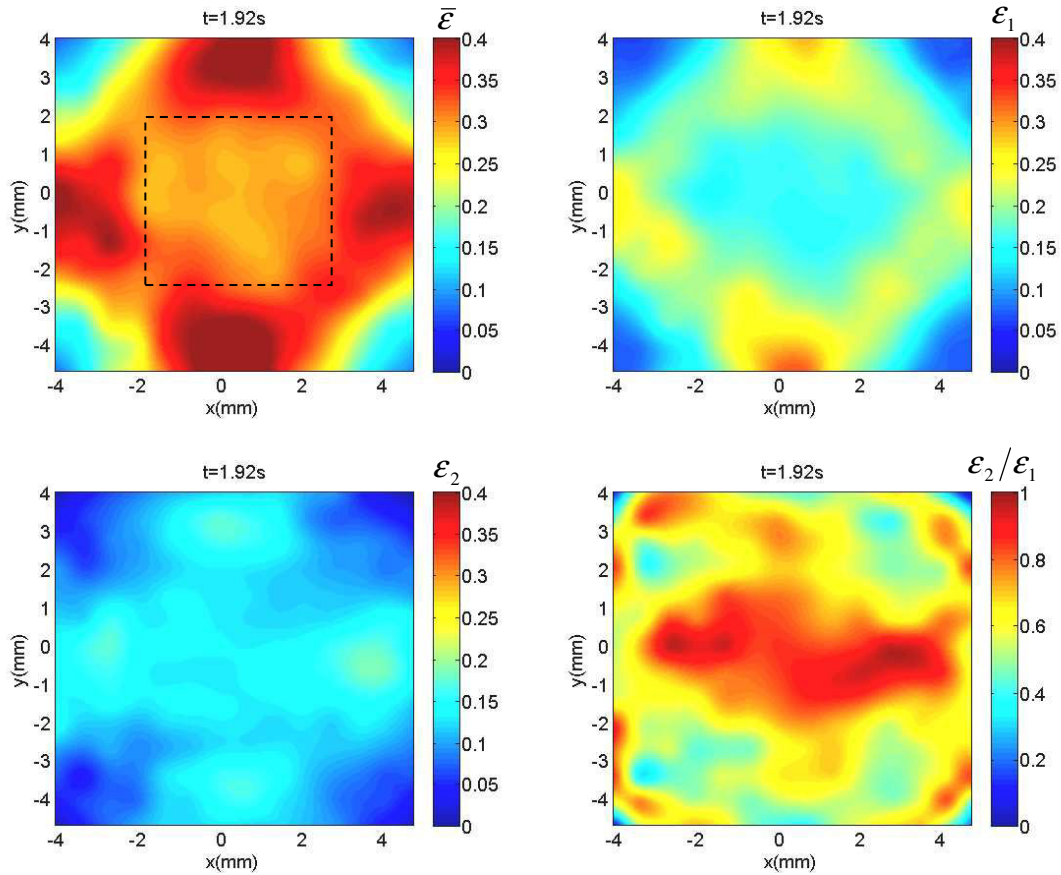


Fig. 4-21 Equivalent and principal strain fields and strain state at 1mm/s

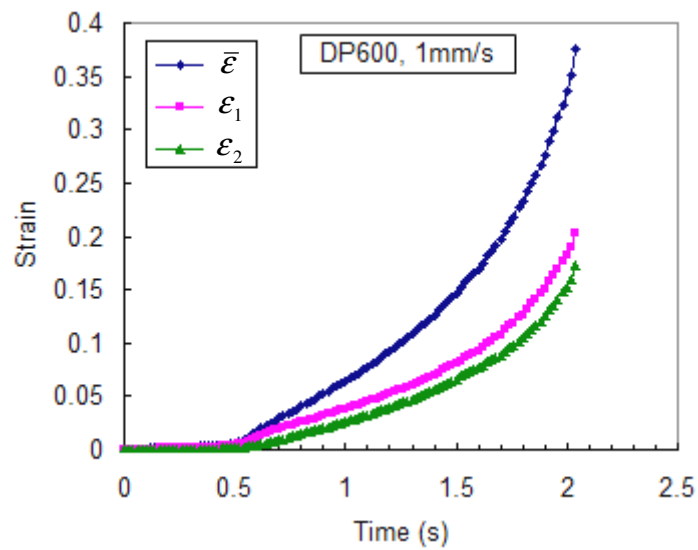


Fig. 4-22 Equivalent and principal strain evolutions at the central point (1mm/s)

The strain path and strain rate evolutions at the central point have been presented in Fig. 4-23. The strain path is about $\varepsilon_2/\varepsilon_1 = 0.8$ after $t = 1s$. The strain rate evolves from $\dot{\varepsilon} = 0.1/s$ to $\dot{\varepsilon} = 0.2/s$, from $t = 0.6s$ to $t = 1.7s$.

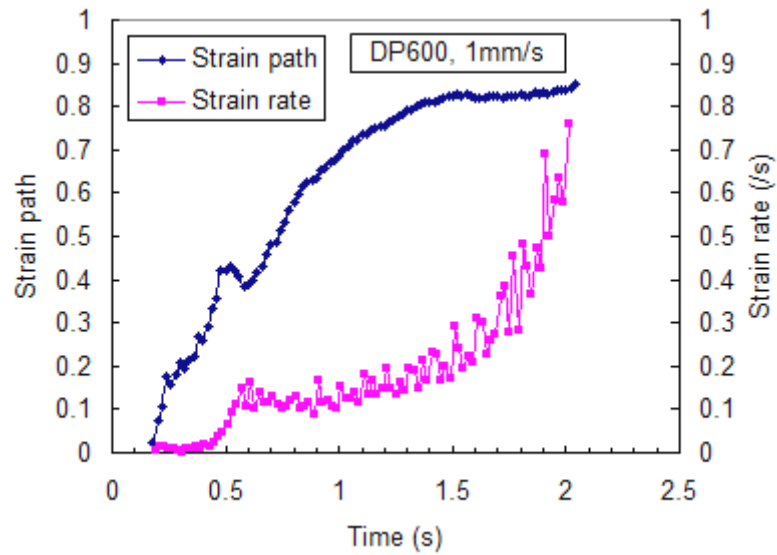


Fig. 4-23 Strain path and strain rate evolution at the central point (1mm/s)

The experimental forces along two arms have been measured, as shown in Fig. 4-22.

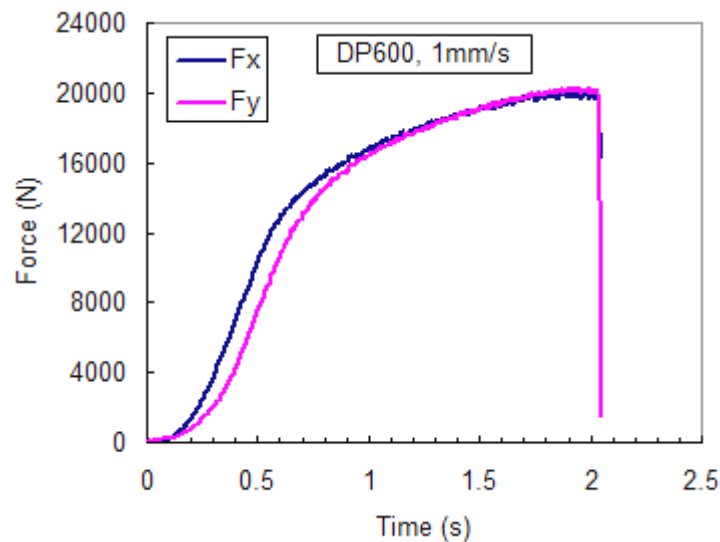


Fig. 4-24 Measured forces along two arms (1mm/s)

The experimental forces along two arms and principal strains at the central point have also been pre-processed for parameter identification, as shown in Fig. 4-25.

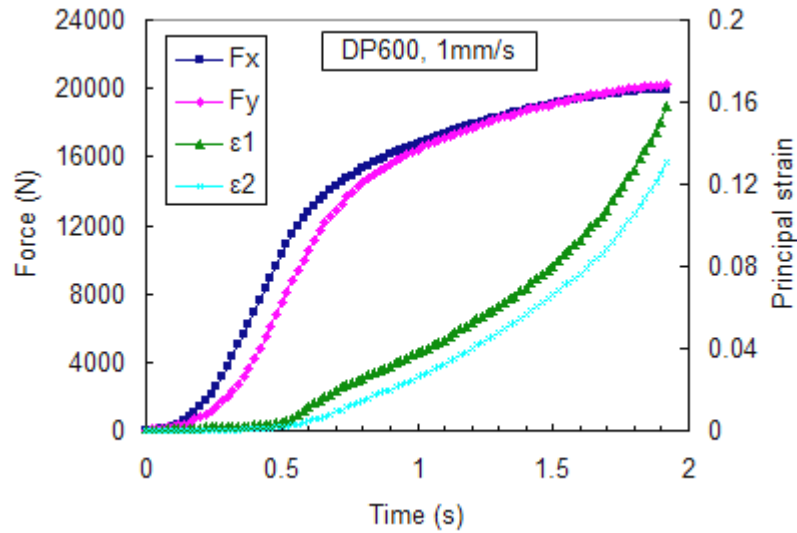


Fig. 4-25 Experimental forces and principal strains for identification (1mm/s)

4.3.2 Loading speed of 250mm/s

For dynamic biaxial tensile test, loading speed of each actuator has been measured, as shown in Fig. 4-26. It can be seen that the velocities are changed from 150mm/s to 250mm/s during test from $t = 10ms$ to $t = 24ms$. The loading speeds are not constant because the machine is controlled in open-loop.

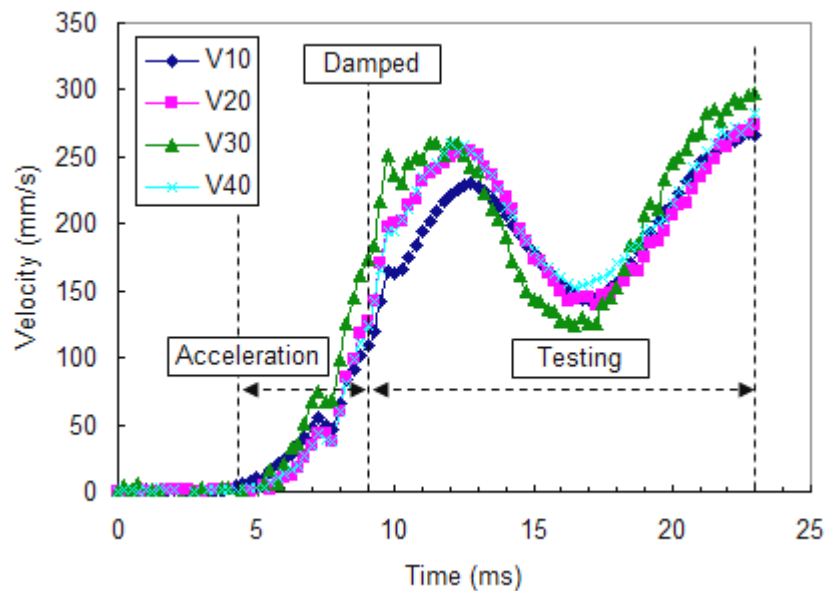


Fig. 4-26 Loading velocities of dynamic biaxial test on DP600

The initial crack of specimen can be seen at the central zone, as shown in Fig. 4-27. For strain calculation by DIC technique, there are 12 subsets and 10 strain points along each direction. The displacement vectors have been shown in Fig. 4-28.

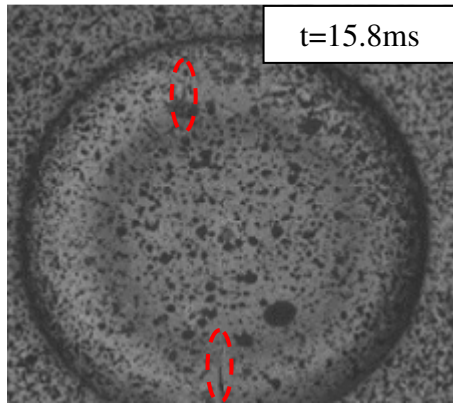


Fig. 4-27 Initial crack at 250mm/s

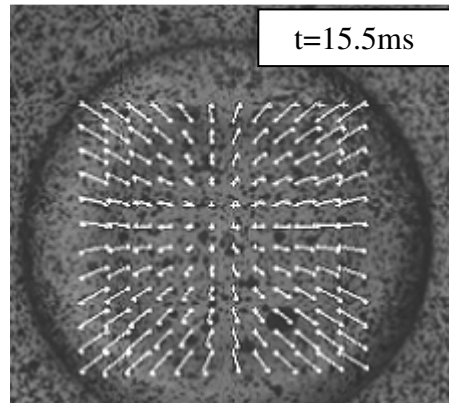


Fig. 4-28 Displacement vectors at 250mm/s

The equivalent, major and minor principal strain fields and strain state at the central zone of specimen are presented in Fig. 4-29. The deformation field at the zone $(-2\text{mm} \leq x, y \leq 2\text{mm})$ are rather uniform. The equivalent strain at this zone reaches up to 30%. The localization of major strain occurs near the points $(x = 0, y = \pm 3\text{mm})$.

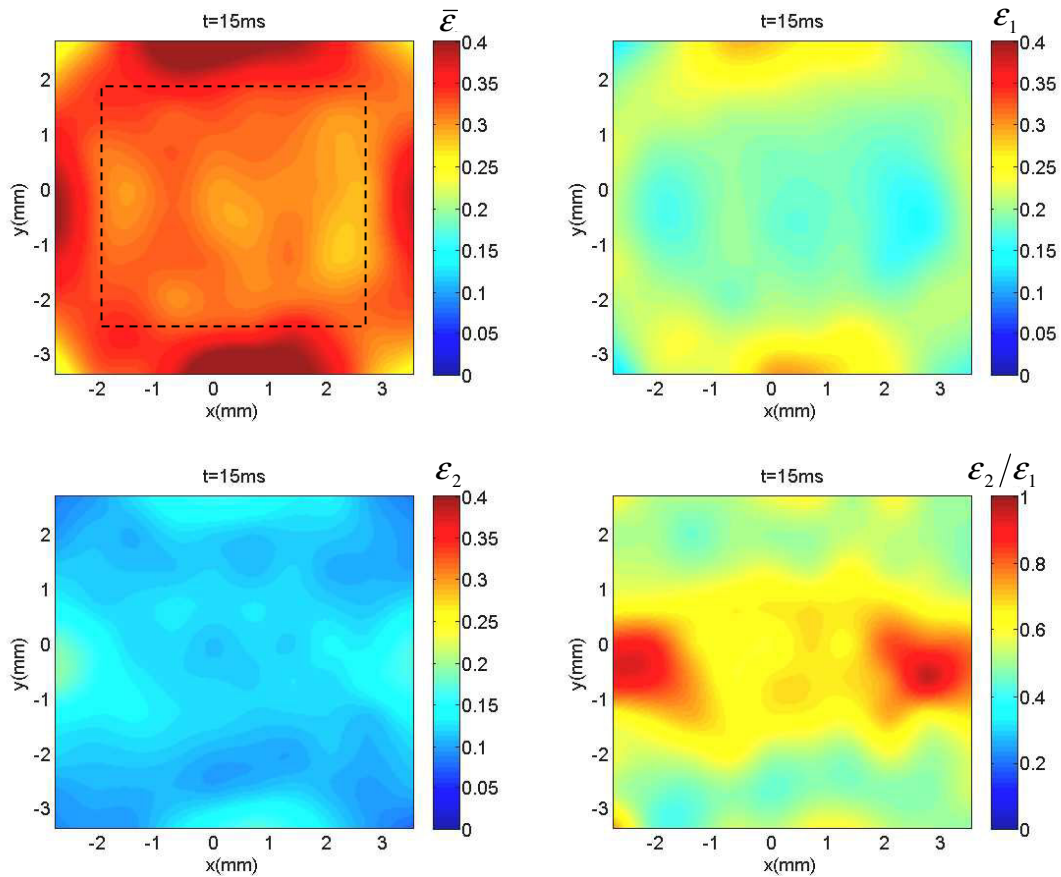


Fig. 4-29 Equivalent and principal strain fields and strain state at 250mm/s

The average equivalent and principal strain evolutions at the central zone of specimen have been given in Fig. 4-30.

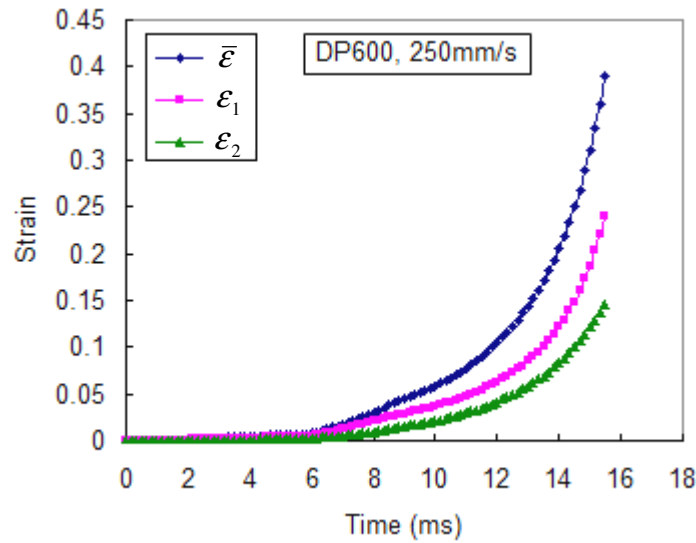


Fig. 4-30 Equivalent, principal strain evolution at the central zone (250mm/s)

The strain path and strain rate evolutions at the central zone are presented in Fig. 4-31. The strain path is changed between $\epsilon_2/\epsilon_1 = 0.4$ and $\epsilon_2/\epsilon_1 = 0.7$ after $t = 7ms$. The strain rate is about $\dot{\bar{\epsilon}} = 20/s$ from $t = 6ms$ to $t = 12ms$.

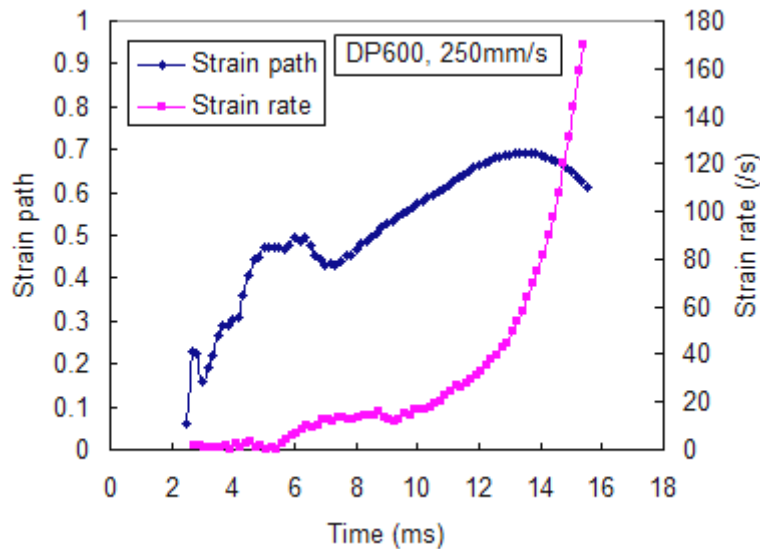


Fig. 4-31 Strain path and strain rate evolution at the central zone (250mm/s)

The experimental forces have been measured (in Fig. 4-32). Although there is a little oscillation at the beginning of test ($8ms \leq t \leq 10ms$), the curves are nearly smooth.

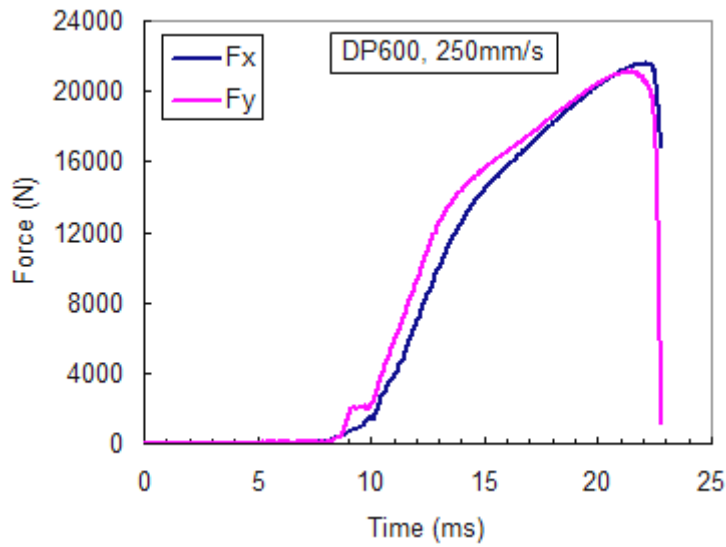


Fig. 4-32 Measured forces along two arms (250mm/s)

The experimental forces along two arms and principal strains at the central point have been pre-processed for parameter identification, as shown in Fig. 4-33. The oscillations of force along axis-x are reduced by a moving average method.

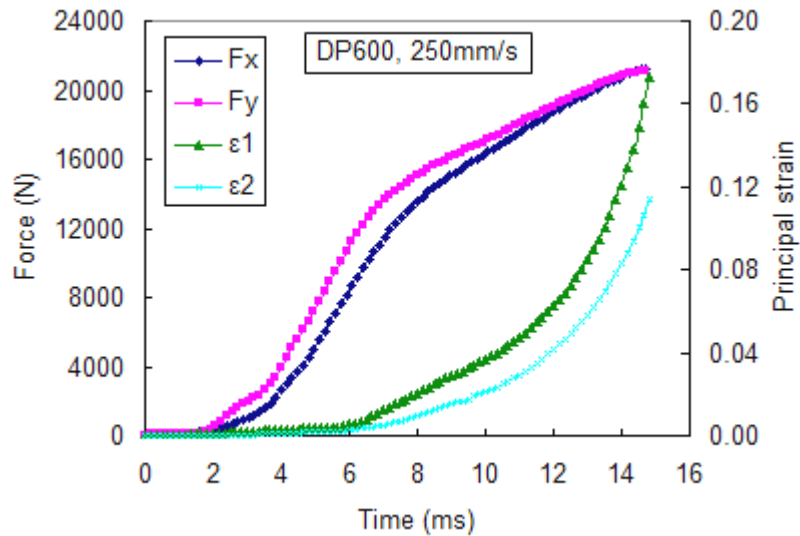


Fig. 4-33 Experimental forces and principal strains for identification (250mm/s)

4.4 Parameter identification of DP600

The biaxial tensile tests of DP 600 have been carried out at different orders of strain rate ($10^{-3} s^{-1}$, $10^{-1} s^{-1}$ and $10^1 s^{-1}$). The experimental forces along the two arms and principal strains at the central point of specimen have been prepared for parameter

identification by inverse analysis based on FE model of biaxial tests. As already presented, the FE model of shell element is adopted.

4.4.1 Material models

For isotropic elasticity of DP600, Young's modulus $E = 200GPa$ and Poisson's ratio $\nu = 0.3$ are considered. The Mises and Hill 48 yield criteria are compared for parameter identification of hardening laws. The parameters of Hill 48 yield criterion have been calculated from three anisotropic coefficients proposed by Ozturk et al. [173], as shown in Table 4-5. These anisotropic coefficients are determined at quasi-static strain rate and strain level $\varepsilon = 0.15$. The shapes of Mises and Hill 48 yield criteria are compared in Fig. 4-34. It is seen that Hill 48 yield locus is outside Mises one.

Table 4-5 Parameters of Hill 48 yield criterion for DP600

Anisotropic coefficients	$r_0 = 0.89, r_{45} = 0.85, r_{90} = 1.12$
Function parameters	$F = 0.4204, G = 0.5291, H = 0.4709, N = 1.2819$

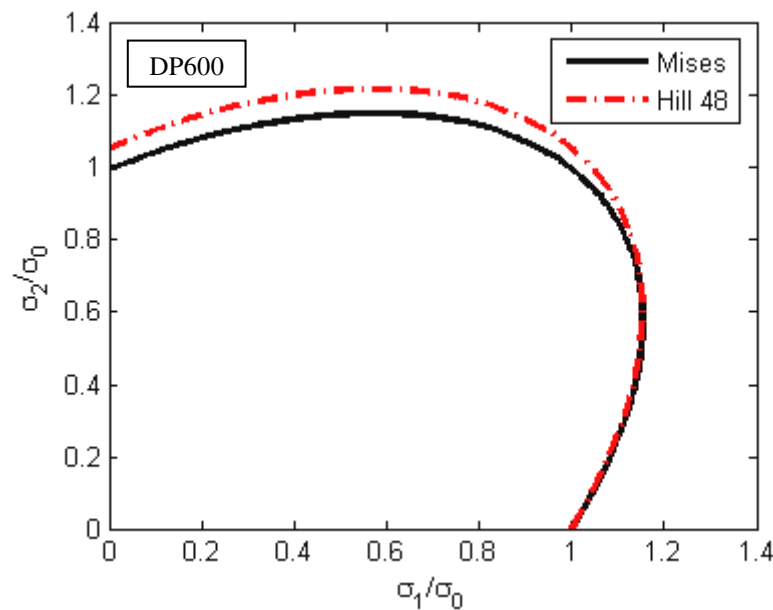


Fig. 4-34 Comparison of yield criteria for DP600

Isotropic hardening model is considered for FE simulation of biaxial tensile tests at different loading velocities. The parameters of yield criteria are supposed to be independent to strain rate and strain level. The adiabatic deformation-induced thermal effects are neglected for hardening law. The hardening laws of Eq. 4-4 (Type_4) on the basis of Ludwick and Voce laws are adopted as follows:

$$\bar{\sigma} = \sigma_0 \dot{\bar{\varepsilon}}^{m_1} + K \bar{\varepsilon}_p^n \dot{\bar{\varepsilon}}^{m_2} \quad \text{Eq. 4-6}$$

$$\bar{\sigma} = \sigma_0 \dot{\bar{\epsilon}}^{m_1} + K(1 - \exp(-n\bar{\epsilon}_p)) \dot{\bar{\epsilon}}^{m_2} \quad \text{Eq. 4-7}$$

4.4.2 Identified results

The optimization process has been performed in modeFRONTIER, in Appendix (V). The cost function is defined by the simulated and experimental principal strains, as given in Eq. 3.6. The results identified on the basis of Mises yield criterion and Ludwick law are given in Table 4-6. The results identified on the basis of Hill 48 yield criterion and Ludwick law are given in Table 4-7. The results identified on the basis of Hill 48 yield criterion and Voce law are given in Table 4-8. Compared with the identified results with Mises yield criterion, better results are obtained with Hill 48 yield criterion. It is seen from these identified models that the influence of strain rate on strain hardening term is more important than that on initial yield stress.

Table 4-6 Identified results of DP600 on basis of Mises and Ludwick

Identified model	$\bar{\sigma} = 354.8\dot{\bar{\epsilon}}^{0.0003} + 871.4\bar{\epsilon}_p^{0.3864}\dot{\bar{\epsilon}}^{0.0251}$						
	0.02mm/s		1mm/s		250mm/s		Average error
Error	$\delta(\epsilon_1)$	$\delta(\epsilon_2)$	$\delta(\epsilon_1)$	$\delta(\epsilon_2)$	$\delta(\epsilon_1)$	$\delta(\epsilon_2)$	
	8.21%	7.64%	14.5%	9.81%	27.7%	7.59%	12.6%

Table 4-7 Identified results of DP600 on basis of Hill 48 and Ludwick

Identified model	$\bar{\sigma} = 339.2\dot{\bar{\epsilon}}^{0.0052} + 839.7\bar{\epsilon}_p^{0.3864}\dot{\bar{\epsilon}}^{0.0158}$						
	0.02mm/s		1mm/s		250mm/s		Average error
Error	$\delta(\epsilon_1)$	$\delta(\epsilon_2)$	$\delta(\epsilon_1)$	$\delta(\epsilon_2)$	$\delta(\epsilon_1)$	$\delta(\epsilon_2)$	
	7.00%	8.45%	13.4%	7.72%	9.18%	6.38%	8.69%

Table 4-8 Identified results of DP600 on basis of Hill 48 and Voce

Identified model	$\bar{\sigma} = 437.9\dot{\bar{\epsilon}}^{0.0032} + 446.2(1 - \exp(-8.2412\bar{\epsilon}_p))\dot{\bar{\epsilon}}^{0.0245}$						
	0.02mm/s		1mm/s		250mm/s		Average error
Error	$\delta(\epsilon_1)$	$\delta(\epsilon_2)$	$\delta(\epsilon_1)$	$\delta(\epsilon_2)$	$\delta(\epsilon_1)$	$\delta(\epsilon_2)$	
	7.99%	9.76%	10.37%	8.91%	11.2%	9.53%	9.63%

The simulated principal strains at the central point of specimen have been compared with the experimental curves, as shown in Fig. 4-35, Fig. 4-36 and Fig. 4-37.

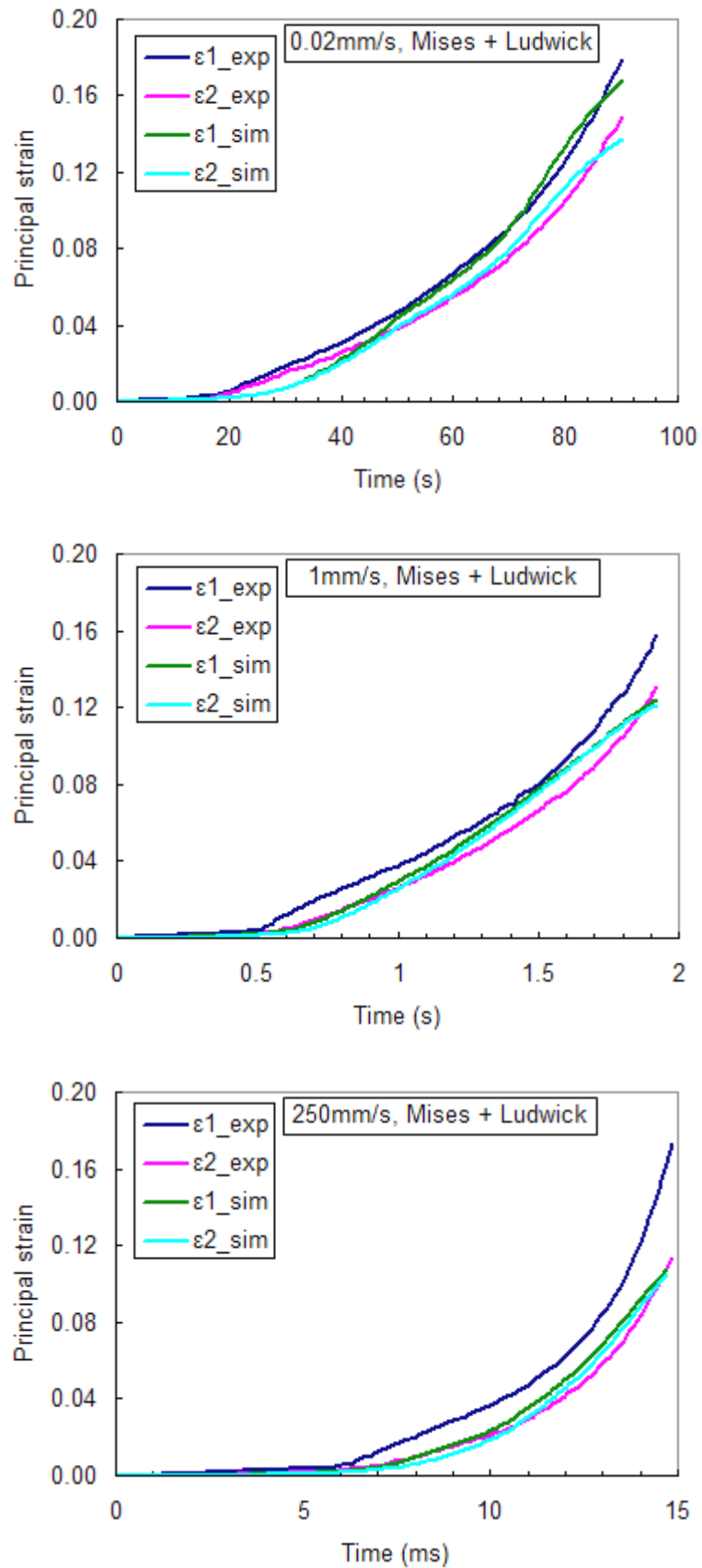


Fig. 4-35 Comparison of experimental and simulated principal strains (Mises + Ludwick)

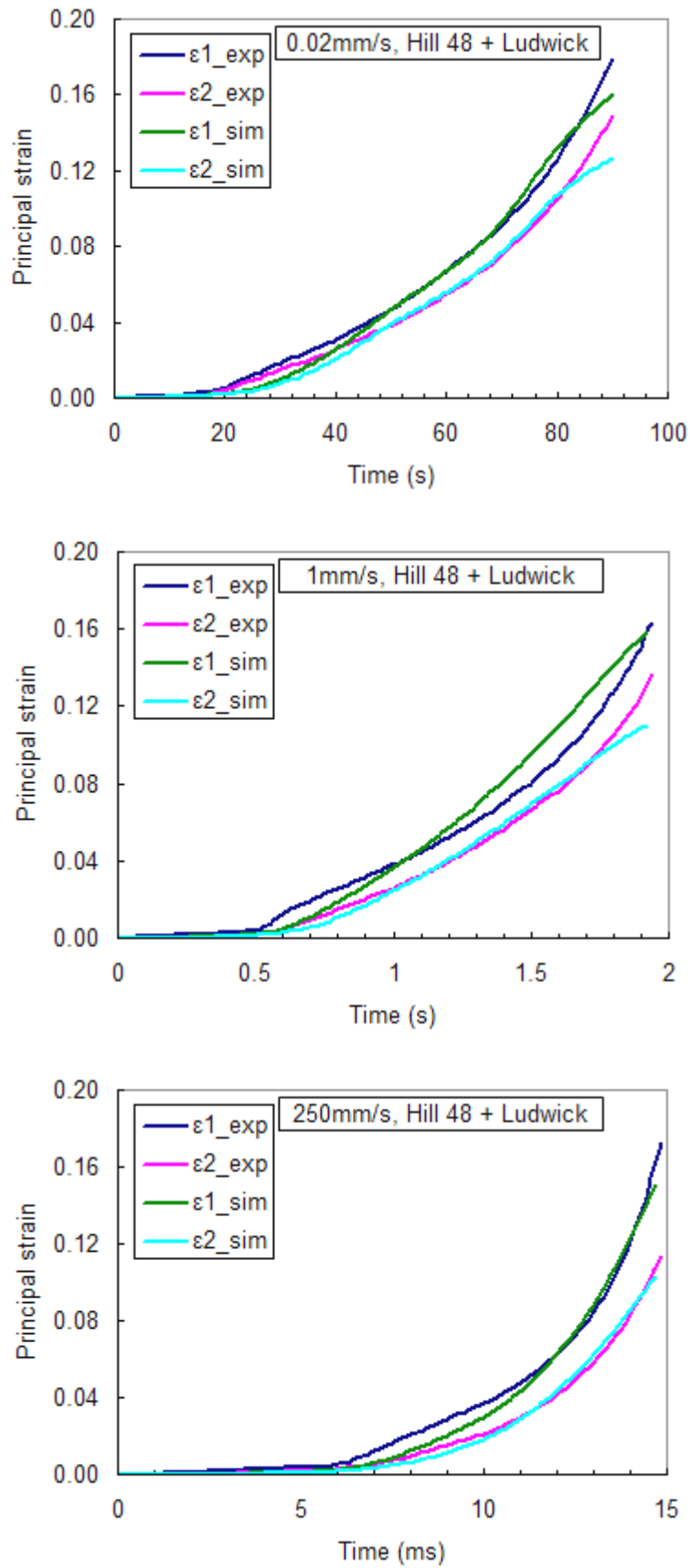


Fig. 4-36 Comparison of experimental and simulated principal strains (Hill 48 + Ludwick)

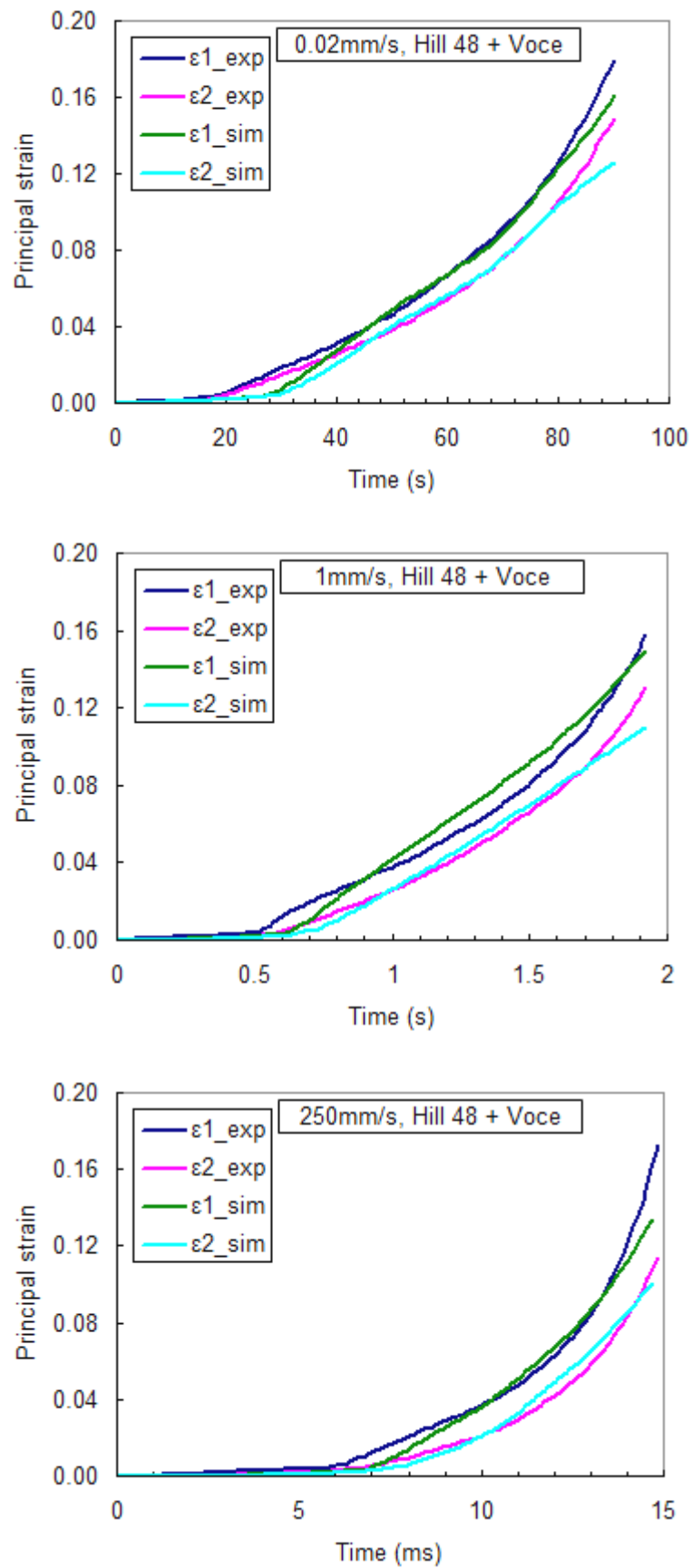


Fig. 4-37 Comparison of experimental and simulated principal strains (Hill 48 + Voce)

It can be seen that Mises yield criterion is not well adapted to describe the evolutions of principal strains, especially at the speeds of 1mm/s and 250mm/s . Nevertheless, the simulated principal strains are lower than the experimental ones at the beginning of biaxial tests. The observed trends of major and minor principal strains simulated with Hill 48 yield criterion are in good agreement with the experimental ones for large strains (above 4%).

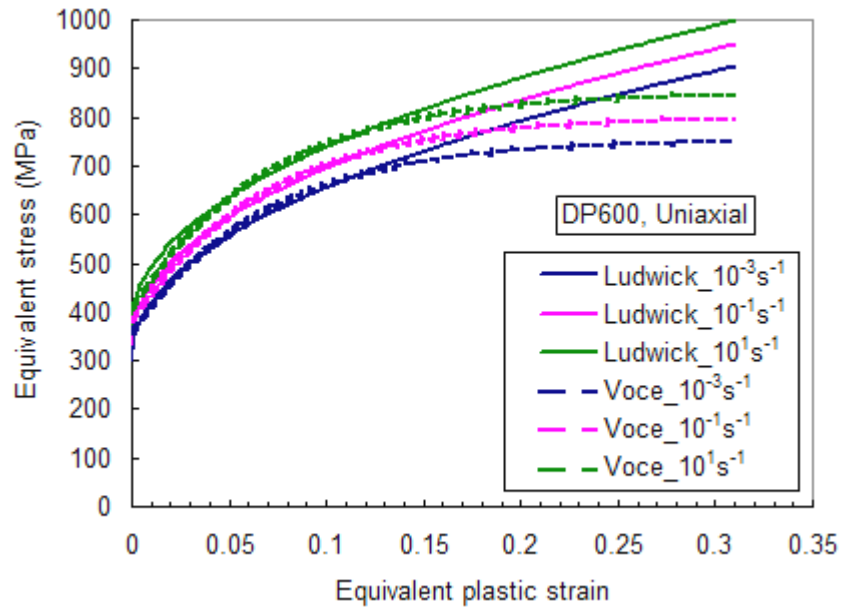


Fig. 4-38 Strain-rate dependent hardening laws identified by uniaxial tests

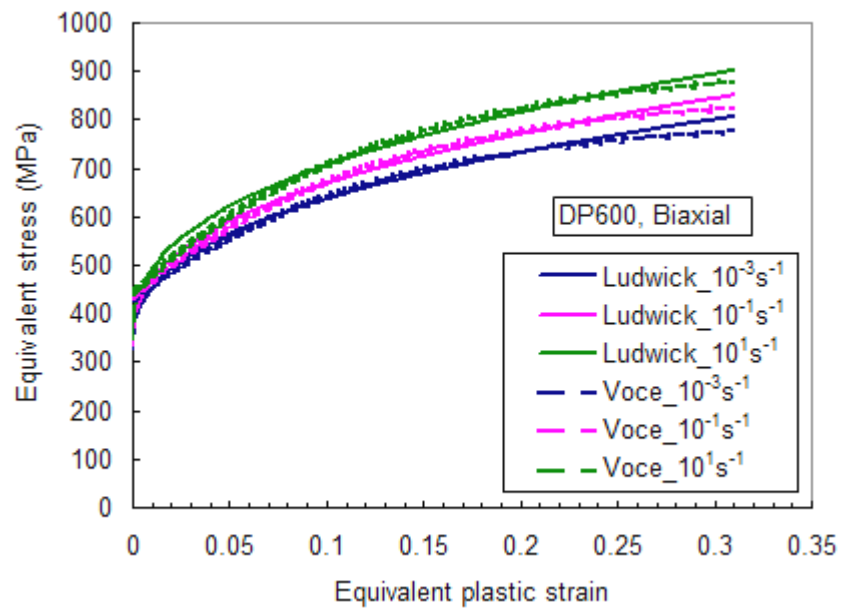


Fig. 4-39 Strain-rate dependent hardening laws identified by biaxial tests

The uniaxial flow stress curves identified with two strain-rate dependent hardening laws (Ludwick_4 and Voce_4) are compared at different strain rates of $10^{-3} s^{-1}$, $10^{-1} s^{-1}$ and $10^1 s^{-1}$, as shown in Fig. 4-38. The parameters of these hardening laws are identified by the uniaxial tensile tests. It is seen that the flow stress curves on the basis of Ludwick law become much higher than those on the basis of Voce law, after an equivalent plastic strain of 15%. Therefore, the uniaxial tests do not permit to identify an appropriate hardening law for large strains (higher than 15%).

The biaxial flow stress curves identified with two strain-rate dependent hardening laws on the basis of Ludwick and Voce models are also compared in Fig. 4-39. The parameters of these hardening laws are identified based on the FE model with Hill 48 yield criterion. It is seen that the strain rate sensitivities of uniaxial and biaxial flow stress curves are identical. Therefore, the dynamic biaxial tensile tests are validated to identify strain-rate hardening laws. The biaxial flow stress curves are relatively close for each strain rate until the equivalent plastic strain of about 30%. It clearly shows that the biaxial tensile tests permit a better hardening identification for large strains.

4.5 Conclusion

The strain-rate dependent hardening behaviour of DP600 has been investigated by uniaxial tensile tests at different strain rates ($\dot{\epsilon} = 0.02 s^{-1}$, $2 s^{-1}$, $10 s^{-1}$ and $20 s^{-1}$). Based on the experimental data, it is found that DP 600 exhibits a positive strain rate sensitivity. Ludwick or Voce laws have been adopted to describe the strain hardening effect and simple power law has been used to represent the strain rate sensitivity. Finally, four multiplicative types of strain-rate dependent hardening laws have been compared to characterize the hardening behaviour of DP600 at room temperature.

Quasi-static and dynamic biaxial tensile tests on cruciform specimens are performed at different loading speeds of $0.02 mm/s$, $1 mm/s$ and $250 mm/s$. Inverse analysis based on FE model has been applied for parameter identification of hardening laws with strain rate sensitivity. By comparison of uniaxial and biaxial flow stress curves at strain rates of $10^{-3} s^{-1}$, $10^{-1} s^{-1}$ and $10^1 s^{-1}$, it is more beneficial of biaxial tensile tests to identify strain-rate dependent hardening behaviour up to large strains.

Conclusions and perspectives

The objective of this thesis was to propose quasi-static and dynamic biaxial tensile tests on flat cruciform specimen to identify strain-rate dependent hardening models of sheet metals from quasi-static to intermediate strain rates. The in-plane biaxial testing procedures and parameter identification strategy have been validated on AA5086 and applied to identify rate-dependent hardening laws for DP600 steel.

The main contributions of this work can be summarized as follows:

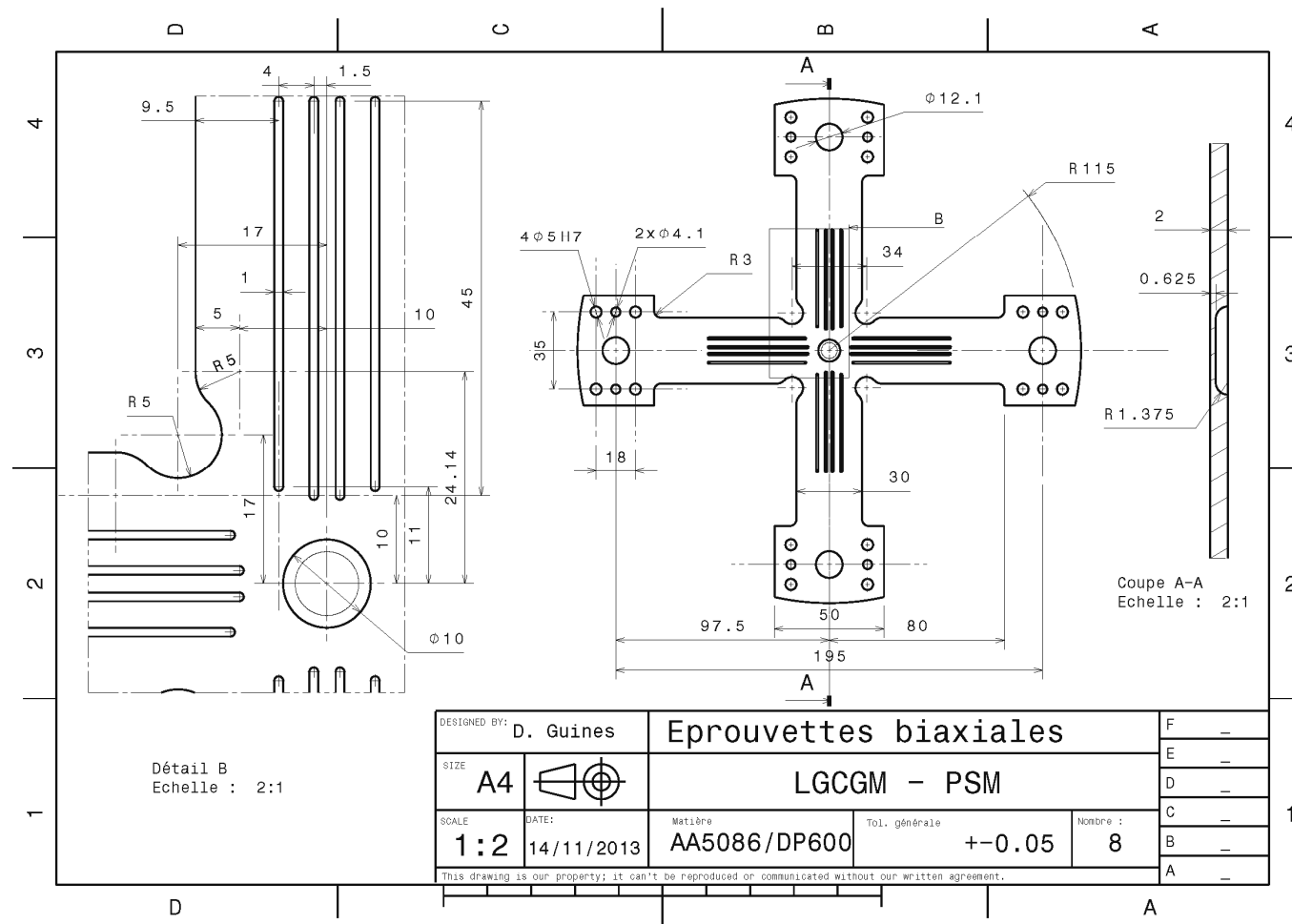
- ✓ A cruciform shape has been successfully designed to obtain large equivalent plastic strains (up to 30%) at the central zone of specimen under biaxial tensile strain path. Specific notches at the intersections of arms, slits in each arm and thickness reduction at the central zone are adopted. As expected, the initial cracks of tested specimens are always observed at the central zone.
- ✓ The parameters of hardening laws are identified by inverse analysis based on a FE model of the test. The experimental forces are applied on the arms of FE model. The simulated principal strains at the central zone are compared with experimental results to optimize the material parameters. By comparison of the identified biaxial flow stress curves with the uniaxial flow stress curves, this parameter identification strategy has been validated.
- ✓ Three yield criteria are compared to identify the parameters of hardening laws for quasi-static biaxial tensile test on AA5086. The biaxial flow stress curve identified with advanced anisotropic yield function of Bron and Besson 2004 coincides with the uniaxial flow stress curve. It is shown that the flow stress curve is precise only if an appropriate yield function is preliminarily chosen.
- ✓ Dynamic biaxial tensile tests on cruciform specimen have been carried out to identify strain-rate hardening behaviour of sheet metals at intermediate strain rates. Damping layers are adopted to reduce loading ringing.
- ✓ Different strain-rate dependent hardening laws have been identified for DP600 steel by biaxial tensile tests. The biaxial flow stress curves identified on the basis of Ludwick and Voce models are close up to equivalent plastic strains of 30% for each strain rate. The benefits of the proposed methodology are clearly shown since the hardening behaviour is now accurately known for an equivalent strain level of 30%.

In the future, several perspectives are suggested as following:

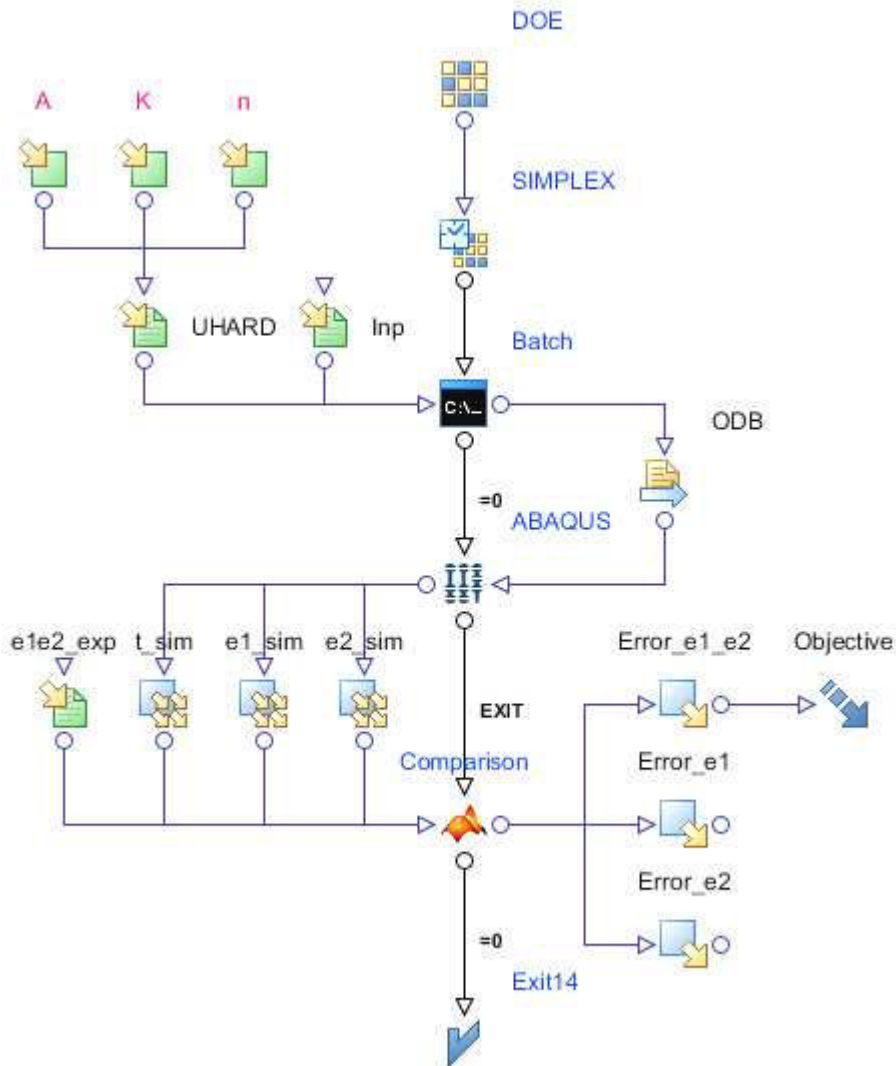
- In this work, only the principal strains at the central zone of cruciform specimen under equi-biaxial path are used for parameter identification of hardening law. If some parameters of the yield criterion are preliminarily unknown, more experimental data under different strain paths can be adopted for inverse analysis to identify all the parameters of constitutive models simultaneously. It could be also interesting to evaluate the influence of strain path on the identified results of hardening law.
- Many other hardening models in the literature can be used for identification of hardening behaviour. As seen in literature, a mixed type of Ludwick and Voce laws is certainly more precise to identify hardening behaviour up to large strains.
- When the deformation level is elevated, the evolution of microstructure and textures in sheet metals may change the parameters of yield functions. Therefore, the effects of strain level on the subsequent yield surface need further study^[174]^[175]^[176]^[177]. The effects of strain rate on the initial yield surfaces are also very interesting^[178]^[179]. The yield functions, which consider the influences of strain level and strain rate, will be more accurate to identify strain-rate dependent hardening models up to large strains.
- Because successive nonlinear deformation path can be realised by biaxial tensile tests on the cruciform specimen, advanced hardening models, like kinematical combined models, could be identified by the proposed methodology.

A. Appendix

(I) Drafting of cruciform specimen



(II) modeFRONTIER flowchart with subroutine UHARD

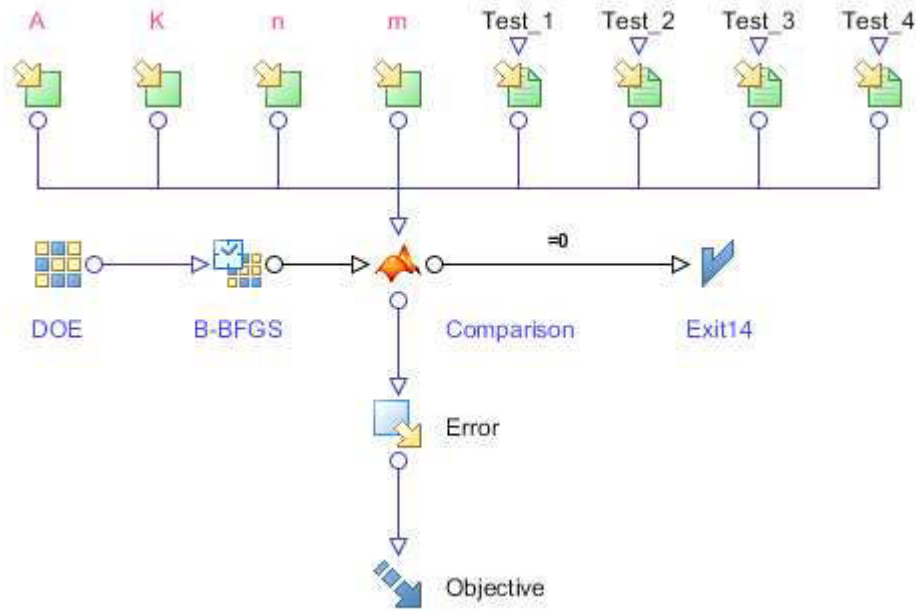


For the user subroutine UHARD of rate-independent hardening law, the yield stress $\bar{\sigma}$ and variation of yield stress with respect to the equivalent plastic strain $\partial\bar{\sigma}/\partial\bar{\epsilon}_p$ are respectively given as follows:

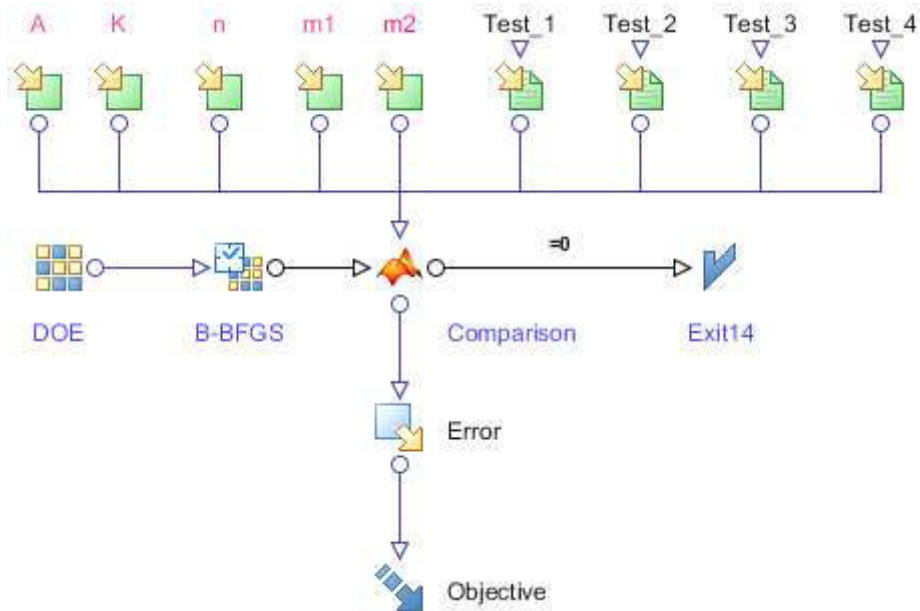
$$\bar{\sigma} = \sigma_0 + K\sqrt{1 - \exp(-n\bar{\epsilon}_p)} \quad \text{Eq. 0-1}$$

$$\frac{\partial\bar{\sigma}}{\partial\bar{\epsilon}_p} = \frac{K \cdot n \cdot \exp(-n\bar{\epsilon}_p)}{2\sqrt{1 - \exp(-n\bar{\epsilon}_p)}} \quad \text{Eq. 0-2}$$

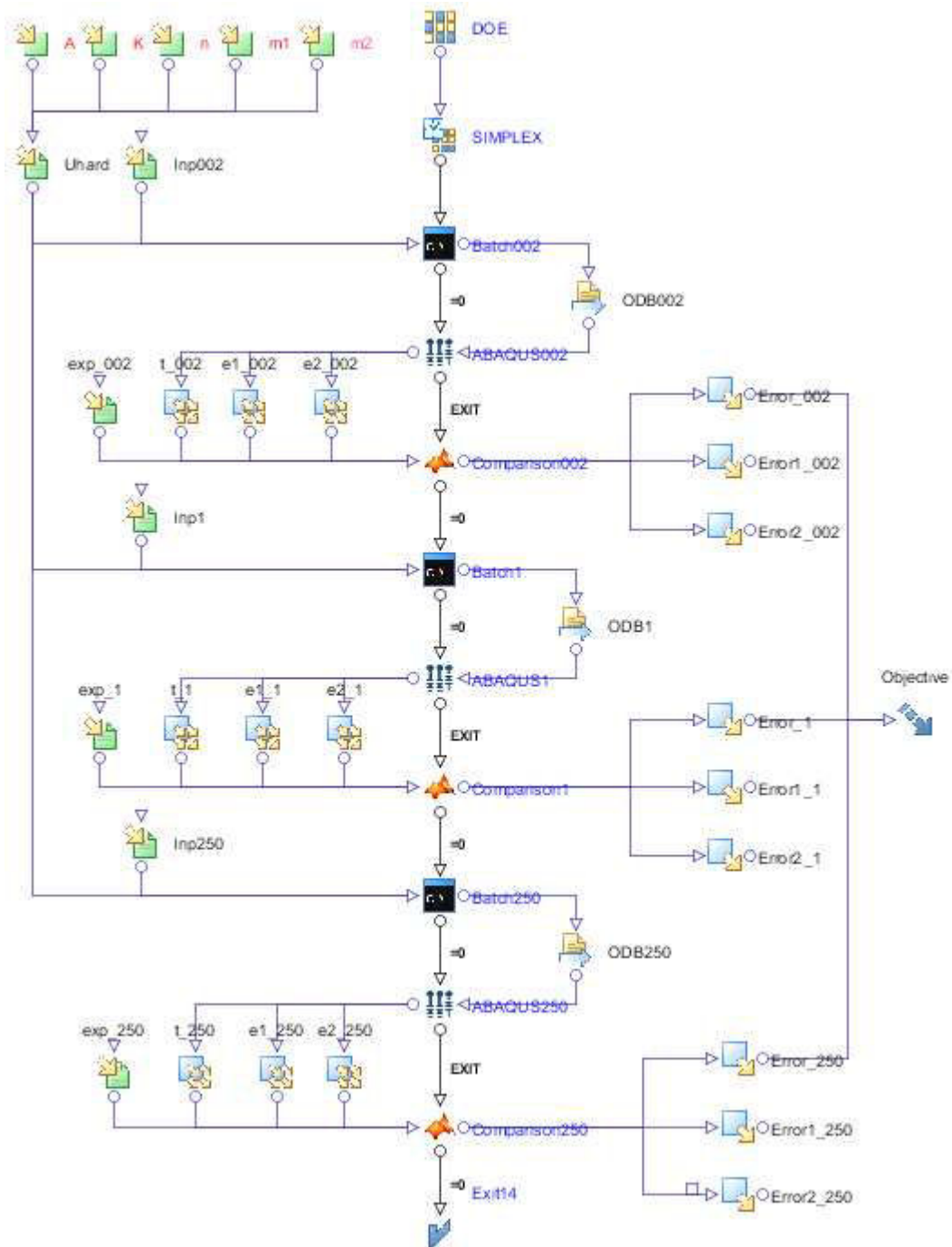
(IV) modeFRONTIER flowchart with SRS by uniaxial tensile tests



(a) For hardening laws of type 1, 2, 3



(b) For hardening laws of type 4

(V) modeFRONTIER flowchart with SRS by biaxial tensile tests

References

- [1] I. Islamoff; Metal forming techniques; Technology utilization report, National aeronautics and space administration (NASA), (1965)
- [2] A. Col; L'emboutissage des aciers; Dunod, Paris (2010) ISBN 978-2-10-0550975
- [3] M. Berveiller; Contribution à la modélisation la mise en forme des tôles métalliques: application au retour élastique et à la localisation; Thèse de doctorat, École Nationale Supérieure d'Arts et Métiers, (2007)
- [4] A. Govik , L. Nilsson, Ramin Moshfegh; Finite element simulation of the manufacturing process chain of a sheet metal assembly; Journal of Materials Processing Technology, 212 (2012) 1453– 1462
- [5] David L. McDowell; A perspective on trends in multiscale plasticity; International Journal of Plasticity 26 (2010) 1280–1309
- [6] T. Boogaard; Thermally enhanced forming of aluminium sheet: modelling and experiments; PhD thesis, University of Twente, (2001)
- [7] M. Rabahallah; Modélisation de l'anisotropie plastique et application à la mise en forme des tôles métalliques; Thèse de doctorat, Université Paul Verlaine de Metz, 2007
- [8] K. Domkin; Constitutive models based on dislocation density: Formulation and implementation into finite element codes; Doctoral thesis, Luleå University of Technology, 2005
- [9] T. Meinders, E. Perdahcioglu, M. Riel, H. Wisselink; Numerical modeling of advanced materials; International Journal of Machine Tools & Manufacture, 48 (2008) 485–498
- [10] Z. Marciniak, J. Duncan, S. Hu; Mechanics of sheet metal forming; Edward Arnold, London (1992) ISBN 0 7506 5300 0
- [11] S. Holmberg, B. Enquist, P. Thilderkvist; Evaluation of sheet metal formability by tensile tests; Journal of Materials Processing Technology, 145 (2004) 72–83
- [12] V. Van; Strain path dependency in sheet metal: Experiments and models; University of Twente, Doctoral thesis, (2009)
- [13] R. Verma, T. Kuwabara, K Chung, A. Haldar; Experimental evaluation and constitutive modeling of non-proportional deformation for asymmetric steels; International Journal of Plasticity, 27 (2011) 82–101
- [14] L. Lang, Z. Wang, D. Kang; Hydroforming highlights: sheet hydroforming and tube hydroforming; Journal of Materials Processing Technology, 151 (2004) 165–177
- [15] C. Hartl, Research and advances in fundamentals and industrial applications of hydroforming; Journal of Materials Processing Technology, 167 (2005) 383–392

- [16] S. Oh, B. Jeon, H. Kim, J. Yang; Applications of hydroforming processes to automobile parts; *Journal of Materials Processing Technology*, 174 (2006) 42–55
- [17] W. Emmens, G. Sebastiani, A. Boogaard; The technology of Incremental Sheet Forming—A brief review of the history; *Journal of Materials Processing Technology*, 210 (2010) 981–997
- [18] G. Zittel; A historical review of high speed metal forming; 4th International Conference on High Speed Forming (2010)
- [19] V. Psyk, D. Risch, B. Kinsey, A. Tekkaya, M. Kleiner; Electromagnetic forming —A review; *Journal of Materials Processing Technology*, 211 (2011) 787–829
- [20] Y. Chu, R. Lee, V. Psyk, A. Tekkaya; Determination of the flow curve at high strain rates using electromagnetic punch stretching; *Journal of Materials Processing Technology*, 212 (2012) 1314– 1323
- [21] T. Altan, A. Tekkaya; Sheet metal forming: processes and applications; ASM International (2012) ISBN 978-1-61503-844-2
- [22] J. Sung, J. Kim, R. Wagoner; A plastic constitutive equation incorporating strain, strain-rate, and temperature; *International Journal of Plasticity*, 26 (2010) 1746–1771
- [23] T. Belytschko, W. Liu, B. Moran; *Nonlinear Finite Elements for Continua and Structures*; Wiley, (2000)
- [24] M. Michno, W. Findley; An historical perspective of yield surface investigations for metals; *International Journal of Non-linear Mechanics*, 11 (1976) 59-82
- [25] M. Teaca; *Caractérisation expérimental et modélisation de la déformation plastique des tôles métalliques*; Thèse de doctorat, Université Paul Verlaines-Metz, (2009)
- [26] A. Phillips, R. Sierakowski; On the concept of the yield surface; *Acta Mechanica*, 1 (1965) 29-35
- [27] D. Banabic; *Sheet metal forming processes: constitutive modelling and numerical simulation*; Springer 2010
- [28] J. Yoon, F. Barlat, R. Dick, M. Karabin; Prediction of six or eight ears in a drawn cup based on a new anisotropic yield function; *International Journal of Plasticity*, 22 (2006) 174–193
- [29] F. Barlat, J. Brem, J. Yoon et al; Plane stress yield function for aluminum alloy sheets—part 1: theory; *International Journal of Plasticity*, 19 (2003) 1297–1319
- [30] F. Barlat, H. Artez, J. Yoon, et al.; Linear transformation-based anisotropic yield functions; *International Journal of Plasticity*, 21 (2005) 1009–1039
- [31] D. Banabic, H. Artez, D.S. Comsa et al; An improved analytical description of orthotropy in metallic sheets; *International Journal of Plasticity*, 21 (2005) 493–512
- [32] F. Bron, J. Besson; A yield function for anisotropic materials: Application to aluminum alloys; *International Journal of Plasticity*, 20 (2004) 937–963
- [33] J. Lemaitre, J. Chaboche; *Mécanique des matériaux solides*; Dunod (1996)

-
- [34] A. Gavrus; Constitutive equation for description of metallic materials behavior during static and dynamic loadings taking into account important gradients of plastic deformation; *Key Engineering Materials*, 504-506 (2012) 697-702
- [35] X. Chu, Caractérisation expérimental et prédiction de la formabilité d'un alliage d'aluminium en fonction de la température et de la vitesse de déformation; Thèse de doctorat, INSA de Rennes, 2013
- [36] H. Huh, K. Ahn, J. Lim, H. Kim, L. Park; Evaluation of dynamic hardening models for BCC, FCC, and HCP metals at a wide range of strain rates; *Journal of Materials Processing Technology*, 214 (2014) 1326–1340
- [37] S. Paul, A. Raj, P. Biswas, G. Manikandan, R. Verma; Tensile flow behavior of ultra low carbon, low carbon and micro alloyed steel sheets for auto application under low to intermediate strain rate; *Materials and Design*, 57 (2014) 211–217
- [38] F. Zerilli, R. Armstrong; Dislocation mechanics based constitutive relations for material dynamics calculations; *Journal of Applied Physics*, 61 (1987) 1816
- [39] H. Yu, Y. Guo, K Zhang et al Constitutive model on the description of plastic behavior of DP600 steel at strain rate from 10^{-4} to 10^3 s⁻¹; *Computational Materials Science*, 46 (2009) 36–41
- [40] A. Khan, S. Huang; Experimental and theoretical study of mechanical behavior of 1100 aluminum in the strain rate range 10^{-5} - 10^4 s⁻¹ ; *International Journal of Plasticity*, 8 (1992) 397-424
- [41] M. Lin, R. Wagoner; An experimental investigation of deformation induced heating during tensile testing; *Metallurgical Transactions A* , 18 (1987) 1035-1042
- [42] H. Zhao; A constitutive model for metals over a large range of strain rates: Identification for mild-steel and aluminum sheets; *Materials Science and Engineering A*, 230 (1997) 95-99
- [43] A. Khan, R. Liang; Behaviors of three BCC metal over a wide range of strain rates and temperatures: experiments and modeling; *International Journal of Plasticity*, 15 (1999) 1089-1109
- [44] A. Rusinek, R. Zaera, J.R. Klepaczko; Constitutive relations in 3-D for a wide range of strain rates and temperatures – Application to mild steels; *International Journal of Solids and Structures*, 44 (2007) 5611–5634
- [45] J. Sung, J. Kim, R. Wagoner; A plastic constitutive equation incorporating strain, strain-rate, and temperature; *International Journal of Plasticity*, 26 (2010) 1746–1771
- [46] S. Paul; Predicting the flow behavior of metals under different strain rate and temperature through phenomenological modeling; *Computational Materials Science*, 65 (2012) 91–99
- [47] S. Diot; Caractérisation expérimentale et numérique du comportement dynamique des matériaux; Thèse de doctorat, INSA de Rennes, (2003)
- [48] S. Bruschi, T. Altan, D. Banabic et al; Testing and modelling of material behaviour and formability in sheet metal forming; *CIRP Annals - Manufacturing Technology*, 63 (2014) 727–749
-

- [49] P. Manach; Lois de comportement et mise en forme des matériaux métalliques; Thèse de HDR, Université de Bretagne sud, (2004)
- [50] R. Larsson; On material modelling of high strength steel sheets;, Linköping University, Dissertations, (2012)
- [51] K. Chen, J. Lin; Material Modeling and Correlative Mechanical Testing on AHSS Sheet Forming Simulation; *Advanced Materials Research*, 337 (2011) 198-202
- [52] J. Field, S. Walley, W. Proud, et al. Review of experimental techniques for high rate deformation and shock studies; *International Journal of Impact Engineering*, 30 (2004) 725–775
- [53] Metallic materials -- Tensile testing -- Part 1: Method of test at room temperature; ISO/DIS 6892-1
- [54] ASTM E8 / E8M - 13a; Standard Test Methods for Tension Testing of Metallic Materials; (2013)
- [55] M.Borsutzki, D. Cornette, Y Kuriyama et al.; Recommendations for dynamic tensile testing of sheet steels; *International iron and steel institute*, (2005)
- [56] S. Kim, J. Song, H. Huh, J. Lim; Dynamic tensile test and specimen design of auto-body steel sheet at the intermediate strain rate; *Transactions on Engineering Sciences*, 57 (2007) 319-328
- [57] H. Huh, J. Lim, S. Park; High speed tensile tests of steel sheets for the stress-strain curve at the intermediate strain rate, *International Journal of Automotive Technology*, 10(2009)195-204
- [58] A. Gilat, T. Matrka; A New Compression Intermediate Strain Rate Testing Apparatus; *EPJ Web of Conferences* 6, 39002 (2010)
- [59] R. Othman, P Guégan, G. Challita, F. Pasco, D. LeBreton; A modified servo-hydraulic machine for testing at intermediate strain rates; *International Journal of Impact Engineering*, 36 (2009) 460-467
- [60] P. Wood, C. Schley; Strain rate testing of metallic materials and their modeling for use in CAE based automotive crash simulation tools (Recommendations and procedures); (2009) ISBN 9781847353740
- [61] J. Fitoussi F. Meraghni, Z. Jendi, et al.; Experimental methodology for high strain-rates tensile behaviour analysis of polymer matrix composites; *Composites Science and Technology*, 65 (2005) 2174–2188
- [62] B. Boyce, M. Dilmore; The dynamic tensile behavior of tough, ultrahigh-strength steels at strain-rates from 0.0002 s^{-1} to 200 s^{-1} ; *International Journal of Impact Engineering*, 36 (2009) 263–271
- [63] X. Xiao; Dynamic tensile testing of plastic materials; *Polymer Testing*, 27 (2008) 164–178
- [64] S. Diot, D. Guines, A. Gavrus, E. Ragneau; Two-step procedure for identification of metal behavior from dynamic compression tests; *International Journal of Impact Engineering*, 34 (2007) 1163-1184

-
- [65] D. Zhu, B. Mobahser, S. Rajan, et al ; Characterization of dynamic tensile testing using aluminum alloy 6061-T6 at intermediate strain rates; *Journal of Engineering Mechanics*, 137 (2011) 669-679
- [66] D. Zhu, S. Rajan, B. Mobasher, et al; Modal analysis of a servo-hydraulic high speed machine and its application to dynamic tensile testing at an intermediate strain rate; *Experimental Mechanics*, 51(2010) 1347-1363
- [67] W. Chen, B. Song; *Split Hopkinson (Kolsky) bar: design, testing and applications*; Springer (2011) ISBN 978-1-4419-7981-0
- [68] M. Quik, K. Labibes, C. Albertini, T. Valentin, P. Magain. Dynamic mechanical properties of automotive thin sheet steel in tension, compression and shear. *Journal de Physique IV*, (1997) 379-384
- [69] M. Khlif; *Adaptation d'un banc d'essai Charpy à la traction rapide des polymères*; Thèse de doctorat, L'École National d'Ingénieurs de Sfax, (2010)
- [70] G. Gutscher, H. Wu, G. Ngaile, T. Altan; Determination of flow stress for sheet metal forming using the viscous pressure bulge (VPB) test; *Journal of Materials Processing Technology*, 146 (2004) 1–7
- [71] F. Abu-Farha, N. Shuaib, M. Khraisheh, K. Weinmann; Limiting strains of sheet metals obtained by pneumatic stretching at elevated temperatures; *CIRP Annals - Manufacturing Technology*, 57 (2008) 275–278
- [72] S. Dziallach, W. Bleck, M. Blumbach, et al; Sheet metal testing and flow curve determination under multiaxial conditions; *Advanced engineering materials*, 9 (2007) 987-994
- [73] L. Lazarescu, D. Comsa, I. Nicodim, et al; Characterization of plastic behaviour of sheet metals by hydraulic bulge test; *Transactions of Nonferrous Metals Society of China* 22(2012) 275-279
- [74] M. Atkinson; Accurate determination of biaxial stress-strain relationships from hydraulic bulging tests of sheet metals; *International Journal of Mechanical Science*; 39 (1997) 761-769
- [75] V. Grolleau, G. Gary, D. Mohr ; Biaxial testing of sheet materials at high strain rates using viscoelastic bars; *Experimental Mechanics*, 48(2008) 293–306
- [76] A. Penin; *Etude sous chargement dynamique biaxial d'une tôle en acier DP450 : influence sur le comportement et la formabilité*; Thèse de doctorat, Université de Bretagne Sud, (2010)
- [77] M. Ramezani, Z. Ripin; Combined experimental and numerical analysis of bulge test at high strain rates using split Hopkinson pressure bar apparatus; *Journal of Materials Processing Technology*, 210 (2010) 1061 – 1069
- [78] Y. An , H. Vegter, A novel and simple method for the measurement of plane strain work hardening; *Journal of Materials Processing Technology*, 155–156 (2004) 1616–1622
- [79] R. Wagoner, N. Wang; An experimental and analytical investigation of in-plane deformation of 2036-T4 aluminum sheet; *International Journal of Mechanical Sciences*, 21(1979) 255–264
- [80] R. Wagoner; Measurement and analysis of plane-strain work hardening;
-

- Metallurgical transaction A, 11 (1980) 165-175
- [81] R. Wagoner; Comparison of plane-strain and tensile work hardening in two sheet steel alloys; Metallurgical transaction A, 12 (1981) 877-882
- [82] P. Flores, V. Tuninetti, G. Gilles, et al.; Accurate stress computation in plane strain tensile tests for sheet metal using experimental data; Journal of Materials Processing Technology, 210 (2010) 1772–1779
- [83] T. Kuwabara; Advances in experiments on metal sheets and tubes in support of constitutive modeling and forming simulations; International Journal of Plasticity, 23 (2007) 385–419
- [84] K. Miyauchi; Deformation path effect on stress-strain relation in sheet metals; Journal of Materials Processing Technology, 34 (1992) 195-200
- [85] S. Bouvier, H. Haddadi, P. Levee, et al; Simple shear tests: Experimental techniques and characterization of the plastic anisotropy of rolled sheets at large strains; Journal of Materials Processing Technology, 172 (2006) 96–103
- [86] Y. An, H. Vegter; Development of simple shear test for the measurement of work hardening; Journal of Materials Processing Technology, 209 (2009) 4248–4254
- [87] Standard Test Method for Shear Testing of Thin Aluminum Alloy Products; ASTM B831-11 (2011)
- [88] Q. Yin, B. Zillmann, S. Suttner, G. Gerstein; An experimental and numerical investigation of different shear test configurations for sheet metal characterization; International Journal of Solids and Structures, 51 (2014) 1066–1074
- [89] A. Rusinek, J. Klepaczko; Shear testing of a sheet steel at wide range of strain rates and a constitutive relation with strain-rate and temperature dependence of the flow stress; International Journal of Plasticity, 17 (2001) 87-115
- [90] T. Kuwabara; Advanced in experiments on metal sheets and tubes in support of constitutive modeling and forming simulations; International Journal of Plasticity, 23 (2007) 382-419
- [91] R. Hill, S. Hecker, M. Stout; An investigation of plastic flow and differential work hardening in orthotropic brass tubes under fluid pressure and axial load. International Journal of Solids and Structures, 31(1994) 2999–3021
- [92] T. Sokolowski, K. Gerke, M. Ahmetoglu, T. Altan; Evaluation of tube formability and material characteristics: hydraulic bulge testing of tubes; Journal of Materials Processing Technology, 98 (2000) 34-40
- [93] M. Koc, Y. Aue-u-lan, T. Altan et al.; On the characteristics of tubular materials for hydroforming — experimentation and analysis; International Journal of Machine Tools & Manufacture, 41(2001) 761–772
- [94] G. Liu, Y. Wu, J. Zhao, K. Wang, S. Yuan; Formability determination of titanium alloy tube for high pressure pneumatic forming at elevated temperature; Procedia Engineering, 81 (2014) 2243–2248
- [95] T. Hakoyama, T. Kuwabara; Biaxial tensile test of high strength steel sheet for large plastic strain range; Key Engineering Materials, 504-506 (2012) 59-64

-
- [⁹⁶] T. Kuwabara, K. Yoshida, K. Narihara, S. Takahashi; Anisotropic plastic deformation of extruded aluminum alloy tube under axial forces and internal pressure; *International Journal of Plasticity*, 21 (2005) 101–117
- [⁹⁷] K. Yoshida, T. Kuwabara; Effect of strain hardening behavior on forming limit stresses of steel tube subjected to non proportional loading paths; *International Journal of Plasticity* 23 (2007) 1260–1284
- [⁹⁸] H. Pijlman; Sheet material characterisation by multi-axial experiments; Doctoral thesis, University of Twente, 2001
- [⁹⁹] P. Flores, F. Bonnet, A. Habraken; Plane Strain Test for Metal Sheet Characterization; *Key Engineering Materials* 344 (2007) 135-142
- [¹⁰⁰] P. Flores, L. Duchene, C. Bouffioux, et al.; Model identification and FE simulations: Effect of different yield loci and hardening laws in sheet forming; *International Journal of Plasticity* 23 (2007) 420–449
- [¹⁰¹] D. Mohr, M. Oswald; A new experimental technique for the multi-axial testing of advanced High strength steel sheets; *Experimental Mechanics*; 48 (2008) 65–77
- [¹⁰²] D. Mohr, J. Jacquemin; Large deformation of anisotropic austenitic stainless steel sheets at room temperature: Multi-axial experiments and phenomenological modeling; *Journal of the Mechanics and Physics of Solids*; 56 (2008) 2935-2956
- [¹⁰³] F. Pierron, M. Grédiac; The virtual fields method: Extracting constitutive mechanical parameters from full-field deformation measurements; Springer (2012) ISBN 978-1-4614-1823-8
- [¹⁰⁴] D. Lecompte, A. Smits, H. Sol, et al; Mixed numerical-experimental technique for orthotropic parameter identification using biaxial tensile tests on cruciform specimens; *International Journal of Solids and Structures*, 44 (2007) 1643-1656
- [¹⁰⁵] A. Guner, A. Brosius, A. Tekkaya; Inverse parameter identification of sheet metals utilizing the distribution of field variables; *International Journal of Material Forming*; 2 (2009) 2455-458
- [¹⁰⁶] D. Debruyne, S. Cooreman, P. Lava, et al.; Identification of the plastic material behaviour through inverse modelling and DIC: influence of the specimen's geometry; *Proceedings of the SEM Annual Conference*, (2009) Albuquerque New Mexico USA
- [¹⁰⁷] J. Kim, F. Barlat, F. Pierron, M. Lee; Determination of anisotropic plastic constitutive parameters using the virtual field method; *Experimental Mechanics* 54 (2014) 1189-1204
- [¹⁰⁸] T. Pottier, P. Vacher, F. Toussaint, H. Louche, T. Coudert; Out-of-plane Testing Procedure for Inverse Identification Purpose: Application in Sheet Metal Plasticity; *Experimental Mechanics*, 52 (2012) 951–963
- [¹⁰⁹] A. Shimamoto, T. Shimomura, J. Nam; The development of servo dynamic biaxial loading device; *Key Engineering Materials*, 243-244 (2003) 99-104
- [¹¹⁰] A. Hannon, P. Tiernan; A review of planar biaxial tensile test systems for sheet metal; *Journal of materials processing technology*, 198 (2008) 1–13
- [¹¹¹] E. Shiatori, K. Ikegami; Experimental study of the subsequent yield surface by using cross-shaped specimens; *Journal of the Mechanics and Physics of Solids*,

- 16 (1968) 373-394
- [112] Metallic materials - Sheet and strip - Biaxial tensile testing method using a cruciform test piece; ISO 16842: 2014(E)
- [113] G. Ferron, A. Makinde; Design and development of a biaxial strength testing device; *Journal of Testing and Evaluation*; 16(1988) 253-256
- [114] C. Tasan, J. Hoefnagels, G. Quaak, et al; In-plane biaxial loading of sheet metal until fracture; *Proceedings of the XIth International Congress and Exposition*; (2008) Florida, USA
- [115] A. Makinde, L. Thibodeau, K. Neale; Development of an apparatus for biaxial testing using cruciform specimens; *Experimental Mechanics*, 32(1992)138-144
- [116] T. Kuwabara, S. Ikeda, K. Kuroda; Measurement and analysis of differential work hardening in cold-rolled steel sheet under biaxial tension; *Journal of Materials Processing Technology* 80-81 (1998) 517-523
- [117] W. Muller, K. Pohlant; New experiments for determining yield loci of sheet metal; *Journal of material processing technology* 60 (1996) 643-648
- [118] D. Banabic; Anisotropy and formability of AA5182-0 aluminium alloy sheets; *CIRP Annals - Manufacturing Technology*, 53(2004) 219-222
- [119] T. Naka, Y. Nakayama, T. Uemori et al; Effects of temperature on yield locus for 5083 aluminum alloy sheet; *Journal of Materials Processing Technology* 140 (2003) 494-499
- [120] T. Naka, Y. Nakayama, T. Uemori, et al.; Effect of Strain-Rate and Temperature on Yield Locus for 5083 Aluminum Alloy Sheet; *Key Engineering Materials Vols. 274-276* (2004) pp 937-942
- [121] T. Kuwabara, S. Ikeda, K. Kuroda; Measurement and analysis of differential work hardening in cold-rolled steel sheet under biaxial tension; *Journal of Materials Processing Technology* 80-81 (1998) 517-523
- [122] T. Kuwabara, A. Bael, E. Lizuka; Measurement and analysis of yield locus and work hardening characteristics of steel sheets with different r-values; *Acta Materialia* 50 (2002) 3717-3729
- [123] T. Kuwabara, T. Nakajima; Material modeling of 980 MPa dual phase steel sheet based on biaxial tensile test and in-plane stress reversal test; *Journal of Solid Mechanics and Materials Engineering*; 5 (2011) 709-720
- [124] M. Geiger, M. Merklein, W. Hubnatter; Specimen for a novel concept of the biaxial tension test; *Journal of Materials Processing Technology* 167 (2005) 177-183
- [125] M. Merklein, W. Hubnatter, M. Geiger; Characterization of yielding behavior of sheet metal under biaxial stress condition at elevated temperatures; *CIRP Annals - Manufacturing Technology* 57 (2008) 269-274
- [126] M. Teaca, I. Charpentier, M. Martiny, et al; Identification of sheet metal plastic anisotropy using heterogeneous biaxial tensile tests; *International Journal of Mechanical Sciences* 52 (2010) 572-580
- [127] M. Teaca; Caractérisation expérimental et modélisation de la déformation

- plastique des tôles métalliques; Thèse de doctorat, Université Paul Verlaines-Metz, 2009
- [128] P. Prates, M. Oliveira, J. Fernandes; A new strategy for the simultaneous identification of constitutive laws parameters of metal sheets using a single test, *Computational Materials Science* 85 (2014) 102–120
- [129] S. Zhang; Characterization of anisotropic yield criterion with biaxial tension test. Thesis of PhD, INSA de Rennes, 2014
- [130] A. Makinde, L. Thibodeau, K. Neale; Development of an apparatus for biaxial testing using cruciform specimens; *Experimental Mechanics*, 32(1992) 138-144
- [131] D. Green, K. Neale S. Macewen, et al; Experimental investigation of the biaxial behaviour of an aluminium sheet; *International Journal of Plasticity* 20 (2004) 1677–1706
- [132] A. Makinde, L. Thibodeau, K. Neale, et al; Design of a biaxial extensometer for measuring strains in cruciform specimens; *Experimental mechanics*; 32(1992)132-137
- [133] J. Gozzi, A. Olsson, O. Lagerqvist; Experimental investigation of the behavior of extra high strength steel; *Experimental Mechanics* , 45(2005) 533-540
- [134] J. Gozzi, A. Olsson; Extra high strength steel plasticity - experimental work and constitutive modelling; *Advances in Steel Structures*, Vol. II (2005) 1571-1576
- [135] J. Gozzi; Plastic behavior of steel: Experimental investigation and modeling; Licentiate thesis, Lulea University of technology, 2004
- [136] D. Kulawinski, K. Nagel, S. Henkel, et al.; Characterization of stress–strain behavior of a cast TRIP steel under different biaxial planar load ratios; *Engineering Fracture Mechanics* 78 (2011) 1684–1695
- [137] T. Uemori, T. Kuramitsu, Y. Mito, et al; Elasto-plasticity behavior of high strength steel sheet in biaxial stress path change; *Materials Transactions*, 51 (2010) 1814 -1818
- [138] M. Merklein, M. Biasutti; Development of a biaxial tensile machine for characterization of sheet metals; *Journal of Materials Processing Technology* 213 (2013) 939–946
- [139] M. Merklein et al; Characterisation of kinematic hardening and yield surface evolution from uniaxial to biaxial tension with continuous strain path change; *CIRP Annals - Manufacturing Technology* 63 (2014) 297–300
- [140] Y. Yu, M. Wan, X. Wu, et al; Design of a cruciform biaxial tensile specimen for limit strain analysis by FEM; *Journal of Materials Processing Technology* 123 (2002) 67–70
- [141] C. Tasan, J. Hoefnagels, G. Quak, et al.; In-plane biaxial loading of sheet metal until fracture; *Proceedings of the XIth International Congress and Exposition*; (2008) Florida USA
- [142] Gerard Quak; *Biaxial Testing of Sheet Metal: An Experimental-Numerical Analysis*; Master Thesis, Eindhoven University of Technology, 2008

- [143] F. Abu-Farha, L. Hector, M. Khraisheh; Cruciform-shaped specimens for elevated temperature biaxial testing of lightweight materials; *JOM* , 61(2009)48-56
- [144] F. Abu-Farha, L. Hector, M. Nazzal et al; On the development of viable cruciform-shaped specimens: towards accurate elevated temperature biaxial testing of lightweight materials; *Key Engineering Materials*, 433 (2010) 93-101
- [145] R. Lee, T Chien; A new method for testing formability in sheet metal forming at biaxial tensile state; *Key Engineering Materials*, 626 (2015) 275-280
- [146] I. Zidane, D. Guines, L Leotoing, et al; Development of an in-plane biaxial test for forming limit curve (FLC) characterization of metallic sheets ; *Measurement Science and Technology*. 21 (2010) 055701 (11pp)
- [147] I. Zidane; Développement d'un banc d'essai de traction biaxiale pour la caractérisation de la formabilité et du comportement élastoplastique de tôles métalliques. Thèse de doctorat, INSA de Rennes, 2009.
- [148] L. Leotoing, D. Guines, I. Zidane, et al; Cruciform shape benefits for experimental and numerical evaluation of sheet metal formability; *Journal of Materials Processing Technology* 213 (2013) 856– 863
- [149] 5xxx Plate information sheet at www.alcoa.com;
- [150] A. Makinde, L. Thibodeau, K. Neale, et al; Design of a biaxial extensometer for measuring strains in cruciform specimens; *Experimental mechanics*; 32(1992)132-137
- [151] H. Schreier, J. Orteu, M. Sutton; *Image Correlation for Shape, Motion and Deformation Measurements: Basic Concepts, Theory and Applications*; Springer (2009)
- [152] J. Dupré, P. doumalin, V. Valle et al. Mode d'emploi du logiciel CORRELA 2006. Université de Poitiers, (2006).
- [153] B. Pan, K. Qian, H. Xie, et al; Two-dimensional digital image correlation for in-plane displacement and strain measurement: a review; *Measurement Science and Technology*, 20 (2009) 1-17
- [154] F. Kabirian, A. Khan, A. Pandey; Negative to positive strain rate sensitivity in 5XXX series aluminum alloys: Experiment and constitutive modeling; *International Journal of Plasticity*, 55(2014) 232-246
- [155] A. Rusinel, J. Rodriguez-Martinez; Thermo-viscoplastic constitutive relation for aluminium alloys, modeling of negative strain rate sensitivity and viscous drag effects; *Materials and Design*, 30 (2009) 4377-4390
- [156] P. Hahner, E. Rizzi; On the kinematics of Portevin-Le Chatelier bands: theoretical and numerical modelling; *Acta Materialia*, 51 (2003) 3385-3397
- [157] P. Manach, S. Thuillier, J. Yoon, J. Coer, H. Laurant; Kinematics of Portevin-Le Chatelier bands in simple shear; *International Journal of Plasticity*, 58 (2014) 66-83
- [158] A. Tarantola; *Inverse problem theory and methods for model parameter estimation*; Society for Industrial and Applied Mathematics, (2005) ISBN 0-89871-572-5
- [159] S. Diot; *Caractérisation expérimental et numérique du comportement dynamique*

- des matériaux; Thèse de doctorat, INSA de Rennes, 2003
- [160] B. Chaparro, S. Thuillier, L. Menezes, P. Manach, J. Fernandes; Material parameters identification: Gradient-based, genetic and hybrid optimization algorithms; *Computational Materials Science*, 44 (2008) 339-346
- [161] Poles S., The SIMPLEX method, ESTECO Technical Report, 2003-005.
- [162] I. Zidane; Développement d'un banc d'essai de traction biaxiale pour la caractérisation de la formabilité et du comportement élastoplastique de tôles métalliques. Thèse de doctorat, INSA de Rennes, 2009.
- [163] S. Zhang; Characterization of anisotropic yield criterion with biaxial tension test; Thesis of PhD, INSA de Rennes, 2014
- [164] B. Roebuck, M. Brooks, M. Gee; Load cell ringing in high rate compression tests; *Applied Mechanics and Materials*, 1-2 (2004) 205-210
- [165] A. M. Horr and L. C. Schmidt; Modelling of nonlinear damping characteristics of a viscoelastic structural damper, *Engineering Structures*, Vol. 18, No. 2, pp. 154-161, 1996
- [166] S. W. Park, Analytical modeling of viscoelastic dampers for structural and vibration control, *International Journal of Solids and Structures* 38(2001) 8065-8092
- [167] Advanced high-strength steel application guidelines v 5.0;
<http://www.worldautosteel.org/>
- [168] DP600 CR: High strength, high ductility, high formability;
<http://www.tatasteelautomotive.com/>
- [169] J. Sung, J. Kim, R. Wagoner; A plastic constitutive equation incorporating strain, strain-rate, and temperature; *International Journal of Plasticity* 26 (2010) 1746-1771
- [170] P. Larour; Strain rate sensitivity of automotive sheet steels: influence of plastic strain, strain rate, temperature, microstructure, bake hardening and pre-strain; Thesis of PhD, RWTH Aachen university, 2010
- [171] Rigoni E., Technical Report 2003-007, Bounded BFGS; ESTCO.
- [172] H. Yu, Y. Guo, K Zhang et al Constitutive model on the description of plastic behavior of DP600 steel at strain rate from 10^{-4} to 10^3 s $^{-1}$; *Computational Materials Science*, 46 (2009) 36-41
- [173] F. Ozturk, S. Toros, S. Kilic; Effects of anisotropic yield functions on prediction of forming limit diagrams of DP600 advanced high strength steel; ICTP 2014, 19-24 October 2014, Japan, *Procedia Engineering* 81 (2014) 760-765
- [174] M. Iadicola, T. Foecke, S. Banovic; Experimental observations of evolving yield loci in biaxially strained AA5754-O; *International Journal of Plasticity*, 24 (2008) 2084-2101
- [175] T. Stoughton, J. Yoon; Anisotropic hardening and non-associated flow in proportional loading of sheet metals; *International Journal of Plasticity*, 25 (2009) 1777-1817
- [176] A. Khan, A. Pandey, T. Stoughton; Evolution of subsequent yield surfaces and

- elastic constants with finite plastic deformation. Part III : Yield surface in tension-tension stress space (Al 6061-T 6511 and annealed 1100 Al); *International Journal of Plasticity*, 26 (2010) 1432-1441
- [177] F. Yoshida, H. Hamasaki, T. Uemori; A model of anisotropy evolution of sheet metals; ICTP 2014, October 2014, Japan, *Procedia Engineering* 81 (2014) 1216-1221
- [178] J. Huh, H. Huh, C. Lee; Effect of strain rate on plastic anisotropy of advanced high strength steel sheets; *International Journal of Plasticity*, 44 (2013) 23-46
- [179] A. Hassanejadasl, T. Rahmaan, D. Green, S. Golovashchenko, M. Worswick; Prediction of DP600 flow surfaces at various strain-rates using Yld2004-18p yield function; ICTP 2014, 19-24 October 2014, Japan, *Procedia Engineering* 81 (2014) 1387-1383

AVIS DU JURY SUR LA REPRODUCTION DE LA THESE SOUTENUE

Titre de la thèse:

Identification of strain-rate dependent hardening sensitivity of metallic sheets under in-plane biaxial loading

Nom Prénom de l'auteur : LIU WEI

Membres du jury :

- Monsieur RAGNEAU ERIC
- Monsieur GUINES Dominique
- Monsieur LEOTOING Lionel
- Madame BOUVIER Salima
- Monsieur MOREL Franck
- Monsieur GROLLEAU Vincent

Président du jury : *F. Morel*

Date de la soutenance : 10 Mars 2015

Reproduction de la these soutenue

Thèse pouvant être reproduite en l'état

~~Thèse pouvant être reproduite après corrections suggérées~~

Fait à Rennes, le 10 Mars 2015

Signature du président de jury

Le Directeur,

M'hamed DRISSE

